POLISH ACADEMY OF SCIENCES
INSTITUTE OF PHYSICS

Established in 1920 by
the Polish Physical Society

ACTA PHYSICA POLONICA

- General Physics
- Atomic and Molecular Physics
- Condensed Matter
- Optics and Quantum Optics
- Quantum Information
- Biophysics
- Applied Physics

Proceedings of "Applications of Physics in Mechanical and Material Engineering" Częstochowa, Poland, June 29, 2023

RECOGNIZED BY THE EUROPEAN PHYSICAL SOCIETY

Volume 144 — Number 5, Warsaw, November 2023

PL ISSN 0587-4246 ATPLB6 144 (5) 273–414 (2023)

Address of the Publisher:
Instytut Fizyki PAN
al. Lotników 32/46
02-668 Warszawa, Poland
e-mail: appol@ifpan.edu.pl

Printed in Poland:
Drukarnia HAJSTRA Sp. z o.o.
M. Langiewicza 28
05-825 Grodzisk Mazowiecki
drukarnia-hajstra.com
e-mail: hajstra.biuro@gmail.com

POLISH ACADEMY OF SCIENCES
INSTITUTE OF PHYSICS

Established in 1920 by
the Polish Physical Society

ACTA PHYSICA POLONICA

- General Physics
- Atomic and Molecular Physics
- Condensed Matter
- Optics and Quantum Optics
- Quantum Information
- Biophysics
- Applied Physics

Proceedings of "Applications of Physics in Mechanical and Material Engineering" Częstochowa, Poland, June 29, 2023

RECOGNIZED BY THE EUROPEAN PHYSICAL SOCIETY

Volume 144 — Number 5, Warsaw, November 2023

PL ISSN 0587-4246 ATPLB6 144 (5) 273–414 (2023)

Proceedings of "Applications of Physics in Mechanical and Material Engineering" (APMME 2023)

Częstochowa, Poland,
June 29, 2023

Editors of the Proceedings:

Wojciech Sochacki
Sebastian Garus
Marcin Nabiałek
Paweł Kwiatoń

WARSAW

POLISH ACADEMY OF SCIENCES
INSTITUTE OF PHYSICS

Scientific Committee:

Wojciech Sochacki *(Chairman)*

Mechanical Engineering Section	**Materials Engineering Section**	**Computer Science and Telecommunications Section**
Janusz Szmidla *(Chairman)*	Marcin Nabiałek *(Chairman)*	Mariusz Kubanek *(Chairman)*
Dawid Cekus *(Vice-Chairman)*	Jerzy J. Wysłocki *(Vice-Chairman)*	Janusz Bobulski *(Vice-Chairman)*

Other Members of the Scientific Committee:

M.M.A.B. Abdullah	G. Golański	A. Rylski
Y. Aksu	J. Gondro	M. Sága
J. Bajkowski	G. Goller	A.V. Sandu
M. Bajkowski	R. Gozdur	A. Sapietová
P. Bała	M. Jarosik	V. Savinkin
K. Błoch	B. Jeż	K. Sokół
W. Borek	M. Klimek	M. Sroka
D. Cekus	M. Kubiak	A. Surleva
K. Chwastek	P. Kwiatoń	R. Szczęśniak
P. Czaja	B. Major	M. Šofer
G. Dercz	A. Markopoulos	A. Śliwa
T. Domański	G. Marmaryan	T. Tański
A. Durajski	P. Pietrusiewicz	S. Uzny
S. Garus	B. Posiadała	P. Vizureanu
P. Gębara	P. Postawa	S. Walters
R. Gnatowska	J. Przybylski	R. Zalewski
A. Gnatowski	H. Purzyńska	A. Zieliński

Organizing Committee:

Chairman:	Sebastian Garus
Vice-Chairman:	Wojciech Sochacki
Vice-Chairman:	Marcin Nabiałek
Vice-Chairman:	Mariusz Kubanek
Secretary:	Paweł Kwiatoń
Members:	Justyna Garus
	Bartłomiej Jeż
	Andrei Victor Sandu
	Renata Gnatowska

Main Topics:

- Physical and chemical properties of materials
- Condensed matter physics
- Applied physics
- Vibrations and stability in physical systems
- Modelling of structural materials
- Modelling and simulation, structural optimization
- Methods and systems in machine design
- Theoretical and applied mathematics and physics in engineering
- Experimental mechanics and numerical validation
- Machine dynamics and multibody systems simulations

Preface

The works included in this special issue were presented during the fourth edition of the international scientific conference "Application of Physics in Mechanical and Materials Engineering" — APMME 2023. This conference took place on June 29, 2023 in Częstochowa. The conference was organized, as usual, by the Department of Mechanics and Fundamentals of Machine Design at the Faculty of Mechanical Engineering and Computer Science at the Czestochowa University of Technology. This year, the scientific meeting of APMME was held in conjunction with the International Exhibition of Innovation — IEI 2023. The honorary patronage over the conference and exhibition was taken by the Rector of the Czestochowa University of Technology, Professor Norbert Sczygiol.

On behalf of the Scientific and Organizational Committee of the APMME 2023 conference, we would like to thank the Rector of the Czestochowa University of Technology for his honorary patronage over the conference. We would also like to thank the Dean of the Faculty, Professor Małgorzata Klimek, for significant help in organizing the conference. Our warm words of thanks go to all participants who kindly responded to the invitation of the Organizing Committee of the APMME 2023 conference. We would like to express our special thanks to the keynote and invited speakers.

The APMME conference has been an international conference for two years and has become a permanent fixture in the calendar of important conferences in our country. During the meeting, participants from Poland and abroad could present and discuss the latest achievements in the field of broadly understood applications of physics in mechanical and materials engineering. Over seventy participants from Poland, Bulgaria, Canada, China, Czech Republic, India, Malaysia, Romania, Taiwan, and Turkey have registered for the APMME 2023 conference. Participants presented their works at plenary sessions and in a poster session. The conference papers submitted to the Scientific Committee were reviewed and sent for approval to the Publishing Team of *Acta Physica Polonica A*.

The Guest Editors would like to thank the Editorial Staff for their effort and help in preparing this issue.

Wojciech Sochacki
Marcin Nabiałek
Sebastian Garus
Paweł Kwiatoń

Guest Editors

Proceedings of "Applications of Physics in Mechanical and Material Engineering" (APMME 2023)

Influence of Chemical Composition on the Curie Temperature Change in Amorphous Alloys

B. Jeż*

Department of Technology and Automation, Faculty of Mechanical Engineering and Computer Science, Czestochowa University of Technology, al. Armii Krajowej 19c, 42-200 Częstochowa, Poland

Doi: 10.12693/APhysPolA.144.281 *e-mail: bartlomiej.jez@pcz.pl

Amorphous alloys are characterized by a disordered structure. The arrangement of atoms is chaotic and it is difficult to determine the parameters describing their properties. In soft magnetic ferromagnets, one of the main parameters describing their applicability is the Curie temperature. However, in amorphous materials, due to their metastable nature, the Curie temperature occurs in a rather narrow range. Using the measurements of the magnetic saturation polarization as a function of temperature and the critical exponent $\beta = 0.36$, the value of the Curie temperature can be determined. The paper presents the results of $\mu_0 M(T)^{1/\beta}$ tests carried out for two amorphous alloys with similar chemical composition. The influence of chemical composition on the course of the $\mu_0 M(T)$ curve and changes in the share of characteristic areas describing rearrangements of atoms in the structure of alloys were observed.

topics: bulk amorphous alloys, Curie temperature, coercieve field, soft magnetic properties

1. Introduction

Depending on their chemical composition, amorphous alloys have much better mechanical and magnetic properties than their crystalline counterparts. In many industries, great emphasis is placed on introducing better and better materials with specific properties into products. Both materials exhibiting the so-called soft magnetic properties [1, 2] and hard magnetic properties [3–5] are desirable. Due to the constantly growing progress in the field of electronics and electrical engineering, materials with good magnetic properties that can be used as transformer cores or chokes are of particular interest [5–7]. Therefore, research is constantly being conducted on amorphous and nanocrystalline alloys, the properties of which can be controlled, among others, by small changes in the chemical composition [8–10]. It should be added here that there are two groups of amorphous materials: classical and bulk amorphous materials [11]. The classic ones include mainly thin tapes with a thickness of about 100 μm. Such tapes are produced at cooling rates up to 106 K/s. Using the melt spinning technique, which involves squirting liquid metal onto a rotating copper wheel, it is possible to produce tapes with an amorphous structure. Unfortunately, this method does not enable the production of thicker samples of given shapes, which significantly limits the application possibilities of the materials. From the 1970s to the end of the 1990s, work was carried out on the possibility of obtaining samples in the form of plates or rods with thicknesses above 0.5 mm [12]. In 1989, A. Inoue from Tohoku University in Japan presented for the first time criteria enabling the systematic production of amorphous materials with thicknesses greater than the maximum for tapes [13, 14]. Since then, a new group of amorphous materials has been distinguished, called bulk amorphous materials. Inoue established in his assumptions that to achieve good glass transition ability, it is necessary to carefully design the chemical composition of the alloy. The most important thing is that the alloy consists of at least three components, the atomic radii of at least the main components differ by more than 12%, and the negative heat of mixing between the components is as high as possible. All these criteria are intended to limit the migration of atoms in the solidifying alloy, which, of course, prevents the formation of a crystalline structure. In amorphous materials, and especially in bulk amorphous materials, there can be changes in the structure within the amorphous state, which is reflected in sensitive property measurements.

The paper presents test results performed for bulk amorphous alloys of composition $Fe_{34}Co_{34}Nb_4W_2Me_3B_{23}$, where Me = Y or Gd. The structure of the alloys and their magnetic properties were examined.

2. Experimental procedure

Polycrystalline alloys were produced in an arc furnace. The process was carried out in a protective atmosphere of argon on a copper plate cooled by water. The ingredients used were 99.99% pure (for boron — 99.9%). Ingots weighing 5 g were melted using a non-fusible tungsten electrode at an intensity of 180–300 A. The remelting process was preceded by melting a titanium getter to capture the remaining oxygen in the working chamber. The process was repeated 5 times to homogenize the structure and chemical composition of the alloy. Rapidly quenched alloys were made by cooling using the injection casting method. Samples were obtained in the form of rods with a diameter of 1 mm and a length of 20 mm. The production process was carried out in a protective atmosphere of argon. The polycrystalline batch was placed in a quartz crucible with a hole of 1 mm in diameter. Melting was carried out using eddy currents, and the liquid alloy was forced into a copper mold cooled by water under argon pressure.

The structure of the alloys was examined using X-ray diffraction. The tests were carried out using a Bruker ADVANCE 8 X-ray diffractogram equipped with a Cu K_α lamp. The measurement was carried out in the range of 30–100° of the 2Θ angle with a time of 5 s per measurement step of 0.02°.

Thermomagnetic curves were measured using a Faraday magnetic balance. The measurement was carried out in the range from room temperature to 850 K at a constant external magnetic field intensity of 0.7 T.

Static magnetic hysteresis loops were measured using a VSM 7307 vibration magnetometer in the range of an external magnetic field up to 2 T.

3. Results

Figure 1 shows X-ray diffraction patterns measured for the produced alloys. The recorded diffractograms show only broad maxima coming from X-rays reflected on atoms chaotically distributed in the volume of the alloys. This proves the amorphous structure of the tested alloys. Samples of the produced alloys were subjected to thermomagnetic tests.

The saturation magnetic polarization curves are shown in Fig. 2. The curves show single mild inflections related to the transition of the magnetic phase from the ferro- to paramagnetic state.

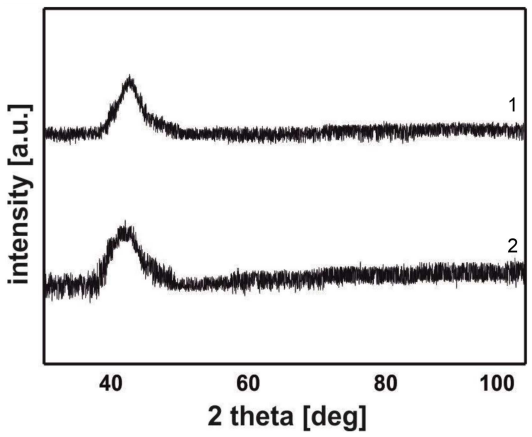

Fig. 1. X-ray diffraction patterns for the rod-form samples of the investigated alloys: 1 — $Fe_{34}Co_{34}Nb_4W_2Y_3B_{23}$, 2 — $Fe_{34}Co_{34}Nb_4W_2Gd_3B_{23}$.

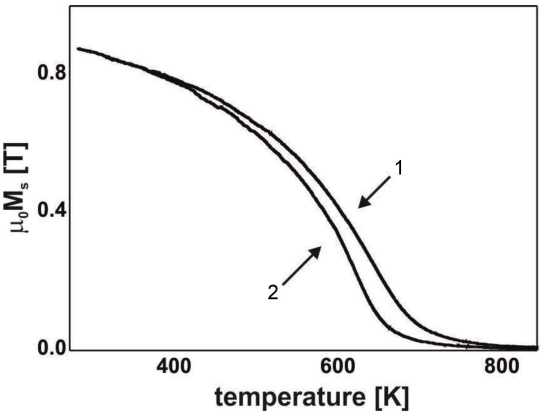

Fig. 2. Thermomagnetic curves obtained for the tested alloy samples: 1 — $Fe_{34}Co_{34}Nb_4W_2Y_3B_{23}$, 2 — $Fe_{34}Co_{34}Nb_4W_2Gd_3B_{23}$.

It should be remembered that for amorphous alloys, the T_C value is rather the temperature range in which the magnetic transition occurs (it is not a discrete value). This is due to the presence of micro-areas in the alloy volume with slightly different atomic arrangements. The measured curves were analyzed using the critical coefficient $\beta = 0.36$ used for ferromagnetics meeting Heisenberg's assumptions [15] (Fig. 3).

Curie temperature T_C values were determined based on the $(\mu_0 M)^{1/\beta}$ curves. It was found that the alloy with the addition of Gd is characterized by a lower T_C value (629 K) compared to the alloy with the addition of Y (643 K).

Figure 4 shows static magnetic hysteresis loops. The measured loops are similar to each other. However, for the alloy with the addition of Gd, a more than twice lower value of the coercive field H_C was determined with almost the same saturation magnetization value M_S.

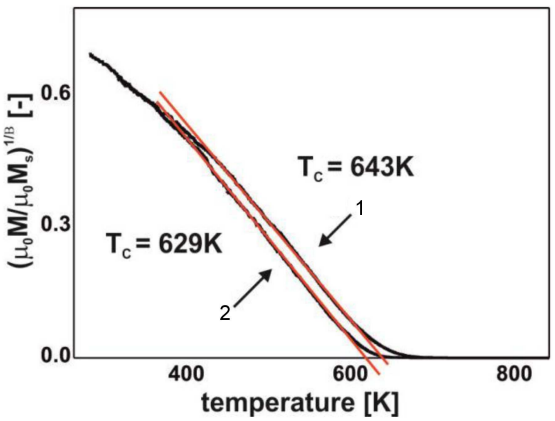

Fig. 3. Relationship of $(\mu_0 M)^{1/\beta}$ with temperature, T, for the tested alloys: 1 — $Fe_{34}Co_{34}Nb_4W_2Y_3B_{23}$, 2 — $Fe_{34}Co_{34}Nb_4W_2Gd_3B_{23}$.

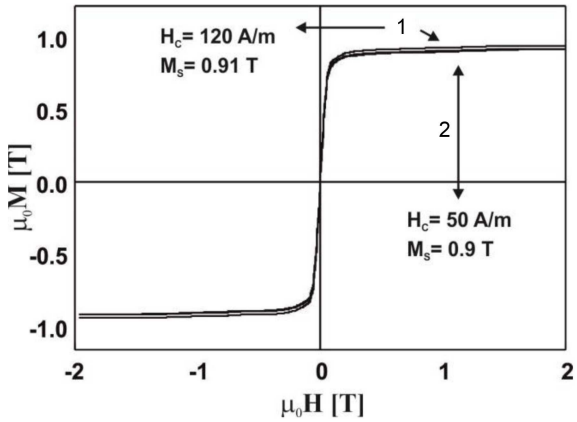

Fig. 4. Static magnetic hysteresis loops for the tested alloys: 1 — $Fe_{34}Co_{34}Nb_4W_2Y_3B_{23}$, 2 — $Fe_{34}Co_{34}Nb_4W_2Gd_3B_{23}$.

Gd has ferromagnetic properties, unlike Y. However, the addition of Gd reduces the T_C value. This is related to the influence of Y on the structure of the alloy. The presence of this element increases the number of free volumes, which causes the stabilization of the subcooled liquid and, consequently, a possible increase in the T_C and M_S values. This influence is related, among other things, to the significant size of Y atoms (atomic radius 182 pm). Such a relationship is observed in the case of the tested alloys.

4. Conclusions

The work showed that the addition of Gd at the expense of Y improves the magnetic properties of Fe–Co–B alloys. Gadolinium and yttrium have similar atomic radius lengths. However, these elements have different properties. Due to its electronic structure, Gd has ferromagnetic properties, while Y is paramagnetic. However, the addition of Gd does not improve M_S and T_C. However, the addition of this component facilitates the magnetization process, as indicated by the value of the coercive field. As is known, the addition of Gd affects the formation of hard magnetic phases. However, as the above test results indicate, a small addition of Gd may improve the soft magnetic properties as long as the rapidly cooled alloy remains in the sphere of the amorphous structure.

References

[1] Y. Han, C.T. Chang, S.L. Zhu, A. Inoue, D.V. Louzguine-Luzgin, E. Shalaan, F. Al-Marzouki, *Intermetallics* **54**, 169 (2014).

[2] Y. Han, J. Ding, F.L. Kong, A. Inoue, S.L. Zhu, Z. Wang, E. Shalaan, F. Al-Marzouki, *J. Alloys Compd.* **691**, 364 (2017).

[3] J.-Y. Cho, M.-S. Song, Y.-H. Choa, T.-S. Kim, *Arch. Metall. Mater.* **66**, 955 (2021).

[4] S. Park, S.-W. Nam, J.-Y. Cho, S.-H. Lee, S.-K. Hyun, T.-S. Kim, *Arch. Metall. Mater.* **65**, 1281 (2020).

[5] H.F. Li, Y.F. Zheng, *Acta Biomater.* **36**, 1 (2016).

[6] W.H. Wang, C. Dong, C.H. Shek, *Mater. Sci. Eng. R* **44**, 45 (2004).

[7] M. E.Mchenry, M. A. Willard, D.E. Laughlin, *Prog. Mater. Sci.* **44**, 291 (1999).

[8] L. Xue, H. Liu, L. Dou, W. Yang, C. Chang, A. Inoue, X. Wang, R.-W. Li, B. Shen, *Mater.d Design* **56**, 227 (2014).

[9] Y. Han, Z. Wang, Y. Xu, Z. Xie, L. Li, *J. Non-Cryst. Solids* **442**, 29 (2016).

[10] X. Li, C. Qin, H. Kato, A. Makino, A. Inoue, *J. Alloys Compd.* **509**, 7688 (2011).

[11] M.-N. Avettand-Fenoel, M. Marinova, R. Taillard, W. Jiang, *J. Alloys Compd.* **854**, 157068 (2021).

[12] H.S. Chen, D. Turnbull, *Acta Metall.* **17**, 1021 (1969).

[13] A. Inoue, T. Zhang, T. Masumoto, *Mater. Trans. JIM* **31**, 177 (1990).

[14] A. Takeuchi, A. Inoue, *Mater. Trans.* **46**, 2817 (2005).

[15] J. Coey, *Magnetism and Magnetic Materials*, Cambridge, 2009.

Proceedings of "Applications of Physics in Mechanical and Material Engineering" (APMME 2023)

The Influence of Medium Movement on the Occurrence of Band Gaps in Quasi Two Dimensional Phononic Crystals

S. Garus[a,*], W. Sochacki[a] and J. Rzącki[b]

[a]*Department of Mechanics and Fundamentals of Machinery Design, Faculty of Mechanical Engineering and Computer Science, Czestochowa University of Technology, Dąbrowskiego 73, 42-201 Częstochowa, Poland*
[b]*Department of Physics, Faculty of Production Engineering and Materials Technology, Czestochowa University of Technology, Dąbrowskiego 73, 42-201 Częstochowa, Poland*

Doi: 10.12693/APhysPolA.144.284 *e-mail: sebastian.garus@pcz.pl

Phononic quasi-two-dimensional structures, due to their properties, namely the lack of propagation of selected frequency ranges of the mechanical wave, can be used as filters of acoustic waves. In the paper, an analysis of the propagation of mechanical waves in these highly dispersive structures in the conditions of a moving medium was carried out. The influence of the number of metaatom layers on the transmission of a mechanical wave for different medium velocities was analysed.

topics: phononic crystal, finite-difference time domain (FDTD), moving medium, band gaps

1. Introduction

Research on sound propagation in periodic structures and the formation of band gaps in phononic crystals is conducted by many research centers around the world. These are works in which the authors, apart from describing the formation of the band gap [1, 2], point to the practical application of this phenomenon in periodic structures. They therefore indicate the possibility of using phononic crystals as acoustic wave filters [3–6], waveguides [7] or acoustic diodes [8]. These studies most often concern cases of sound propagation without movement of the medium in which the sound propagates.

However, taking into account that the speed of sound is only about 34–110 times higher than typical wind speeds in the atmosphere, it should be assumed that wind and turbulence in the atmosphere have a significant impact on sound propagation.

Among the many methods that can be used to describe this issue, such as the curved ray tracing method [9] or the transmission-line matrix method (TLM) [10], the most promising is the finite-difference time domain (FDTD) method. The use of the FDTD method to describe the propagation of acoustic waves in a moving medium is the subject of many works. In [11], the authors proposed two sets of differential equations to describe the propagation of sound in a moving atmosphere. The sound propagation in a moving medium for the case when the typical speed of movement in the medium is slightly lower than the speed of wave propagation through the medium was the subject of work [12]. In turn, works [13, 14] present two-dimensional FDTD calculations for the atmosphere, taking into account the influence of motion (wind and turbulence) in the propagation medium, as well as the interaction with the ground. Extensive literature on a wide range of issues related to the linear propagation of sound in a moving medium is presented in the review article [15].

Using a finite-difference algorithm in the time domain, the work analyzed the influence of medium motion on the propagation and transmission of mechanical waves in quasi-two-dimensional phononic structures with various numbers of layers.

2. Finite difference time domain algorithm for a moving medium

The propagation of a mechanical wave in a moving medium is described by a system of first-order differential equations

$$\frac{\partial p}{\partial t} = -\kappa \nabla \cdot \boldsymbol{w}, \tag{1}$$

$$\frac{\partial \boldsymbol{w}}{\partial t} = -b \nabla p, \tag{2}$$

which for the two-dimensional case gives

$$\frac{\partial p}{\partial t} = -\kappa \left(\frac{\partial w_x}{\partial x} + \frac{\partial w_y}{\partial y} \right), \tag{3}$$

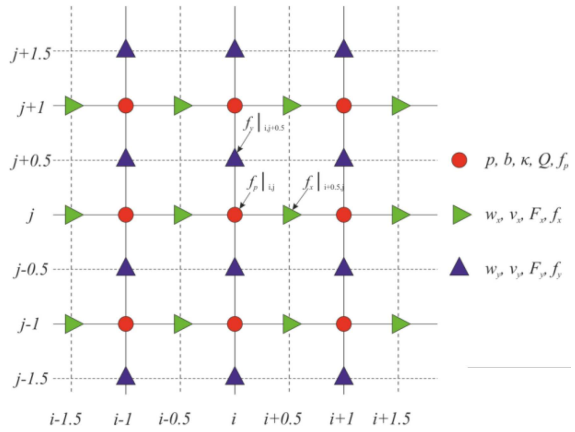

Fig. 1. Spatially staggered finite-difference grid used for the calculations.

$$\frac{\partial w_x}{\partial t} = -b\frac{\partial p}{\partial x}, \tag{4}$$

$$\frac{\partial w_y}{\partial t} = -b\frac{\partial p}{\partial y}, \tag{5}$$

where p is the acoustic pressure, $\boldsymbol{w}$ is the acoustic particle velocity, t is the time. The adiabatic bulk modulus κ $[\frac{\mathrm{kg}}{\mathrm{m\,s^2}}]$ is defined by

$$\kappa = \rho\, c^2, \tag{6}$$

and the mass buoyancy b is defined by

$$b = 1/\rho, \tag{7}$$

where ρ is the ambient medium density, and c is the adiabatic speed of sound.

Assuming that the sound wave causes slight disturbances in the medium, there is no turbulence of the background velocity field, and due to the consideration of sound propagation near the ground, the background pressure gradient is omitted and the medium is adiabatic. Then the propagation of a mechanical wave in a moving medium is described by

$$\frac{\partial p}{\partial t} = -\left(\boldsymbol{v}\cdot\nabla\right)p - \rho\, c^2\nabla\cdot\boldsymbol{w} + \rho c^2 Q, \tag{8}$$

$$\frac{\partial \boldsymbol{w}}{\partial t} = -\left(\boldsymbol{w}\cdot\nabla\right)\boldsymbol{v} - \left(\boldsymbol{v}\cdot\nabla\right)\boldsymbol{w} - \frac{\nabla p}{\rho} + \frac{\boldsymbol{F}}{\rho}. \tag{9}$$

In equations (8) and (9), $\boldsymbol{v}$ is the wind velocity. The sources are represented as $\boldsymbol{F}$ (a force acting on the medium — dipole pressure source) and Q (mass source — monopole pressure source).

Equations (8) and (9) for the two-dimensional case gives

$$\frac{\partial p}{\partial t} = -\left(v_x\frac{\partial p}{\partial x} + v_y\frac{\partial p}{\partial y}\right) - \kappa\left(\frac{\partial w_x}{\partial x} + \frac{\partial w_y}{\partial y}\right) + \kappa Q, \tag{10}$$

$$\frac{\partial w_x}{\partial t} = -\left(w_x\frac{\partial v_x}{\partial x} + w_y\frac{\partial v_x}{\partial y}\right) - \left(v_x\frac{\partial w_x}{\partial x} + v_y\frac{\partial w_x}{\partial y}\right) - b\frac{\partial p}{\partial x} + bF_x, \tag{11}$$

$$\frac{\partial w_y}{\partial t} = -\left(w_x\frac{\partial v_y}{\partial x} + w_y\frac{\partial v_y}{\partial y}\right) - \left(v_x\frac{\partial w_y}{\partial x} + v_y\frac{\partial w_y}{\partial y}\right) - b\frac{\partial p}{\partial y} + bF_y. \tag{12}$$

Figure 1 shows the grid used in the calculations. The spatial coordinates x and y are determined from the product of the appropriate node coordinates i and j and the appropriate grid spacings Δx and Δy by

$$(x, y) = (i\Delta x, j\Delta y)\,. \tag{13}$$

The pressure p is stored in the nodes with the integer values of variables i and j, just like the values of b, κ, Q and the component f_p. The non-integer nodes store the horizontal and vertical components of $\boldsymbol{w}$, $\boldsymbol{v}$ and $\boldsymbol{F}$.

In order to take into account the division of time and space, the notation $p|^n_{i,j}$ was introduced, where for the pressure p the coefficients "i", "j" mean a simplified notation of the position in space, which in full form is defined by $i\,\Delta x$ and $j\,\Delta y$, respectively, while "n" is a simplified notation of the moment $n\,\Delta t$ in time, where Δt is the value of a single time step.

Expanding the derivatives into appropriate differences and assuming that $\Delta x = \Delta y$, equations (10)–(12) take the form

$$\frac{\partial}{\partial t}\,p|^n_{i,j} = -\frac{1}{4\Delta x}\left(v_x|^n_{i+0.5,j} + v_x|^n_{i-0.5,j}\right)\left(p|^n_{i+1,j} - p|^n_{i-1,j}\right) - \frac{1}{4\Delta x}\left(v_y|^n_{i,j+0.5} + v_y|^n_{i,j-0.5}\right)\left(p|^n_{i,j+1} - p|^n_{i,j-1}\right) - \frac{\kappa|^n_{i,j}}{\Delta x}\left(w_x|^n_{i+0.5,j} - w_x|^n_{i-0.5,j} + w_y|^n_{i,j+0.5} - w_y|^n_{i,j-0.5}\right) + \kappa|^n_{i,j}\;Q|^n_{i,j}\,, \tag{14}$$

$$\frac{\partial}{\partial t}\,w_x|^n_{i+0.5,j} = -\frac{w_x|^n_{i+0.5,j}}{2\Delta x}\left(v_x|^n_{i+1.5,j} - v_x|^n_{i-0.5,j}\right) - \frac{v_x|^n_{i+0.5,j}}{2\Delta x}\left(w_x|^n_{i+1.5,j} - w_x|^n_{i-0.5,j}\right) - \frac{v_x|^n_{i+0.5,j+1} - v_x|^n_{i+0.5,j-1}}{8\Delta y}\left(w_y|^n_{i+1,j+0.5} + w_y|^n_{i,j+0.5} + w_y|^n_{i+1,j-0.5} + w_y|^n_{i,j-0.5}\right) - \frac{w_x|^n_{i+0.5,j+1} - w_x|^n_{i+0.5,j-1}}{8\Delta y}\left(v_y|^n_{i+1,j+0.5} + v_y|^n_{i,j+0.5} + v_y|^n_{i+1,j-0.5} + v_y|^n_{i,j-0.5}\right) - \frac{1}{2\Delta x}\left(b|^n_{i+1,j} + b|^n_{i,j}\right)\left(p|^n_{i+1,j} - p|^n_{i,j}\right) + \frac{b|^n_{i+1,j} + b|^n_{i,j}}{2}\;F_x|^n_{i+0.5,j}\,, \tag{15}$$

$$\frac{\partial}{\partial t}\, w_y|_{i,j+0.5}^{n} = -\frac{w_y|_{i,j+0.5}^{n}}{2\Delta x}\left(v_y|_{i,j+1.5}^{n} - v_y|_{i,j-0.5}^{n}\right) - \frac{v_y|_{i,j+0.5}^{n}}{2\Delta x}\left(w_y|_{i,j+1.5}^{n} - w_y|_{i,j-0.5}^{n}\right)$$
$$-\frac{v_y|_{i+1,j+0.5}^{n} - v_y|_{i-1,j+0.5}^{n}}{8\Delta x}\left(w_x|_{i+0.5,j+1}^{n} + w_x|_{i+0.5,j}^{n} + w_x|_{i-0.5,j+1}^{n} + w_x|_{i-0.5,j}^{n}\right)$$
$$-\frac{w_y|_{i+1,j+0.5}^{n} - w_y|_{i-1,j+0.5}^{n}}{8\Delta x}\left(v_x|_{i+0.5,j+1}^{n} + v_x|_{i+0.5,j}^{n} + v_x|_{i-0.5,j+1}^{n} + v_x|_{i-0.5,j}^{n}\right)$$
$$-\frac{1}{2\Delta x}\left(b|_{i,j+1}^{n} + b|_{i,j}^{n}\right)\left(p|_{i,j+1}^{n} - p|_{i,j}^{n}\right) + \frac{b|_{i,j+1}^{n} + b|_{i,j}^{n}}{2}\, F_y|_{i,j+0.5}^{n}\,. \tag{16}$$

In order to simplify the notation, the functions $f_p|_{i,j}^{n}$, $f_x|_{i+0.5\,j}^{n}$ and $f_y|_{i\,j+0.5}^{n}$ are defined, respectively, as

$$f_p|_{i,j}^{n} = -\tfrac{1}{4\Delta x}\left(v_x|_{i+0.5,j}^{n} + v_x|_{i-0.5,j}^{n}\right)\left(p|_{i+1,j}^{n} - p|_{i-1,j}^{n}\right)$$
$$-\tfrac{1}{4\Delta x}\left(v_y|_{i,j+0.5}^{n} + v_y|_{i,j-0.5}^{n}\right)\left(p|_{i,j+1}^{n} - p|_{i,j-1}^{n}\right)$$
$$-\tfrac{\kappa|_{i,j}^{n}}{\Delta x}\left(w_x|_{i+0.5,j}^{n} - w_x|_{i-0.5,j}^{n} + w_y|_{i,j+0.5}^{n} - w_y|_{i,j-0.5}^{n}\right)$$
$$+\kappa|_{i,j}^{n}\, Q|_{i,j}^{n}, \tag{17}$$

$$f_x|_{i+0.5,j}^{n} = -\tfrac{w_x|_{i+0.5,j}^{n}}{2\Delta x}\left(v_x|_{i+1.5,j}^{n} - v_x|_{i-0.5,j}^{n}\right)$$
$$-\tfrac{v_x|_{i+0.5,j+1}^{n} - v_x|_{i+0.5,j-1}^{n}}{8\Delta x}\left(w_y|_{i+1,j+0.5}^{n} + w_y|_{i,j+0.5}^{n}\right.$$
$$\left. + w_y|_{i+1,j-0.5}^{n} + w_y|_{i,j-0.5}^{n}\right)$$
$$-\tfrac{v_x|_{i+0.5,j}^{n}}{2\Delta x}\left(w_x|_{i+1.5,j}^{n} - w_x|_{i-0.5,j}^{n}\right)$$
$$-\tfrac{w_x|_{i+0.5,j+1}^{n} - w_x|_{i+0.5,j-1}^{n}}{8\Delta x}\left(v_y|_{i+1,j+0.5}^{n} + v_y|_{i,j+0.5}^{n}\right.$$
$$\left. + v_y|_{i+1,j-0.5}^{n} + v_y|_{i,j-0.5}^{n}\right) + \tfrac{b|_{i+1,j}^{n} + b|_{i,j}^{n}}{2}\, F_x\big|_{i+0.5,j}^{n}$$
$$-\tfrac{1}{2\Delta x}\left(b|_{i+1,j}^{n} + b|_{i,j}^{n}\right)\left(p|_{i+1,j}^{n} - p|_{i,j}^{n}\right), \tag{18}$$

and

$$f_y|_{i,j+0.5}^{n} = -\tfrac{v_y|_{i+1,j+0.5}^{n} - v_y|_{i-1,j+0.5}^{n}}{8\Delta x}\left(w_x|_{i+0.5,j+1}^{n}\right.$$
$$\left. + w_x|_{i+0.5,j}^{n} + w_x|_{i-0.5,j+1}^{n} + w_x|_{i-0.5,j}^{n}\right)$$
$$-\tfrac{w_y|_{i,j+0.5}^{n}}{2\Delta x}\left(v_y|_{i,j+1.5}^{n} - v_y|_{i,j-0.5}^{n}\right)$$
$$-\tfrac{w_y|_{i+1,j+0.5}^{n} - w_y|_{i-1,j+0.5}^{n}}{8\Delta x}\left(v_x|_{i+0.5,j+1}^{n} + v_x|_{i+0.5,j}^{n}\right.$$
$$\left. + v_x|_{i-0.5,j+1}^{n} + v_x|_{i-0.5,j}^{n}\right) + \tfrac{b|_{i,j+1}^{n} + b|_{i,j}^{n}}{2}\, F_y|_{i,j+0.5}^{n}$$
$$-\tfrac{v_y|_{i,j+0.5}^{n}}{2\Delta x}\left(w_y|_{i,j+1.5}^{n} - w_y|_{i,j-0.5}^{n}\right)$$
$$-\tfrac{1}{2\Delta x}\left(b|_{i,j+1}^{n} + b|_{i,j}^{n}\right)\left(p|_{i,j+1}^{n} - p|_{i,j}^{n}\right). \tag{19}$$

Using (17)–(19), the equations (14)–(16) with the iteratively previous time step proceeding Δt take the form

$$p|_{i,j}^{n+1/2} = p|_{i,j}^{n-1/2} + \Delta t\; f_p|_{i,j}^{n-1/2}\,, \tag{20}$$

$$w_x|_{i+0.5,j}^{n} = w_x|_{i+0.5,j}^{n-1} + \Delta t\; f_x|_{i+0.5,j}^{n-1}\,, \tag{21}$$

$$w_y|_{i,j+0.5}^{n} = w_y|_{i,j+0.5}^{n-1} + \Delta t\; f_y|_{i,j+0.5}^{n-1}\,. \tag{22}$$

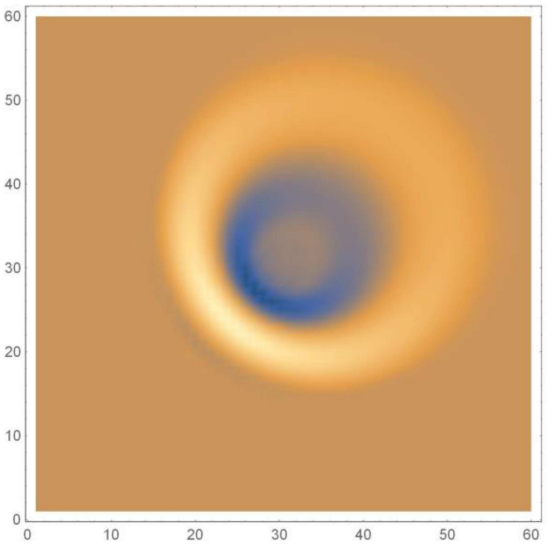

Fig. 2. The influence of wind on the propagation of the sound wave.

Figure 2 shows the pressure distribution for a propagating Gaussian pulse after 3000 time steps in air. The movement of the medium in both horizontal and vertical directions is taken into account. As can be seen, a wave propagating in the direction opposite to the wind decreases in length and at the same time increases in amplitude. An increase in wavelength and a decrease in amplitude occurs when the wind direction and the direction of wave propagation match.

3. Research

The work analyzed the propagation of a Gaussian pulse from a soft wave source marked with point "S" in Fig. 3 through a regular structure composed of metaatoms with a square cross-section and a lattice constant of 2 cm and a fill factor of 68.75%.

The spatial step Δx was 0.125 m, and the time step Δt ensuring simulation stability was 100 times smaller than that resulting from the Courant stability condition for two-dimensional analysis and amounted to 2.6×10^{-6} s. Two sizes of structures

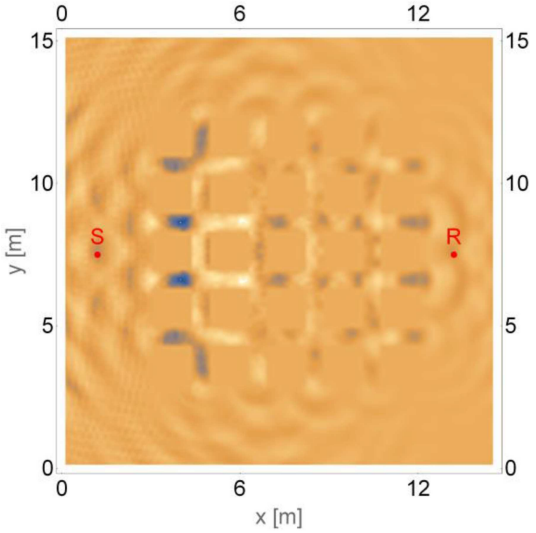

Fig. 3. Pressure distribution for 2×10^4 time steps of impulse propagation in a 5-by-5 structure for the medium velocity $v_x = 60$ m/s.

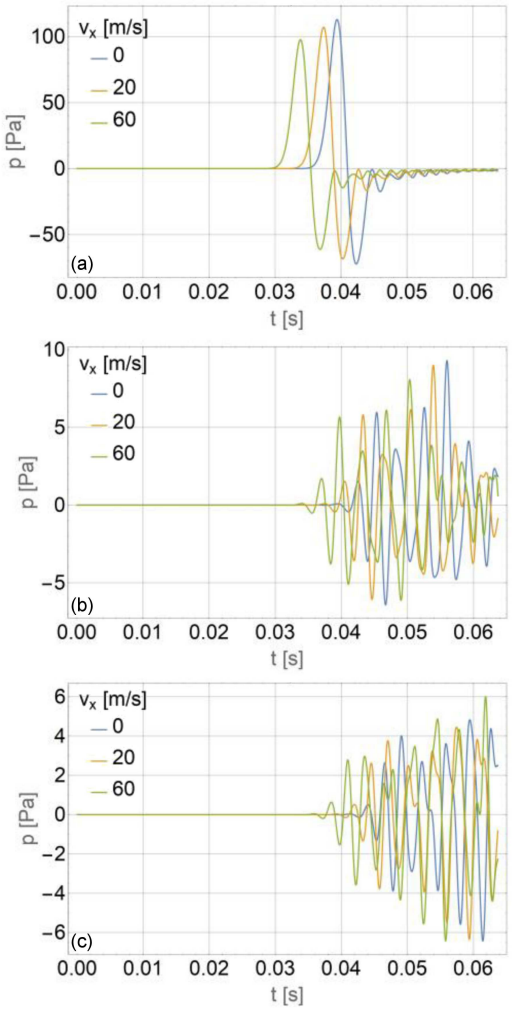

Fig. 4. Pressure time series collected at point R (a) with no structure, (b) for the 3-by-5 structure, and (c) for the 5-by-5 structure for different values of the medium velocity v_x.

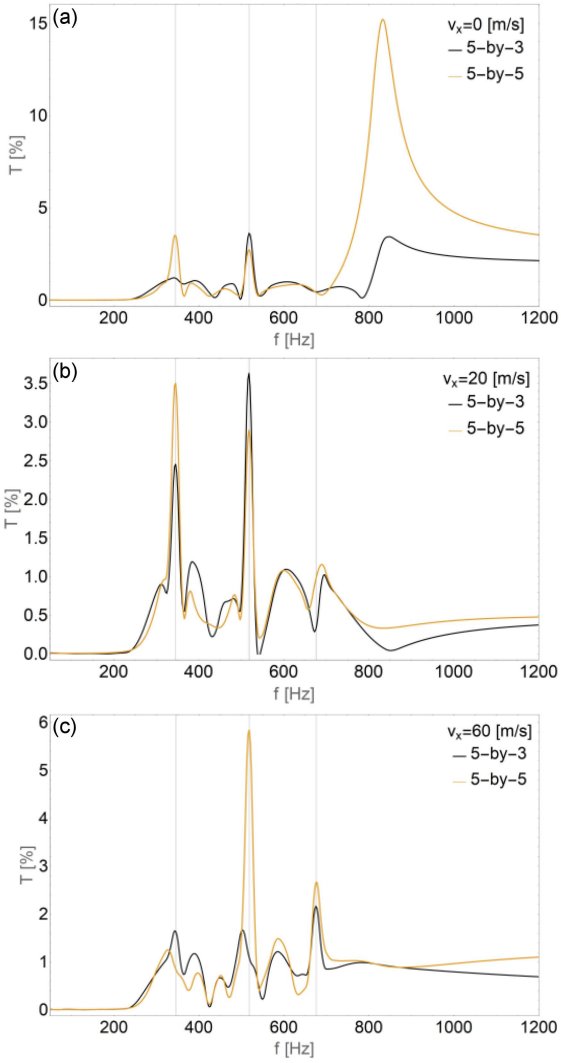

Fig. 5. Wave transmission at point R for different values of the medium velocity (a) $v_x = 0$ m/s, (b) $v_x = 20$ m/s and (c) $v_x = 60$ m/s.

were analyzed in this study. The first one is 3 columns of 5 rows (3-by-5), and the second one is 5 columns of 5 rows (5-by-5). In order to determine the transmission, a study of the propagation of a wave pulse in a space without structures was also carried out. The wave propagated in the air and the metaatoms were simulated as a rigid wall.

At the point marked "R" in Fig. 3, the time series of pressure changes presented for the analyzed cases in Fig. 4 were recorded. As shown in Fig. 4, the velocity of the medium in the direction of wave propagation shortened the time for the wavefront to reach the receiver point R. The presence of the phononic structure caused the wave to slow down and significantly reduce its intensity the greater the number of layers in the structure.

Figure 5 shows transmission graphs for various medium velocities and structure sizes. The tests carried out showed the occurrence of transmission peaks whose frequency (345 Hz and 519 Hz) was

independent of the speed of the medium. The intensity of the peaks changed with the velocity of the medium. These peaks were associated with the emerging areas of local resonances inside the intermetaatomic spaces. The high-intensity peak occurring in the absence of medium movement at 832 Hz, with the increase in the v_x velocity, moved towards lower frequencies (676 Hz for $v_x = 60$ m/s) while decreasing its energy, which was related to the increase in the wavelength due to the coincidence of the medium movement speed with the direction of wave propagation.

4. Conclusions

The work analyzed the influence of the motion of the medium on the propagation and transmission of a mechanical wave through a quasi-two-dimensional phononic structure composed of metaatoms with a square cross-section.

An increase in the propagation speed of the mechanical wave was demonstrated when the direction of the medium's velocity was consistent with it. The phononic structure caused the wave propagation to slow down, the greater the number of layers it consisted of. The formation of transmission peaks was demonstrated as a result of the formation of local resonance areas in the intermetaatomic space, the intensity of which was influenced by the velocity of the medium. The occurrence of a peak was demonstrated, the frequency of which decreased with the increase in the velocity of the medium.

References

[1] W. Witarto, K.B. Nakshatrala, Y-L. Mo, *Mech. Mater.* **134**, 38 (2019).

[2] S-L. Cheng, J-M. Liang, Q. Ding, Q. Yan, Y-T. Sun, T-J. Xin, L. Wang, *Wave Motion* **122**, 103195 (2023).

[3] C.J. Rupp, M.L. Dunn, K. Maute, *Appl. Phys. Lett.* **96**, 111902 (2010).

[4] S. Villa-Arango, R. Torres, P.A. Kyriacou, R. Lucklum, *Measurement* **102**, 20 (2017).

[5] W. Sochacki, *Acta Phys. Pol. A* **138** 328 (2020).

[6] S. Garus, W. Sochacki, *Wave Motion* **98**, 102645 (2020).

[7] B. Morvan, A. Tinel, J.O. Vasseur, R. Sainidou, P. Rembert, A.-C. Hladky-Hennion, N. Swinteck, P.A. Deymier, *J. Appl. Phys.* **116**, 214901 (2014).

[8] X.-F. Li, X. Ni, L. Feng, M.-H. Lu, C. He, Y.-F. Chen, *Phys. Rev. Lett.* **106**, 084301 (2011).

[9] Q. Mo, H. Yeh, M. Lin, D. Manocha, *Appl.Acoust.* **104**, 142 (2016).

[10] Q. Goestchel, G. Guillaume, D. Ecotiere, B. Gauvreau, *J. Sound Vib.* **531**, 116974 (2022).

[11] V.E. Ostashev, D.K. Wilson, L. Liu, D.F. Aldridge, N.P. Symons, D. Marlin, *J. Acoust. Soc. Am.* **117**, 2(2005).

[12] D.K. Wilson, L. Liu, *Engineer Research and Development Center, Cold Regions Research and Engineering Laboratory*, ERDC/CRREL TR-04-12, 2004.

[13] R. Blumrich, D. Heimann, *J. Acoust. Soc. Am.* **112**, 446 (2002).

[14] E.M. Salomons, R. Blumrich, D. Heimann, *Acta Acust. united Ac.* **88**, 483 (2002).

[15] T. Van Renterghem, *Int. J. Aeroacoust.* **13**, 385 (2014).

Proceedings of "Applications of Physics in Mechanical and Material Engineering" (APMME 2023)

Squeezed States Generation in a Three-Mode System of Nonlinear Quantum Oscillators

J.K. Kalaga*

Quantum Optics and Engineering Division, Institute of Physics, University of Zielona Góra, Prof. Z. Szafrana 4a, 65-516 Zielona Góra, Poland

Doi: 10.12693/APhysPolA.144.289 *e-mail: j.kalaga@if.uz.zgora.pl

Three identical, interacting with each other nonlinear oscillators are considered. In addition, they are also externally driven by a coherent field of constant amplitude. The possibility of generating two-mode squeezed states is analyzed in this system. The two-mode principal squeeze variance is used to study the properties of the squeezed states of the system. The time evolution of this variance is analyzed, as well as the effect of the strength of the interaction between the oscillators and the damping strength on the generation of squeezed states.

topics: nonlinear oscillator, three-qubit system, squeezed states

1. Introduction

The nonclassical properties of the states can manifest themselves through various phenomena such as entanglement or squeezing. These two phenomena can often be observed in the same quantum systems [1–3]. Therefore, the squeezed states have found applications in various quantum technologies. These states are a resource in such quantum branches as quantum teleportation [4], quantum metrology [5], or quantum information processing [6, 7].

This paper will study a model of three mutually interacting nonlinear oscillators externally driven by a coherent field. The model discussed here is a source of the strongly entangled states [8]. Therefore, we expect this system also to be a source of two-mode squeezed states.

2. The model

We consider the model of three nonlinear Kerr-like oscillators (subsystems) characterized by the nonlinearity constant χ. The oscillators are mutually coupled by linear interaction in such a way that they form a chain. In addition, the boundary oscillators (the first and the last) are externally driven by a coherent field (see Fig. 1). This system can be described by the following Hamiltonian

$$\hat{H} = \sum_{j=1}^{3} \frac{\chi}{2} \left(\hat{a}_j^\dagger\right)^2 \hat{a}_j^2 + \sum_{j=1}^{2} \varepsilon \left(\hat{a}_j^\dagger \hat{a}_{j+1} + \hat{a}_{j+1}^\dagger \hat{a}_j\right) + \sum_{j=1,3} \alpha \left(\hat{a}_j + \hat{a}_j^\dagger\right), \tag{1}$$

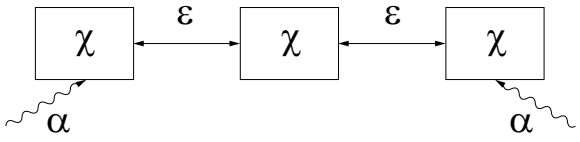

Fig. 1. The model of three interacting nonlinear quantum oscillators driven by an external coherent field.

where the operators $\hat{a}_j^\dagger$ and $\hat{a}_j$ are the bosonic creation and annihilation operators for the mode j ($j = 1, 2, 3$), respectively. The parameter ε describes the linear interaction between the subsystems. For simplicity, we also assume that the external excitations in modes 1 and 3 have the same strength and that two internal interactions ($1 \leftrightarrow 2$ and $2 \leftrightarrow 3$) are equal to each other. Importantly, under some conditions ($\alpha, \varepsilon \ll \chi$), our system behaves as the nonlinear quantum scissors [9–11], and the system's evolution is closed within eight three-mode states (see [8] for details).

In our studies, we assume that the system is initially in a vacuum state. Furthermore, we analyze two cases. In the first case, all damping processes are neglected, and the system's evolution is described by the unitary evolution operator $\hat{U} = \mathrm{e}^{-\mathrm{i}\hat{H}t}$ (we use units of $\hbar = 1$). Then, the wave function describing the state of the system is obtained as follows

$$|\psi(t)\rangle = \hat{U}|\psi(t=0)\rangle. \tag{2}$$

In the second case, the evolution includes a damping process. We assume that the system is damped in all three modes. Therefore, to describe the evolution of our system, we apply the master equation approach.

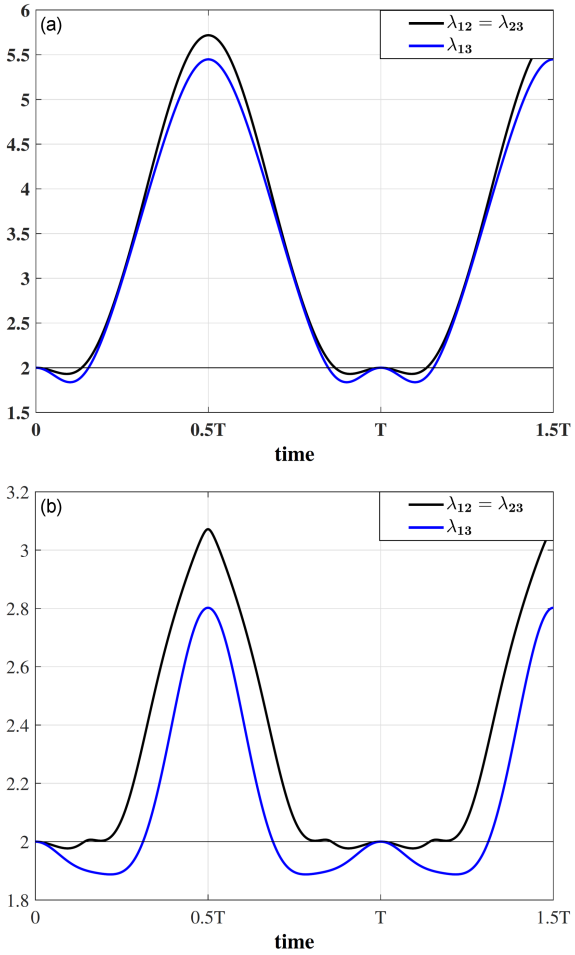

Fig. 2. Time-evolution of the parameter λ_{ij} for $\alpha = 0.001\chi$ and (a) $\varepsilon = \frac{12\alpha}{10+\sqrt{28}}$, (b) $\varepsilon = \frac{12\alpha}{10-\sqrt{28}}$. Time is measured in units of $\frac{1}{\chi}$.

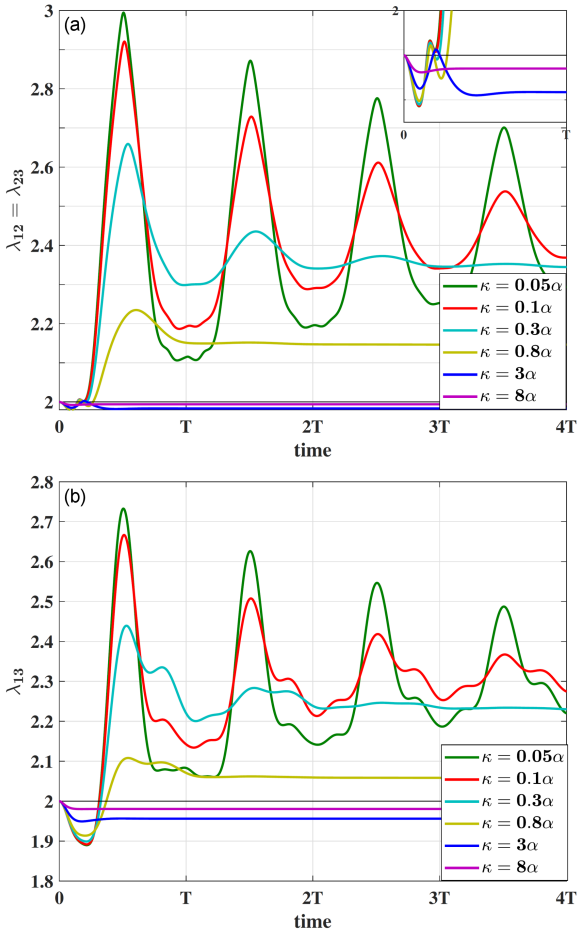

Fig. 3. Time-evolution of the parameter λ_{ij} for $\alpha = 0.001\chi$, $\varepsilon = \frac{12\alpha}{10-\sqrt{28}}$, and for various values of damping parameter κ.

Thus, the time evolution of the density operator $\hat{\rho}$ describing our model is given by

$$\frac{\mathrm{d}\hat{\rho}}{\mathrm{d}t} = -\frac{1}{\mathrm{i}}\left(\hat{\rho}\hat{H} - \hat{H}\hat{\rho}\right) + \sum_{j=1}^{3}\left[\hat{C}_j\hat{\rho}\hat{C}_j^{\dagger} - \frac{1}{2}\left(\hat{C}_j^{\dagger}\hat{C}_j\hat{\rho} + \hat{\rho}\hat{C}_j^{\dagger}\hat{C}_j\right)\right]. \quad (3)$$

The operators $\hat{C}_j$ $(j = 1, 2, 3)$ describe the damping in modes 1, 2, and 3, respectively. These operators are defined as $\hat{C}_j = \sqrt{2\kappa}\,\hat{a}_j$. The parameter κ is the damping constant characterizing the interaction with a zero-temperature bath. We assume here that the damping constants corresponding to all modes are identical ($\kappa = \kappa_1 = \kappa_2 = \kappa_3$).

3. The results and discussion

We focus here on the possibility of generating two-mode squeezed states. To analyze the squeezing phenomena, we use the two-mode principal squeeze variance [12–14]

$$\lambda_{ij} = 2\Big[1+\langle\Delta\hat{a}_i^{\dagger}\Delta\hat{a}_i\rangle+\langle\Delta\hat{a}_j^{\dagger}\Delta\hat{a}_j\rangle+2\mathrm{Re}\langle\Delta\hat{a}_i^{\dagger}\Delta\hat{a}_j\rangle - \big|\langle(\Delta\hat{a}_i)^2\rangle+\langle(\Delta\hat{a}_j)^2\rangle+2\langle\Delta\hat{a}_i\Delta\hat{a}_j\rangle\big|\Big], \quad (4)$$

where $\langle\Delta\hat{a}_i\Delta\hat{a}_j\rangle = \langle\hat{a}_i\hat{a}_j\rangle - \langle\hat{a}_i\rangle\langle\hat{a}_j\rangle$, and i, j denotes the modes. The two-mode squeezed states are produced if the parameter λ_{ij} does not exceed two.

Figure 2 shows the time evolution of the squeezing parameter λ_{ij} for two values of the internal interaction strength corresponding to the periodic solution (see [8] for details). We see here that for all pairs of subsystems, we can observe the two-mode squeezing. Due to the geometry of the system, the variances of λ_{12} and λ_{23} are equal to each other. The degree of two-mode squeezing is weaker for pairs of modes 1–2 and 2–3 than for modes 1–3. The character of the time evolution of the two-mode principal squeezing variances depends on the values of the coupling ε between the oscillators. By changing the strength of the coupling, we can influence the time over which two-mode squeezing is generated.

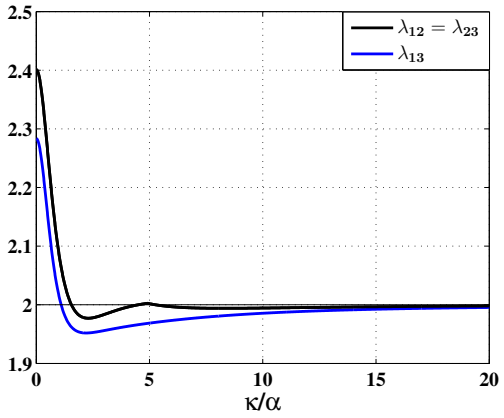

Fig. 4. Steady-state solutions for the two-mode principal squeeze variance vs the value of the damping parameter κ, where $\varepsilon = \frac{12\alpha}{10-\sqrt{28}}$, and $\alpha = 0.001\chi$.

For example, by comparing Fig. 2a and Fig. 2b, we can see that for stronger coupling, the squeezing for modes 1–3 appears for longer periods of time.

In the next step, we will analyze the damped system. In Fig. 3, we can see the time evolution of the parameter λ_{ij} for some values of the damping parameter κ. Since the results for the damped case corresponding to the two previously considered values of the excitation strength ε are very similar, in Fig. 3, we present results only for the stronger internal interaction case, where $\varepsilon = \frac{12\alpha}{10-\sqrt{28}}$. We can see that, as in the case of the system without damping and for the system with damping, we also observe the two-mode squeezing for all pairs of subsystems. For weak damping, the values of the parameters λ_{ij} oscillate. As the parameter κ increases, the oscillatory character of the time-evolution of λ_{ij} disappears.

Importantly, for weak damping, the squeezed states appear only for the initial period of the evolution. For the strongly damped system, the squeezed states can be produced during the whole evolution of the system. Moreover, it can be seen that for the strongly damped systems, we obtain stable squeezed states. Unfortunately, as the damping strength increases, we observe that the degree of stable squeezing decreases. This relationship is better illustrated in Fig. 4, which shows the steady-state solutions for various κ values. This figure also shows that the final value of the two-mode squeezing parameter λ_{ij} depends on the strength of the damping. Furthermore, the final squeezing is the strongest for subsystems 1–3.

4. Conclusions

In this paper, the system containing three nonlinear oscillators characterized by Kerr-type nonlinearity was discussed. The oscillators were coupled with each other in such a way that the system formed a chain, and the first and the last subsystems were coherently excited.

For such a system, the possibility of generating the two-mode squeezed states has been investigated. We have analyzed the time evolution of the two-mode principal squeeze variances for the undamped and damped systems. We have shown that in these two cases (damped and undamped), the analyzed system can be a source of two-mode squeezed states and that the strength of damping influences the produced squeezing. In addition, it has been shown that stable two-mode squeezed states are generated when the system is strongly damped.

Acknowledgments

The author acknowledges the support of the program of the Polish Minister of Science and Higher Education under the name "Regional Initiative of Excellence" in 2019-2022, project no. 003/RID/2018/19, funding amount PLN 11 936 596.10.

References

[1] S.L. Braunstein, H.J. Kimble, *Phys. Rev. Lett.* **80**, 869 (1998).

[2] W. Wasilewski, T. Fernholz, K. Jensen et al., *Opt. Express* **17**, 14444 (2009).

[3] T.J. Bartley, P.J.D. Crowley, A. Datta et al., *Phys. Rev. A* **87**, 022313 (2013).

[4] A. Furusawa, J.L. Sørensen, S.L. Braunstein et al., *Science* **282**, 706 (1998).

[5] B.J. Lawrie, P.D. Lett, A.M. Marino, R.C. Pooser, *ACS Photonics* **6**, 1307 (2019).

[6] A. Ourjoumtsev, R. Tualle-Brouri, J. Laurat, P. Grangier, *Science* **312**, 83 (2006).

[7] C. Weedbrook, S. Pirandola, R. García-Patrón et al., *Rev. Mod. Phys.* **84**, 621 (2012).

[8] J.K. Kalaga, A. Kowalewska-Kudłaszyk, W. Leoński, A. Barasiński, *Phys. Rev. A* **94**, 032304 (2016).

[9] W. Leoński, A. Kowalewska-Kudłaszyk, *Progress in Optics*, Vol. 56, ed. E. Wolf, Elsevier, 2011, p. 131.

[10] W. Leoński, R. Tanaś, *Phys. Rev. A* **49**, R20 (1994).

[11] A. Miranowicz, W. Leoński, *J. Opt. B* **39**, 1683 (2006).

[12] A. Lukš, V. Peřinová, J. Peřina, *Opt. Commun.* **67**, 149 (1988).

[13] N. Korolkova, J. Peřina, *Opt. Commun.* **136**, 135 (1996).

[14] G. Ariunbold, J. Peřina, *Opt. Commun.* **176**, 149 (2000).

Proceedings of "Applications of Physics in Mechanical and Material Engineering" (APMME 2023)

Comparative Study on Primary Recrystallization of Metallic Materials Using Experimental and Numerical Simulations

T.A. Walasek*

Czestochowa University of Technology, 42-201 Czestochowa, Poland

Doi: 10.12693/APhysPolA.144.292 *e-mail: tomasz.walasek@pcz.pl

The phenomenon of primary recrystallization in metallic materials is a complex process that involves nucleation and growth of new grains from the deformed microstructure during post-deformation annealing heat treatment. In this study, we compare the experimental and numerical simulation results of primary recrystallization in metallic materials. The experimental tests were carried out on ARMCO iron samples extruded to 10, 20, and 30% of deformation degree and annealed at 973 K for 300 s. Microsections of the deformed and annealed specimens were analyzed using a metallographic microscope and Joyce–Loebl image analyzer. The numerical simulations were performed using a Monte Carlo algorithm to model the primary recrystallization of variable nucleation rate. On the basis of the classification given by Christian, four types of nucleation were simulated: site-saturated nucleation, constant nucleation rate, increasing nucleation rate, and decreasing nucleation rate, with different magnitudes of stored energy. Our results show that the decreasing nucleation rate model best fits the experimental data. The comparison between the experimental and numerical simulation results provides insights into the nucleation and growth of new grains during primary recrystallization in metallic materials.

topics: Monte Carlo, recrystallization, grain growth, numerical model

1. Introduction

The properties of alloys and metals subjected to plastic deformation and annealing depend significantly on the conditions of recrystallization. One of the ways to model grain growth and recrystallization at the microscopic scale is through Monte Carlo simulation [1–4]. This type of modelling process has several advantages. One of them is the ability to introduce multiple different and often competing driving forces at the fundamental level by defining the energy conditions and forces for each individual element. These relationships determine both the interrelations between elements and the external conditions. Another advantage is that simple assumptions can generate complex microstructures, and it is possible to observe the development of these microstructures at each stage. Additionally, the ability to generate structures consistent with any set of assumptions allows simulation of the nature of local energy conditions and dynamics. Theoretical hypotheses can be investigated by comparing microstructures obtained from simulations and those observed in experiments.

2. Modelling of the recrystallization

The Monte Carlo method was used for modelling recrystallization processes. The procedure used for modelling recrystallization has been described in detail in the author's previous works [5, 6]. A general description of the simulation is presented below. Recrystallization with variable nucleation rate was simulated as a function of free energy and the number of nuclei. The modelling procedure is based on a two-dimensional array. Each element in the array is assigned a grain orientation number (S_i) ranging from 1 to 48, representing the orientation of the grain in which the element is embedded, and a fixed value of grain boundary free energy and internal energy for that grain (E_i). Grain boundaries are determined by elements with different orientations. Potential nuclei are randomly placed in the deformed structure. Recrystallized grains have orientations given by numbers ranging from 49 to 64, distinguishing them from deformed grains. Energy values are also calculated for these grains. In each calculation step, a new number ranging from 1 to 64 is randomly assigned to each element in the array,

determining its new possible orientation. New values of grain boundary free energy and internal energy (E_i^*) are calculated for that element. If the change in energy due to reorientation satisfies the condition $E_i^* - E_i \leq 0$, the orientation S_i of that element is transposed to the new orientation. Otherwise, there is no modification of the orientation S_i. The change in orientation of an element located at the grain boundary to the orientation of the nearest neighbouring element indicates grain boundary motion. The orientations of recrystallized grains can change to other recrystallized grains in subsequent calculation steps.

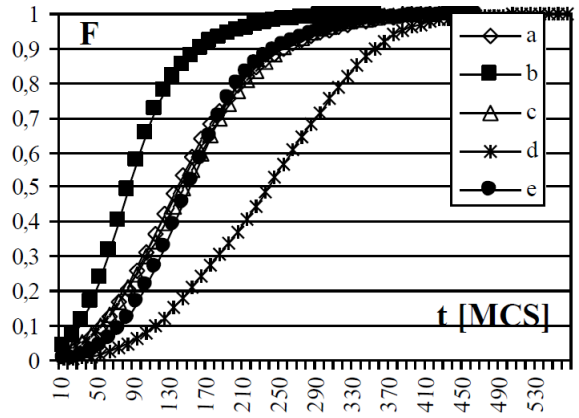

Fig. 1. Recrystallized volume fraction $F(t)$ for the degree of stored energy $H/J = 1$ and different models of nucleation: (a) decreasing nucleation rate I, (b) decreasing nucleation rate II, (c) site-saturated nucleation, (d) increasing nucleation rate, and (e) continuous nucleation rate.

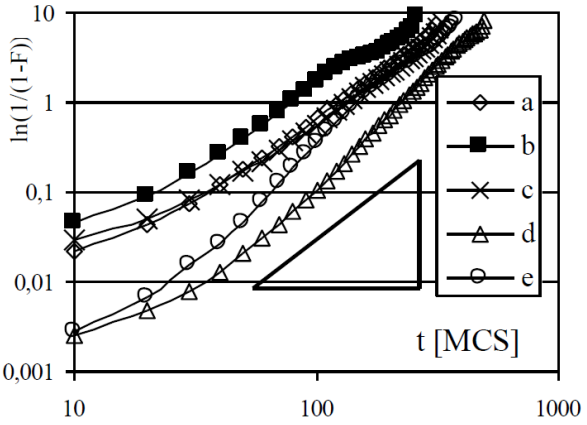

Fig. 2. The Avrami plots for the degree of stored energy $H/J = 1$ and different nucleation models: (a) decreasing nucleation rate I, (b) decreasing nucleation rate II, (c) site-saturated nucleation, (d) increasing nucleation rate, and (e) continuous nucleation rate.

3. Results

3.1. Computer simulation

As an initial structure for modelling recrystallization, the structure obtained from Monte Carlo grain growth simulation was adopted and then "deformed" to a specified degree of deformation. The number of different grain orientations was given as $Q = 48$ for grain growth and $Q + 16$ for recrystallization.

Extensive investigations were conducted for four types of nucleation:

- Variable nucleation with increasing nucleation rate, introducing I new nuclei into the structure every tenth step, until $I = 100$, where $n = 10$ and $i = 1, 11, 21, 31, \ldots, I_{\mathrm{MCS}}$.
- Variable nucleation with decreasing nucleation rate, introducing I new recrystallization nuclei into the structure at every tenth step; in the article, $I = 100$ (decreasing rate I) and $I = 200$ (decreasing rate II) were adopted.
- Continuous nucleation, introducing $I = 10$ nuclei randomly into the structure every ten steps of the Monte Carlo step (MCS).
- Saturation nucleation, introducing $I = 200$ nuclei randomly into the structure at $t = 0$.

For simulation purposes, a dimensionless value of the ratio of stored grain boundary energy to grain interior energy, denoted as H/J, was used to provide a simpler and more understandable description. The above studies were conducted under the same energy conditions, i.e., $H/J = 1$, 1.5, 2, and 2.5.

Figure 1 shows the relationship between the recrystallized volume fraction F and the time t expressed in Monte Carlo steps for four different nucleation rates and a degree of stored energy $H/J = 1$. The observed dependencies exhibit a sigmoidal shape, consistent with experimentally determined curves [7–9]. No incubation period was observed in the simulation since nucleation nuclei were introduced into the system at $t = 0$. It can be observed that the recrystallization kinetics depend significantly on the type of nucleation. The author's studies also indicate a strong dependence on the degree of stored energy H/J (see also [8]).

The most commonly used equation describing recrystallization is the relationship between the recrystallized volume fraction F and time t, known as the Johnson–Mehl–Avrami–Kolmogorov (JMAK) theory, i.e.,

$$F(t) = 1 - \exp(-kt^n), \tag{1}$$

where k and n are constants, and the constant n is referred to as the Avrami exponent. The graphical interpretation of the Avrami exponent is the slope of the Avrami line, which represents the relationship between $\log(-\ln(1-F))$ and $\log(t)$.

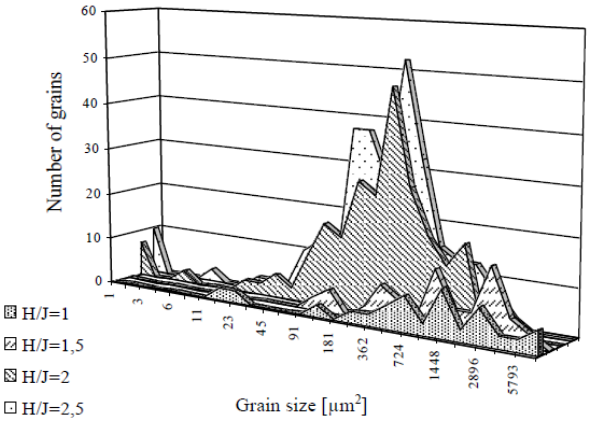

Fig. 3. Histogram of the grain size distribution for the calculated microstructures for saturated nucleation rate and the degree of stored energy $H/J = 1$, 1.5 and 2, and 2,5.

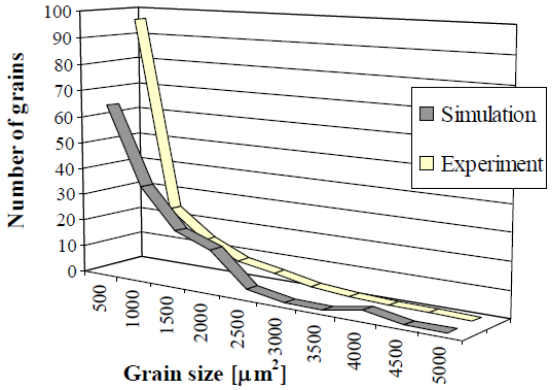

Fig. 4. Histogram of the grain size for the specimen of ARMCO iron deformed 10% and then recrystallized and the microstructure obtained from the simulation for decreasing nucleation rate and $H/J = 1$.

Figure 2 shows the graphical interpretation of the JMAK equation for the four types of nucleation and the degree of stored energy $H/J = 1$. The data plotted on the graph approximately follow parallel lines. The slopes of the Avrami lines are smaller in the initial period, which is attributed to the relatively large number of nuclei introduced into the system at $t = 0$. For all presented Avrami curves, the exponent n is approximately 2, consistent with the predictions of the classical JMAK theory.

Figure 3 presents the logarithmic scale distribution of grain sizes obtained from recrystallization simulations for saturation nucleation and different degrees of stored energy $H/J = 1$, 1.5, 2, and 2.5.

3.2. Experimental results

The experimental verification of the recrystallization model was conducted on ARMCO iron samples that were subjected to plastic deformation. The samples were drawn through a die, resulting in deformations of 10, 20, and 30%. Rectangular-shaped specimens with dimensions of $10 \times 10 \times 55$ mm^3 were prepared and mounted in the jaws of a TCS 1405 thermal cycle simulator manufactured by SMITWELD. The simulator jaws were water-cooled, allowing for controlled temperature conditions within the specimens. The recrystallization experiments were carried out at a constant temperature of $T = 973$ K and a holding time of $t = 300$ s. After cold deformation, the samples were rapidly heated to the desired temperature and held for the specified duration.

Figure 4 shows the comparison between the experimental microstructure and the simulated microstructure for a deformation of 30% and a recrystallization degree of $H/J = 1$. The simulated microstructure exhibits recrystallized grains with distinct boundaries, which align well with the experimental observations.

The comparison between the experimental and simulated microstructures confirms the capability of the recrystallization model to capture the essential features of the recrystallization process. The model successfully predicts the nucleation and growth of recrystallized grains, as well as the evolution of their size and distribution. The discrepancies between the simulated and experimental microstructures can be attributed to simplifications and assumptions made in the model, such as the isotropic nature of grain growth and the neglect of certain microstructural factors.

Further refinements of the model can be made by incorporating additional parameters and considering more complex mechanisms of recrystallization. The comparison between simulation and experimental results provides valuable insights into the recrystallization kinetics and helps to understand the underlying mechanisms governing the process.

4. Conclusions

In this study, a recrystallization model based on the Monte Carlo method was developed and experimentally verified. The model successfully simulates the nucleation and growth of recrystallized grains in deformed materials. By adjusting the energy parameters and the nucleation rate, the model can reproduce different recrystallization scenarios.

The simulated microstructures exhibit recrystallized grains with distinct boundaries, which aligns well with the experimental observations.

In conclusion, the developed recrystallization model based on the Monte Carlo method shows promise in simulating the recrystallization process

in deformed materials. It successfully predicts the nucleation and growth of recrystallized grains and provides valuable insights into the evolution of microstructures.

References

[1] M.P. Anderson, D.J. Srolovitz, G.S. Grest, P.S. Sahni, *Acta Metall.* **32**, 783 (1984).

[2] D.J. Srolovitz, G.S. Grest, M.P. Anderson, *Acta Metall.* **34**, 1833 (1986).

[3] P. Yu, C. Wu, L. Shi, *Acta Mater.* **207**, 116692 (2021).

[4] H. Xu, X. Shu, J. Zuo, A. Yin, Y. Wang, *Mater. Today Commun.* **30**, 103133 (2022).

[5] T.A. Walasek, *J. Mater. Process. Technol.* **157**, 262 (2004).

[6] T.A. Walasek, *Proceedings of the First Joint International Conference on Recrystallization and Grain Growth*, ed. G. Gottstein, D.A. Molodov, Aachen, 2001, p. 1081.

[7] J.W. Christian, *The Theory of Transformation in Metals and Alloys*, Pergamon Press, Oxford 2002.

[8] M. Blicharski, S. Gorczyca, *Rekrystalizacja z udziałem drugiej fazy*, wyd. Śląsk, Katowice 1980.

[9] J.G. Byrne, *Recovery, Recrystallization and Grain Growth*, The Macmillan Company, New York 1965.

Proceedings of "Applications of Physics in Mechanical and Material Engineering" (APMME 2023)

Numerical Evaluation of the Impact of Selected Physical Phenomena and Riser Shape on the Formation of Shrinkage Defects in the Casting–Riser System

L. Sowa* and T. Skrzypczak

Department of Mechanics and Machine Design Fundamentals, Faculty of Mechanical Engineering and Computer Science, Czestochowa University of Technology, Dąbrowskiego 73, 42-201 Częstochowa, Poland

Doi: 10.12693/APhysPolA.144.296 *e-mail: leszek.sowa@pcz.pl

Understanding the complex physical phenomena involved in the casting process simulation requires continuous and complementary research to improve mathematical modelling. The paper presents a mathematical model and numerical simulations of the solidification process of a cylindrical casting, taking into account the filling of the mould cavity with liquid metal and feeding the casting through the riser during solidification. The basic mathematical model that considers only thermal phenomena is often insufficient to analyse the metal solidification process. Therefore, more complex models are formulated that include coupled thermal and flow phenomena. The mathematical description then consists of the system of Navier–Stokes differential equations, the equations of the continuity of flow and energy. Such a mathematical model was used in the paper because the mutual dependence of thermal and flow phenomena has a significant impact on the solidification process. The finite element method was used to solve the problem, and changes in thermophysical parameters were considered as a function of temperature. The impact of the riser shape on the effectiveness of feeding of the solidifying casting was also determined and an appropriate selection of the riser shape was made to obtain a casting without shrinkage defects, which was the aim of this work.

topics: numerical simulations, solidification, Navier–Stokes equations, casting defect

1. Introduction

During the casting process, various types of defects occur that may have a negative impact on the quality of the final product. One of such defects is the formation of shrinkage cavities, which cannot be completely avoided, but the heat transport process can be controlled so as to reduce these defects by moving their location to the riser. Research on real objects is much more difficult, which is why computer simulations are becoming the basic method of controlling the casting solidification process [1–7]. In this paper, the course of the solidification process is analysed in the cylindrical or conical-shaped casting–riser system using a basic or complex model. In the complex model [2, 3, 5, 6], the mutual influence of thermal and flow phenomena was taken into account, starting from the moment of filling the metal mould with molten metal and ending with complete solidification of the casting. For comparison, the solidification process of the casting was analysed using the basic model [4], in which only thermal phenomena are taken into account. In this way, the impact of taking into account or omitting liquid metal movements on the process of making a casting without shrinkage defects was assessed, which was the purpose of this paper. The shape of the solidus line was also observed, assessing whether it was closed in the casting area. Such a situation would mean no inflow of molten metal from the riser to this area in the casting and the formation of a shrinkage defect in this place of the casting, which we try to avoid.

2. The mathematical model

The mathematical model of the casting solidification process considering the liquid metal movements (complex model) is based on the solution of the following system of equations in a cylindrical axial-symmetric coordinate system [2–7]:

- Navier–Stokes equations

$$\mu\left(\frac{\partial^2 v_r}{\partial r^2}+\frac{1}{r}\frac{\partial v_r}{\partial r}+\frac{\partial^2 v_r}{\partial z^2}-\frac{v_r}{r^2}\right)-\frac{\partial p}{\partial r}+\rho g_r$$
$$+\rho g_r\beta\,(T-T_\infty)_r=\rho\frac{\mathrm{d}v_r}{\mathrm{d}t},$$
$$\mu\left(\frac{\partial^2 v_z}{\partial r^2}+\frac{1}{r}\frac{\partial v_z}{\partial r}+\frac{\partial^2 v_z}{\partial z^2}\right)-\frac{\partial p}{\partial z}+\rho g_z$$
$$+\rho g_z\beta\,(T-T_\infty)=\rho\frac{\mathrm{d}v_z}{\mathrm{d}t}, \tag{1}$$

- continuity equation

$$\frac{\partial v_r}{\partial r}+\frac{v_r}{r}+\frac{\partial v_z}{\partial z}=0, \tag{2}$$

- heat conductivity equation with the convection term

$$\lambda\frac{\partial T}{\partial r}+\frac{\partial}{\partial r}\left(\lambda\frac{\partial T}{\partial r}\right)+\frac{\partial}{\partial z}\left(\lambda\frac{\partial T}{\partial z}\right)=$$
$$\rho C_{ef}\frac{\partial T}{\partial t}+\rho C_{ef}\left(v_r\frac{\partial T}{\partial r}+v_z\frac{\partial T}{\partial z}\right), \tag{3}$$

- first order pure advection equation

$$\frac{\partial F}{\partial t}+v_r\frac{\partial F}{\partial r}+v_z\frac{\partial F}{\partial z}=0, \tag{4}$$

where λ is thermal conductivity coefficient [W/(m K)]; $\mu(T)$ — dynamical viscosity coefficient [kg/(m s)]; ρ=$\rho(T)$ — density [kg/m^3]; v_r and v_z — the r- and z-component of velocity [m/s], respectively; T — temperature [K]; C_{ef} = c+$L/(T_L-T_S)$ — effective specific heat of a mushy zone [J/(kg K)]; L — latent heat of solidification [J/kg]; T_L and T_S — the liquidus and solidus temperature of the analysed alloy, [K]; g_r and g_z — the r- and z-component of gravitational acceleration [m/s^2], respectively; p — pressure [N/m^2]; β — volume coefficient of thermal expansion [1/K]; t — time [s]; c — specific heat [J/(kg K)]; r — radius [m]; T_∞ — reference temperature (T_∞=T_{in}) [K]; F — the pseudo-concentration function across the elements lying on the free surface.

The mathematical model of the casting solidification process without taking into account the movements of liquid metal (basic model) is reduced only to the solution of the heat conductivity equation (3) without the convection term [4].

The equations (1)–(4) are completed by appropriate boundary conditions and initial conditions. The initial conditions for temperature and velocity fields are given, respectively, as [3–5]

$$\boldsymbol{v}(r,z,t_0)=\boldsymbol{v}_0(r,z)=v_{in}\Big|_{\Gamma_{1-1}},$$

$$T(r,z,t_0)=T_0(r,z)=\begin{cases}T_{in} & \text{on } \Gamma_{1-1}\\ T_A & \text{in } \Omega_A\\ T_M & \text{in } \Omega_M\end{cases}. \tag{5}$$

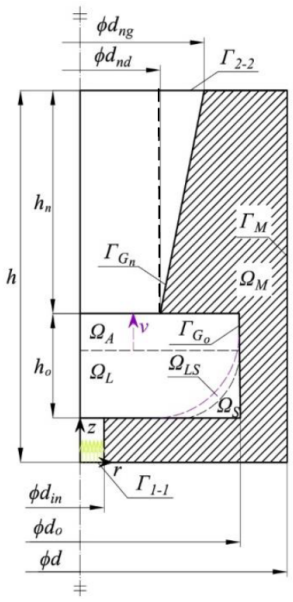

Fig. 1. Scheme and identification of sub-regions of the considered system.

The boundary conditions, specified in the considered problem, on the indicated surfaces (Fig. 1) were as follows:

— for velocity [3, 5],

$$v_t\big|_{\Gamma_{1-1}}=v_t\big|_{\Gamma_{2-2}}=v_n\big|_{\Gamma_{2-2}}=0,$$
$$v_n\big|_{\Gamma_{1-1}}=v_{in}, \qquad v_n, v_t\big|_{\Gamma_G}=0, \tag{6}$$
$$\frac{\partial v_t}{\partial n}\big|_{r=0}=0, \qquad v_n\big|_{r=0}=0,$$

— for temperature [3–6],

$$\lambda_M\frac{\partial T_M}{\partial n}\Big|_{\Gamma_M}=-\alpha_M\left(T_M\Big|_{\Gamma_M}-T_a\right),$$
$$\frac{\partial T}{\partial n}\Big|_{\Gamma_{2-2}}=0, \qquad \lambda_S\frac{\partial T_S}{\partial n}\Big|_{\Gamma_{G-}}=\lambda_G\frac{\partial T_G}{\partial n}\Big|_{\Gamma_{G-}},$$
$$\frac{\partial T}{\partial n}\Big|_{r=0}=0, \qquad \lambda_G\frac{\partial T_G}{\partial n}\Big|_{\Gamma_{G+}}=\lambda_M\frac{\partial T_M}{\partial n}\Big|_{\Gamma_{G+}},$$
$$T\,\big|_{\Gamma_{1-1}}=T_{in}, \tag{7}$$

where T_a is ambient temperature [K]; α_M — heat transfer coefficient between the ambient and the mould [W/(m^2 K)]; T_A — temperature of air inside mould cavity in initial state [K]; T_{in} — initial temperature [K]; T_M, T_G, and T_S — temperature of mould, gap (protective coating), and solid phase, respectively [K]; v_{in} — initial velocity [m/s]; λ_M, λ_S, and λ_G — thermal conductivity coefficient of mould, solid phase, and gap [W/(m K)], respectively; v_t and v_n — tangential and normal component of velocity vector [m/s], respectively; n — outward unit normal surface vector [m].

This task was solved using the finite element method (FEM) in the weighted residuals formulation [3–5].

3. Calculation results and discussion

Numerical calculations of the solidification process of the casting–riser system were made for two riser shapes, i.e., cylindrical and conical risers with the same bottom diameter. The influence of liquid metal movements on the casting solidification process in the following system of casting–riser–mould, shown schematically in Fig. 1, was also analysed.

The outside dimensions of the mould are equal to $d = 0.320$ m and $h = 0.280$ m, whereas the dimensions of the mould cavity are equal to $d_o = 0.200$ m, $h_o = 0.070$ m, $h_n = 0.150$ m, $d_{nd} = 0.080$ m, $d_{ng} = 0.100$ m, $d_{in} = 0.020$ m. For the cylindrical riser, $d_n = d_{nd} = 0.080$ m. The internal surface of the steel mould is covered with a protective coating with a thickness of 2 mm. Numerical simulations were carried out for the casting made of low-carbon cast steel and the steel mould with thermo-physical properties, which were taken from [5]. The overheated metal with the temperature of $T_{in} = 1845$ K was poured from the bottom with the velocity $v_{in} = 0.1$ m/s into the steel mould with the initial temperature $T_M = 345$ K. Other important temperatures were equal to $T_A = 345$ K and $T_a = 300$ K. The heat transfer coefficient (α) between ambient and the mould was equal to $\alpha_M = 200$ W/(m^{2}K). The professional FIDAP program was used to analyse the solidification process of the metal in the considered casting–riser system. The transient calculation process was interrupted when the temperature in the casting lowered below the solidus temperature. The computation process was carried out on a computer with a 2.3 GHz IntelCore-i7 processor and lasted approximately 24 h when using the complex model or approximately 5 h when using the basic model. Such an extension of the computation time in the first case was due to the necessity to use a very small time step in the process of filling the mould cavity.

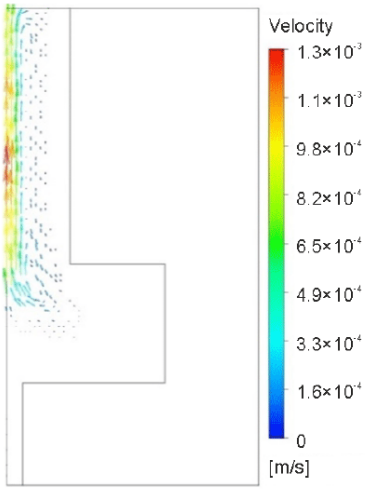

Fig. 2. Velocity vectors at $t = 400$ s, variant I.

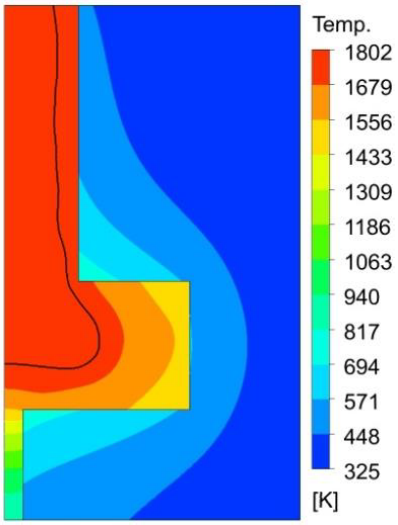

Fig. 3. Temperature distribution at $t = 400$ s, variant I.

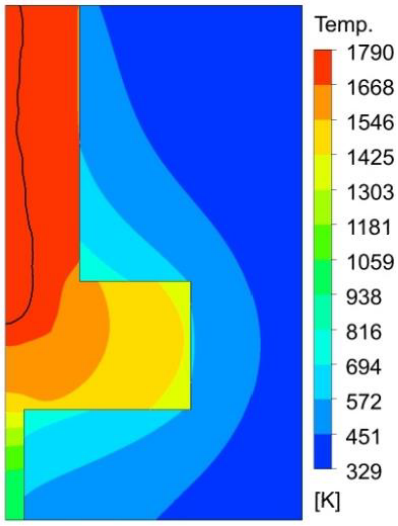

Fig. 4. Temperature field after solidification of the casting at $t = 523$ s, variant I.

Numerical calculations of the solidification process of the casting–cylindrical riser system were carried out using the complex model (variant I), while the solidification process of the casting–conical riser system was carried out using two models: complex (variant II) and basic (variant III). Simulations of the casting formation were performed, starting from the moment of filling the mould cavity with molten metal and ending with its complete solidification. Convection movements of liquid metal are presented in the form of velocity vectors for a selected moment of time (Fig. 2), while the temperature distribution corresponding to this time is shown in Fig. 3, where a solidus line is drawn separating the solid–liquid zone of the casting from its solid area.

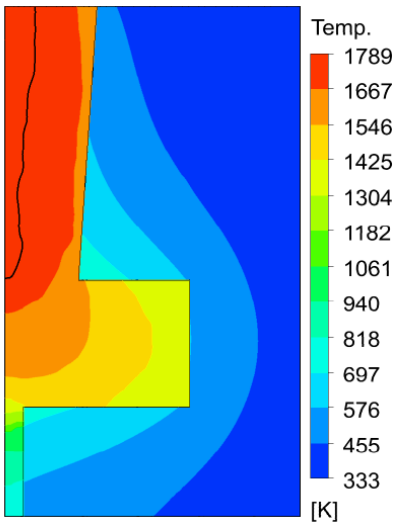

Fig. 5. Temperature field after solidification of the casting at $t = 562$ s, variant II.

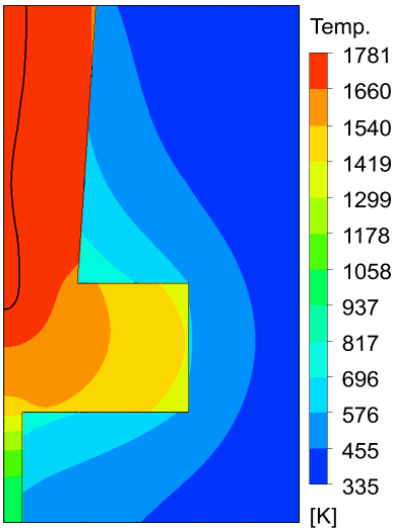

Fig. 6. Temperature field after solidification of the casting at $t = 488$ s, variant III.

Then, the temperature fields after the casting solidification for three calculation models were compared, observing the shape of the solidus line in the final stages of solidification of the casting–riser system (Figs. 4–6). When the solidus line is closed in the casting, the area limited by it will not be fed with liquid metal from the riser, and in this place, as a result of metal shrinkage, a shrinkage defect will occur (Figs. 4 and 6). However, we try to avoid such a situation and move such a defect to the riser, which can be achieved by using the complex model for calculations and the casting–conical riser system (Fig. 5).

4. Conclusions

The paper presents a mathematical model and the results of numerical simulation of the casting solidification, taking into account the process of filling the mould cavity with molten metal and convection movements after its completion (complex model), as well as simulation results in which the movements of the liquid metal were ignored (basic model). Numerical calculations of the casting solidification process were also performed for two riser shapes, i.e., cylindrical and conical riser, assumed in turn. In this way, the influence of the assumed riser shape and molten metal movements on the solidification kinetics and the location of the solidification end in the analysed system were assessed. It was observed that in the final period of solidification of the casting–riser system, a solidus line is visible closing in the upper part of the casting (in some variants). This suggests that shrinkage defects will occur at this location. This situation occurs in the case of simulation of the casting process carried out using a cylindrical riser — variant I (Fig. 4) — or when using the basic model — variant III (Fig. 6). Such a situation was not observed if the casting process was carried out using a conical riser and using a complex model — variant II (Fig. 5). In that case, the end of solidification occurred in the riser, which is desirable because the riser is cut off and reworked. It also proves that the conical-shaped riser fulfilled its task and the casting was made without casting defects, which is very important for foundry practice.

References

[1] S.L. Nimbulkar, R.S. Dalu, *Perspect. Sci.* **8**, 39 (2016).

[2] P.H. Huang, C.J. Lin, *Int. J. Adv. Manuf. Technol.* **79**, 997 (2015).

[3] R.W. Lewis, E.W. Postek, Z. Han, D.T. Gethin, *Int. J. Numer. Methods Heat & Fluid Flow.* **16**, 539 (2006).

[4] T. Skrzypczak, L. Sowa, E. Węgrzyn-Skrzypczak, *Arch. Foundry Eng.* **20**, 37 (2020).

[5] L. Sowa, T. Skrzypczak, P. Kwiatoń, *Arch. Metall. Mater.* **66**, 489 (2021).

[6] P. Kwiatoń, D. Cekus, M. Nadolski, K. Sokół, Z. Saternus, P. Pavlíček, *Acta Phys. Pol. A* **138**, 188 (2022).

[7] P.H. Huang, J.K. Kuo, T.H. Fang, W. Wu, *MATEC Web of Conf.* **185**, 00008 (2018).

Proceedings of "Applications of Physics in Mechanical and Material Engineering" (APMME 2023)

Influence of Thermal Loads on the Microstructure and Mechanical Properties of Structural Steel

T. Domański[a,*], W. Piekarska[b], M. Sága[c], M. Kubiak[a], Z. Saternus[a] and Z. Ságová[c]

[a]*Department of Mechanical Engineering and Computer Science, Częstochowa University of Technology, Dąbrowskiego 69, 42-201 Częstochowa, Poland*
[b]*Faculty of Architecture, Civil Engineering and Applied Arts, University of Technology, Rolna 43, 40-555 Katowice, Poland*
[c]*Department of Applied Mechanics, University of Žilina, Univerzitná 1, 010 26 Žilina, Slovak Republic*

Doi: 10.12693/APhysPolA.144.300 *e-mail: tomasz.domanski@pcz.pl

In this work, the change in the mechanical and microstructural properties of the material exposed to elevated temperatures was investigated in order to determine the variable and temperature-dependent strength parameters. The article presents the results obtained during the uniaxial tensile test of the samples (including modulus of elasticity, yield strength, and tensile strength) under variable thermal conditions. The heating process took place in a modern furnace using T3 lamps in the temperature range up to 1100°C. The MTS extensometer was used for the measurement.

topics: heating, tensile tests, material properties, hot working steel

1. Introduction

Steel products with properties enabling operation at high temperatures have become available on the market in recent years due to the development of metallurgical and production technologies. Steel grade WCL/1.2343/X37CrMoV5-1 is widely used in various industrial sectors, including automotive, aerospace, and machine tools. Many manufacturers of cutting tools use it to produce high-quality, durable, and wear-resistant tools [1, 2]. This steel is used in the production of tools for processing light metal alloys, for hot stamping, and for the production of nuts, rivets, and screws. The stiffness and strength of steel elements may decrease as a result of operation at elevated temperatures, which plays a key role in designing the fire resistance of steel structures. The properties of materials at elevated temperatures are defined in international specifications for steel structures such as European Standard (EC3), American Specification (AISC Specification), and Australian Standard (AS 4100) [3]. However, the material properties at elevated temperatures in these specifications are based primarily on experimental data on normal-strength hot-rolled carbon steel.

Knowledge of the basic strength parameters of the material is important for technologists and structure designers [4–7]. The study of the mechanical and thermomechanical properties of the material is also important for numerical modelling [8]. Nowadays, numerical modelling is increasingly used at the initial stages of production. Reliable processing of appropriate material data increases the computational accuracy of discrete models.

2. Infrared radiant heating chamber

An infrared heating chamber Model E4 is used in experimental tests of rod heating. Figure 1 shows a diagram of the heating chamber. The heating chamber allows for very quick heating of elements using highly concentrated infrared energy. This energy is generated by two halogen lamps and focused on the axis of the furnace using four elliptical reflectors. From a cold start, the lamps reach 90% of the operating temperature within 3 s. The device allows to heat elements up to 1100°C [9, 10].

3. Measuring system

Universal testing machine Zwick/Roell Z100 with maximum load 100 kN and precision 1 N force/0.01 mm displacement (without extensometer, see Fig. 2) is used in the research [8].

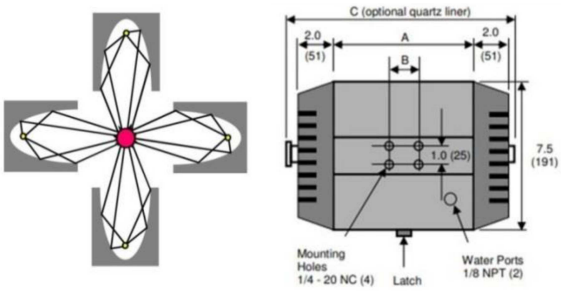

Fig. 1. Diagram of infrared heating chamber [9].

Fig. 2. The measurement system used in experimental tests.

TABLE I

The chemical composition of WCL/1.2343/X37CrMoV5-1 steel.

Element	C	Si	Mn	P
	0.33–0.41	0.80–1.20	0.25–0.50	max–0.030
Element	S	Cr	Mo	V
	max–0.030	4.80–5.50	1.10–1.50	0.30–0.50

The universal machine is coupled with a heating chamber that adjusts temperatures during the tensile test. The elongation measurement is carried out by determining the position of the movable cross-head and an additional MTS extensometer equipped with ceramic fingers that contact the tested sample inside the heating chamber during the measurement.

In order to determine the strength properties (Young's modulus, elasticity and yield strength, ultimate tensile strength), a series of static tensile

Fig. 3. Samples used in experimental tests.

Fig. 4. A set of samples obtained after experimental tests.

tests are carried out on samples with a circular cross-section and a threaded shank part (Fig. 3). The tests are performed for samples at the following temperatures: 20, 100, 200, 300, 400, and 600°C.

The samples are made of hot work tool steel — WCL/1.2343/X37CrMoV5-1. Table I shows the chemical composition of tested steel.

4. The true stress–strain curve

On the basis of tension diagrams for various temperatures, it is possible to develop a numerical (approximated) diagram for the tension of steel. Commercial strength analysis software requires the implementation of true stress–strain diagrams. Therefore, the experimentally obtained steel tension diagram should be transformed into a true stress–strain curve used by the software [11].

The value of true stress σ_{True} is determined on the basis of the actual stress (σ_{En}) diagram, obtained in the testXpert II program,

$$\sigma_{\mathrm{En}} = \frac{F}{A_o}, \qquad \sigma_{\mathrm{True}} = \frac{F}{A}, \tag{1}$$

where $A = A_o\, L_o/L$, and

$$\sigma_{\mathrm{True}} = \frac{F}{\mathrm{A}} = \frac{F\, L}{A_o L_o} = \frac{F}{A_o}\left(1 + \varepsilon_{\mathrm{En}}\right), \tag{2}$$

where F is forces [N], A — actual cross-sectional area [mm^2], A_o — initial cross-sectional area [mm^2], L — measurement length [mm], L_o — initial measurement length [mm], and $\varepsilon_{\mathrm{En}}$ — actual displacement.

Finally,

$$\sigma_{\mathrm{True}} = \sigma_{\mathrm{En}}\left(1 + \varepsilon_{\mathrm{En}}\right). \tag{3}$$

Determining true strain ($\varepsilon_{\mathrm{True}}$) on the basis of the real displacement ($\varepsilon_{\mathrm{En}}$) is performed as follows

$$\varepsilon_{\mathrm{En}} = \frac{\Delta L}{L_o} = \frac{L}{L_o} - 1,$$
$$\varepsilon_{\mathrm{True}} = \int_{L_o}^{L} \frac{\mathrm{d}L}{L} = \ln\left(\frac{L}{L_o}\right). \tag{4}$$

Therefore,

$$\varepsilon_{\mathrm{True}} = \ln\left(1 + \varepsilon_{\mathrm{En}}\right). \tag{5}$$

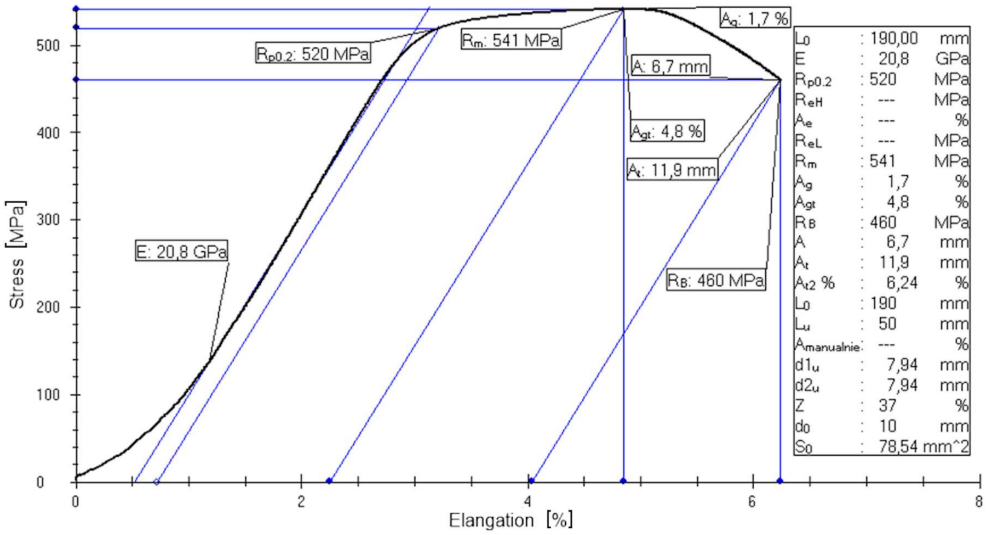

Fig. 5. Diagram of steel tension at temperature of 20°C with characteristic values.

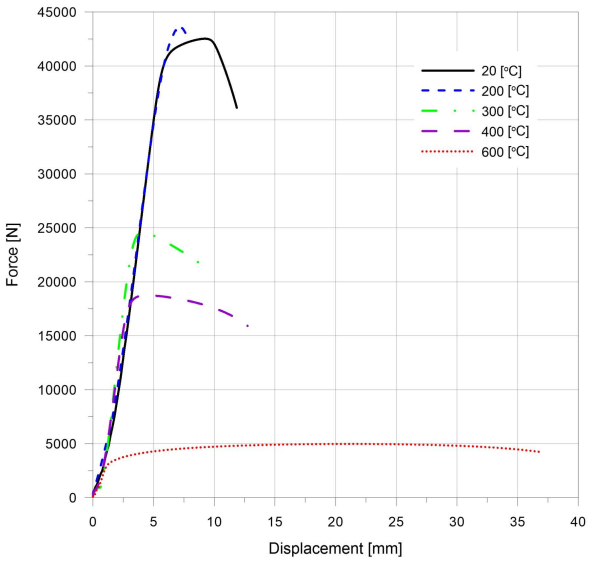

Fig. 6. Stress–displacement curves of WCL/1.2343 steel for different temperatures.

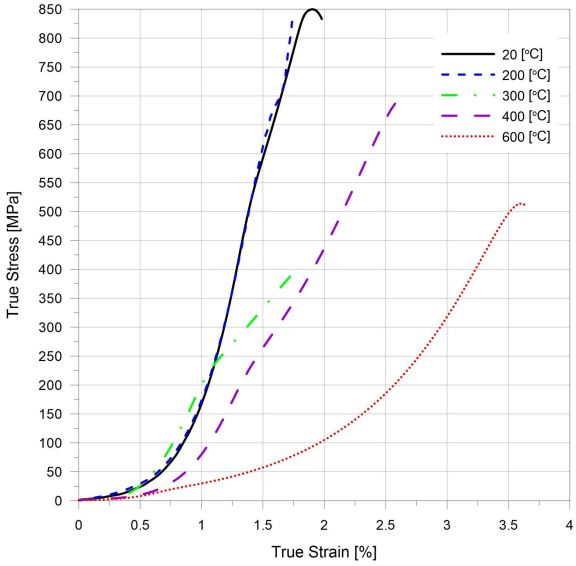

Fig. 7. True stress–strain diagrams for difference temperatures.

5. Experimental results

Figure 4 shows the sample scraps obtained after the tensile test. A quite significant difference in elongation can be noticed in the case of samples stretched at higher temperatures.

Figure 5 shows the actual tensile diagram obtained in the testXpert II program with marked strength values.

Table II shows the material properties obtained from the static tensile test.

Figure 6 shows the results of all tensile tests for 5 different temperatures. It can be observed that plasticity increases and the value of Young's modulus lowers at a higher temperature of the sample.

TABLE II

Material properties obtained of the experimental metods.

No.	T [°C]	E [GPa]	$R_{0.2}$ [MPa]	R_m [MPa]	A_o [%]
1.	20	21.0	518	541	6.24
2.	200	17.8	551	587	5.73
3.	300	25.0	305	313	5.10
4.	400	19.7	231	239	6.71
5.	600	6.26	43.8	63.4	19.42

Using the experimentally obtained strain diagrams (Fig. 6) and equations (3) and (5), it is possible to develop a true stress–true strain diagram (Fig. 7).

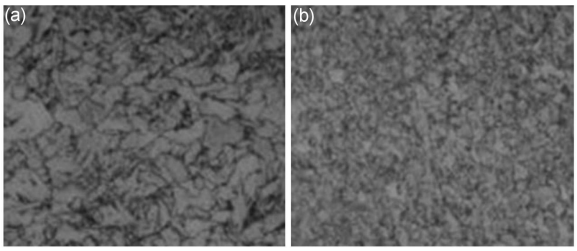

Fig. 8. Microstructure of the tested material for two selected temperatures (a) 20°C, (b) 600°C.

Figure 8 shows photos of the microstructure of two selected samples heated to 20°C (a) and 600°C (b).

6. Conclusions

In this work, a number of experimental tests are performed to determine the material properties of steel at various temperatures. These studies allowed the development of a discrete numerical model of the material, which can be used in computational simulations of analysed steel. Simulation results based on experimental tests increase computational accuracy.

Acknowledgments

The authors' work in this article was carried out as part of project 313011ASY4 by the University of Žilina "Strategic implementation of additive technologies to strengthen the intervention capacities of emergencies caused by the COVID-19 pandemic."

References

[1] Z. Guo, X. Wang, Y. Liu, Y. Liu, F. Li, *J. Constr. Steel Res.* **172**, 106174, (2020).

[2] X. Yan, Y. Xia, H.B. Blum, T. Gernay, *J. Constr. Steel Res.* **174**, 106299, (2020).

[3] H.-T. Li, B. Young, *Thin-Walled Struct.* **115**, 289 (2017).

[4] A. Su, Y. Sun, Y. Liang, O. Zhao, *Thin-Walled Struct.* **152**, 106723 (2020).

[5] P. Ptak, M. Pierzgalski, D. Cekus, K. Sokół, *Proc. Eng.* **177**, 175 (2017).

[6] F. Bárnik, M. Vaško, M. Sága, M. Handrik, A. Sapietová, *MATEC Web Conf.* 11, 01018 (2019).

[7] D. Wilczyński, I. Malujda, K. Talaśka, R. Dlugi, *Proc. Eng.* **177**, 411 (2017).

[8] T. Domański, W. Piekarska, Z. Saternus, M. Kubiak, S. Stano, *Materials* **15**, 3243 (2022).

[9] ChamberIR, E4 Data Sheet.

[10] ChamberIR, E4 User Manual.

[11] I. Faridmehr, M.H. Osman, A.B. Adnan, A.F. Nejad, R. Hodjati, M. Azimi, *Am. J. Civ. Eng. Archit.* **2**, 53 (2014).

Proceedings of "Applications of Physics in Mechanical and Material Engineering" (APMME 2023)

Influence of Hf and Y Content on the Local Occurrence of Antiferromagnetic Interactions in Amorphous Fe-Based Alloys

M. Nabiałek[a], D.S. Che Halin[b,c], J. Gondro[a], M.M.A.B. Abdullah[b,c], A.V. Sandu[d,e] and B. Jeż[f]

[a] *Department of Physics, Czestochowa University of Technology, Armii Krajowej 19 Av., 42-200 Częstochowa, Poland*
[b] *Center of Excellence Geopolymer and Green Technology, Universiti Malaysia Perlis, Taman Muhibbah, 02600 Arau, Perlis, Malaysia*
[c] *Faculty of Chemical Engineering and Technology, Universiti Malaysia Perlis, Taman Muhibbah, 02600, Arau, Perlis, Malaysia*
[d] *Gheorghe Asachi Technical University of Iasi, Faculty of Materials Science and Engineering, Blvd. D. Mangeron 41, 700050, Iaşi, Romania*
[e] *Romanian Inventors Forum, Str. Sf. P. Movila 3, Iaşi, Romania*
[f] *Department of Technology and Automation, Faculty of Mechanical Engineering and Computer Science, Czestochowa University of Technology, Al. Armii Krajowej 19c, 42-200 Częstochowa, Poland*

Doi: 10.12693/APhysPolA.144.304 *e-mail: barlomiej.jez@pcz.pl

Fe-based, rapid-quenched alloys are characterized by good magnetic properties. For alloys with ferromagnetic properties, an important parameter is the saturation magnetization. Its value depends on many factors, including: chemical composition, content of ferromagnetic elements, and structure of the material. For alloys with an amorphous structure, there is a chaotic arrangement of atoms in the alloy volume. Locally, however, the atoms may be in an order close to the crystal structure. The distances between magnetic atoms in such areas determine the magnetization process of the alloy. These distances can be adjusted with various alloy additions. The study investigated the effect of the content of Y and Hf on the distance between magnetic atoms and the value of saturation magnetization. It was found that a higher content of Y (characterized by a longer atomic radius compared to Hf) reduces the distance between Fe atoms and causes a decrease in the value of saturation magnetization. This is related to the local presence of antiferromagnetic order.

topics: bulk amorphous alloys, antiferromagnetic, Mössbauer spectroscopy

1. Introduction

The rapid development of human civilization, especially in the field of electronics and electrical engineering, constantly forces manufacturers to use newer and newer materials. These materials must meet rigorous shape quality standards and constantly improved performance parameters. Nowadays, electricity is a strategic medium and limiting its consumption is crucial. Therefore, materials that can be used to produce energy-saving electronic and electrical devices are being sought. Such materials are obtained by mixing appropriate ingredients while maintaining the rigor of production and obtaining the expected structure, both material and magnetic structure. Commonly known crystalline materials do not promise further development, therefore work is underway to change their structure. The change in structure may be related to the fragmentation of crystal grains present in the material, a change in their easy magnetization direction, or the complete elimination of the crystal structure. In conventionally used transformer sheets, their properties are improved in the texturing process, where a Goss or cube structure is obtained [1]. Such sheets can also be classified in terms of the directionality of their magnetic properties into isotropic and anisotropic. The former show the same magnetic properties in all measurement directions. The latter, however, have one specified direction of easy magnetization. From the point of view of magnetic properties, anisotropic steels are much better, but they have much worse mechanical properties. Both transformer sheets are obtained by cold rolling. The main difference in these materials is the Si content, which is approximately 1% for

isotropic steel and from 3.5 to 6.5% for anisotropic steel [2]. The most desirable in terms of operational profitability is a transformer sheet with increased Si content, despite the observed decrease in saturation induction. The reason for this is that the phenomenon of magnetostriction is reduced to almost zero, which significantly reduces the operating costs of transformers. The group of electrical alloys showing a negligible value of magnetostriction includes a significant number of amorphous alloys, which are commonly called amorphous [3, 4]. These types of materials do not contain crystal grains and do not require additional plastic processing. In the production process itself, amorphous alloys become an anisotropic material, which, if necessary, can only be subjected to an annealing treatment, also known as relaxation annealing. The production of this type of electrical materials takes place at very high cooling rates (10^2–10^6 K/s), which significantly reduces their thickness. A very important factor determining the magnetic properties is the chemical composition of the material produced. The basis for the production of amorphous materials for use in the production of transformers is the FeCoB matrix. Of course, at this point, it is necessary to mention nanocrystalline materials (not discussed in this study), which are created as a result of the thermal treatment of amorphous materials and have properties different from them. In the case of rapid quenching materials after production, it can be shown that the elements are not evenly distributed in their volume, which leads to disturbances in their magnetic properties. The main reason may be the occurrence of the Invar phenomenon [5] or the competition between ferro- and antiferromagnetic ordering.

The paper will present the results of Mössbauer tests performed for the bulk $Fe_{65}Nb_5Y_{5+x}Hf_{5-x}B_{20}$ ($x = 0, 1$) amorphous alloys after solidification.

2. Experimental procedure

The test samples were prepared in two stages. The first stage involved making ingots, and the second stage involved casting rapid quenched alloys. Amorphous plates were obtained from high-purity ingredients: Fe — 99.99 at.%, Co — 99.999 at.%, Y — 99.99 at.%, Hf — 99.9999 at.%. Boron was introduced in the form of an alloy with the chemical composition of $Fe_{45.6}B_{54.4}$. The alloy ingots were made using an arc furnace operating in an argon atmosphere. The alloy components were weighed, placed on a water-cooled copper plate and melted using an electric arc (350 A). The sample was melted three times on each side. Before each melting, pure titanium was first melted, which acted as an absorber of the oxygen remaining in the chamber. After final melting, the ingots were left to cool to minimize oxidation of the ingot surface. The thus obtained ingots weighing 20 g were cleaned mechanically and in an ultrasonic bath.

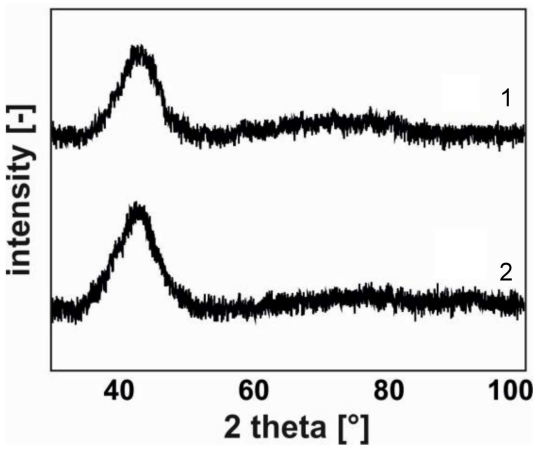

Fig. 1. X-ray diffraction images obtained for samples of the tested $Fe_{65}Nb_5Y_{5+x}Hf_{5-x}B_{20}$ alloys in the form of 0.5 mm plates: $x = 0$ (curve 1), $x = 1$ (curve 2).

After cleaning, they were crushed into smaller batch portions into an induction furnace, where bulk metallic glasses were produced. The plates were made in a chamber with a fixed argon atmosphere. Pieces of alloy melted using eddy currents were sprayed into a copper mold cooled by water. The liquid melt was solidified into a plate approximately 0.5 mm thick.

After solidification, the plates were subjected to X-ray diffraction (XRD) tests using a Bruker model ADVANCE 8 device. The device was equipped with a Cu X-ray tube, and the measurement was performed in the 2θ angle range from 30 to 100° with scanning density of 0.02° per measurement step and measurement time of 5 s. Mössbauer tests were performed on a POLON spectrometer. ^{57}Co was used as a Mössbauer source in a Rh matrix, with an activity of 50 mCi and a half-life of 270 days. The spectrometer was calibrated with 20 μm thick iron foil. Mössbauer spectra were recorded in transmission geometry. From the analysis of Mössbauer transmission spectra, the distributions of hyperfine field induction on ^{57}Fe nuclei were obtained. Primary magnetization curves were measured using a LakeShore vibration magnetometer operating at a magnetic field strength of up to 2 T. All measurements, i.e., XRD, vibrating-sample magnetometry (VSM) and Mössbauer measurement, were performed at room temperature.

3. Presentation of results

Figure 1 shows X-ray diffractograms obtained for samples of the tested alloys.

The X-ray diffractograms shown in Fig. 1 are similar and consist of a single broad maximum. This shape of the diffractograms indicates a chaotic arrangement of atoms in the sample volume for which

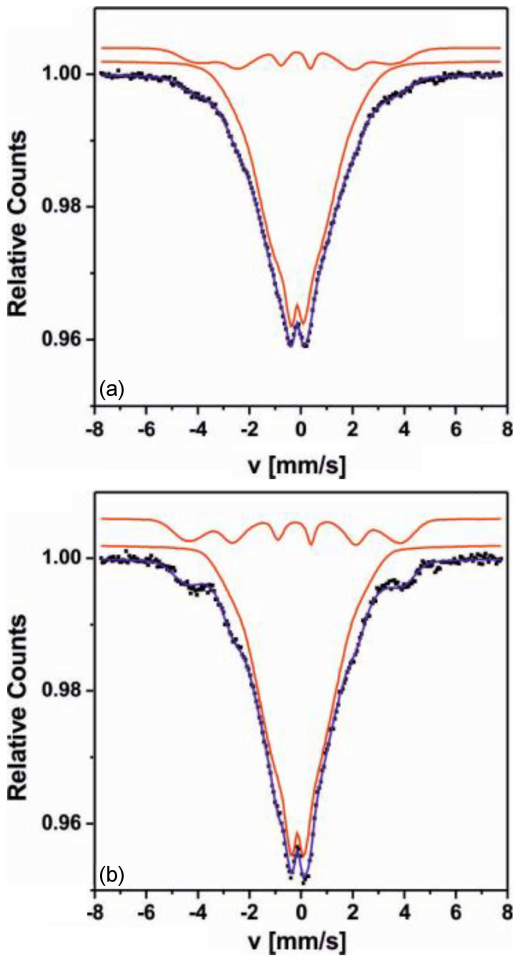

Fig. 2. Mössbauer transmission spectra obtained for the tested $Fe_{65}Nb_5Y_{5+x}Hf_{5-x}B_{20}$ alloys in the form of 0.5 mm plates: (a) $x = 0$, (b) $x = 1$.

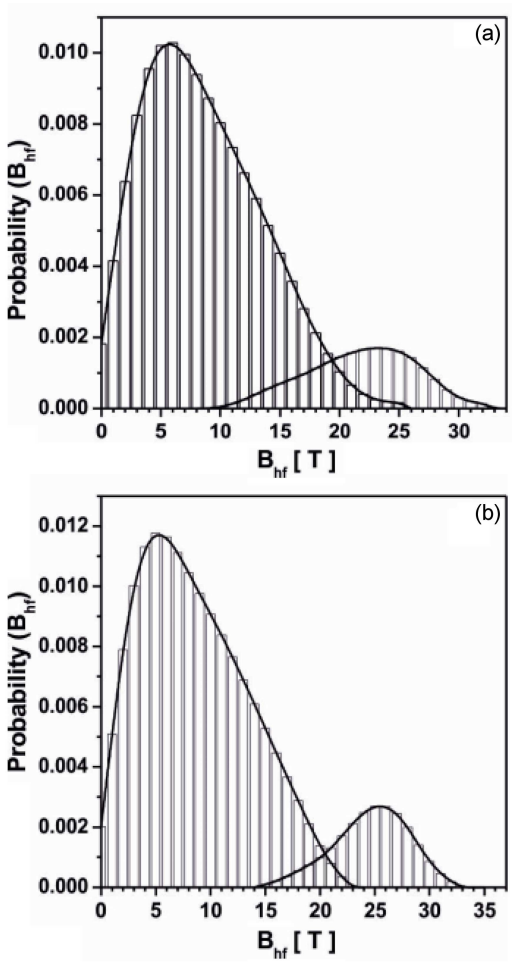

Fig. 3. Distributions of hyperfine field induction obtained based on the analysis of Mössbauer transmission spectra for the tested $Fe_{65}Nb_5Y_{5+x}Hf_{5-x}B_{20}$ alloys in the form of 0.5 mm plates: (a) $x = 0$, (b) $x = 1$.

there is no pattern, which in the case of crystalline materials gives an image in the form of a narrow peak related to the periodicity of the arrangement of atoms while maintaining the angular translations between them. The amorphousness of the samples was additionally confirmed by tests using Mössbauer spectroscopy. Figure 2 shows the Mössbauer transmission spectra measured for samples of the tested alloy after solidification.

The obtained Mössbauer spectra are typical for amorphous alloys. These spectra are asymmetric and consist of broad and overlapping lines. The so-called Zeeman sextets indicate that the tested material is an alloy with ferromagnetic properties. Based on the analysis of Mössbauer transmission spectra, the distributions of hyperfine field induction on ^{57}Fe nuclei were obtained (Fig. 3).

The distributions of hyperfine field induction on ^{57}Fe nuclei, obtained from the spectra (Fig. 2a and b), consist of two components, i.e., low field and high field. This shape of the presented distributions is related to the presence of different surroundings of iron atoms. As for the low-field component, it is associated with areas with high iron content. Increased concentrations of iron atoms force the distance between them to locally decrease, which may ultimately lead to the formation of antiferromagnetism. However, the high-field component is associated with iron atoms, which are also adjacent to Y and Hf atoms. For the sample with Y content = 5 (i.e, sample with $x = 0$), the average hyperfine field decreases, which probably leads to a local increase in the packing of Fe alloys. This state in the magnetic structure may manifest itself in the deterioration of saturation magnetization due to competition between ferro- and antiferromagnetic interactions. According to the Sleter–Bethe theory [6], reducing the distance between neighboring iron atoms results in a weakening of the ferromagnetic interactions and leads to a decrease in the hyperfine field of the low-field component in the hyperfine field distributions. This means that an increase in the share of the low-field component with a simultaneous decrease in its average hyperfine field may lead to the

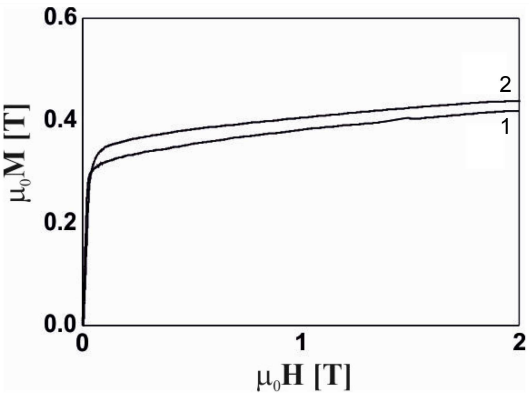

Fig. 4. Primary magnetization curves obtained for the tested $Fe_{65}Nb_5Y_{5+x}Hf_{5-x}B_{20}$ alloys in the form of 0.5 mm plates: $x = 0$ (curve 1), $x = 1$ (curve 2).

occurrence of areas with antiferromagnetic properties in the sample volume. Figure 4 shows the primary magnetization curves measured for the tested alloys.

For samples containing Y, a slight decrease in saturation is observed, which confirms the results of Mössbauer tests.

4. Conclusions

When designing amorphous alloys for use in electrical engineering, the phenomenon of rearrangement of ferromagnetic atoms in the sample volume should be taken into account. This rearrangement occurs already in the production process, which means that the most important element is developing the appropriate chemical composition of the alloy. As one can see, the introduction of elements with a large atomic radius has a negative impact on the homogeneity of the alloys after solidification. The observed increase in the low-field component with a simultaneous decrease in its average hyperfine field contributes to the competition between ferromagnetic and antiferromagnetic interactions.

References

[1] V. Jain, P. Modak, S. Patra, A. Ghosh, *Materialia* **22**, 101398 (2022).

[2] E. Reiplinger, *J. Magn. Magn. Mater.* **21**, 257 (1980).

[3] M. Nabiałek, S. Walters, K. Błoch, K. Jez, M. Talar, M.A.A. Mohd Salleh, D.S. Che Halin, B. Jez, *Acta Phys. Pol. A* **139**, 503 (2021).

[4] W. Lin, Y.Z. Yang, J. Xu, W. Li, *J. Alloys Compd.* **735**, 1195 (2018).

[5] V.A. Makarov, A. Ya. Belenkii, O.S. Kozlova, *Phys. Stat. Sol. (a)* **139**, 172 (1999).

[6] K.A. Gallagher, M.A. Willard, V.N. Zabenkin, D.E. Laughlin, M.E. McHenry, *J. Appl. Phys.* **85**, 5130 (1999).

Proceedings of "Applications of Physics in Mechanical and Material Engineering" (APMME 2023)

Influence of Meta-Atom Geometry on the Occurrence of Local Resonance Regions in Two-Dimensional Finite Phononic Structures

S. Garus[a,*], W. Sochacki[a], J. Garus[a], M. Šofer[b], P. Šofer[c] and K.M. Gruszka[d]

[a] *Department of Mechanics and Fundamentals of Machinery Design, Faculty of Mechanical Engineering and Computer Science, Czestochowa University of Technology, Dąbrowskiego 73, 42-201 Częstochowa, Poland*
[b] *Department of Applied Mechanics, Faculty of Mechanical Engineering, VSB — Technical University of Ostrava, 17. listopadu 2172/15, 708 00 Ostrava, Czech Republic*
[c] *Department of Control Systems and Instrumentation, Faculty of Mechanical Engineering, VSB — Technical University of Ostrava, 17. listopadu 2172/15, 708 00 Ostrava, Czech Republic*
[d] *Department of Computer Science, Czestochowa University of Technology, Dąbrowskiego 73, 42-201 Częstochowa, Poland*

Doi: 10.12693/APhysPolA.144.308 *e-mail: sebastian.garus@pcz.pl

In this work, the influence of different cross-sections of meta-atoms and their distribution on the occurrence of local resonance regions in inter-meta-atomic spaces of finite phononic structures was investigated. Software based on the Mathematica package was designed and implemented using the finite difference algorithm in the time domain to simulate mechanical wave propagation in phononic structures. Then, for the recorded time series from the inter-meta-atomic spaces, resonant frequency distributions were determined using Fourier transforms, and an analysis of the differences in frequency distributions depending on the location of the inter-meta-atomic space was carried out.

topics: finite-difference time domain (FDTD), discrete Fourier transform (DFT), local resonant regions, phononic structures

1. Introduction

In the realm of phononic structures, the study of how meta-atom geometry influences acoustic wave filtering properties has emerged as a critical research focus. Researchers are keenly interested in harnessing the controllability of such structures. Much of the attention in this field has traditionally been directed toward understanding phononic band gaps (PhnBG), which represent frequency bands where the passage of acoustic waves through a crystal is prohibited. This area of study has seen significant contributions, as evident in works such as [1–6], which delve into the characteristics and properties of these band gaps. Furthermore, researchers have delved into the geometry and arrangement of scatterers within phononic crystals. By altering the shape and layout of these scatterers, they aim to achieve specific properties within the PhnBG, including its width or blocking of a particular frequency band. For instance, research has examined the influence of scatterer orientation on tuning acoustic bands in two-dimensional phononic crystals [7], used numerical methods to explore tunable acoustic bandgaps [8], and even developed analytical models for tuning rods within phononic crystals to attenuate waves at particular frequencies [9]. The concept of active phononic crystals (APC) has also been a subject of interest, as highlighted in studies [10, 11]. APCs are a specialized class of phononic crystals that incorporate active components or materials to actively control and manipulate the propagation of acoustic or mechanical waves within the structure. Unlike traditional (passive) phononic crystals, which rely solely on the inherent properties of the crystal's structure to control the flow of waves, active phononic crystals use external energy sources or active materials to modify the wave properties in real time. These studies have shown the potential of active phononic crystals in controlling the propagation of waves at specific frequencies, offering the possibility of serving as directional mechanical filters. Another area of exploration has focused on understanding how factors such as the filling factor, lattice constant, and the shape and type of meta-atomic material affect the transmission of mechanical waves in quasi-two-dimensional phononic

structures [12]. Such investigations provide crucial insights into designing structures with desired wave properties. In supporting these investigations, numerical methods, particularly the finite-difference time-domain (FDTD) method, have played a pivotal role. FDTD is widely used to simulate wave propagation within periodic acoustic structures, making it a valuable tool for understanding and analyzing the characteristics of phononic crystals [2, 13–16]). In sum, the research surrounding the influence of meta-atom geometry in phononic structures is a multifaceted field, covering band gaps, scatterer properties, active control, and numerical simulations. These efforts are fundamental to advancing our knowledge and capabilities in designing phononic structures with a wide range of practical applications.

In this paper, by performing a series of calculations, we demonstrate how the spatial geometry of meta-atoms influences the resulting resonance regions localized in between them. For this reason, we constructed a special arrangement of meta-atoms, distributed evenly in part of the computational domain, and changed their geometry simultaneously, leaving their spatial location unchanged. The change in geometry was very limited and came down to changing the outer edge of the meta-atom while maintaining the distances between the centers of meta-atoms and their external dimension (radius). This approach allowed us not only to study the frequency response of both kinds of structures, but also made it possible to provide a direct comparison.

2. Computational details

In Fig. 1, we present a schematic representation of the calculation domain. The simulation was naturally divided into two parts: (i) the part in which the meta-atoms were rods made of polylactide (PLA) plastic ($\rho_r = 1240$ kg/m^3 and $V_r = 2220$ m/s) immersed in air ($\rho_a = 1.29$ kg/m^3 and $V_a = 331.45$ m/s) with a square cross-section and (ii) the part in which they were replaced with rods with a circular cross-section. The diameter of each rod corresponds to the side length of the square rod and equals $d = 2.75$ cm. The lattice constant (the distance between the centers of the rods) was set to 4 cm in each case, both for horizontal and vertical spacing. The simulation area is surrounded by PML layers (perfectly matched layers), which prevents the return of the acoustic wave reflected from the end of the computational domain. Through preliminary tests, it was determined that in order to absorb this unwanted reflected acoustic wave, it is necessary to use 16 PML layers with a resulting thickness of 4 cm. The simulation used a soft source located on the left side of the tested structures and marked in the drawing as SRC. This source is a continuous wave type with a sinusoidal envelope and

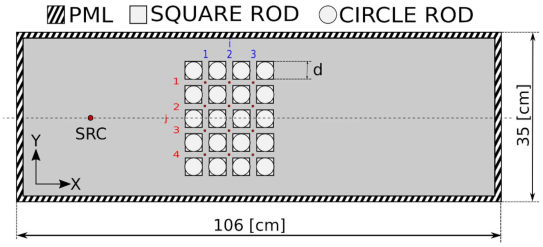

Fig. 1. Schematic diagram of the simulation domain. The square or circle meta-atoms are placed in rectangular array shifted to the left side of computational domain. The small red points indicate measurement locations P_{ij}, while the larger red point is the source of the acoustic wave.

frequency set to 1500 Hz. This frequency of the wave source causes the size of the sound wave (22 cm) to be comparable to the size of meta-atoms, ensuring their interesting interaction.

Data for further frequency analysis were collected from the area marked with red points in Fig. 1 (localised between meta-atoms, exactly in the geometric center between them). Each point in this area has been marked as P_{ij}, where index i stands for a column, while index j denotes a row of the array. According to this designation, point P_{11} is located in the upper left corner of the structure, while point P_{34} is located in the lower right corner of the structure. The overall size of the computational domain was selected in such a way as to limit the possibility of the formation of a standing wave as a result of possible interaction of the source with the boundaries of the box. Also, for this reason, the position of the whole meta-atom array is shifted relative to the center of the volumetric region. The time step in the simulation was set to $d_t = 5.4 \times 10^{-7}$ s, and the total simulation time was more than 32 ms. Data for frequency analysis were collected only after 16 ms of simulation duration, therefore reducing the influence of transient states on results.

3. Results and discussion

First, the frequency behavior of the structure was examined when the meta-atoms had a square cross-section. Figure 2 shows a series of graphs containing frequency analysis (Fourier analysis) for points $P_{11} - P_{34}$ collected during the simulation for all 9 examined spaces between the rods. For the convenience of analysis, the charts have been arranged in such a way that they spatially correspond to the location of the points from which the data for their creation was collected. For example, points P_{11}, P_{12}, P_{13}, and P_{14} are the points lying between the first and second columns of meta-atoms (counting from the source side), analogous to charts that present them. As one can see, each of the presented graphs

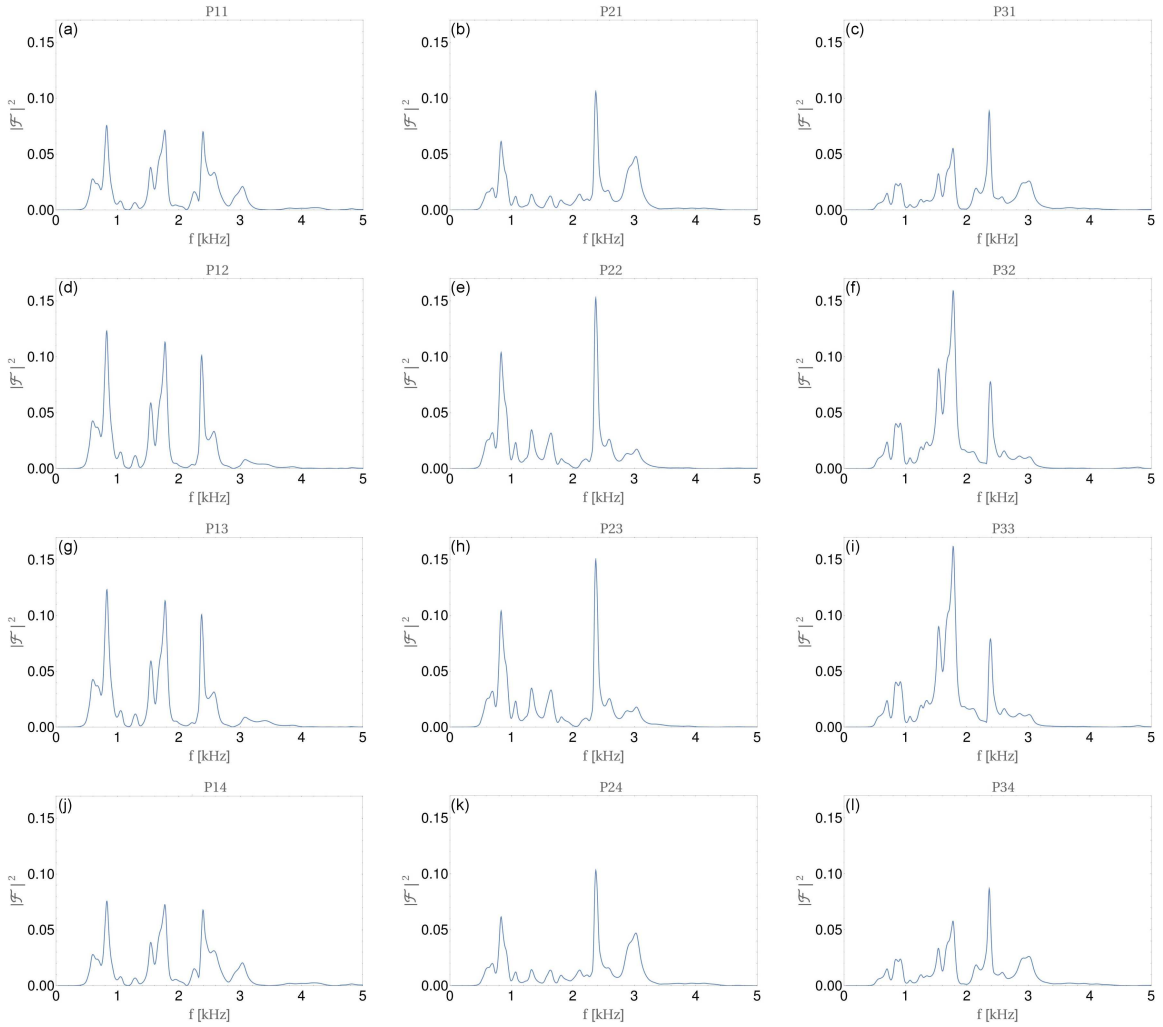

Fig. 2. Frequency analysis $|\mathscr{F}|^2$ recorded at points P_{11} to P_{34} for the structure made of square cross-section PLA rods. The source frequency was set to 1.5 kHz.

shows the presence of more than one frequency unrelated to the source frequency (1.5 kHz); in particular, the presence of the several most intense peaks can be distinguished. At the same time, in the frequency characteristics at each of the tested points, the presence of the main frequency of the sound wave emerging from the source is strongly suppressed. In the case where the measurement points lie in the same layer (column) as the point group PGC1 consisting of P_{11}, P_{12}, P_{13}, and P_{14}, group PGC2 — consisting of P_{21}, P_{22}, P_{23}, P_{24}, and the last group PGC3 (points $P_{31} - P_{34}$), a characteristic feature is the occurrence of the same frequencies within the same group with a simultaneous change in the relative intensity of the maxima. Detailed analysis also reveals that similarities in both the frequency distribution and the relative intensity of peaks occur between groups implementing point rows, e.g., between the group consisting of points P_{11}, P_{21}, P_{31} (PGR1) and the group consisting of points P_{14}, P_{24}, P_{34} (PGR4). These similarities also occur between the groups formed from points P_{12}, P_{22}, P_{32} (PGR2) and P_{13}, P_{23}, P_{33} (PGR3). Such relationships between groups of recording points suggest that the frequency behavior of the system reflects axial symmetry to some extent, assuming that the axis of symmetry is horizontal and passes through the source of the acoustic wave (marked in Fig. 1 as a central dashed line). This means that by moving transversely (along the y-axis) to the direction of acoustic wave propagation, one can easily control which acoustic frequencies are to be included in a given spectrum (and thus, in a sense, modify the frequency characteristics of the system).

In the case where rods with a square cross-section are replaced by rods with a circular cross-section, as presented in Fig. 3, characteristic symmetries are also observed, as in the first case mentioned. The mutual relations in the frequency spectrum between the points forming the columns of points (PGC1, PGC2, and PGC3) covering the positions of frequency peaks are of an identical nature, and within one column of measurement points, the differences occur mainly in the intensity of the peaks,

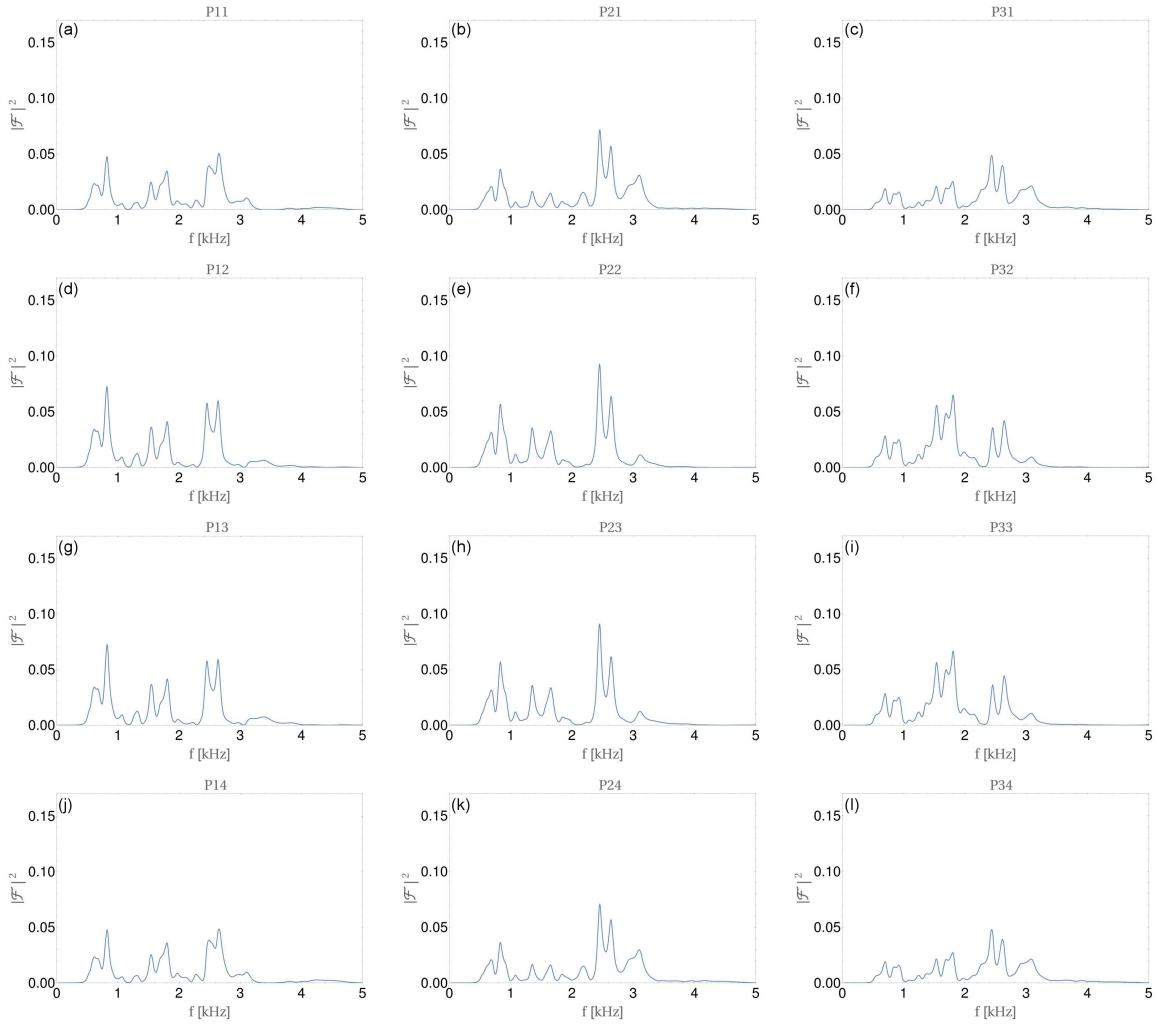

Fig. 3. Frequency analysis $|\mathscr{F}|^2$ recorded at points P_{11} to P_{34} for the structure made of circular cross-section PLA rods. The source frequency was set to 1.5 kHz.

and not in their position or number. Similarly, when considering symmetry along the horizontal axis, in this case it can be seen that the similarity between the groups of points in the rows (PGR1 and PGR4 as well as between PGR2 and PGR3) was preserved despite the change in the geometry of the meta-atoms. This observation confirms that the similarities between groups of points are related to the symmetry of the entire system, and not to the shape of the meta-atoms. As for the differences in spectrograms observed for different shapes of meta-atoms, it can be stated that these differences mainly come down to differences in the intensity of the peaks. The resonance of the acoustic wave between meta-atoms results mainly from the specific structure of the space between them. In the first case, in which the cross-section of the meta-atoms was square, the space between the meta-atoms is essentially parallel along the entire length of both sides of the meta-atom. This creates favorable conditions for the formation of a standing wave in these areas. Unlike the first case, when the meta-atoms have a circular cross-section, although the symmetry of the space between them is preserved, this space is much more complicated in terms of shape, and therefore it is much more difficult to create a standing wave in such a variable area, because standing waves generally require the presence of flat and parallel surfaces. The presence of these local resonance areas has a quite strong and positive effect on the intensity of the observed peaks in the first case examined. Although the nature of the spectra is similar in both cases, an almost twofold reduction in peak intensity is observed in the second case.

4. Conclusions

In this study, we investigated the influence of meta-atom geometry on the occurrence of local resonance regions in two-dimensional finite phononic structures. Our analysis involved two distinct scenarios, namely one where the meta-atoms had a square cross-section and another where the

meta-atoms were replaced by rods with a circular cross-section. The results of our investigation offer valuable insights into the role of meta-atom shape in shaping the acoustic response of the system. When considering the case with square cross-section meta-atoms, our findings revealed a complex frequency behavior characterized by the presence of multiple frequencies unrelated to the source frequency. Additionally, the primary frequency of the source wave was significantly suppressed. The analysis also unveiled a certain degree of axial symmetry, particularly concerning the vertical axis passing through the source, allowing for the modification of the system's frequency characteristics by transversely shifting recording points. For the square cross-section meta-atoms, we observed a complex frequency behavior characterized by multiple unrelated frequencies and significant suppression of the source wave's primary frequency. Our analysis revealed axial symmetry, allowing for the modification of frequency characteristics by shifting recording points transversely. In the case of circular cross-section meta-atoms, similar symmetries in frequency spectra were evident, indicating that the system's behavior is primarily determined by overall symmetry rather than meta-atom shape. The differences between the two scenarios mainly concerned the intensity of frequency peaks, with square meta-atoms exhibiting a strong local resonance effect. In conclusion, our study demonstrates that meta-atom geometry significantly influences the frequency behavior of two-dimensional finite phononic structures. The choice of meta-atom shape can enable control over the system's frequency characteristics, making it a key factor to consider when designing phononic structures for specific applications. These findings provide a foundation for further research in the field of acoustic wave manipulation and the design of novel phononic devices.

Acknowledgments

This research was supported in part by PLGrid Infrastructure.

References

[1] M.S. Kushwaha, P. Halevi, L. Dobrzyński, B. Djafari-Rouhani, *Phys. Rev. Lett.* **71**, 2022 (1993).

[2] S. Garus, W. Sochacki, *J. Appl. Math. Comput. Mech.* **17**, 19 (2018).

[3] A. Sukhovich, Li Jing, J.H. Page, *Phys. Rev. B* **77**, (2008).

[4] Jin-Chen Hsu, Tsung-Tsong Wu, *IEEE Trans. Ultrason. Ferroelectr. Freq. Control* **53**, 1169 (2006).

[5] M. Bold, S. Garus, W. Sochacki, in: *Engineering Mechanics 2018* Institute of Theoretical and Applied Mechanics of the Czech Academy of Sciences, Prague 2018.

[6] Gang Wang, Xisen Wen, Jihong Wen, Lihui Shao, Yaozong Liu, *Phys. Rev. Lett.* **93**, 154302 (2004).

[7] Xiaoling Li, Fugen Wu, Hefei Hu, Shao Zhong, Youyan Liu, *J. Physics D Appl. Phys.* **36**, L15 (2002).

[8] Wen-Pei Yang, Lien-Wen Chen, *Smart Mater. Struct.* **17**, 015011 (2007).

[9] T. Chen, M. Ruzzene, A. Baz, *J. Vib. Control* **6**, 1065 (2000).

[10] A. Baz, *J. Vib. Acoust.* **123**, 472 (2001).

[11] Youngjoon Kim, A.M. Baz, in: *Smart Structures and Materials 2004: Damping and Isolation*, ed. by Kon-Well Wang, SPIE, 2004.

[12] S. Garus, W. Sochacki, P. Kwiaton, M. Nabiałek, J. Petru, M. Kubanek, *Bull. Pol. Acad. Sci. Tech. Sci.* **73**, e144609 (2023).

[13] Y. Tanaka, M. Takigahira, S. Tamura, *Phys. Rev. B* **66**, 075409 (2002).

[14] W. Sochacki, *Acta Phys. Pol. A* **138**, 328 (2020).

[15] K.M. Gruszka, M. Dośpiał, *Acta Phys. Pol. A* **142**, 101 (2022).

[16] G.V. Norton, J.C. Novarini, *Comput. Phys. Commun.* **174**, 961 (2006).

Proceedings of "Applications of Physics in Mechanical and Material Engineering" (APMME 2023)

The Influence of the Shape of Acoustic Impedance Change on the Propagation of a Mechanical Wave in Multilayer Phononic Structures

S. Garus*

Department of Mechanics and Fundamentals of Machinery Design, Faculty of Mechanical Engineering and Computer Science, Czestochowa University of Technology, Dąbrowskiego 73, 42-201 Częstochowa, Poland

Doi: 10.12693/APhysPolA.144.313 *e-mail: sebastian.garus@pcz.pl

Thanks to the use of modern intelligent materials, such as composites consisting of piezoceramic fibers embedded in epoxy resin and covered with alternating electrodes, electroactive polymers, dielectric elastomers, magnetostrictive composites with epoxy resin or ferromagnetic alloys with shape memory, it is possible to control the geometry or properties of materials using pressure, external magnetic or electric fields. The paper analyzes multilayer quasi-one-dimensional phononic structures in which the selected layer is made of a material with time-varying acoustic impedance. The influence of the shape of the material properties changes over time (square wave, triangle wave, sawtooth wave) on the propagation of mechanical waves in the structure is analyzed.

topics: mechanical wave, finite difference time domain (FDTD), propagation, multilayers

1. Introduction

Many studies have been carried out describing the usefulness of phononic crystals as acoustic barriers [1], waveguides [2, 3], mechanical wave filters [4–7], acoustic diodes [8], or sensors [9]. One of the most interesting phenomena occurring during wave propagation in multilayer structures is the presence of a phononic band gap (PhnBG). Despite many years of research on PhnBG, many authors continue to develop this research and obtain interesting results [10–13].

The latest trends in the study of phononic crystals concern structures that can be "steerable." The building blocks of such crystals may be composite materials consisting of layered piezoceramic fibers embedded in epoxy resin and covered with electrodes [14, 15], magnetostrictive composites [16, 17], electroactive polymers (EAP) [18, 19], ferroelectric shape memory alloys [20], or carbon nanotubes [21].

The work analyzed the influence of changing the shape of the material parameters on the propagation of a mechanical wave in a multilayer structure.

2. Research

The propagation of a mechanical wave is described by differential equations

$$\frac{\partial P_{x,y,z,t}}{\partial t} = \rho_{x,y,z,t}\, c^2_{x,y,z,t} \nabla \cdot \boldsymbol{v}_{x,y,z,t}, \tag{1}$$

$$\rho_{x,y,z,t}\, c_{x,y,z,t} \frac{\partial \boldsymbol{v}_{x,y,z,t}}{\partial t} = \nabla P_{x,y,z,t}, \tag{2}$$

where $P_{x,y,z,t}$ is a scalar pressure field determined in time t and Euclidean space (x, y, z); $\rho_{x,y,z,t}$ and $c_{x,y,z,t}$ describe the material parameters (mass density and phase velocity, respectively), which for layer B are variable in time t; $\boldsymbol{v}_{x,y,z,t}$ is a vector of the velocity field.

By transforming equations (1) and (2) into a form describing a quasi-one-dimensional space in a form adapted to the finite difference algorithm in the time domain (FDTD), we obtained

$$P_x^{t+1/2} = P_x^{t+1/2} + C\, \rho_{x,t} c^2_{x,t} \left(v^t_{x+1/2} - v^t_{x-1/2} \right) \tag{3}$$

$$v^{t+1}_{x+1/2} = v^t_{x+1/2} + C \frac{1}{\rho_{x,t}} \left(P^{t+1/2}_{x+1} - P^{t+1/2}_{x} \right), \tag{4}$$

where

$$C = \frac{\Delta t}{\Delta z}. \tag{5}$$

The steps in time Δt and space Δz that ensure simulation stability are related to the Courant condition via

$$\Delta t \leq \frac{\Delta z}{c_{\max}}, \tag{6}$$

where $c_{\max}$ is the highest possible speed of mechanical wave propagation in the structure.

The paper analyzed the propagation of a mechanical wave in the BABAB structure. The material of the A layers and the surrounding material

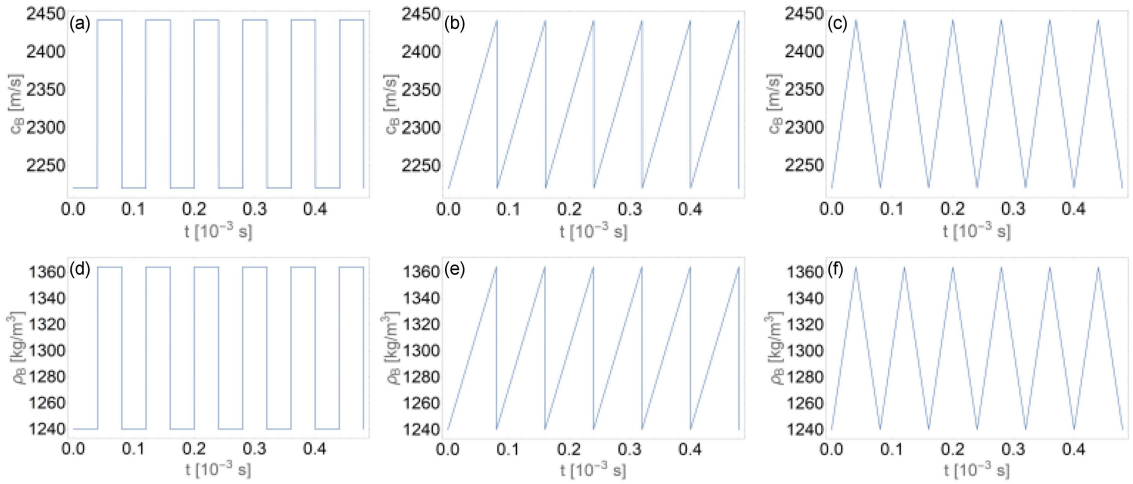

Fig. 1. Change in material parameters of layer B over time with (a, d) square, (b, e) sawtooth, and (c, f) triangle shape.

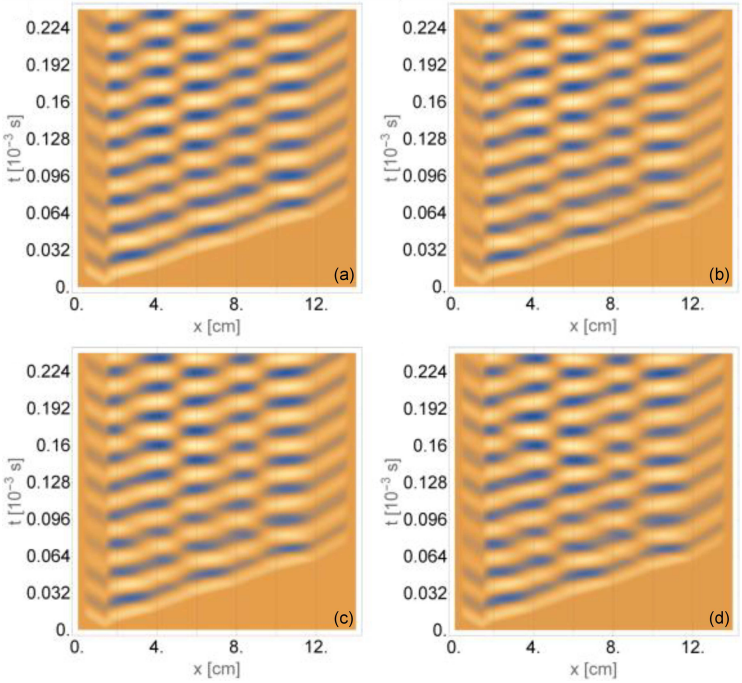

Fig. 2. Pressure distribution in time and space for changing material parameters of layer B with (a) solid, (b) triangle, (c) sawtooth, and (d) square shape.

was water, for which the assumed values of the material parameters were $\rho_A = 1000$ kg/m^3 and $c_A = 1480$ m/s [22]. In turn, material B was a material with time-varying properties, for which the basic values were the material parameters suitable for polylactic acid (PLA) ($\rho_B = 1240$ kg/m^3 and $c_B = 2220$ m/s [23]), which varied over time between the minimum value of material parameters corresponding to those suitable for PLA and the maximum values that were 10% higher than the base values. Changes in the values of material parameters over time are shown in Fig. 1.

The work used a soft mechanical wave source, and the simulation was surrounded by perfectly matched layer (PML) boundary conditions in order to extinguish the wave at the simulation boundary. In the tests, the frequency of the mechanical wave source was assumed to be 40 kHz, the thickness of the individual layers was 2 cm, the maximum assumed phase velocity of the mechanical wave was 5000 m/s, the step in space was $\Delta z = 0.4 \times 10^{-3}$ m, and the step in time was $\Delta t = 8 \times 10^{-8}$ s. The period of changes in the values of material parameters presented in Fig. 1 was $T = 80 \times 10^{-6}$ s. The analysis was performed for 10^4 time steps.

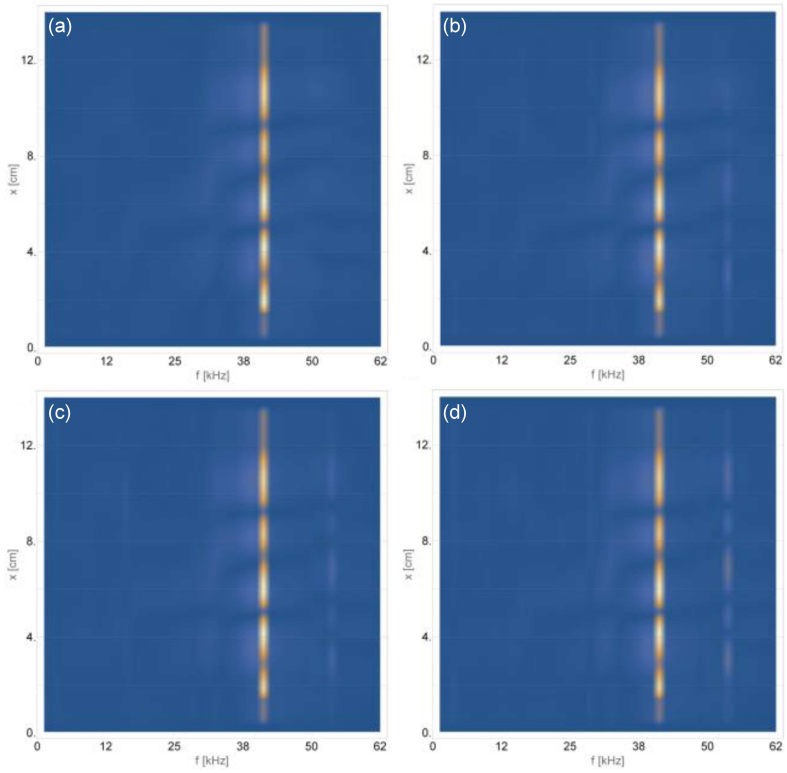

Fig. 3. Distribution of local resonance fields for changing the material parameters of layer B with (a) solid, (b) triangular, (c) sawtooth, and (d) square shape.

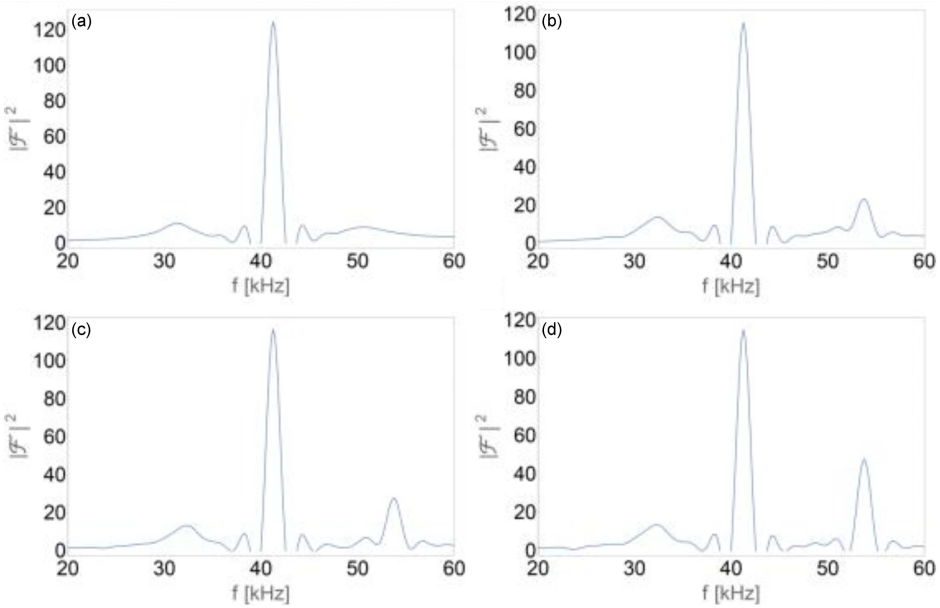

Fig. 4. Fourier transforms of signals occurring at the midpoint of the analyzed structure for changing the material parameters of layer B with (a) solid, (b) triangular, (c) sawtooth, and (d) square shape.

Figure 2 shows the pressure distribution in time and space for the first 3000 time steps. Figure 2a shows the results for a material with constant parameters suitable for PLA, while Fig. 2b–d shows the results for changes in material parameters in the (b) triangle, (c) sawtooth, and (d) square shape. As can be seen in Fig. 2a, when the wave reflected from the last boundary of the media reaches the first boundary of the media, a stable system of standing waves is created inside the phononic structure. Dynamically changing values of the material parameters of layers B (Fig. 2b–d) destabilize the rapid

formation of standing waves inside the multilayer structure. Maximum pressure changes occur at the boundaries of the centers. The longest stabilization time of standing waves inside the structure occurred for changes in material parameters with a square shape.

Figure 3 shows the intensity of frequencies occurring in the analyzed space. In all analyzed cases, there was a peak related to the frequency of the mechanical wave source. When introducing changes in the material properties over time (Fig. 3b–c), an additional peak was created in the wave spectrum at the frequency 53.75 kHz. The spectrum of the signal from the central point of the structure is also shown in Fig. 4. As can be seen, the intensity of the peak was related to the shape of changes in the material parameters of layer B and was the highest for the square shape (Fig. 4d), and then increasingly lower for the sawtooth (Fig. 4c) and triangular (Fig. 4b) shape. The energy introduced into the system is proportional to the square of the amplitude of material changes and is highest for the square shape, where the highest peak intensity occurs.

3. Conclusions

As part of the research, the influence of the shape of changes in material parameters of layers B of a multilayer structure on the propagation of a mechanical wave inside the structure was analyzed.

The introduction of additional energy in the form of changes in the material parameters of layer B resulted in a slowdown in the process of creating standing waves inside the structure and the creation of an additional peak in the frequency distribution inside the multilayer structure. The highest intensity of the obtained peak occurred for square-shaped material changes and was associated with the highest amount of energy introduced into the system.

References

[1] J.V. Sanchez-Perez, C. Rubio, R. Martinez-Sala, R. Sanchez-Grandia, V. Gomez, *Appl. Phys. Lett.* **81**, 5240 (2002).

[2] J. Wen, D. Yu, L. Cai, X. Wen, *J. Phys. D: Appl. Phys.* **42**, 115417 (2009).

[3] B. Morvan, A. Tinel, J.O. Vasseur, R. Sainidou, P. Rembert, A.-C. Hladky-Hennion, N. Swinteck, P.A. Deymier, *J. Appl. Phys.* **116**, 214901 (2014).

[4] W. Sochacki, *Acta Phys. Pol. A* **138**, 328 (2020).

[5] S. Villa-Arango, R. Torres, P.A. Kyriacou, R. Lucklum, *Measurement* **102**, 20 (2017).

[6] C.J. Rupp, M.L. Dunn, K. Maute, *Appl. Phys. Lett.* **96**, 111902 (2010).

[7] S. Garus, W. Sochacki, *Wave Motion* **98**, 102645 (2020).

[8] X.-F. Li, X. Ni, L. Feng, M.-H. Lu, C. He, Y.-F. Chen, *Phys. Rev. Lett.* **106**, 084301 (2011).

[9] S. Garus, *Rev. Chim.* **70**, 3671 (2019).

[10] W. Witarto, K.B. Nakshatrala, Y-L. Mo, *Mech. Mater.* **134**, 38 (2019).

[11] Y.F. Li, F. Meng, S. Li, B. Jia, S. Zhou, X. Huang, *Phys. Lett. A.* **382**, 10, 679 (2018).

[12] E. Li, Z.C. He, G. Wang, *Comput. Mater. Sci.* **122**, 72 (2016).

[13] S-L. Cheng, J-M. Liang, Q. Ding, Q. Yan, Y-T. Sun, T-J. Xin, L. Wang, *Wave Motion* **122**, 103195 (2023).

[14] M. Melnykowycz, X. Kornmann, C. Huber, M. Barbezat, A.J. Brunner, *Smart Mater. Struct.* **15**, 204 (2006).

[15] R. Paradies, P. Ciresa, *Smart Mater. Struct.* **18**, 035010 (2009).

[16] S. Levgold, J. Alstad, J. Rhyne, *Phys. Rev. Lett.* **10**, 509 (1963).

[17] C. Rodrígueza, M. Rodrigueza, I. Oruec, J.L. Vilas, J.M. Barandiaránb, M.L.F. Gubiedab, L.M. Leona, *Sens. Actuators A* **149** 251 (2009).

[18] W-P. Yang, L-W. Chen, *Smart Mater Struct.* **17**, 015011 (2008).

[19] J-S. Plante, S. Dubowsky, *Smart Mater. Struct.* **16**, 227 (2007).

[20] Y. Ganora, D. Shilo, J. Messier, T.W. Shield, R.D. James, *Rev. Sci. Instrum.* **78**, 073907 (2007).

[21] A.E. Aliev, J. Oh, M.E. Kozlov, A.A. Kuznetsov, S. Fang, A.F. Fonseca, R. Ovalle, M.D. Lima, M.H. Haque, Y.N. Gartstein, M. Zhang, A.A. Zakhidov, R.H. Baughman, *Science* **323**, 1575 (2009).

[22] Y. Wang, W. Song, E. Sun, R. Zhang, W. Cao, *Physica E* **60**, 37 (2014).

[23] D. Tarrazó-Serrano, S. Castiñeira-Ibáñez, E. Sánchez-Aparisi, A. Uris, C. Rubio, *Appl. Sci.* **8**, 2634 (2018).

Proceedings of "Applications of Physics in Mechanical and Material Engineering" (APMME 2023)

Transmission of a Phononic Superlattice Made of Dynamic Materials

S. Garus[a,*], W. Sochacki[a], J. Garus[a], J. Rzącki[b], P. Vizureanu[c,d] and A.V. Sandu[c,e,f]

[a] *Department of Mechanics and Fundamentals of Machinery Design, Faculty of Mechanical Engineering and Computer Science, Czestochowa University of Technology, Dąbrowskiego 73, 42-201 Częstochowa, Poland*
[b] *Department of Physics, Faculty of Production Engineering and Materials Technology, Czestochowa University of Technology, Dąbrowskiego 73, 42-201 Częstochowa, Poland*
[c] *Faculty of Materials Science and Engineering, Gheorghe Asachi Technical University of Lasi, Blvd. D. Mangeron 71, 700050, Iaşi, Romania*
[d] *Technical Sciences Academy of Romania, Dacia Blvd 26, 030167 Bucharest, Romania*
[e] *Romanian Inventors Forum, Str. Sf. P. Movila 3, 700089 Iaşi, Romania*
[f] *Academy of Romanian Scientists, 54 Splaiul Independentei St., Sect. 5, 050094, Bucharest, Romania*

Doi: 10.12693/APhysPolA.144.317 *e-mail: sebastian.garus@pcz.pl

In one-dimensional phononic crystals, as a result of multiple destructive interferences of a mechanical wave, the phononic band gap phenomenon occurs, i.e., the lack of propagation of a wave of a given frequency through the structure due to internal reflections at the layer boundary and destructive interference. In dynamic phononic crystals, the incident monochromatic mechanical wave at the boundary of the media does not propagate according to Fresnel's relations, but is transformed into a wave spectrum, which affects the phononic properties of the examined structures and allows them to be dynamically controlled. The paper analyzes the transmission and influence of the frequency of changes in the properties of the elements of the finite phononic structure described by sinusoidal functions on the propagation of mechanical waves.

topics: bandgap, finite-difference time-domain (FDTD), discrete Fourier transform (DFT), superlattice

1. Introduction

The first works on wave propagation in phononic crystals were written at the end of the 19th century. Initial considerations concerned static periodic structures. These structures exhibit unique dynamic properties, thanks to which they act as mechanical wave propagation filters only for specific material solids and geometries. It is in such structures that the so-called band gaps are created, i.e., frequency bands for which waves do not pass through a given structure. Among the many literature items describing this issue in various contexts, one can mention works such as [1–8].

Other structures that have been studied for many decades are quasi-static structures. In these structures, a specific parameter is changed and the properties of the phononic crystal are measured again. Works in this field include, for example, [9–13].

Controlling periodic phononic structures is a more complex issue and concerns the so-called dynamic phononic crystals. The work [14] presents the control of wave propagation in order to stop or limit the propagation of undesirable disturbances resulting from vibrations of the tested structure. A proposal to dynamically change the behavior of phononic crystals by changing material parameters as a function of time is presented in [15]. An interesting study on the propagation of time-varying parameters for phononic crystals was performed in [16] and [17]. The analysis of the time-varying Bragg reflector was presented by the authors in [18].

One way to determine the influence of time-varying material parameters is to use the finite-difference time-domain (FDTD) method, which is a common and versatile approach to acoustic simulation [19] and a starting point for the analysis of time-varying phononic crystals [20].

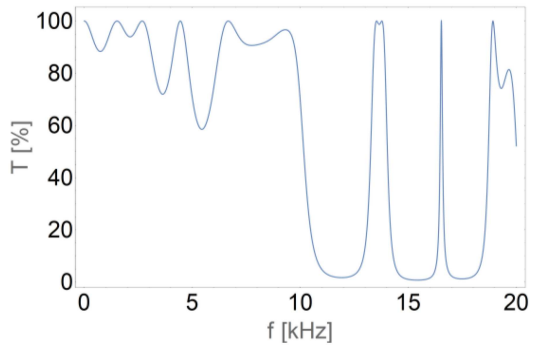

Fig. 1. Transmission of mechanical waves for a static Severin structure.

TABLE I

Material parameters used for calculations for the static phononic structure for the environment and layer A (water) [21] and for layer B (PLA) [22].

Layer	c [m/s]	ϱ [kg/m^3]	Z ($\times 10^6$) [kg/(s m^2)]
A (water)	1480	1000	1.48
B (PLA)	2220	1240	2.7528

In this work, the influence of dynamic material coefficients on the propagation and transmission of a mechanical wave inside the aperiodic quasi-one-dimensional Severin structure is analized.

2. Research

The propagation of a mechanical wave in a fifth-generation aperiodic Severin superlattice with a $(AB)_2B_2(AB)_3B_2(AB)_3AB_3(AB)_3B_2AB$ layer distribution was analyzed. The subscript indicates the number of repetitions of a given layer or (in brackets) a group of layers. The material parameters of the analyzed layers are summarized in Table I. The assumed thickness of each layer was 0.02 m, and the structure was immersed in water.

In order to determine the frequency values for which the phononic band gap occurs (no propagation of a wave of a given frequency in the structure due to the interference of a destructive mechanical wave occurring inside the phononic crystal) and the frequency for the high transmission band, the transfer matrix algorithm presented in [23] was used. Figure 1 shows the obtained transmission distribution for the analyzed Severin structure.

As shown in [23], in the transmission structure there is a high transmission peak with a small half-width for the propagating wave frequency of 16529 Hz surrounded by bandgap areas.

In order to analyze the mechanical wave propagation in the dynamic aperiodic Severin structure, the finite-difference time-domain (FDTD) algorithm was used, in which the mechanical wave propagation is described by

$$\begin{cases} \frac{\partial P(x,y,z,t)}{\partial t} = Z\left(t\right) c\left(t\right) \nabla \cdot \boldsymbol{v}\left(x,y,z,t\right), \\ \frac{Z(t)}{c(t)} \frac{\partial \boldsymbol{v}(x,y,z,t)}{\partial t} = \nabla P\left(x,y,z,t\right), \end{cases} \tag{1}$$

where $P(x,y,z,t)$ is the pressure field described in three-dimensional space (x,y,z) and at time t, $\boldsymbol{v}(x,y,z,t)$ is the vector velocity field. The material properties are described by time-dependent functions of the acoustic impedance $Z(t)$ and the phase velocity $c(t)$.

In the formalism of the FDTD method, taking into account the dynamic properties of the material, the system of equations (1) for the quasi-one-dimensional case can be written as

$$\begin{cases} P_k^{n+\frac{1}{2}} = P_k^{n+\frac{1}{2}} + \frac{\Delta t\, Z_k(t) c_k(t) \left[v_{k+\frac{1}{2}}^n - v_{k-\frac{1}{2}}^n \right]}{\Delta z} \\ v_{k+\frac{1}{2}}^{n+1} = v_{k+\frac{1}{2}}^n + \frac{\Delta t\, c_k(t) \left[P_{k+1}^{n+\frac{1}{2}} - P_k^{n+\frac{1}{2}} \right]}{\Delta z Z_k(t)} \end{cases} \tag{2}$$

Here, Δz and Δt define steps in space and time, respectively, and to ensure the stability of the simulation they must satisfy the Courant stability condition $\Delta t \leq \Delta z / c_{\max}$, where $c_{\max}$ means the highest possible phase velocity of a propagating mechanical wave. In (2), k is the spatial step number. In this work, PML boundary conditions were used to extinguish the wave going beyond the examined area. A soft mechanical wave source with a frequency f_S was used

$$\begin{cases} Z_n\left(t\right) = Z_{n,0} + \frac{D_n}{2} Z_{n,0} \sin(2\pi f_n t) \\ c_n\left(t\right) = c_{n,0} + \frac{D_n}{2} c_{n,0} \sin(2\pi f_n t) \end{cases} \tag{3}$$

where n corresponds to a given type of material in the layer (A or B), $Z_{n,0}$ and $c_{n,0}$ are the acoustic impedance and phase velocity of the material in the layer n, respectively, and D_n is percentage change in the amplitude of the variable component of material parameters.

In the first analyzed case, a ten percent change in the amplitude of material values ($D_A = D_B = 10\%$) was assumed with a frequency equal to the frequency of the wave source ($f_S = f_A = f_B = 16529$ Hz) for high transmission peak. Using the FDTD and discrete Fourier transform (DFT) algorithms, the distribution of local resonance fields was determined (Fig. 2). Figure 3 shows the spatial distribution of local resonance areas that occurred at the frequency of 8375 Hz. Vertical or horizontal lines in the graphs, respectively, indicate layer boundaries.

The shift in the frequency of the local resonance areas from the source frequency of 16529 Hz to the frequency of 8375 Hz compared to the static structure [23] and the significant increase in the amplitude of the mechanical wave in the analyzed areas is caused by the resonance occurring due to the correspondence of the vibrations of the medium and the source.

In the second case (Fig. 4 and Fig. 5), only the time-varying values of the material parameters of layers B were analyzed with a frequency consistent

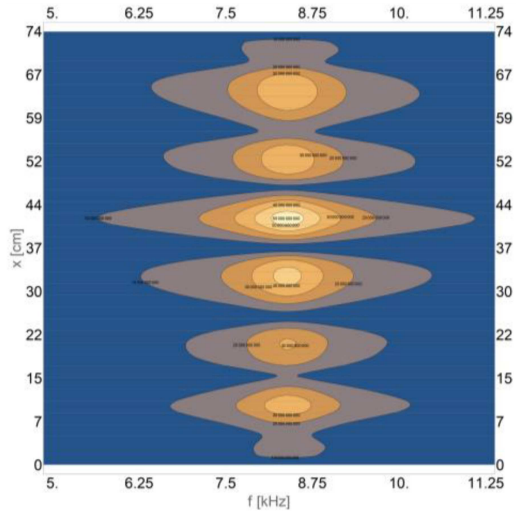

Fig. 2. Distribution of local resonance fields for the source frequency equal to f_S=16529 Hz for materials values pulsating with the frequency of the source with the vibration amplitude equal to 10% of the mediums parameters.

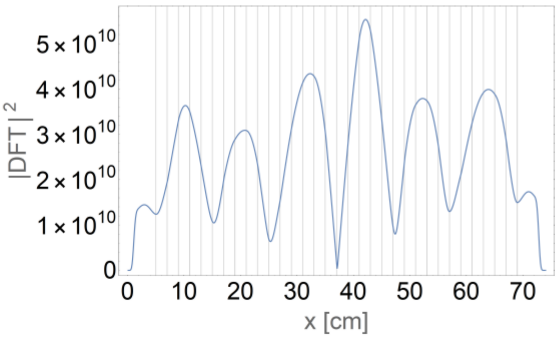

Fig. 3. Spatial distribution of local resonance areas that occurred at the frequency of 8375 Hz in the case of D_A=D_B=10% and f_S=f_A=f_B=16529 Hz.

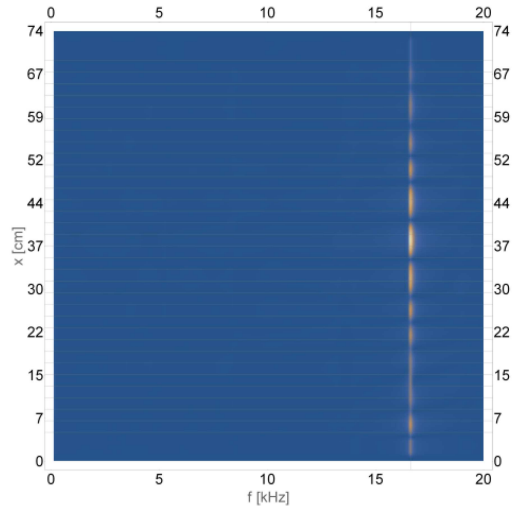

Fig. 4. Distribution of local resonance fields for $f_S = f_B = 16529$ Hz, $f_A = 0$ Hz, $D_A = 0$, and $D_B = 10\%$.

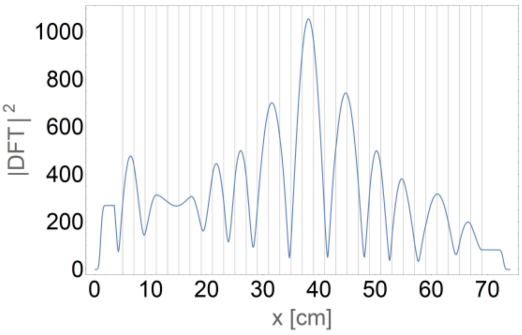

Fig. 5. Spatial distribution of local resonance areas that occurred at the frequency of 16529 Hz in the case of $f_S = f_B = 16529$ Hz, $f_A = 0$ Hz, $D_A = 0$, and $D_B = 10\%$.

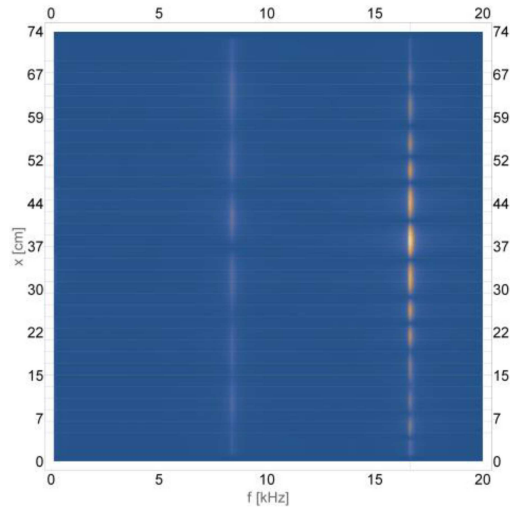

Fig. 6. Distribution of local resonance fields for $f_S = f_B = 16529$ Hz, $f_A = 0$ Hz, $D_A = 0$, and $D_B = 12\%$.

with the frequency of the mechanical wave source ($f_S = f_B = 16529$ Hz, $f_A = 0$), where the amplitude change was 10% ($D_A = 0$, $D_B = 10\%$). Compared to a structure made of materials with static properties [23], the value of the amplitude of mechanical vibrations in local resonance areas was reduced by two times. By increasing the value of the amplitude change to $D_B = 12\%$ (Fig. 6 and Fig. 7), an additional frequency was observed in the spectrum, which corresponded to the value from the first analyzed case in which resonance was observed.

In the last analyzed case (Fig. 8 and Fig. 9), the oscillation frequency of material B was reduced in relation to the source frequency by 10% ($f_B = 90\%$, $f_S = 14876$ Hz, $f_A = 0$ Hz), with the amplitude of changes in the values of material parameters equal to 10% ($D_A = 0$, $D_B = 10\%$).

Apart from the source frequency, two additional frequencies were also observed in the spectrum, i.e., 13375 Hz and 1750 Hz, for which there were local resonance areas within the analyzed phononic structure.

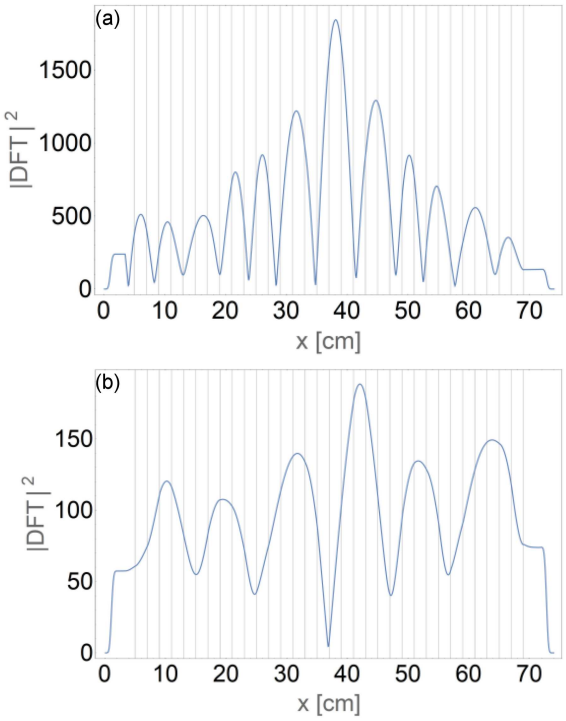

Fig. 7. Spatial distribution of local resonance areas in the case of $f_S = f_B = 16529$ Hz, $f_A = 0$ Hz, $D_A = 0$, and $D_B = 12\%$, which occurred at frequencies (a) 16529 Hz and (b) 8375 Hz.

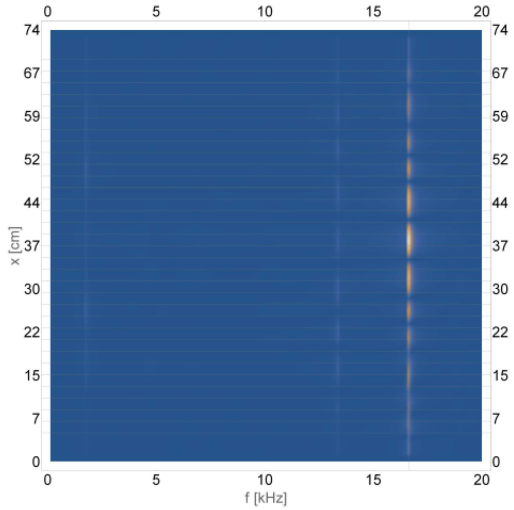

Fig. 8. Distribution of local resonance fields for $f_B = 90\%$, $f_S = 14876$ Hz, $f_A = 0$ Hz, $D_A = 0$, and $D_B = 10\%$.

3. Conclusions

The tests carried out showed the existence of band gaps in the transmission spectrum for the Severin aperiodic phononic structure. The introduction of vibrations in the values of material parameters (acoustic impedance and density) for all simulation

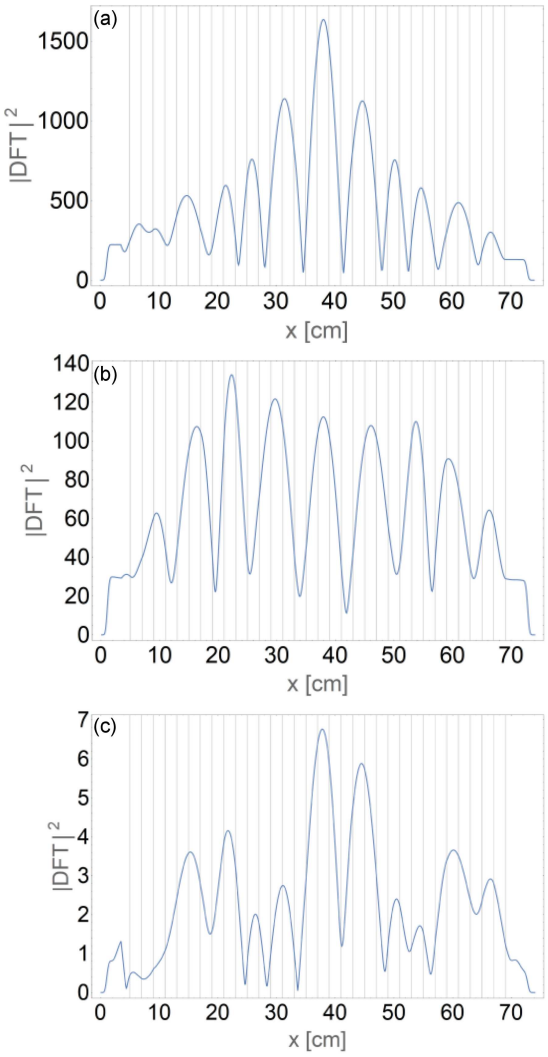

Fig. 9. Spatial distribution of local resonance areas in the case of $f_B = 90\%$, $f_S = 14876$ Hz, $f_A = 0$ Hz, $D_A = 0$, and $D_B = 10\%$, which occurred at frequencies (a) 16529 Hz, (b) 13375 Hz, and (c) 1750 Hz.

materials with a frequency equal to the frequency of the wave source caused the phenomenon of resonance and a shift of the transmission peak towards lower frequencies, reducing the number of local resonance areas and increasing the amplitude of the mechanical wave propagating in the material. The introduction of 10% changes in the vibration amplitudes of the acoustic impedance and the density of only the B material resulted in a reduction of the amplitude and energy of the mechanical wave in local resonance areas and changed their distribution. Another increase in the amplitude by 2% resulted in the creation of an additional local resonance region at the frequency of 8.3 kHz. For the vibration frequency of parameters of the material B equal to 90% of the source vibration frequency, there were 3 groups of local resonance areas: 1.6 kHz, 13.3 kHz, and 16.6 kHz.

References

[1] X.-F. Li, X. Ni, L. Feng, M.-H. Lu, C. He, Y.-F. Chen, *Phys. Rev. Lett.* **106**, 084301 (2011).

[2] R. Martínez-Sala, J. Sancho, J.V. Sánchez, V. Gómez, J. Llinares, F. Meseguer, *Nature* **378**, 241 (1995).

[3] M.S. Kushwaha, P. Halevi, L. Dobrzyński, B. Djafari-Rouhani, *Phys. Rev. Lett.* **71**, 2022 (1993).

[4] S. Garus, W. Sochacki, *J. Appl. Math. Comput. Mech.* **16**, 17 (2017).

[5] A. Sukhovich, L. Jing, J.H. Page, *Phys. Rev. B* **77**, 014301 (2008).

[6] Jin-Chen Hsu, Tsung-Tsong Wu, *IEEE Trans. Ultrason. Ferroelectr. Freq. Control* **53**, 1169 (2006).

[7] S. Garus, W. Sochacki, M. Bold, *Eng. Mech.* **2018**, 229 (2018).

[8] G. Wang, X. Wen, J. Wen, L. Shao, Y. Liu, *Phys. Rev. Lett.* **93**, 154302 (2004).

[9] X. Li, F. Wu, H. Hu, S. Zhong, Y. Liu, *J. Phys. D Appl. Phys.* **36**, L15 (2003).

[10] W-P. Yang, L-W. Chen, *Smart Mater. Struct.* **17**, 015011 (2008).

[11] M. Ruzzene, A. Baz, *J. Vib. Acoust.* **122**, 151 (2000).

[12] O. Thorp, M. Ruzzene, A. Baz, *Smart Mater. Struct.* **10**, 979 (2001).

[13] A. Singh, D.J. Pines, A. Baz, *Smart Mater. Struct.* **13**, 689 (2004).

[14] A. Baz , *J. Vib. Acoust.* **123**, 472 (2001).

[15] D.W. Wright, R.S.C. Cobbold, *Smart Mater. Struct.* **18**, 015008 (2009).

[16] E.S. Cassedy, *Proc. IEEE* **55**, 1154 (1967).

[17] C. Elachi, *IEEE Trans. Antennas Propag.* **20**, 534 (1972).

[18] J.H. Wu, T.H. Cheng, A.Q. Liu, *Appl. Phys. Lett.* **89**, 263103 (2006).

[19] Y. Tanaka, Y. Tomoyasu, S-I. Tamura, *Phys. Rev. B* **62**, 7387 (2000).

[20] X. Liu, D.A. McNamara, *Int. J. Infrared Milli. Waves* **28**, 759 (2007).

[22] Y. Wang, W. Song, E. Sun, R. Zhang, W. Cao, *Physica E* **60**, 37 (2014).

[23] D. Tarrazó-Serrano, S. Castiñeira-Ibáñez, E. Sánchez-Aparisi, A. Uris, C. Rubio, *Appl. Sci.* **8**, 2634 (2018).

[24] S. Garus, W. Sochacki, J. Garus, J. Rzącki, *Acta Phys. Pol. A* **142**, 7 (2022).

Proceedings of "Applications of Physics in Mechanical and Material Engineering" (APMME 2023)

Changes in the Initial Magnetic Susceptibility in Amorphous Alloys Exhibiting Soft Magnetic Properties

M. Nabiałek[a], P. Pietrusiewicz[a], P. Palutkiewicz[b], K. Błoch[a], M.M.A.B. Abdullah[c], A.V. Sandu[d,e] and B. Jeż[b,*]

[a] *Department of Physics, Czestochowa University of Technology, Armii Krajowej 19, 42-200 Częstochowa, Poland*
[b] *Department of Technology and Automation, Faculty of Mechanical Engineering and Computer Science, Czestochowa University of Technology, Armii Krajowej 19c, 42-200 Częstochowa, Poland*
[c] *Center of Excellence Geopolymer and Green Technology, Universiti Malaysia Perlis, Taman Muhibbah, 02600 Arau, Perlis, Malaysia*
[d] *Gheorghe Asachi Technical University of Iasi, Faculty of Materials Science and Engineering, Blvd. D. Mangeron 41, 700050, Iaşi, Romania*
[e] *Romanian Inventors Forum, Str. Sf. P. Movila 3, Iaşi, Romania*

Doi: 10.12693/APhysPolA.144.322 *e-mail: bartlomiej.jez@pcz.pl

In weak magnetic fields, there are changes in the arrangement of atoms, which are otherwise called magnetic relaxations. The exact phenomenon that will be investigated in this paper concerns the disaccomodation of magnetic susceptibility, which is one of the most frequently observed effects of magnetic lag. During this magnetic delay, there is a reorientation of the axes of pairs of atoms corresponding to two different energy levels. This energy is related to the energies of exchange and spin–orbit coupling. The paper presents the results of magnetic susceptibility disaccomodation and describes its influence on the relaxation time matching spectrum.

topics: initial magnetic susceptibility, amorphous alloy, X-ray diffraction

1. Introduction

A very important utility parameter of soft-magnetic ferromagnetic alloys is the temperature stability of magnetic susceptibility. This applies not only to materials with a crystalline structure but to all consumer materials with soft magnetic properties [1–3]. In amorphous materials, the initial magnetic susceptibility shows a slightly different behavior than that observed in crystalline materials. Many papers have presented and described the results of measurements of the initial magnetic susceptibility as a function of temperature for amorphous and nanocrystalline materials [4–6]. When measuring the susceptibility at time t after demagnetizing the sample, a random distribution of the orientation of the axis of atom pairs occurs. Atom pairs tend to align their axes according to the spontaneous magnetization of the domain wall, thus introducing a distribution of local anisotropy and deepening the potential well. As a result, the domain wall stabilizes, which in turn results in a reduction in compliance over time (Fig. 1) [4, 5].

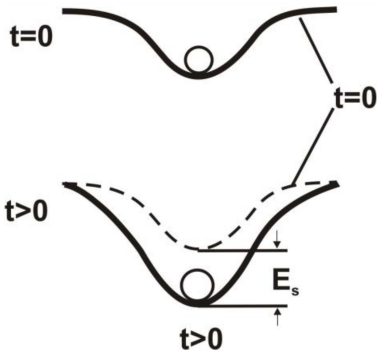

Fig. 1. Development of the domain wall stabilization potential over time [5].

The decrease in magnetic susceptibility over time is related to the temporary stabilization of the domain wall potential ($E_ś$). After demagnetizing the sample, the position of the domain wall is determined by the anchoring potential of this wall, E_0, which is the result of the presence of structural defects and surface irregularities.

In this case, for $t > 0$, the total potential associated with the movement of the domain wall is determined by the relationship [6]

$$E(U,t) = E_0(U) + E(U,t). \tag{1}$$

The total process of relaxation of magnetic susceptibility between time t_0 and t is presented by the relationship [3]

$$\Delta\frac{1}{\chi} = \frac{1}{\chi(t)} - \frac{1}{\chi(0)} = \frac{1}{2M_s^2 S_{ś}} \frac{\mathrm{d}^2 E_{ś}(U,t)}{\mathrm{d}U^2}\bigg|_{U=0}, \tag{2}$$

where $S_{ś}$ it is the area of the domain wall per unit volume; U — a distance of displacement of the domain wall after time t from its initial position; $E_{ś}(U,t)$ — domain wall stabilization potential described according to the formula [7]

$$E_{ś}(U,t) = -c_0(t)\left\langle \frac{1}{\cosh^2\left(\frac{\Delta_s}{k_\mathrm{B}T}\right)}\right\rangle \left(1 - \mathrm{e}^{t/\tau_R}\right) \times \int\limits_{-\infty}^{+\infty} \mathrm{d}z \left\langle \Delta_m(z-U)\Delta_m(z)\right\rangle. \tag{3}$$

Here, $c_0(t) = n_0(t) = n_\infty + (n_0(0) - n_\infty)\,\mathrm{e}^{-t\tau_A}$ is the average number of pairs of atoms per unit volume; $\tau_A = \tau_{0A}\,\mathrm{e}^{Q_A/(k_\mathrm{B}T)}$ and $\tau_R = \tau_{0R}\,\mathrm{e}^{Q_R/(k_\mathrm{B}T)}$ — relaxation times related, respectively, to the change in defect density and the reorientation of the axes of thermally activated atom pairs (Q_A, Q_R — activation energies); Δ_m and Δ_s are the energies of magnetic and structural fission between two orientations of atom pairs.

The paper presents the results of initial magnetic susceptibility tests performed for the $Fe_{63}Co_9Y_8B_{20}$ bulk amorphous alloys in the form of a plate, made using two production methods: injection method or suction casting method.

2. Experimental procedure

The test material in the form of amorphous samples was made of high-purity ingredients: Fe — 99.99 at.%, Co — 99.999 at.%, Y — 99.99 at.%, Zr — 99.99 at.%. Boron was added in the form of a previously prepared alloy with the chemical composition of $Fe_{45.6}B_{54.4}$. Adding boron in the form of an alloy ensures that the nominal boron values in the alloy are achieved. An attempt to introduce boron as a pure component did not make it possible to maintain the assumed chemical composition. Boron is a material that can spray in the furnace chamber during remelting, which changes the chemical composition of the alloy and makes it difficult to obtain the intended research material. The prepared batches of alloying elements are mixed and placed in a cavity on a copper plate in an arc furnace. The weighed samples have a mass of 10 g. The alloy components are melted in a protective atmosphere of argon, which promotes amorphization. The material is melted several times on each side (at least 3 times), which ensures good mixing. After cooling in the furnace, the ingots prepared in this way are cleaned mechanically and using an ultrasonic bath. Then, as a result of crushing, they are divided into smaller portions of a few grams each. The samples were produced using two methods: the injection method and the method of sucking the liquid alloy into a water-cooled copper mold. In these methods, the liquid alloy is placed in a copper mold in a protective atmosphere of argon. In the case of the suction method, the alloy is melted using an electric arc, and in the injection method — using eddy currents. The samples thus obtained were tested for structure and magnetic properties. Structure tests were performed using a Bruker X-ray diffractometer, model ADVANCE 8. The tests were performed for low-energy powders, which made it possible to test the material in volume. The X-ray measurement was performed in the range of the 2θ angle from 30 to 100° with a measurement step of 0.02° and a measurement time per step of 3 s. Tests of magnetic properties in low magnetic fields were performed using an automated system for measuring magnetic susceptibility. Measurements were made in the temperature range from room temperature (20°C) to the temperature of the ferromagnetic–paramagnetic magnetic transition. The samples produced were so-called open ones, in which the magnetic circuit had to be closed. The magnetic circuit was closed using a yoke made of superpermalloy. Two windings of 30 turns each are wound. One winding was secondary, the other primary.

3. Results

Figure 2 shows the X-ray diffraction patterns obtained for the samples prepared after solidification using injection and suction methods.

Both X-ray diffractograms are similar. Only a broad halo with a maximum near angle of 50° is visible. This shape of X-ray diffractograms is typical for materials with an amorphous structure.

Figure 3 shows the initial magnetic susceptibility curves measured for the tested samples produced by two methods. The measurement was performed in the magnetic field range of $0.4H_C$, the so-called Rayleigh's area.

The initial magnetic susceptibility curves obtained for the tested alloys are similar. Generally, in the temperature range from 300 to about 500 K, a weakly temperature-dependent background is visible, which increases with increasing temperature. The sudden drop in the initial magnetic susceptibility is associated with the magnetic transition from the ferromagnetic state to the paramagnetic state. However, the influence of the production method is visible.

Relaxation processes of magnetic susceptibility are directly related to the time dependence of potential stabilization (1). After demagnetizing the

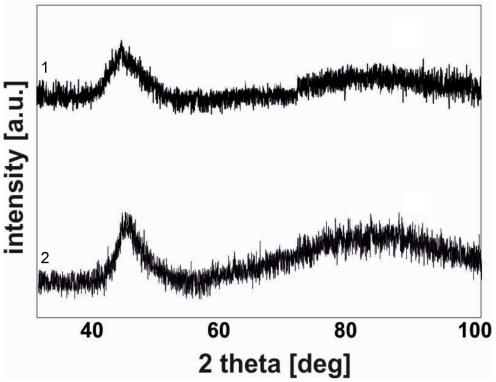

Fig. 2. X-ray diffractograms obtained for the tested samples of the $Fe_{63}Co_9Y_8B_{20}$alloy made by: line 1 — injection, line 2 — suction.

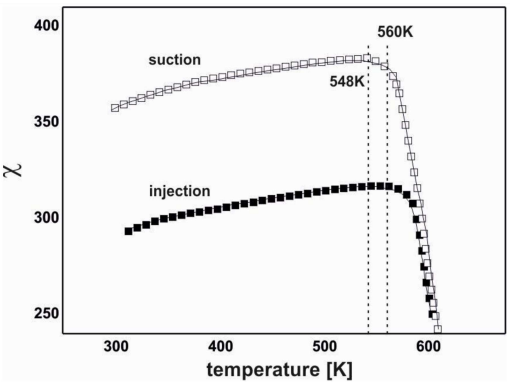

Fig. 3. Initial magnetic susceptibility curves measured for the tested samples of the $Fe_{63}Co_9Y_8B_{20}$ alloy made by: injection (full symbols), suction (empty symbols).

sample with a current with amplitude decreasing to zero, the position of the domain walls is determined by the static anchoring potential of the domain wall $E_0(U)$ (1), which is the result of the presence of structural defects and surface irregularities. Due to the magnetic interactions between spontaneous magnetization and mobile defect configurations within domain walls, defect rearrangement provides the opportunity to reduce the total magnetic interaction energy of domain walls with structural defects. As a result, it leads to a time-dependent so-called "stabilization potential" (3), within which domain walls move. It should follow from the above that for production methods with the same cooling rate, the obtained samples should have a very similar value of initial magnetic susceptibility and maintain a similar course as a function of temperature.

4. Conclusions

The value of the initial magnetic susceptibility is related to the presence of free volumes in the melt after solidification. The two production methods used, i.e., the method of forcing and the method of sucking liquid alloy into a water-cooled copper mold, have a similar cooling speed ranging from 10^{-1} to 10^3 K/s. One would expect very similar curves obtained for the same alloy. However, as the research results show, it is different. X-ray diffraction patterns clearly indicate that the samples have an amorphous structure. Also, the curves from the measurements of the initial magnetic susceptibility are similar to those for amorphous materials. It is clearly visible that in both tested samples there is a different number of structure defects in the form of free volumes. The Curie temperature determined on the basis of the analysis of the initial magnetic susceptibility curves is different. This indicates that amorphous materials are thermodynamically unstable materials in which atoms are constantly rearranged in their volume. Atoms try to create configurations with lower and lower internal energy. This means that despite repeated melting of alloys, areas with different concentrations of alloy components are formed during solidification, which explains the small change in the Curie temperature. In crystalline materials, where the structure is the same throughout the volume, the Curie temperature has a constant value. Please remember that the production process is a very important factor. In this case, production methods with the same liquid melt cooling rates were used. However, the method of placing the material in the mold was different, and, most importantly, the melt temperature was different. The liquid material obtained by injection had a lower temperature than that melted by the arc method. From these considerations, it can be concluded that the key factor is the determination of all parameters of the manufacturing process, which is often omitted in scientific studies.

References

[1] B. Jeż, M. Nabiałek, K. Jeż, *Acta Phys. Pol. A* **142**, 14 (2022).

[2] S. Hasani, P. Rezaei-Shahreza, A. Seifoddini, *Metall. Mater. Trans. A* **50**, 63 (2019).

[3] P. Pietrusiewicz, M. Nabiałek, K. Błoch, B. Jeż, S. Walters, A.V. Sandu, M.M.A.B. Abdullah, *Acta Phys. Pol A* **142**, 32 (2022).

[4] E. Kneller, *Ferromagnetismus*, Springer-Verlag, Berlin, 1962.

[5] M. Bourrous, H. Kronmuller, *Phys. Stat. Sol. (a)* **113**, 169 (1989).

[6] H. Kronmüller, *Philos. Mag. B* **48**, 127 (1983).

[7] W.H. Ciurzyńska, *Seria: Fizyka nr 2*, Wydawnictwo WIPMiFS, Częstochowa 2002 (in Polish).

Proceedings of "Applications of Physics in Mechanical and Material Engineering" (APMME 2023)

Influence of a Small Addition of Cu on the Magnetization Process of Rapid Quenched Alloys in Strong Magnetic Fields

B. Jeż[a], P. Postawa[a], A. Kalwik[a], M. Nabiałek[b], J. Gondro[b] and M.M. Nabiałek[b]

[a] *Department of Technology and Automation, Faculty of Mechanical Engineering and Computer Science, Czestochowa University of Technology, al. Armii Krajowej 19c, 42-200 Częstochowa, Poland*
[b] *Department of Physics, Faculty of Production Engineering and Materials Technology, Czestochowa University of Technology, al. Armii Krajowej 19, 42-200 Częstochowa, Poland*

Doi: 10.12693/APhysPolA.144.325 *e-mail: bartlomiej.jez@pcz.pl

The magnetization process is based on bringing about a unified arrangement of the magnetic domains. During this process, there are shifts and then the rotations of the domain walls. At a later stage, domains with a direction of magnetization that do not correlate with the applied magnetic field disappear. The turnover depends on the size of the domains. For an amorphous structure, the key factors determining the size of the magnetic domains are the distance between the magnetic atoms and the possible presence of crystalline grains. The paper presents the results of research on the influence of Cu addition on the distances between magnetic atoms and the magnetization process in high magnetic fields. The structure of the alloys was studied using X-ray diffraction. The mean grain size was estimated using the Scherrer method. The magnetic properties were determined on the basis of measurements with a vibrating magnetometer. A numerical analysis of the primary magnetization curves was performed. Despite the significant reorganization of the structure, no changes in the distance between the magnetic atoms were observed, as indicated by slight changes in the D_{spf} parameter. It was found that a small addition of Cu positively influences the improvement of the magnetic properties, in particular the reduction of the value of the coercive field.

topics: Cu addition, nanocrystallization, Curie temperature, soft magnetic properties

1. Introduction

Rapid quenched alloys with a high Fe content are characterized by good magnetic properties. Depending on the cooling rate and chemical composition, it is possible to produce alloys with an amorphous or nanocrystalline structure in a one-stage process [1]. The type of phases formed during solidification determines the properties of these materials — rapid quenched alloys may have hard magnetic properties (for example, with the $Y_2Fe_{14}B$ phase [2]), semi-hard magnetic properties (with the Fe_5Y phase [3]), or soft magnetic properties (with the α-Fe, Fe_2B, $Fe_{23}B_6$, Fe_3B [4–6]). The properties of these alloys are related, among other things, to the distances between magnetic atoms [7] and the size of crystal grains [8].

Designing an alloy with good soft magnetic properties in a one-step process is quite a difficult task. Additions of some transition metals in amounts below 1% cause very large changes in the alloy's glass-forming ability [9–12]. Appropriate selection of the chemical composition allows obtaining a nanocrystalline alloy with phases improving soft magnetic properties.

The aim of the work is to determine the effect of Cu addition on the structure and magnetic properties of rapidly quenched FeCo-based alloys.

2. Experimental procedure

Polycrystalline alloy ingots were produced in an arc furnace under a protective atmosphere of argon (Ar pressure 0.3 atm). The alloys were melted from high-purity ingredients: B — 99.9%, other ingredients — 99.99%. The melting process was carried out on a copper plate cooled by water. The charge was melted 5 times, and the ingot was turned over each time to homogenize it. The ingots were cleaned mechanically and, after being divided into smaller pieces, in an ultrasonic bath. Samples of

rapid quenched alloys were produced by the injection method. Plate-shaped samples with dimensionss of $10 \times 10 \times 0.5$ mm^3 were obtained. The injection process was carried out in a protective atmosphere of argon (Ar pressure 0.3 atm).

The structure of the alloys was examined using X-ray diffraction (XRD). A Bruker ADVANCE 8 diffractometer was used. Measurements were carried out with a measuring step of 0.02° and an exposure time of 5 s. The measured diffractograms were analyzed using the Match! program. The data obtained from the analysis were used to determine the average grain sizes using the Scherrer method [13]

$$D = \frac{\lambda K}{2\beta_0 \cos(\theta)}, \quad (1)$$

where:

K — Scherrer form factor ($K = 0.91$),

λ — wavelength of characteristic radiation,

β_0 — half width at half peak intensity (background included),

θ — Bragg's angle.

Static magnetic hysteresis loops and primary magnetization curves were measured using a Lake Shore VSM 7307 vibration magnetometer in the range of external magnetic field intensity up to 2 T. Based on the analysis of the primary magnetization curve, the spin wave stiffness parameter D_{spf} was calculated. For this purpose, the direction parameter of the line, b, should be determined, which fits the magnetization course as a function of $(\mu_0 H)^{1/2}$, where H is the external magnetic field. The b parameter is related to the spin wave stiffness parameter by the relationship [7]

$$b = 3.54\, g\mu_0\mu_\mathrm{B} \left(\frac{1}{4\pi D_{spf}}\right)^{3/2} k_\mathrm{B} T\, (g\mu_\mathrm{B})^{1/2}, \quad (2)$$

where:

b — slope of the linear fit corresponding to the thermally-induced suppression of spin-waves by a magnetic field of high intensity,

μ_0 — magnetic permeability of a vacuum,

k_B — Boltzmann's constant,

μ_B — Bohr magneton,

g — gyromagnetic factor,

T — temperature.

3. Results

Figure 1 presents X-ray diffraction images obtained for the tested alloys in the solidified state.

The measured diffractograms differ significantly from each other. The $Fe_{36}Co_{36}Y_8B_{20}$ alloy is characterized by an amorphous structure, as indicated by the presence of a single wide, diffuse maximum (Fig. 1a). The minimal addition of Cu caused partial crystallization of the alloy during its solidification. The presence of crystalline phases α-Fe and

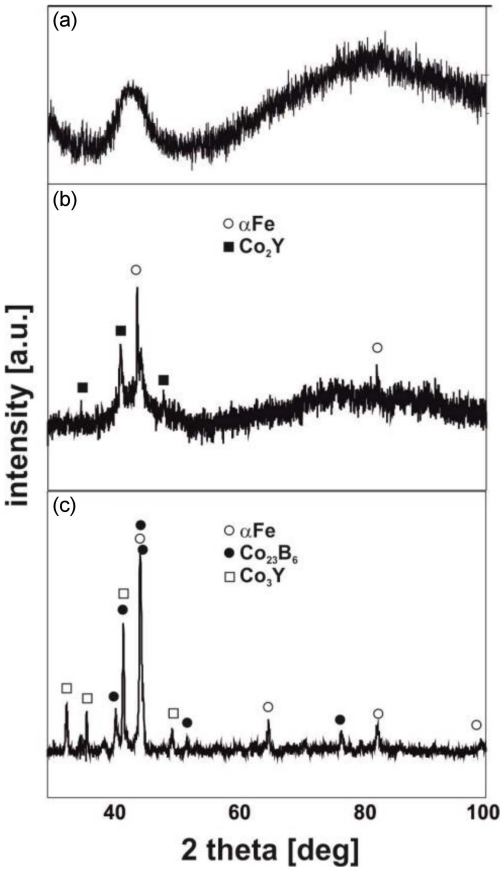

Fig. 1. X-ray diffraction patterns for the rod-form samples of the investigated alloys: (a) $Fe_{36}Co_{36}Y_8B_{20}$, (b) $(Fe_{36}Co_{36}Y_8B_{20})_{99.9}Cu_{0.1}$, (c) $(Fe_{36}Co_{36}Y_8B_{20})_{99}Cu_1$.

TABLE I

Results of analysis for XRD measured for the tested alloys.

Alloy	Medium grain size [nm]			
	Co_2Y	α-Fe	$Co_{23}B_6$	Co_3Y
$(Fe_{36}Co_{36}Y_8B_{20})_{99.9}Cu_{0.1}$	18	32	–	–
$(Fe_{36}Co_{36}Y_8B_{20})_{99}Cu_1$	–	22	20	18

Co_2Y was identified (Fig. 1b). In this case, the maximum indicating the presence of a disordered phase is still very clear. Together with the low intensity of the peaks, this indicates a small share of crystals in the melt volume. An alloy with 1% copper is much more crystallized. Co_3Y, α-Fe, and $Co_{23}B_6$ phases were identified in the sample volume. The maximum associated with the amorphous phase is barely noticeable. Based on the diffractograms, average grain sizes were determined for the tested alloys. The results are given in Table I.

For all identified phases, the grain size does not exceed 35 nm. Taking into account the type of phases present in the alloys, it should be assumed that they should not have a negative impact on the soft magnetic properties of the tested alloys.

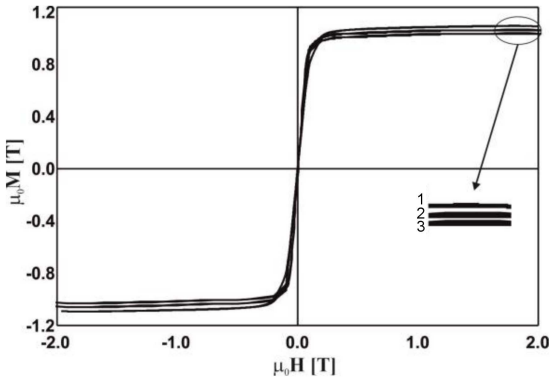

Fig. 2. Static magnetic hysteresis loops for the tested alloy samples: (a) $Fe_{36}Co_{36}Y_8B_{20}$, (b) $(Fe_{36}Co_{36}Y_8B_{20})_{99.9}Cu_{0.1}$, (c) $(Fe_{36}Co_{36}Y_8B_{20})_{99}Cu_1$.

TABLE II

Magnetic properties of investigated alloys.

	M_S [T]	H_C [A/m]	D_{spf} [meV nm^2]	Phases
$Fe_{36}Co_{36}Y_8B_{20}$ [14]	1.09	208	51	amorp.
$(Fe_{36}Co_{36}Y_8B_{20})_{99.9}Cu_{0.1}$	1.03	74	49	α-Fe, Co_2Y
$(Fe_{36}Co_{36}Y_8B_{20})_{99}Cu_1$	1.07	185	51	α-Fe, Co_3Y, $Co_{23}B_6$

Figure 2 shows static magnetic hysteresis loops for the produced alloy samples. The measured loops have a shape typical for soft magnetic materials. On the basis of the loop, the saturation magnetization value (M_S) and the value of the coercive field (H_C) were determined; the data are presented in Table II (see also [14]).

Figure 3 shows the magnetization curves as a function of $(\mu_0 H)^{1/2}$. The primary magnetization curves were subjected to numerical analysis. On its basis, the spin wave stiffness parameter D_{spf} was determined (Table II).

It turns out that the presence of crystalline phases does not affect the distances between magnetic atoms, moreover, the presence of only two crystalline phases (alloy $(Fe_{36}Co_{36}Y_8B_{20})_{99.9}Cu_{0.1}$) significantly reduces the H_C value. The presence of three crystalline phases complicates the magnetic structure and, to some extent, hinders the process of magnetizing the alloy. This may be related to the obstruction of the rotation of the domain walls by one of the crystalline phases present.

4. Conclusions

The work showed that even 0.1% of Cu addition reduces the alloy's glass-forming ability. With a 1% addition, this effect is much more visible.

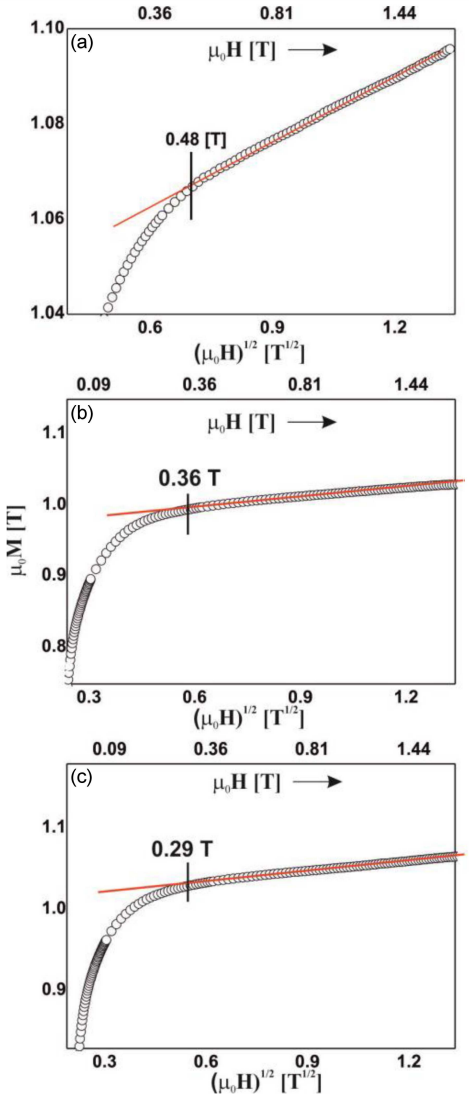

Fig. 3. Magnetization as a function of $(\mu_0 H)^{1/2}$ for the investigated alloys: (a) $Fe_{36}Co_{36}Y_8B_{20}$, (b) $(Fe_{36}Co_{36}Y_8B_{20})_{99.9}Cu_{0.1}$, (c) $(Fe_{36}Co_{36}Y_8B_{20})_{99}Cu_1$.

A small addition of Cu resulted in the formation of two crystalline phases, while a larger addition resulted in three phases. The magnetization process of all tested alloys is similar, but the alloy $(Fe_{36}Co_{36}Y_8B_{20})_{99.9}Cu_{0.1}$ shows the best magnetic properties. Due to the similar average grain size for nanocrystalline alloys, it should be stated that this effect is related to the less complicated magnetic structure of the $(Fe_{36}Co_{36}Y_8B_{20})_{99.9}Cu_{0.1}$ alloy.

References

[1] B. Jeż, K. Błoch, J. Gondro, K. Jeż, M. Talar, B. Płoszaj, P. Pietrusiewicz, S. Walters, A. Kalwik, D.S. Che Halin, P. Sikora, M. Nabiałek, *Acta Phys. Pol. A* **139**, 495 (2021).

[2] P. Vizureanu, M. Nabiałek, A.V. Sandu, B. Jeż, *Materials* **13**, 835 (2020).

[3] S.S. Chandrasekaran, M.R. Ponnaiah, P. Murugan, P. Saravanan, *J. Magn. Magn. Mater.* **418**, 92 (2016).

[4] L. Zhang, Z. Wang, Y. Jia, *Mater. Sci. Eng. B* **231**, 1 (2018).

[5] H.Y. Jung, S. Yi, *Intermetallics* **49**, 18 (2014).

[6] M.E. McHenry, F. Johnson, H. Okumura, T. Ohkubo, V.R.V. Ramanan, D.E. Laughlin, *Scr. Mater.* **48**, 881 (2003).

[7] T. Holstein, H. Primakoff, *Phys. Rev.* **59**, 388 (1941).

[8] Y. Li, X Jia, W. Zhang, Y. Zhang, G. Xie, Z. Qiu, J. Luan, Z. Jiao, *J. Mater. Sci. Technol.* **65**, 171 (2021).

[9] Y. Zhang, Y. Wang, A. Makino, *AIP Adv.* **8**, 047703 (2018).

[10] Z. Jaafari, A. Seifoddini, S. Hasani, *Metall. Mater. Trans. A* **50A**, 2875 (2019).

[11] X. Jia, Y. Li, G. Xie, T. Qi, Zhang, *J. Non-Cryst. Solids* **481**, 590 (2018).

[12] W. Lin, Y.Z. Yang, J. Xu, W. Li, *J. Alloys Compd.* **735**, 1195 (2018).

[13] G.T. Xia, Y.G. Wang, J. Dai, Y.D. Dai, *J. Alloys Compd.* **690**, 281 (2017).

[14] K. Błoch, M. Nabiałek, P. Postawa, A.V. Sandu, A. Śliwa, B. Jeż, *Materials* **13**, 846 (2020).

Proceedings of "Applications of Physics in Mechanical and Material Engineering" (APMME 2023)

Critical Behavior Studies in the Vicinity of the Curie Temperature in the MnCoGe Alloy

K. Kutynia[a,*], A. Przybył[a], M. Gębara[b], M. Rychta[a], I. Wnuk[a] and P. Gębara[a]

[a] *Department of Physics, Częstochowa University of Technology, Armii Krajowej 19, 42-200 Częstochowa, Poland*
[b] *Office of European Projects, Jan Długosz University in Częstochowa, Waszyngtona 4/8, 42-200 Częstochowa, Poland*

Doi: 10.12693/APhysPolA.144.329 *e-mail: karolina.kutynia@pcz.pl

The main goal of the present work was to study the critical behavior in the MnCoGe alloy in the vicinity of the critical temperature T_C. The second-order phase transition from ferro- to paramagnetic state was preliminarily confirmed by the positive slope of the Arrott plots. The critical exponents have been revealed using the Kouvel–Fisher method and yield $\beta = 0.474 \pm 0.005$, $\gamma = 0.917 \pm 0.005$, and $\delta = 2.985 \pm 0.005$. The Curie temperature for the MnCoGe equals 293.3 ± 0.1 K.

topics: magnetocaloric materials, critical behavior, the Curie temperature

1. Introduction

Nowadays, energy saving is the main theme of public discussion. Novel ergonomic techniques are extremely important, especially in cooling devices. The most efficient technique for lowering temperature is magnetic cooling based on the magnetocaloric effect (MCE) [1]. The MCE causes the temperature variations of magnetic material under the change of external magnetic field. For over twenty years, the MCE has been studied in a wide range of materials. A natural magnetocaloric material working at room temperature is pure Gd [2, 3]. Moreover, rare earth–transition metal alloys, i.e., $Gd_5Ge_2Si_2$- or $La(Fe,Si)_{13}$-type [1–4], are also characterized by relatively good magnetocaloric properties. For several years, the MM'X group of alloys (M and M' denote 3*d* transition elements, and X denotes main group elements) have been intensively studied due to their excellent magnetocaloric properties [5–8]. The MM'X family of alloys manifests good physical properties and promising application potential. This type of alloy has two crystalline structures: orthorhombic TiNiSi-type structure and hexagonal Ni_2In-type structure [9].

In the present paper, the critical exponents analysis of the MnCoGe alloy in the vicinity of the Curie temperature was conducted. The thermomagnetic investigation was described in the previous paper [10]. The studies were conducted in order to better understand the behavior of the physical quantities of continuous phase transition in MnCoGe alloy. The analysis of critical behavior was carried out using two techniques, namely the Kouvel–Fisher method and scaling analysis.

2. Experimental techniques

The polycrystalline MnCoGe alloy sample was prepared by arc-melting of the high-purity constituent elements under a protective atmosphere (Ar gas). Samples were re-melted several times in order to ensure their homogeneity. Thermomagnetic curves and magnetic isotherms were measured using a Quantum Design physical property measurement system (PPMS), the vibrating sample magnetometer (VSM) option, in a magnetic field up to 5 T and in a wide temperature range.

3. Results and discussion

The critical phenomena in the vicinity of the Curie temperature were analyzed for the MnCoGe alloy. Measured isothermal magnetization against the applied field allowed the construction of the Arrott plots using critical exponents corresponding to mean field theory ($\beta = 0.5$ and $\gamma = 1$). A positive slope of the M^2 vs B/M isotherms is clearly seen in Fig. 1, and it is related to second-order phase transition, according to the Banerjee criterion [11].

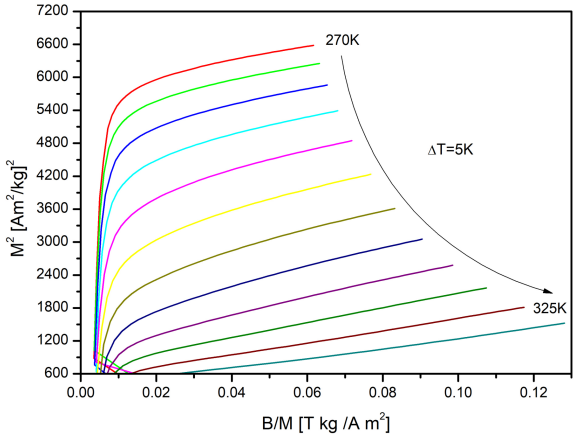

Fig. 1. The Arrott plots constructed for the MnCoGe alloy using mean field values of critical exponents.

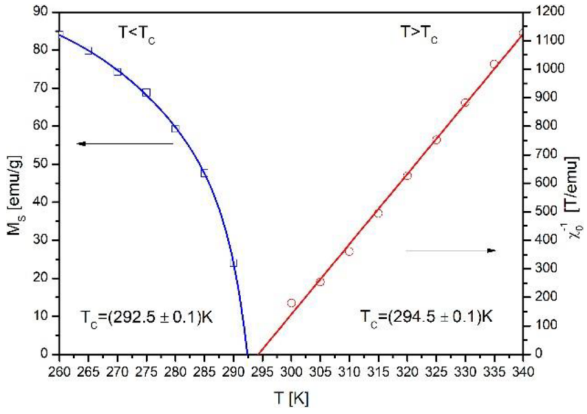

Fig. 2. The temperature dependences of spontaneous magnetization M_S and inverse initial susceptibility χ_0^{-1} of the MnCoGe alloy.

The second-order phase transition is defined by the critical exponents β, γ, and δ related to spontaneous magnetization M_S, initial susceptibility χ_0, and critical magnetization isotherm at the Curie temperature, respectively. The relations between physical magnitudes and critical exponents are described by the following relations [12]

$$M_S(T) = M_0\Big(-\frac{T-T_C}{T_C}\Big)^{\beta}, \qquad T < T_C, \qquad (1)$$

$$\chi_0^{-1}(T) = \frac{H_0}{M_0}\left(\frac{T-T_C}{T_C}\right)^{\gamma}, \qquad T > T_C, \qquad (2)$$

$$M = D\,H^{1/\delta}, \qquad T = T_C, \qquad (3)$$

where M_S is spontaneous magnetization and H_0, M_0, and D are critical amplitudes.

In order to reveal values of M_S and inverse susceptibility $1/\chi_0$, linear extrapolation was done. The temperature evolution of M_S and $1/\chi_0$ was presented in Fig. 2.

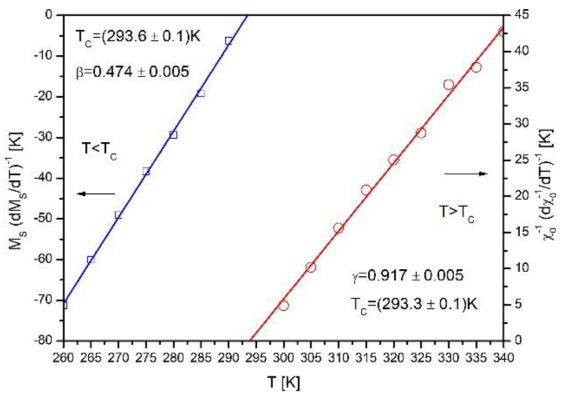

Fig. 3. The Kouvel–Fisher plots for determination β and γ in the MnCoGe alloy.

The M_S and χ_0^{-1} vs T dependences allowed us to reveal more detailed values of the Curie point of 292.5 K and 294.5 K for ferromagnetic ($T < T_C$) and paramagnetic ($T > T_C$) state, respectively.

Kouvel and Fisher in [13] proposed a relatively simple technique for calculating the critical exponents. Taking into account the Kouvel–Fisher approach, the equations (1) and (2) should be rewritten in the following form

$$\frac{M_S(T)}{\left[\mathrm{d}M_S(T)/\mathrm{d}T\right]} = \frac{T-T_C}{\beta}, \qquad (4)$$

$$\frac{\chi_0^{-1}(T)}{\left[\mathrm{d}\chi_0^{-1}(T)/\mathrm{d}T\right]} = \frac{T-T_C}{\gamma}. \qquad (5)$$

Such modification of these relations, according to the Kouvel and Fisher guidelines, allows their linearization with slopes $1/\beta$ and $1/\gamma$. Linear fitting revealed values of critical exponents β and γ. Extrapolation of generated linear dependences to T-axis has shown the Curie points. The Kouvel–Fisher plots are plotted in Fig. 3.

The last critical exponent δ could be determined based on the Widom scaling relation [14]

$$\delta = 1 + \frac{\gamma}{\beta}. \qquad (6)$$

Taking into account values of exponents β and γ delivered by the Kouvel–Fisher method and equation (7), the exponent δ is 2.935.

Another way to determine exponent δ is based on a simple modification of (3). The M vs $\mu_0 H$ isotherm measured in the vicinity of the Curie point on a log–log scale is shown in Fig. 4. The Curie temperature revealed during the current analysis was established as 293.3 K, and it corresponds well with the results described in paper [8]. Due to this fact, the field dependence of magnetization collected at 295 K was chosen as critical isothermal magnetization and used to determine exponent δ. The linear fitting with a slope of $1/\delta$ has revealed that the δ value is 2.985 ± 0.005. Such value corresponds well with δ determined by the Widom scaling relation.

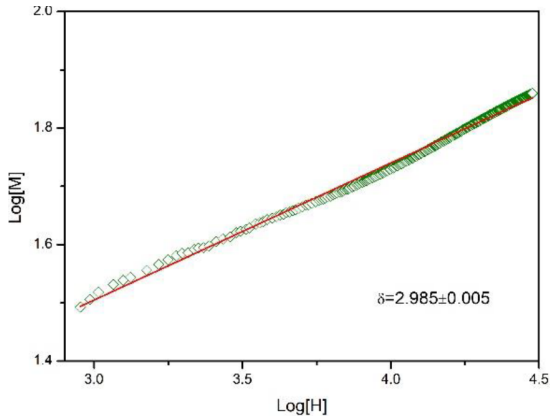

Fig. 4. The M vs $\mu_0 H$ isotherm on a log–log scale at 295 K. The red line is the linear fitting according to (3).

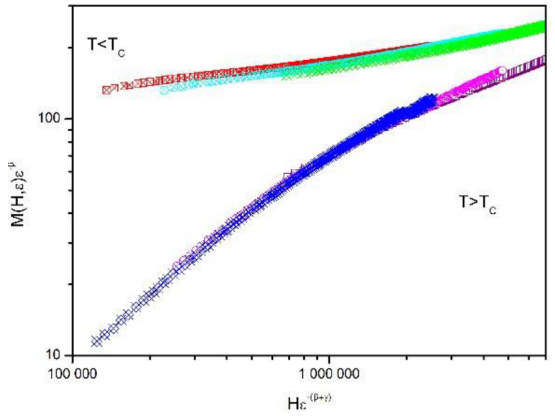

Fig. 5. Scaling plots (on a log–log scale) constructed for the MnCoGe alloy.

The validation of calculated critical exponents is possible taking into account magnetic state relation [15]

$$M(H,\varepsilon) = \varepsilon^{\beta} f_{\pm}\left(\frac{H}{\varepsilon^{\beta+\gamma}}\right), \tag{7}$$

where $\varepsilon = (T - T_{\mathrm{C}})/T_{\mathrm{C}}$, $f_{\pm}$ mean regular functions with f_{+} and f_{-} for $T > T_{\mathrm{C}}$ and $T < T_{\mathrm{C}}$, respectively. Relation (7) shows dependence between $M(H,\varepsilon)\varepsilon^{-\beta}$ and $H\varepsilon^{-(\beta+\gamma)}$. Such construction with correct critical exponents should produce two universally different curves: (i) first for temperatures higher than T_{C} and (ii) second one for temperatures lower than T_{C}. All curves in a specific temperature range (below or higher than T_{C}) should collapse in these two independent scaling curves. In the present case, the independent scaling curves (on a log–log scale) for exponents β and γ calculated by the Kouvel–Fisher method are shown in Fig. 5.

The data presented in Fig. 5 collapse on two independent curves related to ferromagnetic and paramagnetic states. It is clear evidence that revealed values of critical exponents are reasonable and reliable.

Calculated critical exponents are comparable to those delivered by Debnath and coworkers in [16]. They analyzed the critical phenomena for the $Mn_{0.94}Nb_{0.06}CoGe$ alloy and revealed the following values of critical exponents $\beta = 0.576$, $\gamma = 1.002$, and $\delta = 2.716$. Moreover, Rahman et al. in [9] investigated the critical behavior in the $MnCoGe_{0.97}Al_{0.03}$ and delivered similar results, i.e., $\beta = 0.44$, $\gamma = 0.83$, and $\delta = 2.89$.

The calculated values correspond quite well with the mean-field model.

4. Conclusions

In the present paper, the critical phenomena in the MnCoGe alloy were investigated at Curie point using the Kouvel–Fisher technique. Calculated values of critical exponents were reliable and reasonable, which was confirmed by appropriate tests. The values of the critical exponents of $\beta = 0.474$, $\gamma = 0.917$, $\delta = 2.985$, and the Curie temperature 293.3 K have been achieved.

Acknowledgments

This work was supported by statutory fundings of the Department of Physics, Częstochowa University of Technology.

References

[1] V.K. Pecharsky, K.A. Gschneidner, *Appl. Phys. Lett.* **70**, 3299 (1997).

[2] V. Franco, A. Conde, V. Provenzano, R.D. Shull, *J. Magn. Magn. Mater.* **322**, 218 (2010).

[3] A. Diaz-Garcia, J.Y. Law, P. Gębara, V. Franco, *JOM* **72**, 2845 (2020).

[4] P. Gębara, M. Cesnek, J. Bednarcik, *Curr. Appl. Phys.* **19**, 188 (2019).

[5] U. Devarajan, D. Nair, *Mater. Res. Express* **6**, 106117 (2019).

[6] L.F. Bao, F.X. Hu, R.R. Wu, J. Wang, L. Chen, J.R. Sun., B.G. Shen, L. Li, B. Zhang, X.X. Zhang, *J. Phys. D Appl. Phys.* **47**, 055003 (2014).

[7] K. Kutynia, P. Gębara, *Materials* **14**, 3129 (2021).

[8] K. Kutynia, A. Przybył, P. Gębara, *Materials* **16**, 5394 (2023).

[9] A.R.A. Rahman, M.F. Md Din, J. Wang, N.S. Suhaimi, N.H. Idris, S.X. Dou, M. Ismail, M.Z. Hassan, M.T. Jusoh, *Crystals* **11**, 694 (2021).

[10] P. Gębara, Z. Śniadecki, *J. Alloy Compd.* **796**, 153 (2019).

[11] S.K. Banerjee, *Phys. Lett.* **12**, 16 (1964).

[12] M.E. Fisher, *Rep. Prog. Phys.* **30**, 615 (1967).

[13] J.S. Kouvel, M.E. Fisher, *Phys. Rev.* **136**, A1626 (1964).

[14] B. Widom, *J. Chem. Phys.* **43**, 3898 (1965).

[15] Z.R. Zhao, G.F. Wang, X.F. Zhang, *Adv. Mater. Res.* **873**, 855 (2014).

[16] J.C. Debnath, P. Shamba, A.M. Strydom, J.L. Wang, S.X. Dou, *J. Appl. Phys.* **113**, 093902 (2013).

Proceedings of "Applications of Physics in Mechanical and Material Engineering" (APMME 2023)

Magnetic Interactions and Coercivity Mechanism in Nanocrystalline Nd–Fe–B Ribbons with Nb Addition

A. Przybył[a,*], I. Wnuk[a], J. Wysłocki[a], K. Kutynia[a], M. Kaźmierczak[b], M. Rychta[a] and P. Gębara[a]

[a] *Department of Physics, Czestochowa University of Technology, Armii Krajowej 19, 42-200 Częstochowa, Poland*
[b] *Complex of Schlools in Goleniowy, Kościuszki 20, 42-445 Szczekociny, Poland*

Doi: 10.12693/APhysPolA.144.333 *e-mail: anna.przybyl@pcz.pl

In the present paper, the phase structure, magnetic properties, and magnetization reversal processes in the $(Nd_{10}Fe_{67}B_{23})_{93}Nb_7$ alloy ribbon were investigated. The X-ray diffraction analysis revealed a coexistence of the following phases: hard magnetic $Nd_2Fe_{14}B$, metastable soft magnetic $Nd_2Fe_{23}B_3$, and paramagnetic $Nd_{1+\varepsilon}Fe_4B_4$. Moreover, the changes in phase composition were noticed after heat treatment. In order to check magnetic measurements, the hysteresis loops were collected. The magnetization reversal curves were studied by constructing the reversible part of magnetization dependence on the irreversible part of magnetization.

topics: X-ray diffraction (XRD), magnetic properties, magnetization reversal processes

1. Introduction

Although the Nd–Fe–B permanent magnets have been well-known for over forty years, they are still intensively studied. Moreover, magnets of this type, due to their excellent properties and relatively low price, are widely used in the latest technologies [1–4]. The good magnetic properties of the Nd–Fe–B alloys, such as coercivity ${}_JH_C$, remanence B_r, or maximum energy product $(BH)_{max}$, are related to the appropriate structure and phase composition of these alloys. For some time, they have been produced using rapid quenching methods such as suction casting, melt-spinning, or injection casting. Selective modification of chemical composition and specific annealing conditions are required to achieve the best magnetic properties [5]. For many years, the chemical compositions of the Nd–Fe–B-type alloys have been selectively modified in order to change their phase structure and magnetic properties. Among others, the Nb alloying has been intensively studied due to its influence on glass forming ability or reduction of growth of nanocrystalline grains formed during heat treatment [6–9] and, in consequence, modification of magnetic properties. The time and temperature of heat treatment are also extremely important, taking into account the formation of the microstructure and specific phase constitution. These two parameters have significant influence on the coercivity of produced magnets. The mechanisms of coercivity could be better understood by investigation of magnetization reversal processes.

According to that, the structure, magnetic properties, magnetic interactions, and coercivity mechanisms of the $(Nd_{10}Fe_{67}B_{23})_{93}Nb_7$ alloy ribbons.

2. Material and experimental techniques

The ingot sample with nominal composition $(Nd_{10}Fe_{67}B_{23})_{93}Nb_7$ was produced by arc-melting of the high purity (min. 4 N) elements under low pressure of inert gas (Ar). Boron was added in the form of Fe–B alloy with a well-known composition. Ribbons were produced by the melt-spinning technique under low pressure of a protective atmosphere (Ar). Produced ribbons were sealed off in quart tubes under a low pressure of Ar gas and annealed in a wide range of temperatures for 5 min. The X-ray diffraction (XRD) studies were performed using Bruker D8 ADVANCE diffractometer with Cu K_α radiation and LYNXEYE semiconductor detector. Magnetic properties were measured using the Lake Shore 7307 vibrating sample magnetometer working in an external magnetic field up to ~ 2 T.

3. Results and discussion

Fig. 1 shows the X-ray diffraction pattern of the $(Nd_{10}Fe_{67}B_{23})_{93}Nb_7$ alloy ribbon in an as-cast state and after heat treatment at 1003 K for 5 min. The analysis revealed that the sample in an as-cast state is partially amorphous. However, a coexistence of the expected ferromagnetic $Nd_2Fe_{14}B$ phase, paramagnetic $Nd_{1+\varepsilon}Fe_4B_4$ phase, and metastable $Nd_2Fe_{23}B_3$ phase was detected. A significant increase in the content of the $Nd_2Fe_{14}B$ phase at the expense of the amorphous phase was observed after annealing at 1003 K for a relatively short time.

Magnetic hysteresis loops of the $(Nd_{10}Fe_{67}B_{23})_{93}Nb_7$ alloy were collected in Fig. 2. Hysteresis loops of the studied sample in an as-cast state and annealed at 923 K are typical for soft magnetic materials (Fig. 2a). However, a heat treatment at 943 K induces some changes in the shape of hysteresis loops. The shape of the hysteresis loop (at 943 K) is called a wasp-waisted loop [10] and is typical for samples with a small content of ferromagnetic phases in phase constitution and multiphase samples. The minority

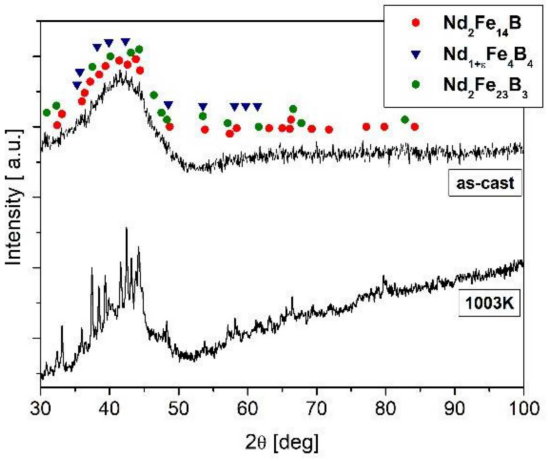

Fig. 1. XRD patterns of the $(Nd_{10}Fe_{67}B_{23})_{93}Nb_7$ alloy ribbon in as-cast state and after heat treatment at 1003 K for 5 min.

TABLE I

Magnetic parameters of the $(Nd_{10}Fe_{67}B_{23})_{93}Nb_7$ alloy ribbon annealed at 963–1063 K with step 20 K for 5 min.

Annealing temperature [K]	J_r [T]	$_JH_C$ [kA/m]	$(BH)_{max}$ [kJ/m^3]
963	0.42	1083	30.7
983	0.44	835	27.1
1003	0.36	924	34.0
1023	0.45	852	30.4
1043	0.51	856	38.6
1063	0.50	702	30.6

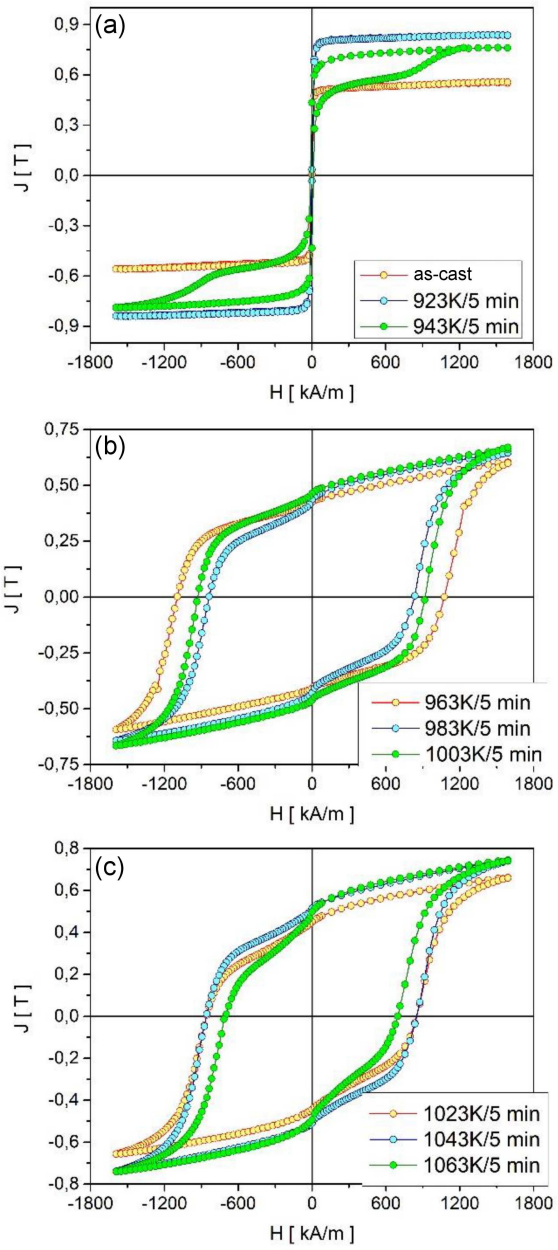

Fig. 2. Magnetic hysteresis loops of the $(Nd_{10}Fe_{67}B_{23})_{93}Nb_7$ alloy ribbon in as-cast state and after heat treatment in the temperature range from 923 to 1063 K for 5 min.

content of the hard magnetic $Nd_2Fe_{14}B$ phase with the majority content of soft magnetic $Nd_2Fe_{23}B_3$ phase and paramagnetic $Nd_{1+\varepsilon}Fe_4B_4$ phase causes a contraction of the hysteresis loop in the vicinity of coercivity. An increase in temperature of heat treatment caused the broadening of hysteresis loops, which resulted in an increase in hard magnetic phase content. Moreover, the shapes of hysteresis loops in the range 963–1063 K are typical for multiphase samples, which was confirmed by the XRD studies. Basic magnetic properties determined from hysteresis loops are summarized in Table I.

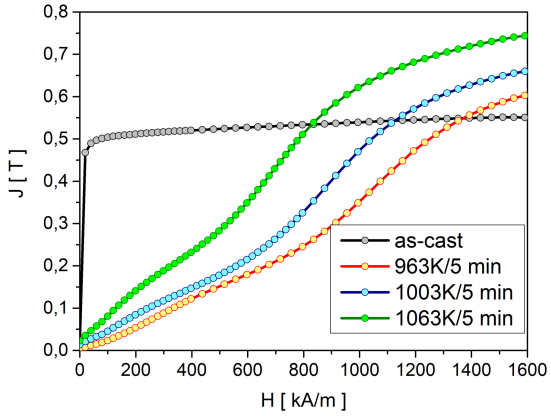

Fig. 3. Magnetization virgin curves of the studied alloy ribbon in the as-cast state and after heat treatment at selected temperatures.

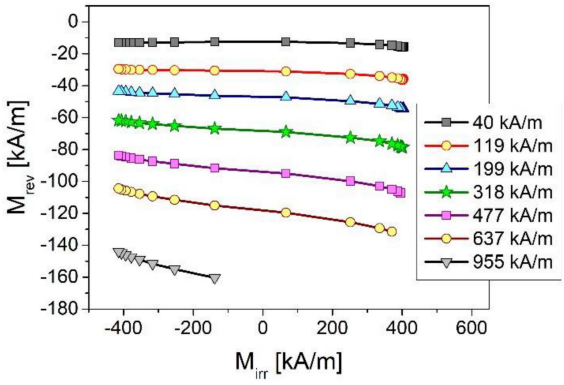

Fig. 4. The M_{rev} vs M_{irr} curves constructed for studied $(Nd_{10}Fe_{67}B_{23})_{93}Nb_7$ alloy ribbon annelaed at 1003 K for 5 min.

Maximum coercivity was revealed for the sample annealed at 963 K. However, the highest remanence and maximum density of magnetic energy were detected for ribbon heated at 1043 K. Magnetization virgin curves for the sample in an as-cast state and for selected annealing temperatures were plotted in Fig. 3. Measurements of the virgin curves were carried out for thermally demagnetized samples. The shape of virgin curve for the sample in an as-cast state is typical for soft magnetic materials. Short time (5 min) annealing at 963 K and higher temperatures induces noticeable changes in the shape of magnetization virgin curves, and a characteristic inflection point was observed. Such behavior is typical for materials in which the magnetization reversal process is based on the pinning of domain walls. Based on them, a further analysis of the magnetization reversal curves was carried out [11–13]. These data were used for the calculation of the dependence of the irreversible part of magnetization on the reversible part of magnetization [14] under the change of several values of an external magnetic field. These curves were collected in Fig. 4.

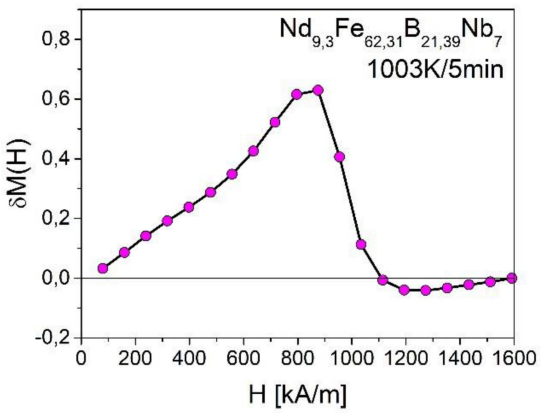

Fig. 5. Henkel plot constructed for studied alloy annealed at 1003 K for 5 min.

A trend of the M_{rev} vs M_{irr} curves is related to the distribution of nucleation fields H_{N} and pinning field H_{P} and the degree of overlapping between these fields [15]. Observed curves were not characterized by any visible minimum. The analysis of the curves indicated that the nucleation process started at stronger magnetic fields, while the pinning field was weaker than the nucleation field. The reversible part of magnetization decreased monotonically, while an increase in the irreversible part of magnetization was observed.

The magnetic interactions between grains in the investigated alloy were studied by the construction of $\delta M(H)$ dependence, called the Henkel plot (see Fig. 5).

The XRD studies confirmed the coexistence of the $Nd_2Fe_{14}B$ and $Nd_2Fe_{23}B_3$ phases. An occurrence of these two phases induces interactions between them. A sharp increase in the range of field 0–800 kA/m in the $\delta M(H)$ curve suggests the strengthening of exchange interactions between grains of these two phases. Positive values of the Henkel plot are caused by strong exchange interactions between soft and hard magnetic phases, while the negative ones are related to weak dipole interactions lowering the magnetization. The observed maximum of the Henkel plot is related to the energy of the interactions.

4. Conclusions

In the present studies, the magnetic properties, magnetization reversal processes, and magnetic interactions were investigated. The XRD measurements revealed the coexistence of the hard ($Nd_2Fe_{14}B$) and soft ($Nd_2Fe_{23}B_3$) magnetic phases. The ribbon in an as-cast state was soft magnetic, however, annealing induced changes in the phase constitution, which caused an improvement in magnetic properties. The analysis of magnetic reversal processes revealed the pinning mechanism as a dominant in produced material.

Acknowledgments

The Authors would like to thank Professor Jan Świerczek, Head of Department of Physics, Częstochowa University of Technology, for financial support.

References

[1] A. Manaf, R.A. Buckley, H.A. Davies, M. Leonowicz, *J. Magn. Magn. Mater.* **101**, 360 (1993).

[2] A. Przybył, *Acta Phys. Pol. A* **135**, 288 (2019).

[3] R. Tamura, S. Kobayashi, T. Fukuzaki, M. Isobe, Y. Ueda, *J. Phys. Conf. Ser.* **144**, 012068 (2009).

[4] M. Szwaja, P. Pawlik, J.J. Wysłocki, P. Gębara, *Archiv. Mettal. Mater.* **57**, 233 (2012).

[5] A. Przybył, K. Pawlik, P. Pawlik, P. Gębara, J.J. Wysłocki, *J. Alloys Compd.* **536S**, 333 (2012).

[6] H.R. Kirchmayr, *J. Phys. D Appl. Phys.* **29**, 2763 (1996).

[7] J. Zhang, K.Y. Lim, Y.P. Feng, Y. Li, *Scr. Mater.* **56**, 943 (2007).

[8] I. Wnuk, A. Przybył, M. Kaźmierczak, *Acta Phys. Pol. A* **138**, 166 (2020).

[9] A. Przybył, *Acta Phys. Pol. A* **138**, 144 (2020).

[10] I. Wnuk, A. Przybył, K. Kutynia, J.J. Wysłocki, *Acta Phys. Pol. A* **135**, 292 (2019).

[11] D.C. Crew, L.H. Lewis, D.O. Welch, *J. Appl. Phys.* **87**, 4744 (2000).

[12] D.C. Crew, K.H. Lewis, *J. Appl. Phys.* **87**, 4783 (2000).

[13] H. Zhang, Ch. Rong, X. Du, J. Zhang, S. Zhang, B. Shen, *Appl. Phys. Lett.* **82**, 4098 (2003).

[14] M. Szwaja, K. Pawlik, P. Pawlik, P. Gębara, B. Michalski, *Acta Phys. Pol. A* **127**, 623 (2015).

[15] P.E. Kelly, K. O'Grady, P.I. Mayo, R.W. Chantrell, *IEEE Trans. Magn.* **25**, 3881 (1989).

Proceedings of "Applications of Physics in Mechanical and Material Engineering" (APMME 2023)

Strong-Coupling Character of Superconducting Phase in Heavily-Doped cg-C_4H_4

M.W. Jarosik*

Division of Physics, Częstochowa University of Technology, al. Armii Krajowej 19, 42-200 Częstochowa, Poland

Doi: 10.12693/APhysPolA.144.337 *e-mail: marcin.jarosik@pcz.pl

Hydrocarbon compounds have recently been considered as highly promising materials for phonon-mediated superconductors, exhibiting high values of critical temperature (T_C) in ambient pressure. In this study, we present a quantitative characterization of the superconducting properties of heavily-doped cg-C_4H_4. By using the Migdal–Eliashberg formalism, we demonstrate that the critical temperature in this material is relatively high ($T_C = 96.54$ K) assuming that the Coulomb pseudopotential takes a value of 0.1. Furthermore, the used theoretical model allows for the characterization of other essential thermodynamic properties, such as the superconducting band gap, free energy, specific heat, and critical magnetic field. We observe that the characteristic thermodynamic ratios for the above-mentioned parameters differ from the predictions of the Bardeen–Cooper–Schrieffer theory. Our analysis suggests that strong-coupling and retardation effects play a crucial role in the discussed superconducting state, which cannot be described within the weak-coupling regime.

topics: Eliashberg formalism, cg-C_4H_4 superconductor, thermodynamic properties

1. Introduction

In recent years, the pursuit of novel materials with enhanced superconducting properties has captivated the attention of the scientific community, driven by the promise of potential technological advancements and the fundamental understanding of condensed matter physics. Among the various classes of materials explored for their superconducting potential, high-pressure hydrides have shown the remarkable capability to exhibit superconductivity at T_C values well above room temperature [1]. However, they requite the application of extreme pressures, often reaching several megabars, to achieve such states [2, 3]. This requirement, although scientifically fascinating, poses significant engineering and practical challenges for technical applications. In contrast, the emergence of heavily-doped cg-C_4H_4 as a superconductor presents an exciting departure from this paradigm [4]. This material demonstrates the capacity to achieve relatively high critical temperatures under ambient pressure conditions. In this study, we delve into the superconducting properties of heavily-doped cg-C_4H_4, shedding light on its potential as a viable, ambient-pressure superconductor. Additionally, we explore the pivotal role of strong-coupling effects in shaping the superconducting behavior of this remarkable material. The numerical analysis was based on the Eliashberg equations on the imaginary axis [5–7].

It is worth emphasizing that the Eliashberg formalism represents a significant extension of the fundamental concept originally proposed by Bardeen, Cooper, and Schrieffer (BCS) [8]. This approach goes beyond the BCS theory by explicitly accounting for the electron–phonon interaction. Within the framework of the Eliashberg formalism, the magnitude of the strong coupling corrections to the BCS predictions is intricately tied to the value of a key parameter $k_B T_C/\omega_{\ln}$. The symbol $\omega_{\ln}$ is called the logarithmic phonon frequency

$$\omega_{\ln} \equiv \exp\left[\frac{2}{\lambda}\int_0^{\Omega_{\max}} \mathrm{d}\Omega\ \frac{\alpha^2F(\Omega)}{\Omega}\ln(\Omega)\right], \quad (1)$$

and in this case, it is equal to 58.58 meV. For the cg-C_4H_4 superconductor, an accurate determination of its Eliashberg function ($\alpha^2F(\Omega)$) was achieved through the utilization of *ab initio* density functional perturbation theory [9], as detailed in paper [4]. This comprehensive analysis revealed crucial parameters, specifically, the maximum phonon frequency ($\Omega_{\max}$) and the electron–phonon coupling constant (λ), to be 374.33 meV and 1.41, respectively. In the case of the BCS limit, the Eliashberg function is non-zero only for very high frequency, so that $k_B T_C/\omega_{\ln} \to 0$. In cg-$C_4H_4$, the value of the ratio $k_B T_C/\omega_{\ln}$ is equal to 0.14. This divergence from the BCS limit necessitates alternative approaches for the precise calculation of its thermodynamic parameters.

2. The model

Directly solving the Eliashberg equations poses a significant challenge due to the necessity of performing highly complex numerical integral calculations, in addition to requiring substantial computational resources. This process can be significantly streamlined by first solving the Eliashberg equations defined along the imaginary axis and subsequently conducting an analytical continuation to the real axis.

The Eliashberg equations, specifically formulated for a half-filled electron band and represented on the imaginary axis, can be succinctly expressed as follows [5]

$$\Delta_n Z_n = \frac{\pi}{\beta} \sum_{m=-M}^{M} \frac{K(n,m) - \mu^* \theta(\omega_c - |\omega_m|)}{\sqrt{\omega_m^2 + \Delta_m^2}} \Delta_m \tag{2}$$

and

$$Z_n = 1 + \frac{\pi}{\beta\omega_n} \sum_{m=-M}^{M} \frac{K(n,m)}{\sqrt{\omega_m^2 + \Delta_m^2}} \omega_m, \tag{3}$$

where the symbol $\Delta_n \equiv \Delta(\mathrm{i}\omega_n)$ denotes the order parameter and $Z_n \equiv Z(\mathrm{i}\omega_n)$ is the wave function renormalization factor; n-th Matsubara frequency is expressed by $\omega_n \equiv \frac{\pi}{\beta}(2n-1)$, where $\beta \equiv 1/(k_B T)$. The depairing electron effects are parameterized by the Coulomb pseudopotential (μ^*). The symbol θ denotes the Heaviside unit function, ω_c is the cut-off energy, and $\omega_c = 5\Omega_{\max}$. The electron–phonon pairing kernel $K(n,m)$ can be defined as follows

$$K(n,m) \equiv 2 \int_0^{\Omega_{\max}} \frac{\mathrm{d}\Omega\ \Omega}{(\omega_n - \omega_m)^2 + \Omega^2} \alpha^2 F(\Omega). \tag{4}$$

3. The numerical results

The Eliashberg equations have been solved for 2201 Matsubara frequencies ($M = 1100$) by using the method presented in [10, 11] and recently tested in [12]. In the considered case, the obtained Eliashberg solutions are stable for $T \geq 20$ K.

In the calculations, a typical Coulomb pseudopotential value for systems of this kind, set at $\mu^* = 0.1$, was employed. Taking into account the following condition $[\Delta_{m=1}(\mu^*)]_{T=T_C} = 0$, it was demonstrated that the critical temperature value for the heavily-doped cg-C_4H_4 is 96.54 K.

Figure 1a presents the form of the order parameter on the imaginary axis for the selected values of temperature. It can be seen that the maximum value of the function Δ_m is taken for $m = 1$. Furthermore, successive Matsubara frequencies tend to approach a constant value more rapidly as temperature increases. Therefore, the conclusion can be drawn that for temperatures close to absolute zero, it is advisable to consider as many Matsubara frequencies as possible, as they make a significant contribution to the solutions of the equations.

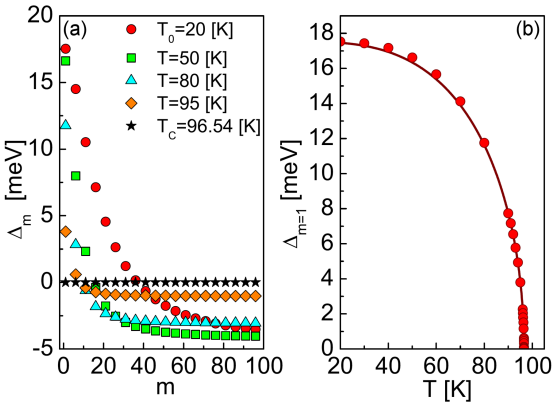

Fig. 1. (a) The order parameter on the imaginary axis for the selected values of temperature. The first 100 values of the function Δ_m are plotted. (b) The influence of temperature on the maximum value of the order parameter. The symbols represent the numerical results. The line was obtained by using (5).

In contrast, in the vicinity of the critical temperature, the contribution from successive Matsubara frequencies becomes negligibly small.

The temperature dependence of the order parameter is convenient to be traced by plotting the curve $\Delta_{m=1}(T)$ (Fig. 1b).

In the case of cg-C_4H_4, the obtained numerical data can be reproduced by the formula

$$\Delta_{m=1}(T) = \Delta_{m=1}(T_0) \sqrt{1 - \left(\frac{T}{T_C}\right)^{\kappa}}, \tag{5}$$

where $\Delta_{m=1}(T_0) \approx \Delta_{m=1}(T = 20K) = 38.85$ meV, and $\kappa = 3.09$.

It should be emphasized that the determination of the values of the function $\Delta_{m=1}(T)$ cannot be adequately established within the confines of the BCS theory, given that $[\kappa]_{\mathrm{BCS}} = 3$ [13].

The solutions of Eliashberg equations for the wave function renormalization factor on the imaginary axis are visually depicted in Fig. 2a. Similar to the behavior observed for the order parameter, the function Z_m attains its maximum value when $m = 1$.

Conversely, the influence of temperature on $Z_{m=1}$ remains relatively minor, as illustrated in Fig. 2b. However, across the entire temperature range under scrutiny, the wave function renormalization factor consistently maintains elevated values. It is worth mentioning that within the framework of the BCS theory, there is $[Z_m]_{BCS} = 1$.

The notable elevations in the function $Z_{m=1}(T)$ can be attributed to the significant influence of strong-coupling effects inherent to the cg-C_4H_4 system. Notice that from a physical perspective, the first Matsubara frequency of the wave function renormalization factor delineates the ratio of the effective electron mass (m_e^*) to the electron band mass (m_e), namely $Z_{m=1} = \frac{m_e^*}{m_e}$.

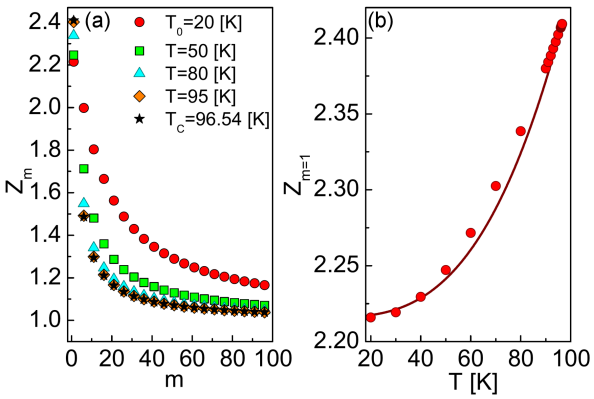

Fig. 2. (a) The wave function renormalization factor on the imaginary axis for the selected values of temperature. The first 100 values of the function Z_m are plotted. (b) The influence of temperature on the maximum value of the renormalization factor. The symbols represent the numerical results. The line was obtained by using (6).

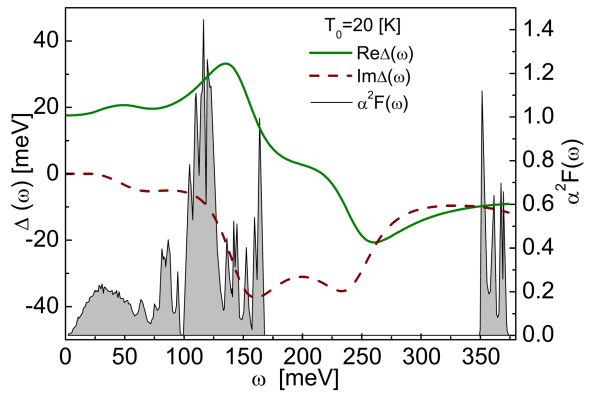

Fig. 3. Real and imaginary part of the order parameter on the real axis for $T = 20$ K. The Eliashberg function [4] is present in the background — the correlation between the course of the order parameter and the spectral function is clearly visible.

Remarkably, it is possible to reproduce the numerical results obtained for the wave function renormalization factor employing the following formula

$$Z_{m=1}(T) = Z_{m=1}(T_0) + \Big[Z_{m=1}(T_C) - Z_{m=1}(T_0)\Big]\left(\frac{T}{T_C}\right)^{\kappa}, \tag{6}$$

where $Z_{m=1}(T_0) = 2.21$, and $Z_{m=1}(T_C) = 1+\lambda$.

The determination of the physical value of the order parameter necessitates an analytical continuation of the solutions of the Eliashberg equations onto the real axis, represented as $(\Delta_m \to \Delta(\omega))$. To accomplish this, the following formula can be employed

$$\Delta(\omega) = \frac{p_1 + p_2\omega + \cdots + p_r\omega^{r-1}}{q_1 + q_2\omega + \cdots + q_r\omega^{r-1} + \omega^r}. \tag{7}$$

The values of the parameters p_j and q_j have been determined according to the method presented in publication [14]. Additionally, it has been assumed that $r = 50$.

The results for the order parameter have been visually represented in Fig. 3. It is evident that the real part of the function $\Delta(\omega)$ assumes non-zero values exclusively within the realm of low frequencies. From a physical perspective, this signifies the absence of significant damping effects. Conversely, as frequency values increase, both the real part, $\mathrm{Re}[\Delta(\omega)]$, and $\mathrm{Im}[\Delta(\omega)]$ exhibit intricate behaviors. The distinct peaks and troughs observed in these functions align with frequency ranges characterized by notably high electron–phonon coupling.

Subsequently, the next phase involves the determination of the physical value of the order parameter, which can be computed using the following equation

$$\Delta(T) = \mathrm{Re}\Big[\Delta(\omega{=}\Delta(T), T)\Big]. \tag{8}$$

For $T_0 = 20$ K, the following result has been obtained: $\Delta(0) = 18.08$ meV, while $\Delta(0) \equiv \Delta(T_0)$.

The free energy difference between the superconducting and normal state (ΔF) for the cg-C_4H_4 superconductor as a strong electron–phonon coupling system should be determined by using the expression [15]

$$\frac{\Delta F}{\rho(0)} = -\frac{2\pi}{\beta}\sum_{n=1}^{M}\left(\sqrt{\omega_n^2+\Delta_n^2} - |\omega_n|\right) \times\left(Z_n^S - Z_n^N\frac{|\omega_n|}{\sqrt{\omega_n^2+\Delta_n^2}}\right), \tag{9}$$

where Z_n^S and Z_n^N represent the wave function renormalization factors for the superconducting (S) and normal (N) states, respectively, while $\rho(0)$ signifies the electron density of states at the Fermi level. In Fig. 4 (lower part), the dependence of ΔF on temperature has been plotted. In the context of physical interpretation, the presence of negative values for ΔF provides compelling evidence that the superconducting state remains stable below the critical temperature.

The values of the thermodynamic critical field were calculated in the next step (CGS units)

$$\frac{H_C}{\sqrt{\rho(0)}} = \sqrt{-8\pi\frac{\Delta F}{\rho(0)}}. \tag{10}$$

The temperature dependence of $H_C/\sqrt{\rho(0)}$ has been shown in Fig. 4 (upper part). As readily observed, the thermodynamic critical field attains its maximum value at T_0 and diminishes as temperature increases, ultimately approaching zero at T_C.

The specific heat difference between superconducting and normal state ($\Delta C = C^S - C^N$) is given by

$$\frac{\Delta C(T)}{k_B\,\rho(0)} = -\frac{1}{\beta}\frac{\mathrm{d}^2[\Delta F/\rho(0)]}{\mathrm{d}(k_B T)^2}. \tag{11}$$

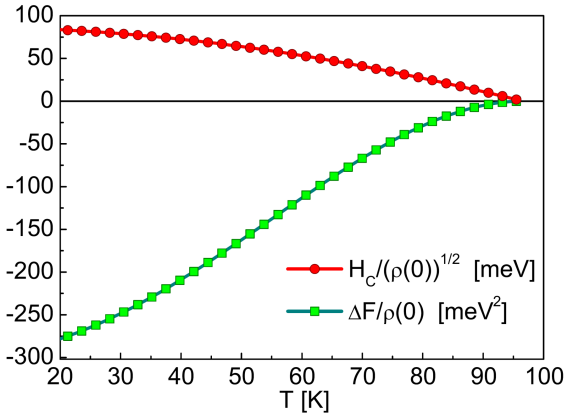

Fig. 4. (Lower part) The free energy difference between the superconducting state and the normal state as a function of temperature. (Upper part) The thermodynamic critical field as a function of temperature.

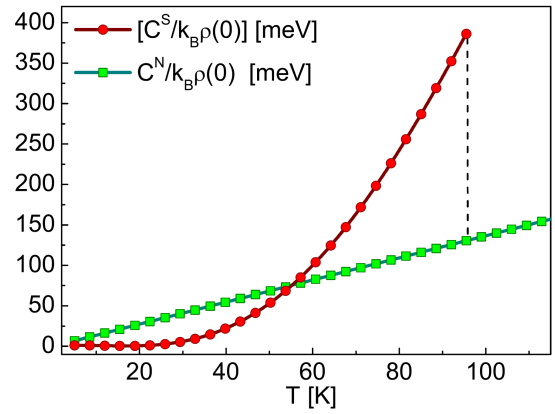

Fig. 5. The dependence of the specific heat in the superconducting state and the normal state on temperature.

The specific heat of the normal state is most conveniently estimated by the formula

$$\frac{C^N(T)}{k_{\mathrm{B}}\,\rho(0)} = \frac{\gamma}{\beta}, \tag{12}$$

where the Sommerfeld constant is given by $\gamma \equiv \frac{2}{3}\pi^2(1+\lambda)$. The relationship between temperature and specific heat for both the superconducting and normal states is illustrated in Fig. 5. A distinct discontinuity associated with the phase transition between superconducting and normal states is observed just at the critical temperature, which is marked with a vertical dashed line.

The thermodynamic functions outlined in this study enable the calculation of the values for the characteristic dimensionless ratios

$$R_\Delta \equiv \frac{2\Delta(0)}{k_{\mathrm{B}}T_C} = 4.35, \tag{13}$$

$$R_C \equiv \frac{\Delta C(T_C)}{C^N(T_C)} = 2.01, \tag{14}$$

$$R_H \equiv \frac{T_C C^N(T_C)}{H_C^2(0)} = 0.146. \tag{15}$$

It should be noted that the parameter $(R_\Delta - R_H)$ in the framework of the BCS theory take the universal values equal to 3.53, 1.43, and 0.168, respectively [8, 15].

4. Conclusions

In this study, an in-depth exploration of the superconducting phase in heavily-doped cg-C_4H_4 has been conducted. The findings presented in this article underscore the remarkable characteristics of this material and its potential significance in the realm of superconductivity.

One of the standout discoveries is the high critical temperature (T_C) of 96.54 K that heavily-doped cg-C_4H_4 exhibits even under ambient pressure conditions. This observation is particularly promising as it positions this hydrocarbon compound as a strong contender among superconductors with practical applications.

In the case of heavily-doped cg-C_4H_4, very interesting is its departure from the predictions of the traditional Bardeen–Cooper–Schrieffer (BCS) theory. Notably, the dimensionless parameters R_Δ, R_C, and R_H, with values of 4.35, 2.01, and 0.146, respectively, significantly deviate from what the BCS theory anticipates. This deviation underscores the strong-coupling character of this superconducting material.

The ratio of the effective electron mass (m_e^*) to the bare electron mass (m_e) reaches its maximum at 2.41 at the critical temperature, indicating a substantial enhancement in electron mass. This further solidifies the strong-coupling nature of the superconducting state in heavily-doped cg-C_4H_4.

Crucially, our analysis demonstrates that the BCS theory cannot adequately describe this material. Instead, the superconductivity in heavily-doped cg-C_4H_4 is governed by strong-coupling and retardation effects. These effects play a pivotal role in shaping its superconducting behavior.

The favorable thermodynamic properties exhibited by heavily-doped cg-C_4H_4 in its superconducting state, in conjunction with its high T_C, suggest that it holds great promise for practical applications in various technological domains.

References

[1] A.P. Drozdov, M.I. Eremets, I.A. Troyan, V. Ksenofontov, S.I. Shylin, *Nature* **525**, 73 (2015).

[2] D. Duan, Y. Liu, F. Tian, X. Huang, Z. Zhao, H. Yu, B. Liu, W. Tian, T. Cui, *Sci. Rep.* **4**, 6968 (2014).

[3] M. Somayazulu, M. Ahart, A.K. Mishra, Z.M. Geballe, M. Baldini, Y. Meng, V.V. Struzhkin, R.J. Hemley, *Phys. Rev. Lett.* **122**, 027001 (2019).

[4] T. Zhang, *New J. Phys.* **22**, 123017 (2020).

[5] G.M. Eliashberg, *J. Exp. Theor. Phys.* **11**, 696 (1960).

[6] J.P. Carbotte, *Rev. Mod. Phys.* **62**, 1027 (1990).

[7] R. Szczęśniak, *Acta Phys. Pol. A* **109**, 179 (2006).

[8] J. Bardeen, L.N. Cooper, J.R. Schrieffer, *Phys. Rev.* **106**, 162 (1957).

[9] S. Baroni, P. Giannozzi, A. Testa, *Phys. Rev. Lett.* **58**, 1861 (1987).

[10] R. Szczęśniak, A.P. Durajski, D. Szczęśniak, *Solid State Commun.* **165**, 39 (2013).

[11] D. Szczęśniak, I.A. Wrona, E.A. Drzazga, Z.A. Kaczmarek, K.A. Szewczyk, *J. Phys. Condens. Matter* **29**, 445602 (2017).

[12] I.A. Wrona, M. Kostrzewa, K.A. Krok, A.P. Durajski, R. Szczęśniak, *J. Appl. Phys.* **131**, 113901 (2022).

[13] H. Eschrig, *Theory of Superconductivity a Primer*, Citeseer, 2001.

[14] K.S.D. Beach, R.J. Gooding, F. Marsiglio, *Phys. Rev. B* **61**, 5147 (2000).

[15] J. Bardeen, M. Stephen, *Phys. Rev.* **136**, A1485 (1964).

Proceedings of "Applications of Physics in Mechanical and Material Engineering" (APMME 2023)

Numerical Investigations of the Influence of Cooling Rate During Solidification on Shrinkage Cavities and Grain Formation Process

T. Skrzypczak*, E. Węgrzyn-Skrzypczak and L. Sowa

[a] *Czestochowa University of Technology, 42-201 Częstochowa, Poland*

Doi: 10.12693/APhysPolA.144.342 *e-mail: tomasz.skrzypczak@pcz.pl

The presented work focuses on the numerical modeling of the solidification process, with a particular emphasis on two significant physical phenomena: shrinkage cavities and grain formation, which are influenced by the cooling rate. Cooling rate plays a crucial role in determining grain size and casting defects. Higher cooling rates result in finer grain structures, while slower rates promote larger grains. During solidification, atoms arrange into crystalline structures, forming grains. The cooling rate affects grain growth kinetics. Faster rates lead to smaller grains due to limited atomic diffusion, while slower rates allow for larger grain growth. Shrinkage cavities, localized regions in solidified material, form due to volume contraction during cooling, negatively impacting mechanical properties. In this paper, the main assumptions of the mathematical and the numerical model are presented. The numerical description of the problem is based on the finite element method, which is a widely used numerical technique for solving complex physical problems. The algorithm for the shrinkage cavity creation process is described, and an original computer program was developed using the numerical model. The computer simulation was conducted to obtain distributions of temperature, grain size, as well as the position and shapes of the shrinkage cavities.

topics: solidification, grain size, cooling rate, shrinkage cavity

1. Introduction

Technological processes such as casting involve the consideration of various thermal phenomena. Casting is a process where a liquid metal solidifies within a mold made of sand or cast iron. During this process, heat is transferred out of the casting. As the casting forms, the liquid and solid phases contract due to the cooling process. Additionally, shrinking occurs during the transformation of the material from the liquid to the solid state. The temperature decrease in different parts of the casting leads to contraction, which is the primary cause of the formation of micro- and macroscopic defects. Cone-shaped open voids observed at the top of the riser and closed voids located deeper within the solidifying system are the most frequently encountered macroscopic defects [1–2]. Extensive discussions on numerical models concerning the formation of shrinkage defects can be found in the literature [3–11]. Books [3, 4] provide fundamental insights into the formation of shrinkage cavities during casting solidification. In one particular study [5], the focus lies on predicting the distribution of defects in a casting with a simple shape. As computational power has increased, researchers have been able to model the formation of shrinkage cavities in three-dimensional spaces [6–11]. This has been achieved using proprietary software [6] as well as commercially available software [7–11]. These models also consider additional factors such as porosity formation [8] and the macrosegregation of components [7, 9, 10].

The cooling rate of the casting has a significant impact on the formation of its primary structure. The primary structure of the casting refers to the arrangement of crystals that form during the material solidification process. The cooling rate determines the solidification rate and affects the size and distribution of crystals within the casting. Fast cooling promotes rapid solidification, resulting in a fine-grained primary structure. A shorter solidification time means that the crystals have less time to grow, resulting in smaller grain sizes. A fine-grained primary structure exhibits higher mechanical strength, a harder surface, and improved resistance to cracking. On the other hand, slow cooling leads to a slower solidification process and the formation of a coarse-grained primary structure. A longer solidification time allows the crystals to grow more extensively, resulting in larger grain sizes. A coarse-grained primary structure may have lower mechanical strength, a less hard surface, and increased susceptibility to cracking. The cooling rate has a significant influence on the size of the frozen crystal zone, columnar crystal zone, and equiaxed grain zone.

2. Mathematical and numerical description

In the analysis, a solidifying casting with a riser is taken into account (see Fig. 1). Heat transfer through the casting's side and top surfaces is incorporated through appropriate boundary conditions. The region under consideration is divided into several zones based on the amount of liquid, solid, and gas present. The primary domains of the solidifying casting include the solid region Ω_S, the liquid region Ω_L, and the region Ω_A filled with air. Additionally, during the solidification process, the solid-liquid area Ω_{S+L} is also observed. The outer boundaries of the analyzed casting are the side surface Γ_{side} and the top surface Γ_{top}. Due to symmetry, only half of the system was considered, which also involved the introduction of a symmetry plane Γ_{sym}.

The problem's mathematical description includes the transient heat transfer partial differential equation

$$\nabla \cdot (\lambda \nabla T) = c\rho \frac{\partial T}{\partial t} \tag{1}$$

and encompasses the related boundary-initial conditions

$$(x, y, z) \in \Gamma_{top}, \Gamma_{side}: \quad -\boldsymbol{n} \cdot \lambda \nabla T = \alpha (T - T_\infty), \tag{2}$$

$$(x, y, z) \in \Gamma_{sym}: \quad -\boldsymbol{n} \cdot \lambda \nabla T = 0, \tag{3}$$

$$T(x, y, z, t{=}0) = T_0. \tag{4}$$

The symbols in this context hold the following meanings: λ [J/(s m K)] represents the coefficient of thermal conductivity, T [K] denotes the temperature. The effective specific heat parameter c [J/(kg K)] describes the release of heat during solidification. The density ρ [kg/m^3] determines the mass per unit volume. The variable t [s] signifies time, while $\boldsymbol{n}$ denotes the normal vector to the external boundaries Γ_{side} and Γ_{top}. The heat transfer coefficient α [J/(s m^2 K)] represents the convective heat transfer outside Γ_{side} and Γ_{top}, respectively. Next, T_0 [K] represents the initial temperature distribution, and T_∞ [K] corresponds to the temperature of an external medium, such as a mold or air. Lastly, ∇ symbolizes the Nabla operator.

To determine the density ρ and the thermal diffusion coefficient λ, their average values can be computed using the following formulas

$$\begin{aligned} \rho &= f_S \rho_S + (1 - f_S)\rho_L, \\ \lambda &= f_S \lambda_S + (1 - f_S)\lambda_L, \end{aligned} \tag{5}$$

$$f_s = \frac{T_L - T}{T_L - T_S}, \tag{6}$$

$$\begin{cases} T < T_S: & c = c_S, \\ T_S \le T \le T_L: & c = \dfrac{c_L + c_S}{2} + \dfrac{L_H}{T_L - T_S}, \\ T > T_S: & c = c_L, \end{cases} \tag{7}$$

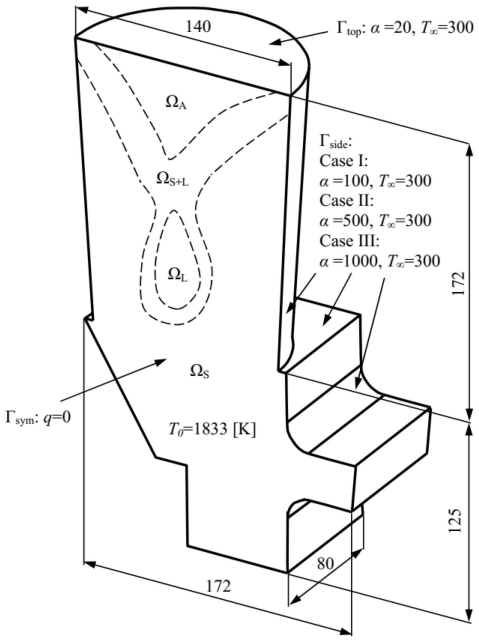

Fig. 1. Solidifying casting with marked characteristic zones and boundary-initial conditions. Dimensions in millimeters.

where f_S [-] represents the fraction of the solid phase, and T_L [K] and T_S [K] denote the liquidus and solidus temperature, respectively. The effective specific heat c (7) is expressed in reference [12]. The subscripts L and S denote the liquid and solid phases, respectively, and L_H [J/kg] signifies the latent heat of solidification. The numerical model is built using the finite element method (FEM), where (1) is employed along with the initial and boundary conditions (2)–(4). The weighted residuals criterion has been applied in formulating FEM,

$$\int_\Omega \mathrm{d}\Omega \; w \left[-c\rho \frac{\partial T}{\partial t} + \nabla \cdot (\lambda \nabla T) \right] = 0. \tag{8}$$

In the above equation, w is the test function, and Ω represents the total volume of the casting. Utilizing the standard Galerkin formulation, a set of equations is derived. Specifically, for each finite element (e), the following equation can be obtained

$$\begin{aligned} \lambda^{(e)} \int\int_{\Omega^{(e)}} \mathrm{d}\Omega \; \left(\boldsymbol{D}_x^{\mathrm{T}} \boldsymbol{D}_x + \boldsymbol{D}_y^{\mathrm{T}} \boldsymbol{D}_y + \mathrm{D}_z^{\mathrm{T}} \mathrm{D}_z \right) \boldsymbol{T} = \\ - \int_{\Gamma^{(e)}} \mathrm{d}\Gamma \; q\boldsymbol{N} - c^{(e)} \rho^{(e)} \int\int_{\Omega^{(e)}} \mathrm{d}\Omega \; \boldsymbol{N}^{\mathrm{T}} \boldsymbol{N} \dot{\boldsymbol{T}}. \end{aligned} \tag{9}$$

To compute the temperature distribution, the equation utilizes the shape functions $\boldsymbol{N}$ of the finite element, along with the spatial derivatives $\boldsymbol{D}_x$, $\boldsymbol{D}_y$, and $\boldsymbol{D}_z$ of the shape functions with respect to x, y, and z, respectively. The nodal values of temperature and its time derivatives are contained in $\boldsymbol{T}$. Additionally, the boundary heat flux is represented by q. The computation employs the backward Euler method for time discretization,

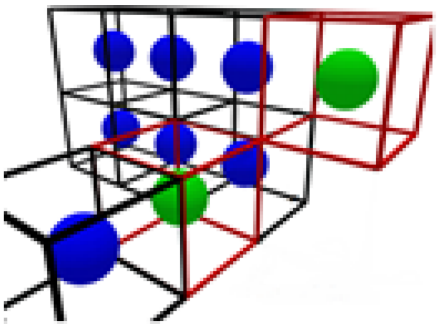

Fig. 2. Simplified structure of the mushy zone.

TABLE I

Material properties used in the calculations.

Material property	Liquid phase	Solid phase	Air
λ	23	35	0.3
ρ	6915	7800	1.0
c	837	644	1008.2
Parameter of solidification	Value		
L	270000		
T_L	1774.0		
T_S	1718		
S_h	0.05		
$d_{\max g}$	0.0002		

resulting in the following scheme

$$\left((\Delta t)^{-1}\boldsymbol{M}+\boldsymbol{K}\right)\boldsymbol{T}^{j+1}=\boldsymbol{B}+(\Delta t)^{-1}\boldsymbol{M}\boldsymbol{T}^{j}. \tag{10}$$

In this model, the assumption was made that the mushy zone comprises spherical grains that grow within a liquid matrix (see Fig. 2). It was also assumed that liquid flow between grains remains feasible until neighboring grains make contact with each other.

The size of the cell $d_{\max l}$ [m] in which the grain grows was calculated using the equation [13]

$$d_{\max l}=d_{\max g}\left(1-\mathrm{e}^{-1/CR}\right), \tag{11}$$

where $d_{\max g}$ [m] represents the maximum grain size that can form in the casting, and CR [K/s] denotes the cooling rate of solidification.

The critical value of the solid phase fraction at which fluid flow occurs in the mushy zone is $f_{skr}=0.52$, based on the assumption made

$$f_{skr}=\frac{V_{grain}}{V_{cell}}=\frac{4\pi}{3}\left(\frac{a}{2}\right)^{3}a^{-3}=\frac{\pi}{6}=0.52. \tag{12}$$

The algorithm for shrinkage cavity growth consists of the following stages at each time step:

- Calculation of the increment of the solid phase based on the temperature field in the current and previous time steps.

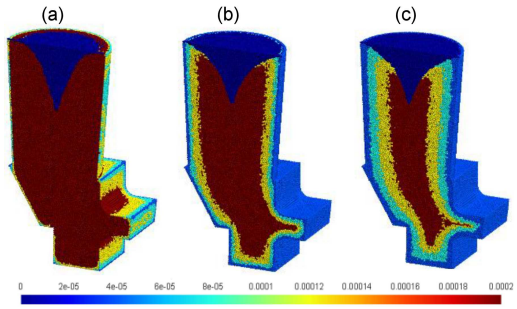

Fig. 3. Primary structure of the casting and location of the shrinkage cavity for cases I (a), II (b), and III (c).

- Computation of the material shrinkage by multiplying the volume of the solid phase by the shrinkage coefficient S_h [-].
- Assigning the calculated volumetric loss to the highest located nodes in the corresponding liquid regions, changing their state from liquid (L) to air (A). This procedure forms one or more shrinkage cavities.

This process should be repeated at each time step until no L nodes remain in the casting.

3. Example of calculations

Three variants of calculations were performed for the geometry shown in Fig. 1. The geometry was modeled and spatially discretized using the open-source software Gmsh. The mesh was composed of tetrahedral elements and consisted of 95501 nodes. Each simulation case was conducted with a different cooling intensity on Γ_{side}, corresponding to a specified value of the coefficient α (Fig. 1). The time step was $\Delta t=0.1$ s. The material properties of steel are presented in Table I. The casting was initially filled with molten alloy at a temperature of 1833 K.

In Fig. 3, the structure of the casting after solidification is shown. It is evident that the cooling rate influences the location and extent of regions with different grain sizes. In the case of slow cooling, a zone dominated by equiaxed grains is observed (Fig. 3a), while in the case of intense cooling (Fig. 3c), frozen and columnar grain regions are visible, along with a central region occupied by the largest equiaxed grains. The shrinkage cavity exhibits a similar shape and depth in all three cases.

4. Conclusions

The cooling rate was found to have a significant influence on the primary structure of the casting. Different cooling rates resulted in varying proportions of frozen columnar and equiaxed grain regions.

Slow cooling led to the dominance of equiaxed grain regions, while intense cooling promoted the formation of frozen and columnar grain regions. The cooling rate did not have a substantial influence on the shrinkage cavity itself. Although there was a slight difference in depth, with a slightly deeper shrinkage cavity observed under slower cooling conditions, the overall shape and location of the shrinkage cavity remained relatively consistent across the different cooling rates.

References

[1] Ch. Pequet, M. Rappaz, M. Gremaud, *Metall. Mater. Trans. A* **33**, 2095 (2002).

[2] M. Bellet, O. Jaouen, I. Poitrault, *Int. J. Numer. Method. H.* **15**, 120 (2005).

[3] J. Campbell, *Castings*, 2nd ed., Butterworth-Heinemann, Oxford 2003.

[4] M.C. Flemings, *The solidification processing*, Mc Graw-Hill, New York 1974.

[5] C.J. Kim, S.T. Ro, *J. Heat. Trans.* **115**, 1078 (1993).

[6] A.S. Jabur, F.M. Kushnaw, *J. Appl. Computat. Math.* **6**, 7 (2017).

[7] A. Ludwig, M. Wu, A. Kharicha, in: *CFD Modeling and Simulation in Materials Processing 2016*, Springer 2016, p. 3.

[8] C. Zhang, Y. Bao, M. Wang, L. Zhang, *Arch. Foundry Eng.* **16**, 27 (2016).

[9] M. Wu, A. Ludwig, A. Kharicha, *Appl. Math. Model.* **41**, 102 (2017).

[10] M. Xie, H. Shen, *Front. Mater.* **7**, 13 (2020).

[11] K. Zheng, Y. Lin, W. Chen, L. Liu, *Adv. Mech. Eng.*, **12**, 1 (2020).

[12] B. Mochnacki, J.S. Suchy, *Numerical Methods in Computations of Foundry Processes*, Polish Foundrymen's Technical Association, Kraków 1993.

[13] N. Sczygiol, *Modelowanie Numeryczne Zjawisk Termomechanicznych w Krzepnącym Odlewie i Formie Odlewniczej*, Wydawnictwo Politechniki Częstochowskiej, Częstochowa 2000.

Proceedings of "Applications of Physics in Mechanical and Material Engineering" (APMME 2023)

Numerical Investigation of the Optical Properties Related to Combined Periodic and Porous Surface Structures

M. Dośpiał* and K.M. Gruszka

Department of Physics, Czestochowa University of Technology, Armii Krajowej Ave. 19, 42-200 Częstochowa, Poland

Doi: 10.12693/APhysPolA.144.346 *e-mail: marcin.dospial@pcz.pl

In this paper, the results of studies on sub-micrometer planar structures used for aimed frequency-dependent electromagnetic radiation dissipation are presented. The proposed specific geometry of periodic parts of surface structures should enable the occurrence of phenomena related to selective reflectance and interference. The inner porous structure should lead to the formation of destructive interference of electromagnetic radiation and its dissipation. The investigated structures were irradiated by a Gaussian-type radiation source. The propagation was analyzed using the MEEP software package for electromagnetic simulation via the finite-difference time-domain method. The reflectance spectra were obtained by the Fourier transform of the response to the short pulse. The obtained results showed that the surface structures are mainly responsible for reflected electromagnetic spectrum composition, while the porous parts were responsible for thermal radiation dissipation.

topics: finite-difference time-domain (FDTD), electromagnetic (EM) propagation, structural colors, electromagnetic radiation dissipation

1. Introduction

In nature, there are many structures, the mapping of which allows the transfer of evolutionarily optimized patterns in order to achieve selected functional properties of chosen technical solutions [1, 2]. Examples of such an approach include the application of structure types met in shark scales in the production of algae-resistant hulls [3], or abalone shells, the structure of which is an inspiration for reinforcement applied in materials engineering [4]. One of such designs is also the wing structure of butterflies from the Archaeoprepona demophon family [5] (see Fig. 1), which was the inspiration for the research carried out in this paper.

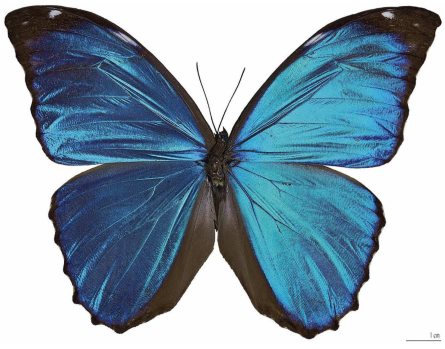

Fig. 1. Photo of the butterfly of the Archaeoprepona demophon family [5].

The biological function of this butterfly wing surface is to obtain angle-dependent reflections, known in science as structural colors, as well as to absorb heat energy from infrared radiation. The introduction of solutions inspired by these phenomena into technical devices may allow for the improvement of heat dissipation technology [6] in devices exposed to high temperatures or the improvement of methods for obtaining colored surfaces that do not lose their properties due to pigment fading [7]. In this paper, we performed a theoretical analysis of the absorption and reflection spectra of structures based on a butterfly wing. For this reason, we have presented the results of FDTD calculations of Gaussian pulse propagation and transmittance spectra evaluated on both porous and periodic surfaces of biologically inspired structures.

2. Computational methods

For all calculations, we have used the MEEP software package [8], which implements the finite-difference time-domain (FDTD) method for simulating electromagnetic wave propagation. Based on the areas marked in Fig. 2, the parameters of pores present in the substrate structure were determined. It was found that their moderate size was about 0.4 μm. Figure 3 was used to determine the structural parameters of the periodic pattern present in a wing surface [9]. The analyzed transmission electron microscopy (TEM) images

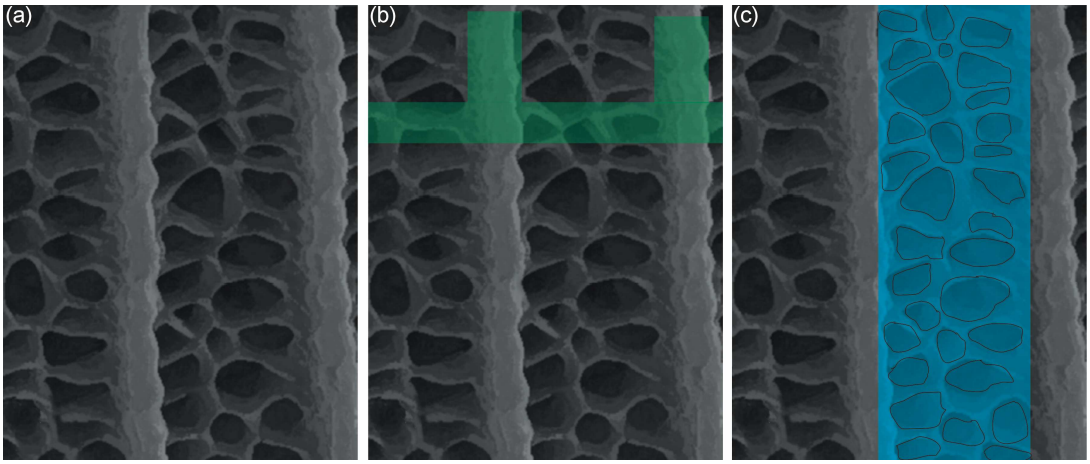

Fig. 2. TEM images of butterfly wing with marked characteristic patterns that were transferred to theoretical model [9].

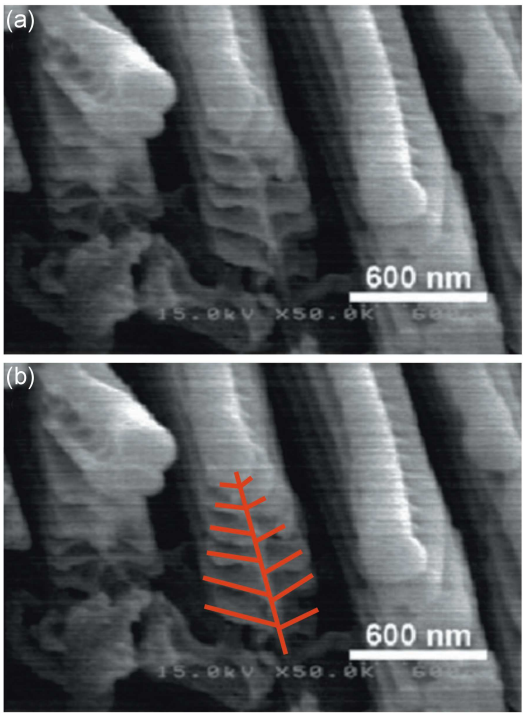

Fig. 3. TEM images of butterfly wing with cross-section pattern with marked characteristic structures that were transferred to theoretical model [9].

revealed that the observed structures have tree-like patterns. The height of observed trees was moderately 1.5 μm. The branches on that pattern had about 0.05 μm thickness and the same distance between themselves. Their length decreased with the distance from the base of the trunk from 0.4 to 0.05 μm. The distances between neighboring patterns were around 0.05 μm on the bottom of the structure.

The obtained parameters allowed us to create 6 basic shapes of different complexity. All analyzed shapes are presented in Fig. 4a–f.

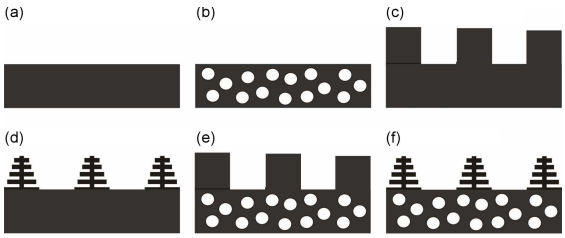

Fig. 4. Types of structures analyzed in the model: (a) reference structure of substrate, (b) substrate with holes, (c) substrate with a surface ridge (comb structure), (d) substrate with surface Christmas tree pattern, (e) substrate with holes and surface ridge, (f) substrate with holes and Christmas tree pattern.

A substrate in the form of a simple block was used as a basic reference structure, as presented in Fig. 4a. Then, the porous substrate, as well as substrates with surface periodic patterns, were chosen for further analysis (see Fig. 4b–d). The last part of the analysis was performed for combined structures, as presented in Fig. 4e, f. The optical property, i.e., ϵ value, was set to 2.44 for all solid structures, which is similar to values found in the literature [9]. The light source was placed in front of the structure, in the middle, at a distance of 6 μm. In applied simulation, space was set as a 2D 16×16 μm^2 and was digitized. The 60 pixels represented a length of 1 μm. Also, in order to reach numerical stability, a 0.5 Courant criterion was used. Based on such assumed variables and the working area, the time step in the simulation was 5 ns. The Gaussian pulse was set in TE mode (TE — electric part of the electromagnetic wave) in such a way that in 2D simulation the E_x and E_y components of the electromagnetic field were parallel to the x and y axis of the computational domain, respectively. The component E_z was the current component, which was modulated in time. Due to the

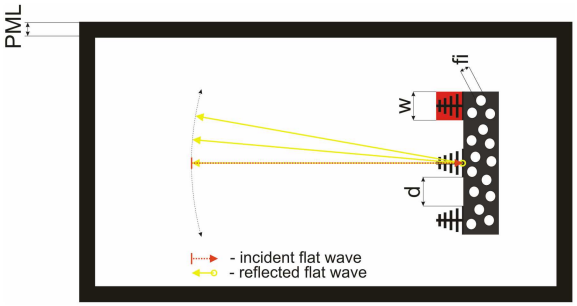

Fig. 5. Scheme of the measurement environment implemented in the MEEP program to perform theoretical research.

MEEP program using current types of sources, the source used in the simulation was not a hard type. Such prepared structures and the light source were placed in the air area surrounded by PMLs (perfectly matched layers) of 1 μm thickness, as can be seen in Fig. 5.

The transmittance spectra were obtained by the Fourier transform of the response to a short pulse of a flat wave. The Fourier transform was calculated just after an analyzed structure, before PML. The calculations were performed along a vector perpendicular to the longer side of the substrate. The obtained transmittance results were normalized by a similar calculation performed for a source placed in an empty box filled with air. Gaussian-pulse radiation source, with 1.875 $[2\pi C/a]$ central frequency and 3.223 $[2\pi C/a]$ width, which represents UV(A)–VIS–IR(A) wavelength area, was used for both types of calculations.

3. Results and discussion

In Fig. 6, the electromagnetic (EM) wave propagation in the computational cluster with different types of reflecting/absorbing structures was presented. Red and blue colors on the exposed picture represent positive and negative peaks of E_z component of the electromagnetic field with respect to the surroundings in white, which are treated as zero amplitude. The EM source applied in the simulation generated flat pulses that have a temporal intensity profile, which has a Gaussian shape. Subjecting such an impulse to a Fourier analysis reveals that in its spectrum, different frequencies appear, distributed around the 1.875 $[2\pi C/a]$ central frequency, with a width of distribution equal to 3.223 $[2\pi C/a]$. In all the panels of Fig. 6, three different areas of EM distribution can be seen. The first area represents the emitted pulse modified by its backward superposition with a reflected wave from the surface of a structure. The second one represents internal propagation in the substrate region. The last area represents the transmittance region behind the structure. As can be seen in Fig. 6a, b, d, e, the EM pulse for any periodic structure results in the presence of a reflected flat return pulse in the backward direction, but also a clearly visible symmetrical bent at an accurate angle for the Christmas tree-shaped structure and at a wide angle of deflection for the comb structure. For a substrate without a periodic structure, we only observe distinctive back reflection. In the second area, the inner zone of the substrate, the pulse propagation frequency is changed. It increases the most for solid areas without a periodic structure or with a structure in the form of a comb; for the substrate behind the Christmas tree structure, the observed changes in the propagation frequency are weaker. In porous areas, they remain unchanged in relation to the incident pulse. EM propagation for the last area in the transmittance region behind the examined structure was focused and significant for the comb surface pattern, dissipated but clearly present for the Christmas tree surface pattern, and almost vanished for the plane surface and porous structure. The presence of combined structures resulted in moderate transmittance compared to less complex structures (lower than for surface patterns with a solid substrate and smaller than for those with a plain porous substrate).

In Fig. 7, the transmission, reflectance, and summarized loss spectra for all investigated structures are presented. As can be seen in Fig. 7a, the substrate made of a flat block has the smoothest shape of all dependencies for VIS–IR(A) wavelengths. In the UV(A) region, sharp peaks on transmission and reflectance curves are present. This type of structure strongly reflects selective values of UV(A) and the whole VIS area, especially wavelengths from the blue VIS region. Reflectance rapidly decreases in the IR(A) area. Transmittance spectra in the reference structure show reversed behavior to reflectance spectra, i.e., high values for selective wavelengths in the UV(A) region and rapid growth in the red VIS–IR(A) wavelength area. Losses observed for that structure have very low values for short waves, starting from about a few percent and increasing systematically to approximately 20% for a wavelength of 700 nm. The introduction of periodic structures (Fig. 7b and d) on the surface of the analyzed sample leads to the creation of irregular, jagged dependence for all measured quantities. The analysis of the loss dependence shows that for both tested structures, there is a clear increase in their overall value. For the comb-shaped surface structure, the greatest changes occur within UV(A) and VIS regions up to a value of approximately 600 nm. Their value reaches an average of 50% and a maximum of 75% for the 450 nm peak. For wavelengths above 600 nm, they assume an average value of 20%. All these changes mainly correspond with a reduction of reflectance, with the exception of the UV(A) region, where changes correspond to a reduction in both transmittance and reflectance quantities. Analysing Fig. 7c, it can be seen that the presence of holes in the substrate leads to

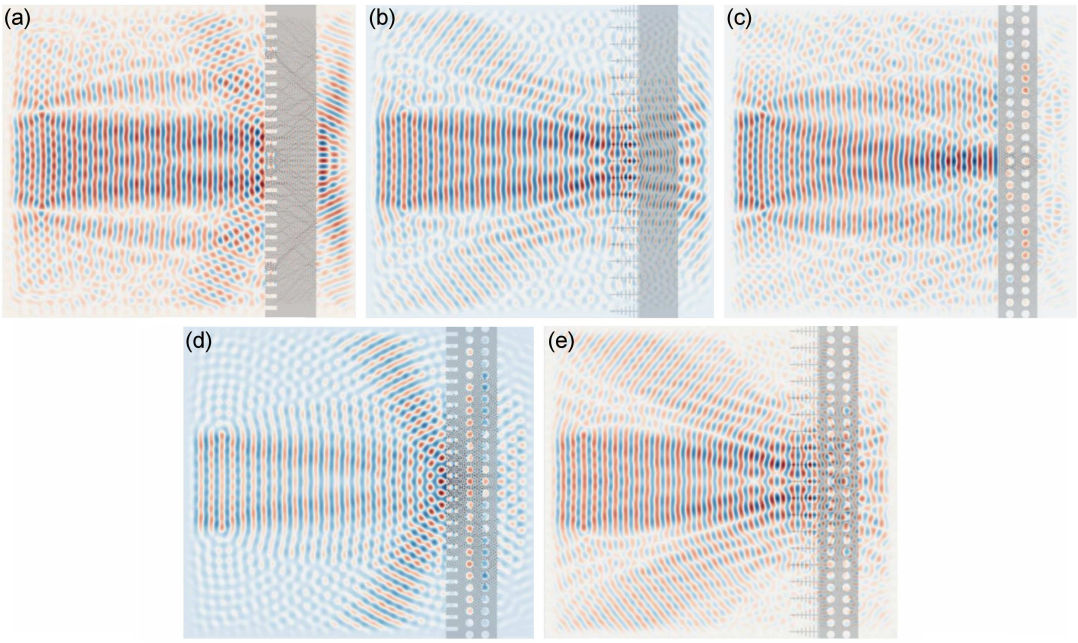

Fig. 6. EM wave propagation in the computational cluster, with five types of reflecting structures: (a) substrate with holes, (b) substrate with surface ridge (comb structure), (c) substrate with surface Christmas tree pattern, (d) substrate with holes and surface ridge, (e) substrate with holes and Christmas tree pattern.

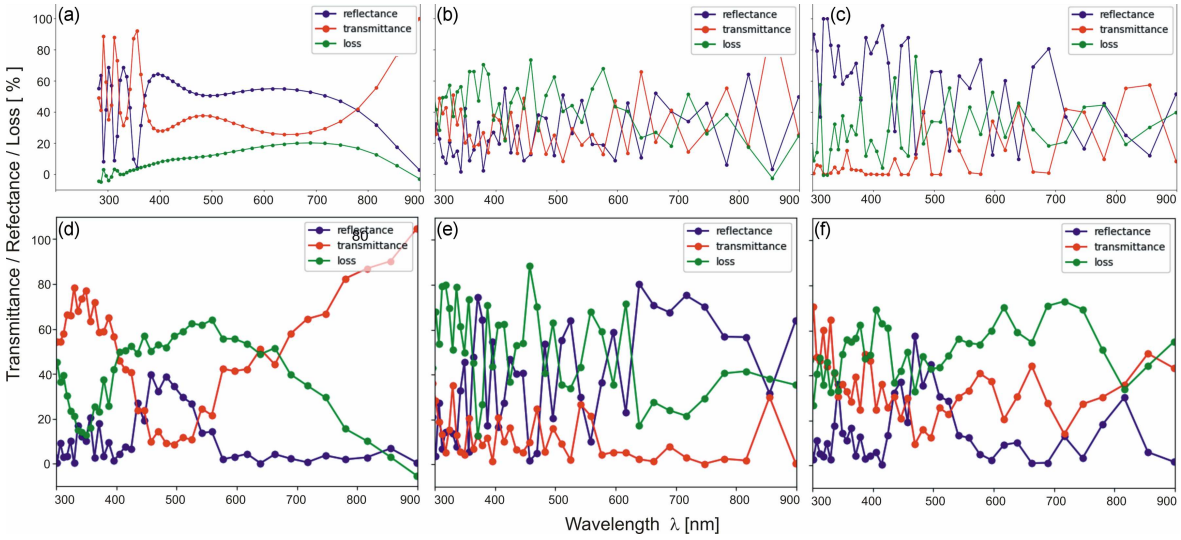

Fig. 7. Transmission spectra for EM wave propagated in the computational cluster, with five types of reflecting structures: (a) reference block substrate, (b) block substrate with surface ridge (comb structure), (c) block substrate with holes, (d) block substrate with surface Christmas tree pattern, (e) block substrate with holes and surface ridge, (f) block substrate with holes and Christmas tree pattern.

vanishing transmittance almost on the whole spectrum, with exceptions seen for chosen frequency peaks of intensities lower than 50%. We also note a large increase in reflected rays in the short wave region, which is slowly fading till 700 nm wavelength. Over that value, reflectance varies around 50%. The losses generally increased to moderately 35%, achieving the highest value of 75% for a peak near 475 nm. Interesting results were also obtained for tree-like surface structure in Fig. 7d. All dependencies had a less jagged structure than that observed for the rest of the modified samples. It was observed that the maximum of losses shifted from the red-VIS region in the direction of shorter wavelengths, compared to the reference structure. Its middle was found at 550 nm and had a 3.5 times higher value. The changes observed in the transmittance spectrum were also significant. The presence

of a wide optic window for UV(A) was found. Over that window, transmittance fell down to almost 10%, and starting from 550 nm, grew systematically to reach 100% near 900 nm. From an analysis of reflectance spectra in Fig. 7d, one can see that almost in all examined regions, reflectance was close to 0% except in the area of wavelengths from 400 to 550 nm. That shows the presence of reflection in the blue–green VIS region. The combination of surface structure and holes in the substrate leads to different effects. In the case of a comb structure with holes on the substrate, we can see the growth of losses, especially for shorter waves, and an increase in reflectance for longer wave area (over 600 nm). Transmittance fades almost to 0% except in some narrow areas, especially for short waves in the UV(A) region. In the case of a tree-like surface structure with pores in the substrate, we can see that the strongest reflection is still present in the blue–green VIS region, but there are also small amounts of rays reflected in the IR(A) region from 750 to 850 nm. The losses are quite high, but transmittance is higher than for the sample with the same surface structure and lack of holes.

4. Conclusions

In this paper, a theoretical analysis of the absorption and reflection spectra of structures based on a butterfly wing was performed.

The results of FDTD calculations of Gaussian pulse propagation and transmittance spectra evaluated on biologically inspired structures revealed that the porous structure of the substrate was responsible for a dissipation of the electromagnetic radiation. This observation is based on the increase in recorded losses as well as reflected radiation. The obtained results are coherent with postulated assumptions.

The periodic comb-like structure led to a more jagged dependence of all quantities, while another periodic structure, a tree-like one, was responsible for the increase in losses as well as transmittance in UV(A), VIS-red, and IR(A) areas. In this case, the reflectance was reduced to blue and green VIS region. The reflectance in such a range is coherent with the structural colors of the investigated biological structure and is a proof that the structure parameters for the tree-like surface model have been selected correctly.

To sum up, the use of structures based on pores leads to the dissipation of EM radiation, and the Christmas tree structure allows to obtain structural colors.

Acknowledgments

This research was supported in part by PLGrid Infrastructure.

References

[1] H. Xue, D. Liu, D. Chi, C. Xu, S. Niu, Z. Han, L. Ren, *Adv. Mater. Interfaces* **8**, 2100142 (2021).

[2] M. Dośpiał, K.M. Gruszka, *Acta Phys. Pol. A* **142**, 35 (2022).

[3] X. Pu, G. Li, H. Huang, *Bio. Open* **5**, 389 (2016).

[4] Y.-Y. Sun, Z.-W. Yu, Z.-G. Wang, *Adv. Civil Eng.* **2016**, 1 (2016).

[5] *Nymphalidae*, Wikipedia, 15.11.2023 (in Polish).

[6] Y. Cui, D. Li, H. Bai, *Ind. Eng. Chem. Res.* **56**, 4887 (2017).

[7] F. Chen, Y. Huang, R. Li, S. Zhang, B. Wang, W. Zhang, X. Wu, Q. Jiang, F. Wang, R. Zhang, *Chem. Commun.* **57**, 13448 (2021).

[8] A.F. Oskooi, D. Roundy, M. Ibanescu, P. Bermel, J.D. Joannopoulos, S.G. Johnson, *Compu. Phys. Commun.* **181**, 687 (2010).

[9] G. Zyla, A. Kovalev, M. Grafen, E.L. Gurevich, C. Esen, A. Ostendorf, S. Gorb, *Sci. Rep.* **7**, 17622 (2017).

Proceedings of "Applications of Physics in Mechanical and Material Engineering" (APMME 2023)

UV-Filtration Properties of a Quasi-One-Dimensional Photonic Crystal

K.M. Gruszka* and M. Dośpiał

Department of Physics, Czestochowa University of Technology, Armii Krajowej Av. 19, 42-200 Częstochowa, Poland

Doi: 10.12693/APhysPolA.144.351 *e-mail: konrad.gruszka@pcz.pl

The paper presents a comprehensive investigation of the ultraviolet-filtration properties of a quasi-one-dimensional photonic crystal using the transfer matrix method. The photonic crystal structure forms a periodic stack that exhibits photonic suppression regions. By tailoring the layer thicknesses, we have designed a photonic crystal filter that selectively transmits ultraviolet light while efficiently suppressing unwanted wavelengths. Moreover, we demonstrate that a similar effect can be achieved by introducing an interlayer air gap, which, in turn, makes it possible to adjust the system during operation. Through rigorous simulations, the transmission characteristics of the proposed photonic crystal filter have been analyzed. The simulation results demonstrate that the filter exhibits a high degree of ultraviolet light transmission within a specific wavelength range, while effectively suppressing other wavelengths in the visible and near-infrared regions. The ability to selectively transmit ultraviolet light can be utilized in various fields, such as solar energy harvesting, ultraviolet photodetection, and optical sensing.

topics: matrix method, UV filters, tunable, electromagnetic (EM) propagation

1. Introduction

Tunable ultraviolet (UV) filters that allow for the transmission of specific UV light wavelengths are highly desired in various scientific applications due to their application versatility and precise control over the spectral range. The significance of such filters may be demonstrated when considering such fields as spectroscopy, photobiology and photomedicine, optoelectronics and nanotechnology, solar research, or photovoltaics, which remains a very active research area nowadays. For example, in spectroscopy, the ability to transmit specific wavelengths of UV allows the study of the unique spectral signatures of different compounds, which in turn enables the identification, quantification, and analysis of substances in fields such as chemistry, biochemistry, and environmental science [1–3]. In the field of photobiology, the effects of UV radiation on living organisms are studied because different wavelengths of UV light have varying biological impacts, ranging from DNA damage to influence on cellular processes. Tunable UV filters facilitate precise manipulation of the UV spectrum incident on biological samples, enabling researchers to investigate the specific effects of different wavelengths on cellular mechanisms, photoreceptors, and photosensitive molecules [4]. In photomedicine, tunable UV filters are crucial for selecting the most appropriate wavelengths for therapeutic applications, such as targeted photodynamic therapy or UV-induced sterilization [5]. In optoelectronic and nanotechnology, certain semiconductor materials, such as gallium nitride (GaN), are widely used in UV LEDs and UV detectors [6]. Tunable filters allow researchers to optimize the transmission characteristics of these devices, enhancing their efficiency, sensitivity, and performance. Additionally, in nanofabrication processes, tunable UV filters are utilized for precise control of the UV exposure, enabling the patterning and structuring of nanoscale features on substrates [7, 8]. As for solar research and photovoltaics, the study of solar radiation and its interaction with the Earth's atmosphere is essential for understanding climate dynamics, atmospheric chemistry, and solar energy conversion [9]. Different UV wavelengths have distinct effects on the Earth's energy budget, ozone layer, and photochemical reactions. Tunable UV filters help scientists isolate and investigate specific UV bands, allowing them to gain insights into the detailed mechanisms of these processes and accurately quantify their impact on climate change and environmental systems.

The above examples are only a small part of the various applications faced by this type of devices, however, these examples clearly show that the demand for this type of solutions not only does not decrease, but also promises further increased exploration of photonics and its future applications, simply leading to advancements in various scientific disciplines and technological applications [10].

Quasi-one-dimensional photonic crystals (PCs) have emerged as a fascinating area of research in the field of photonics due to their unique optical properties and potential applications. These structures consist of alternating layers or periodic arrays of materials with different refractive indices, which leads to the formation of bandgaps and selective reflection or transmission of specific wavelengths of light. In recent years, there has been growing interest in utilizing quasi-one-dimensional photonic crystals for the fabrication of tunable UV filter devices, enabling precise control over the transmission of ultraviolet (UV) light. The design and analysis of such devices often rely on computer simulations based on the transfer matrix method (TMM) [11], which is well-suited for investigating the optical properties of these complex structures [12]. In this paper, we present a comprehensive study on the design, simulation, and characterization of tunable UV filters based on quasi-one-dimensional photonic crystals, employing the transfer matrix method as a powerful tool for analyzing their optical behavior. By exploring the tunability of these filters, we aim to contribute to the development of advanced UV filtering technologies with applications in spectroscopy, photomedicine, optoelectronics, and beyond.

2. Computational methods

The TMMs method governing equation [13, 14]

$$\begin{bmatrix} E_{in}^{(+)} \\ E_{in}^{(-)} \end{bmatrix} = \Gamma \begin{bmatrix} E_{out}^{(+)} \\ E_{out}^{(-)} \end{bmatrix} \tag{1}$$

describes incident wave $E_{in}^{(+)}$ incident on the boundary of the mediums, $E_{in}^{(-)}$ is reflected wave propagating in an antiparallel direction, $E_{out}^{(+)}$ is wave coming out of the system, while characteristic matrix Γ is defined as

$$D_{in,j}\Big(\prod_{j=1}^{J} P_j D_{j,j+1}\Big) = \begin{bmatrix} \Gamma_{11} & \Gamma_{12} \\ \Gamma_{21} & \Gamma_{22} \end{bmatrix} \tag{2}$$

and

$$P_j = \begin{bmatrix} \mathrm{e}^{\mathrm{i}\varphi_j} & 0 \\ 0 & \mathrm{e}^{-\mathrm{i}\varphi_j} \end{bmatrix}, \tag{3}$$

$$\varphi_j = d_j n_j \frac{2\pi}{\lambda} \cos(\phi_j), \tag{4}$$

where d_j is j-th layer thickness, n_j — j-th layer refractive index, λ — incident wavelength, and ϕ_j — j-th layer incidence angle.

The last one, $D_{j,j+1}$, called the transmittance matrix is defined as

$$D_{j,j+1} = \frac{1}{t_{j,j+1}} \begin{bmatrix} 1 & r_{j,j+1} \\ r_{j,j+1} & 1 \end{bmatrix}, \tag{5}$$

where the symbols $t_{j,j+1}$ and $r_{j,j+1}$ denote the Fresnel reflectance and transmittance coefficients of the electromagnetic wave at the transition from medium j to medium $j+1$, assuming that the wave propagates towards the positive values of the X axis of the multilayer system (parallel to normal vector of the system layers, while these layers are parallelograms). The schematic illustration of the studied system is presented in Fig. 1. The system consists of 7 layers made using two materials, namely fused silica and Vitron IG, and their refractive indexes are $n_A = 1.4570$ and $n_B = 2.5385$, respectively. When the air gap was used, the refractive index was set to $n_X = 1.0$. Whenever an air gap was introduced into the system, it was placed after layer 3 (see Fig. 1). Simulation takes into account the extinction coefficients of these materials, which are 4.4788×10^{-7} for Vitron. In the case of fused silica and air gap, their corresponding extinction coefficients are $k = 0$.

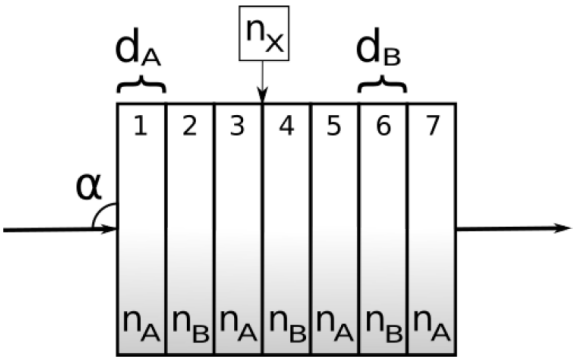

Fig. 1. Schematic diagram of waveguide with variable hole-defects. The spacing between hole centers is always fixed to 2 μm on both sides of the defect. For ease of readability, we present only selected defect sizes.

3. Results and discussion

The first quasi-one-dimensional photonic crystal was prepared to be centro-symmetric with a symmetry axis located at layer 4. The thickness of A material, d_A, was fixed to 15 nm, while the thickness of layer B, d_B, was systematically reduced from 20 down to 11 nm in a 1 nm step. The topology of the system was binary, implementing $\{A, B, A, B, A, B, A\}$ structure. Figure 2 shows the transmission spectra for this photonic crystal. As can be seen, for each case the single transmission spectrum consists of one sharp peak with a transmittance maximum at 100% (all transmittance spectra and maps are normalized to 1, where 1 corresponds to 100%) and a long "tail" with nearly 47% average transmission for the case when $d_X = 11$ nm and 67% when $d_X = 20$ nm. Reducing the thickness of the layer d_B leads to a twofold behavior of the overall transmission. Firstly, it is visible that the transmission maximum shifts towards shorter wavelengths, while not only maintaining the

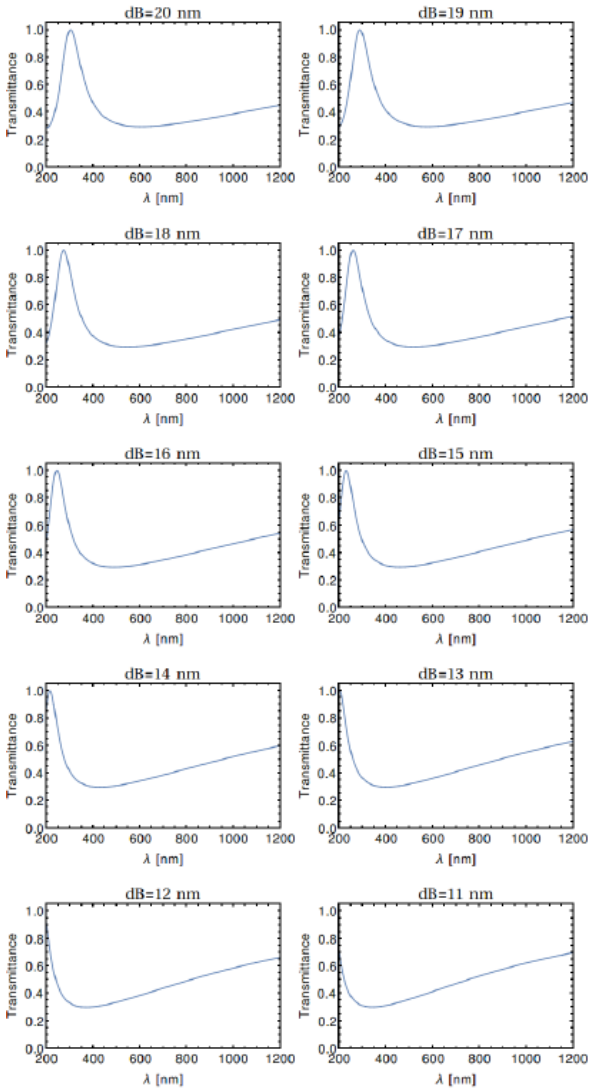

Fig. 2. Transmittance in function of incident wavelength at incident angle $\theta = \pi/4$. The B layer thickness (Vitron) was systematically decreased, as denoted.

transmittance maximum but also conserving the transmission peak shape. A narrow half-width of the transmittance peak is desirable as it limits the range of wavelengths passing through the system. Secondly, the transmittance from the infrared wavelength side (above 800 nm) increases, which is undesirable in this case. It should be noted, however, that the high transmittance at the peak of the maximum, due to the fact that it reaches as much as 100% in this place, allows for assembling several filters in a cascade, one after the other, assuming that the distance between the filters is sufficiently large (i.e., much greater than the desired wavelength of the transmitted UV light). Maintaining such a large gap (e.g., 10 μm or more) will limit the interaction between the filters to a minimum and will allow for undisturbed operation as if it were single.

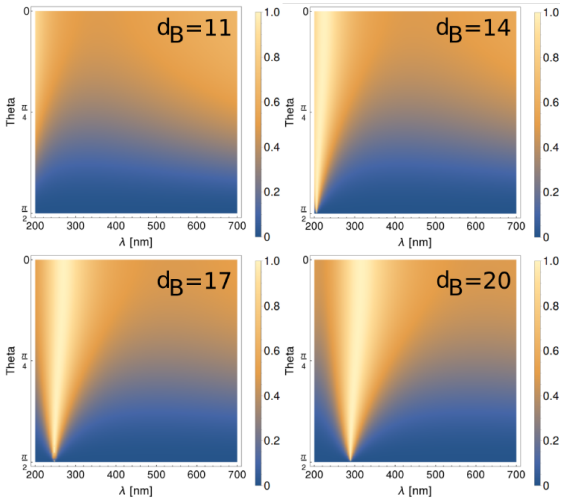

Fig. 3. Transmittance maps for the structure without air gap; d_B is the layer B thickness. The θ angle is the angle of incidence measured to the layer normal, and brightness is the transmittance.

Figure 3 shows in the form of transmission maps the behavior of the system when the angle of incidence α of light is changed in the range from 0 to 90° (0 to $\pi/2$). As can be seen, the selectivity of the filter increases as the incident wave tends to $\theta = \pi/2$ (please note that θ is defined with respect to the normal of the layer). The usable range for this photonic structure seems to lay between $\pi/4$ and $pi/2$; below this angle, the filter starts to transmit significant amounts of electromagnetic waves over a wide range of wavelengths.

Next, we introduced a variable air gap between layers number 3 and 4 (for reference, see Fig. 1). The presence of an air gap is very desirable because it basically allows one to modify the parameters of the filter without having to manufacture new photonic crystal, as it was a necessity in the first photonic crystal (PC) case. Unfortunately, the introduction of such an air gap may introduce potentially undesirable properties and deteriorate the filtering properties of the system. Air, on the other hand, does not strongly block UV radiation and allows modifications to the geometry of the PC structure to be made relatively easily. The introduction of the air gap required additional fine-tuning of the rest of the PC layers and a decrease in layer A thickness to $d_A = 13$ nm. Figure 4 shows the transmittance of the air gap photonic crystal, depending on the decreasing thickness of the air layer. As can be seen, the shape of the transmittance curve is similar in character to the first PC (without an air gap). In this case, a single peak can also be observed, although its transmittance at the peak of the maximum is lower and amounts to 89% for the structure in which the thickness of the air layer is $d_X = 30$ nm, but increases to 99% for $d_X = 3$ nm. The half-width of the peak has

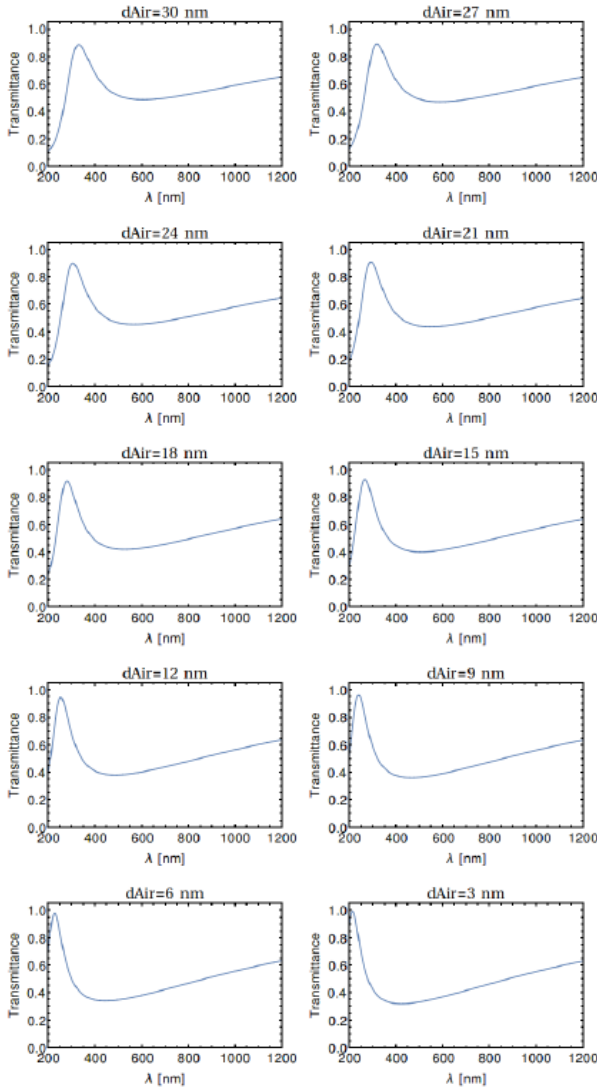

Fig. 4. Transmittance in function of incident wavelength at incident angle $\theta = \pi/4$ for the system with air gap. The gap size (d_{Air}) was systematically reduced, as denoted.

also increased, which, as mentioned earlier, negatively affects the selectivity of the filter. As in the first case, reducing the thickness of this layer shifts the transmittance peak towards lower wavelengths of electromagnetic radiation, while increasing the transmittance in the infrared region.

The transmittance maps presented in Fig. 5 are also of a similar nature as in the case of the first studied structure. Their in-depth analysis shows that this time the filter usability range (understood as the possibly narrow transmittance peak and the smallest possible transmittance for infrared light) is narrower than in the case of a structure without an air gap. This range can be extended by using a narrower air gap, but this involves shifting the transmittance maximum towards the light from the infrared range.

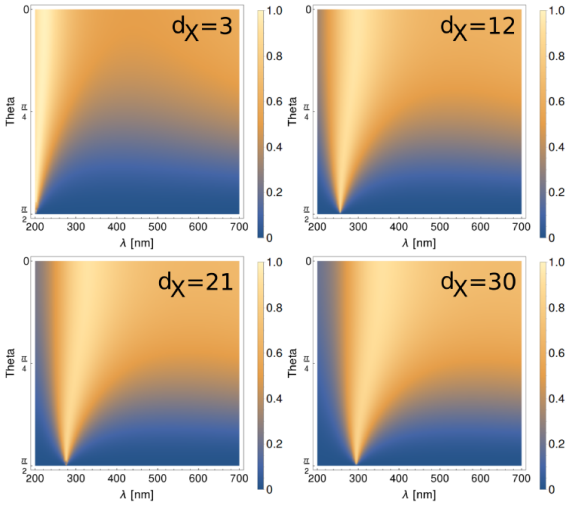

Fig. 5. Transmittance maps for the structure with air gap; d_X is the air gap thickness. The θ angle is the angle of incidence measured to the layer normal, and brightness is the transmittance.

4. Conclusions

The investigation into the UV-filtration properties of a quasi-one-dimensional photonic crystal has yielded valuable insights into the performance of the studied photonic structure. Through comprehensive analysis, several crucial findings have emerged. The transmittance spectra exhibit a distinctive behavior characterized by a sharp transmission peak with a transmittance maximum of 100%, accompanied by an extended "tail" exhibiting average transmissions of approximately 47% and 67% for respective thicknesses of $d_X = 11$ nm and $d_X = 20$ nm. The manipulation of the layer thickness d_B revealed intriguing outcomes, resulting in a dual effect on overall transmission. Firstly, a shift of the transmission peak towards shorter wavelengths was observed, while maintaining its shape and maximizing transmittance. The subsequent increase in transmittance at longer wavelengths was noted, albeit being undesirable. The filter's optimal operational range was found between $\pi/4$ and $\pi/2$; deviating beyond this range resulted in broader transmission of electromagnetic waves. The introduction of a variable air gap allowed for real-time parameter adjustments. Considering the air gap configuration, the transmittance curves maintained a single-peak nature, albeit with peak transmittance values decreasing to 89% for $d_X = 30$ nm and increasing to 99% for $d_X = 3$ nm. This led to a wider peak half-width, diminishing filter selectivity. Transmittance maps paralleled those of the initial structure, revealing a narrower usability range due to the air gap, and although this range could expand with a smaller air gap, it shifted the transmittance peak towards infrared light.

In summary, our study unveils the intricate interplay of layer parameters, incident angles, and air gap presence in influencing UV-filtration properties of quasi-one-dimensional photonic crystals. These findings offer practical design insights for optimizing photonic filters for UV applications, prompting further exploration and refinement of such systems.

Acknowledgments

This research was supported in part by PLGrid Infrastructure.

References

[1] Y. Zhang, S. Wu, P. Sun, *Sci. Total Environ.* **899**, 165702 (2023).

[2] S. Arsenault-Escobar, J.F. Fuentes-Galvez, C. Orellana, S. Bollo, P. Sierra-Rosales, S. Miranda-Rojas, *Spectrochim. Acta A* **292**, 122400 (2023).

[3] K. Gruszka, *Acta Phys. Pol. A* **139**, 617 (2021).

[4] K. Prabakaran, H. Oh, R. Manivannan, S. Hyeong Park, Y.-A Son, *Spectrochim. Acta A* **279**, 121437 (2022).

[5] C. Ruiz-Díez, M. Navarro-Segarra, R. Barrena, T. Gea, J.P. Esquivel, *Environ. Technol. Innov.* **31**, 103199 (2023).

[6] W. Ding, X. Meng, *J. Alloys Compd.* **866**, 157564 (2021).

[7] J. Yan, X. Fan, Y. Liu, K. Qu, Y. Yu, R.-Z. Li, *Appl. Mater. Today* **32**, 101840 (2023).

[8] J.H. Lee, D.H. Kim, J. Won, D.W. Lee, J.Y. Oh, Y. Liu, Y.-P. Park, H.-C. Jeong, D.-S. Seo, *Mater. Chem. Phys.* **269**, 124771 (2021).

[9] F. Yíldrim, Z. Orhan, Ş. Aydoğan, *Mater. Res. Bull.* **159**, 112113 (2023).

[10] K.M. Gruszka, M. Dośpiał, *Acta Phys. Pol. A* **142**, 101 (2022).

[11] M. Asif, A. Afaq, M. Amin, K. Raouf, A. Majeed, M. Asif, *Mater. Today Commun.* **37**, 106966 (2023).

[12] S. Garus, J. Garus, M. Szota, M. Nabiałek, K. Gruszka, K. Błoch, *Arch. Mater. Sci. Eng.* **64**, 110 (2013).

[13] T.G. Mackay, A. Lakhtakia, *The Transfer Matrix Method in Electromagnetics and Optics*, Springer International Publishing, 2020.

[14] M. Born, E. Wolf, A.B. Bhatia, P.C. Clemmow, D. Gabor, A.R. Stokes, A.M. Taylor, P.A. Wayman, W.L. Wilcock, *Principles of Optics: Electromagnetic Theory of Propagation, Interference and Diffraction of Light*, 7th ed., Cambridge University Press, 1999.

Proceedings of "Applications of Physics in Mechanical and Material Engineering" (APMME 2023)

Influence of Extinction Coefficient on Electromagnetic Wave Transmission in Thin Superlattices

K.M. Gruszka*

Department of Physics, Czestochowa University of Technology, Ave. Armii Krajowej 19, 42-200 Częstochowa, Poland

Doi: 10.12693/APhysPolA.144.356 *e-mail: konrad.gruszka@pcz.pl

In this paper, the impact of the extinction coefficient on electromagnetic wave transmission in a quasi-one-dimensional thin superlattice structure is investigated. The system consists of several layers of optical materials with different densities, and the focus is put on the transmission of light through this arrangement. Using theoretical modeling via the transfer matrix method, it is found that the extinction coefficient significantly influences transmission properties. Furthermore, the impact of altering the extinction coefficient of specific layers on the overall transmission behavior is investigated through systematic variations of the extinction coefficient and exploration of how changes in the optical properties of individual layers influence the transmission spectrum and the emergence of transmission peaks and valleys. These results provide valuable insights into the design and optimization of superlattice structures for various applications, including optical devices and photonic systems enabling precise light control.

topics: transfer matrix method, UV filters, tunable, electromagnetic (EM) propagation

1. Introduction

In the realm of optical materials and their intricate interactions with light, the optical extinction coefficient stands as a fundamental parameter that significantly influences light transmission behavior [1]. This coefficient characterizes the attenuation of light intensity as it traverses a material due to absorption and scattering processes. Its accurate determination is pivotal in understanding and engineering the optical response of various systems, ranging from thin films to multilayered structures [2–5]. By quantifying the rate at which electromagnetic energy is dissipated within a material, the extinction coefficient serves as a cornerstone in predicting the material's behavior across a wide spectral range. In this pursuit, computer simulations grounded in the transfer matrix method have emerged as a powerful analytical tool [6, 7]. Leveraging its prowess in modeling the propagation of light through layered media, this method offers an effective means to unravel the intricate interplay between material properties, layer thicknesses, and incident wavelengths.

In the context of thin superlattices, the impact of the extinction coefficient on light transmittance cannot be simply omitted. These systems, composed of alternating layers of different materials, exhibit unique optical characteristics driven by the layer material type and its spatial configuration, including thickness, refractive index, and optical extinction coefficient [8]. Fundamental studies elucidating the relationship between the extinction coefficient and light transmission in such intricate arrangements hold paramount significance. These investigations provide invaluable insights into the underlying mechanisms governing light–matter interactions, enabling the tailoring of optical responses for a myriad of applications ranging from advanced coatings and optical filters to photovoltaics and sensors. By comprehensively exploring the impact of the extinction coefficient on the propagation and behavior of light within thin superlattices, this study not only advances our understanding of fundamental optical principles but also lays the groundwork for the design and optimization of next-generation optical devices with enhanced performance and versatility.

In the present study, the capabilities of the transfer matrix method are used to explore the influence of the optical extinction coefficient on light transmission, shedding light on the nuanced interrelationships that underpin the optical performance of complex multilayer systems.

2. Computational methods

2.1. Transfer matrix and extinction coefficient

The transfer matrix method (TMM) [1, 9] provides a robust framework for analyzing the optical properties of multilayer systems, such as thin

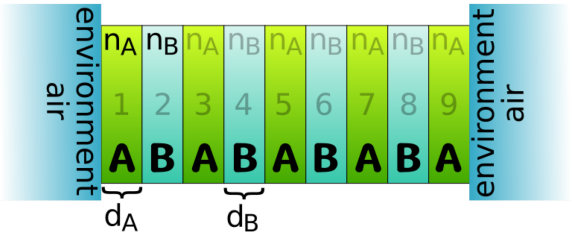

Fig. 1. Schematic diagram of studied superlattice; d_A and d_B represent layer thickness. The superlattice is submerged in $n = 1.0$ and $\kappa = 0$ environment.

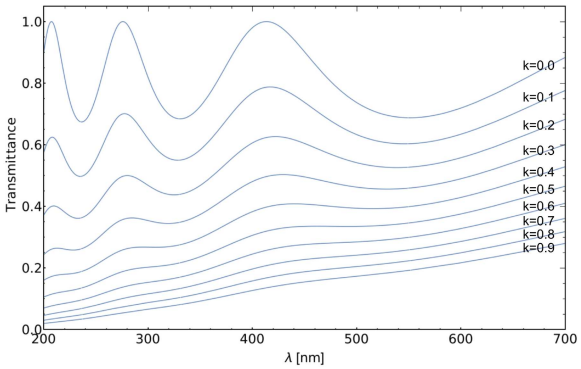

Fig. 2. The influence of layer B extinction coefficient κ increase on system transmittance.

superlattices. This method allows for the efficient calculation of the transmission and reflection coefficients by treating each layer within the system as a linear optical element [10]. The main equation of this method is as follows

$$\begin{bmatrix} E_{in}^{(+)} \\ E_{in}^{(-)} \end{bmatrix} = \Gamma \begin{bmatrix} E_{out}^{(+)} \\ E_{out}^{(-)} \end{bmatrix} \tag{1}$$

and describes incident wave $E_{in}^{(+)}$ incident on the boundary of the mediums, and $E_{in}^{(-)}$ is reflected wave propagating in an anti-parallel direction, $E_{out}^{(+)}$ is a wave coming out of the system, and the last term $E_{out}^{(-)}$ is zero. The characteristic matrix Γ defined as

$$\Gamma = D_{in,j}\Big(\prod_{j=1}^{J} P_j D_{j,j+1}\Big) \tag{2}$$

is a central component in the calculations. The characteristic matrix, also known as the transfer matrix, relates the incoming and outgoing electromagnetic fields at the interfaces between different layers. This matrix describes how the incident electric and magnetic fields are transformed as they propagate through the layer. By multiplying the characteristic matrices of all the layers in the multilayer structure, the overall transformation of the fields and the transmission and reflection coefficients for the entire structure can be calculated. In (2),

$$P_j = \begin{bmatrix} \mathrm{e}^{\mathrm{i}\varphi_j} & 0 \\ 0 & \mathrm{e}^{-\mathrm{i}\varphi_j} \end{bmatrix} \quad \text{and} \quad \varphi_j = d_j n_j \frac{2\pi}{\lambda} \cos(\phi_j) \tag{3}$$

describe all the parameters of the system, such as refractive indices n_j, quantities describing the physical dimensions (d_j) of incident wavelength λ and at layer incidence angle ϕ_j. In fact, $D_{j,j+1}$ is called the transmittance matrix. The optical extinction coefficient, represented by the imaginary component κ in the complex refractive index $n = n + \mathrm{i}\kappa$, plays a crucial role in elucidating the interaction between light and materials. As light traverses a medium, it undergoes absorption, leading to a reduction in intensity. This phenomenon is inherently captured by κ, which is responsible for the exponential decay observed in the propagation of light through a material, aligning with the principles outlined in the Beer–Lambert law. The relationship between κ and the absorption coefficient α is manifested in the expression $\alpha = 4\pi\kappa/\lambda_0$, where λ_0 is the vacuum wavelength, offering a direct quantification of the material's absorptive characteristics. Further insight into the penetration depth δp, the distance after which intensity diminishes by a factor of $1/\mathrm{e}$, reveals $\delta p = \lambda_0/(4\pi\kappa)$. Both the real part n and the imaginary part κ are frequency-dependent, with $\kappa > 0$ indicating absorption and $\kappa = 0$ implying lossless propagation.

2.2. System parameters

In the present calculations, the following materials were used for the multilayer system: material A, which is BK7 glass ($n = 1.5168$, $\kappa = 9.7525 \times 10^{-9}$), and material B, which is fused silica ($n = 1.45704$, $\kappa = 0$). The layer structure consists of 9 alternating layers in the form of $\{A, B, A, B, A, B, A, B, A\}$. The system is quasi-one-dimensional due to an infinite layer size in the X–Y directions, while the layer thicknesses d_A and d_B were kept fixed at 50 nm and 15 nm, respectively. Then, the extinction coefficient κ of layer B was systematically changed, and the transmission characteristics were calculated.

The schematic illustration of the studied system is presented in Fig. 1.

3. Results and discussion

Figure 2 presents the transmission for a set of structures, where the κ extinction coefficient was increased from $\kappa = 0.0$ to $\kappa = 0.9$ in 0.1 step size. Note that the extinction coefficients of all layers denoted as B were changed together uniformly. Also, the angle of incidence of the incoming electromagnetic wave is set to 45° to the plane of the first layer. In this case, there are two kinds of effects visible, namely a lowering in total transmission as κ increased and a simultaneous flattening of the peak

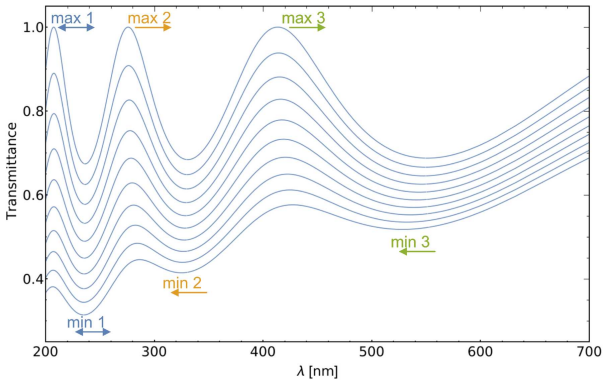

Fig. 3. Single *layer 2* extinction coefficient change from $\kappa = 0.0$ (top line) to $\kappa = 0.9$ (bottom line).

intensity. Obviously, because the extinction coefficient increases, the absorption of the electromagnetic wave of each B layer also increases, therefore, the last mentioned effect is the most expected behavior.

The aforementioned flattening of the transmittance peaks is less intuitive, as, in general, the formation of peaks and valleys is usually related to the geometrical parameters of the layers and their topological ordering. However, since the appearance of these local extremes is also associated with the phenomenon of reduced impact of constructive interference at the boundary of layers A and B, a strong influence of this phenomenon is observed when increasing the κ coefficient.

In order to investigate the effect of changing the extinction coefficient in a single layer from a multilayer system, in this step, only layer number 2 (for reference, please see Fig. 1) was modified, and the results of this modification are shown in Fig. 3.

Please note that, as in Fig. 2, the extinction coefficient also changes from $\kappa = 0.0$ to $\kappa = 0.9$; this time, however, the results differ. First, as in the case of changing the extinction coefficient in each layer B, a decrease in transmittance intensity is also observed this time. It is worth noting, however, that although the number of affected layers has decreased from 4 to just one layer, the total transmittance drops roughly by half, which is unexpected. Secondly, the positions of minima and maxima on the wavelength axis are shifting. It is also worth noting that although there is a flattening effect of the transmittance maxima, this effect is much less visible compared to the original change in the extinction coefficient for 4 layers simultaneously.

From the further analysis of Fig. 3, data on displacements of local extremes were collected and are presented in Fig. 4. As can be seen, not all local transmission maxima shift towards increasing wavelengths (the first maxima after $\kappa > 0.4$ changes its shift direction). The same applies to the minima positions, where the first minimum also changes its shift direction. This shows how complicated the na-

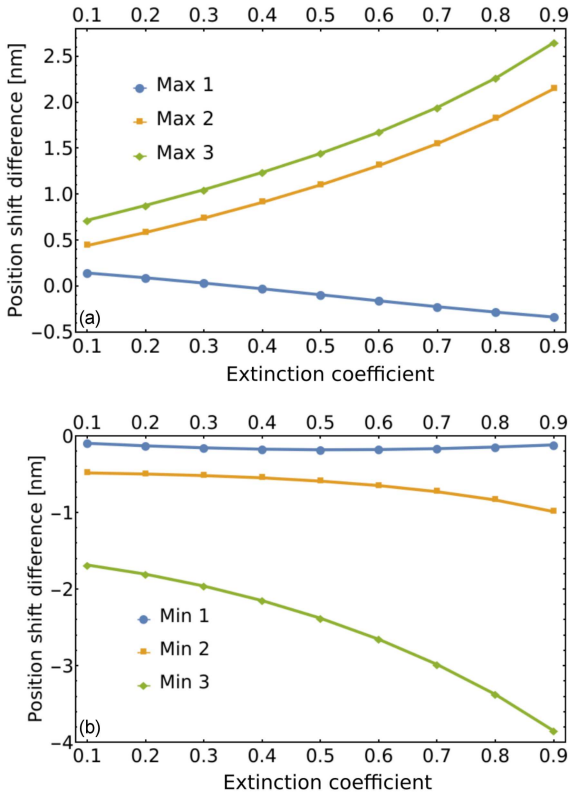

Fig. 4. The impact of increasing the coefficient κ on the change in the location of local transmission extremes.

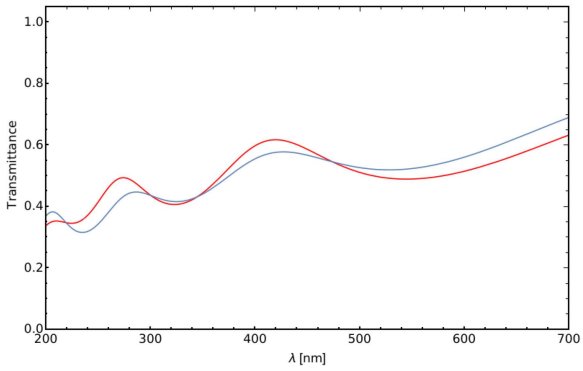

Fig. 5. Red line presents transmission spectra of the system with modified κ of layers 2 or 7; blue line is the transmission where κ of layers 4 or 6 is modified.

ture of the simple increase in wave absorption in one layer is introduced, while giving the possibility of quite precise tuning of the position of these extremes. In this study, the symmetry breaking of the modified layer was also investigated. In the next step, the number of layers in which the extinction coefficient increased was modified so that it now applied to layers $1, 2, 3$, or 4 (the fifth layer lies in the middle, therefore it was not considered this time). The results of this simulation are shown in Fig. 5.

Through the analysis of Fig. 5, it can be seen that modification of κ extinction coefficient results in the same transmission when layers 2 or 7 are set to the same value of κ. The same situation is when considering the change in layers 4 or 6. Therefore, the system maintains symmetry about the center (layer no. 5), while the difference in transmittance between the two curves is visible.

4. Conclusions

In this paper, a comprehensive investigation of the influence of the extinction coefficient on electromagnetic wave transmission in thin superlattices sheds light on the intricate relationship between the optical extinction coefficient and the transmission properties of these multilayer systems. Through meticulous computational analyses, we have unveiled several trends. Specifically, an increase in the extinction coefficient yields a noticeable flattening of the electromagnetic wave transmission profile across the superlattice structure. This phenomenon is accompanied by a proportional reduction in the overall transmittance of the system. Intriguingly, elevating the extinction coefficient, whether universally across all layers or within a single layer, introduces intricate shifts in the positions of local extreme transmission peaks. The nature of these shifts, while complex, underscores the intricate interplay between material properties and wave propagation dynamics. Notably, even a singular augmentation of the extinction coefficient of a solitary layer results in a substantial reduction in total transmission, underscoring the sensitivity of the system to such perturbations. Remarkably, the alteration of the extinction coefficient in a single layer induces modest shifts in the extreme peak positions, a characteristic that offers fine-tuning capabilities. Additionally, it was established that symmetrical adjustments to a single layer maintain the system's symmetry about its center. These findings collectively contribute to a deeper understanding of the interdependence between extinction coefficients and wave transmission within thin superlattices, paving the way for informed design strategies in the realm of advanced optical systems.

Acknowledgments

This research was supported in part by PLGrid Infrastructure.

References

[1] M. Born, E. Wolf, A.B. Bhatia, P.C. Clemmow, D. Gabor, A.R. Stokes, A.M. Taylor, P.A. Wayman, W.L. Wilcock, *Principles of Optics: Electromagnetic Theory of Propagation, Interference and Diffraction of Light*, 7th ed., Cambridge University Press, 1999.

[2] S. Garus, J. Garus, M. Szota, M. Nabiałek, K. Gruszka, *Arch. Mater. Sci. Eng.* **64**, 110 (2013).

[3] O.V. Penkov, I.A. Kopylets, V.V. Kondratenko, M. Khadem, *Mater. Design* **198**, 109318 (2021).

[4] Z.-H. Tang, Z.-S. Jiang, T. Chen, D.-J. Lei, J.-Q. Huang, F. Qiu, C.-Z. Jiang, M. Yao, X.-Y. Huang, *Phys. Lett.* **A382**, 3090 (2018).

[5] H. Han, B. Xiang, *Optik* **212**, 164691 (2020).

[6] L.C. Lohithakshan. P. Kannan, *Mater. Today Proc.* **66**, 1671 (2022).

[7] M. Asif, A. Afaq, M. Amin, K. Raouf, A. Majeed, M. Asif, *Mater. Today Commun.* **37**, 106966 (2023).

[8] Z. Huangfu, J. Wang, X. Cheng, S. Feng, Y. Liang, C. Yuan, X. Zhu, Z. Wang, H. Zhang, K. Yang, *J. Alloys Compd.* **961**, 170998 (2023).

[9] T.G. Mackay, A. Lakhtakia, *The TransferMatrix Method in Electromagnetics and Optics*, Springer International Publishing, 2020.

[10] M.C. Troparevsky, A.S. Sabau, A.R. Lupini, Z. Zhang, *Opt. Express* **18**, 24715 (2010).

Proceedings of "Applications of Physics in Mechanical and Material Engineering" (APMME 2023)

Theoretical and Experimental Studies of Thermomagnetic Properties of the $LaFe_{11.0}Co_{0.8}Si_{1.2}$ Alloy

P. Gębara*

Department of Physics, Czestochowa University of Technology, Armii Krajowej 19, 42-200 Częstochowa, Poland

Doi: 10.12693/APhysPolA.144.360 *e-mail: piotr.gebara@pcz.pl

In the present paper, the theoretical and experimental investigation of the thermomagnetic properties of the $LaFe_{11.0}Co_{0.8}Si_{1.2}$ alloys was conducted. The field dependences of magnetization in a wide range of temperatures were collected. Based on the thermomagnetic Maxwell's relation, the magnetic entropy change ΔS_M was calculated. Moreover, temperature dependences of magnetization in a wide range of fields were simulated using the phenomenological model. The values of thermomagnetic properties, such as magnetic entropy change and refrigeration capacity, were calculated.

topics: magnetic entropy change, relative cooling power (RCP), $La(Fe,Si)_{13}$-type alloys

1. Introduction

Nowadays, the protection of the natural environment and the reduction of energy consumption are extremely important. A lot of energy is used to lower temperature, i.e., in domestic refrigerators or air-conditioning systems. Most of them are based on compression/decompression of gases with a maximum efficiency of about 45%. A more effective method of lowering a temperature is magnetic refrigeration based on the magnetocaloric effect (MCE). MCE is observed in all magnetic materials and is characterized as temperature changes in magnetic material under an external magnetic field. MCE is measured as an adiabatic change in temperature ΔT_{ad} and also as an isothermal magnetic entropy change ΔS_M [1]. A natural magnetocaloric material is pure gadolinium with a Curie temperature of $\sim$ 296 K and magnetic entropy change of 10 J/(kg K) [2, 3]. Since the discovery of giant magnetocaloric effect in the $Gd_5Si_2Ge_2$ compound by Pecharsky and Gschneidner [4] in 1997, an exponential increase in the number of papers concerning this topic has been noticed.

Another interesting group of magnetocaloric materials is pseudobinary $La(Fe,Si)_{13}$-type alloys [5]. Their structure is based on a face-centered cubic lattice with an $Fm3c$ space group [6]. A subsequent substitution of La by Ce [7], Pr, Ho [8], Dy [9], or Fe by Co [10, 11], Ni [12], Mn [13, 14] causes modifications in Curie temperature and magnetic entropy change.

The thermomagnetic characteristics of the $LaFe_{11.0}Co_{0.8}Si_{1.2}$ alloy were intensively studied in [10, 11]. Due to its relatively good magnetocaloric properties, it was chosen to check the validation of the phenomenological model delivered in [15].

The aim of the present work was to simulate the magnetic entropy change and refrigeration capacity for the $LaFe_{11.0}Co_{0.8}Si_{1.2}$ alloy using the phenomenological model.

2. Experimental section

The ingot sample with nominal composition $LaFe_{11.0}Co_{0.8}Si_{1.2}$ was prepared by arc-melting of the high purity (min. 3 N) constituent elements under low pressure of protective gas Ar. The sample was remelted several times in order to ensure its homogeneity. Due to the evaporation of La during the process, the 5 wt% addition was used in order to compensate for the losses. Then, samples were sealed-off in quartz tubes under low pressure of Ar and annealed at 1323 K for 5 days. Phase structure was studied by Bruker D8 ADVANCE diffractometer with Cu K_α radiation and very fast semiconductor LynxEye detector. Thermomagnetic properties were studied using the magnetic properties measuring system MPMS XL 5 (Quantum Design) working in a wide range of temperatures and magnetic fields. The magnetic entropy change was calculated using magnetic isotherms and following Maxwell relation [4]

$$\Delta S_M(T, \Delta H) = \mu_0 \int_0^H \mathrm{d}H \left(\frac{\partial M(T,H)}{\partial T}\right)_H, \quad (1)$$

where μ_0, H, M, and T mean magnetic permeability of vacuum, strength of the magnetic field, magnetization, and temperature, respectively.

The *RCP* values were calculated based on ΔS_M vs T curves using the following equation [16]

$$RCP = -\Delta S_{M\,\max} \times \delta T_{\mathrm{FWHM}}, \tag{2}$$

where *RCP* is relative cooling power, and δT_{FWHM} is the full width at half maximum of magnetic entropy change peak.

3. Phenomenological model

M.A. Hamad, in the paper [15], proposed a phenomenological model according to which the temperature dependence of magnetization is given by the following formula

$$M = \left(\frac{M_i+M_f}{2}\right)\tanh\left[A\left(T_{\mathrm{C}}-T\right)\right] + BT + C, \tag{3}$$

where T_{C} is the Curie temperature, M_i and M_f are an initial and final value of magnetization at ferromagnetic–paramagnetic transition. The chosen points were marked in Fig. 1. Marked points were used during modeling. Constants A, B, C are described by equations

$$A = \frac{2\,(B - S_C)}{M_i - M_f}, \tag{4}$$

$$B = \frac{\mathrm{d}M}{\mathrm{d}T}, \tag{5}$$

$$C = \left(\frac{M_i-M_f}{2}\right) - BT_{\mathrm{C}}, \tag{6}$$

$$S_{\mathrm{C}} = \frac{\mathrm{d}M}{\mathrm{d}T} \quad \text{at} \quad T = T_{\mathrm{C}}. \tag{7}$$

Taking into account relations (1) and (3), the magnetic entropy change equation could be rewritten as follows

$$\Delta S_M = \left[-\frac{A\,(M_i-M_f)}{2}\mathrm{sech}^2\left(A\,(T_{\mathrm{C}}-T)\right)+B\right] H_{\max}. \tag{8}$$

Analyzing the relation (8), it is clear to seen that the value of magnetic entropy change rises with an increase in magnetization sensitivity $\mathrm{d}M/\mathrm{d}T$ at the Curie point. Large magnetic entropy change is related to the high magnetic moment and rapid change in magnetization at T_{C}. The maximum value of magnetic entropy change is given by

$$\Delta S_M = \left[-A\left(\frac{M_i-M_f}{2}\right) + B\right] H_{\max}. \tag{9}$$

TABLE I

Experimental and theoretical magnetocaloric properties of the $LaFe_{11.0}Co_{0.8}Si_{1.2}$ alloy under the change in external magnetic field ~ 5 T.

	ΔS_M [J/(kg K)]	δT_{FWHM} [K]	*RCP* [J/kg]
Experimental	12.95	25	320
Theoretical	13.59	40.5	550

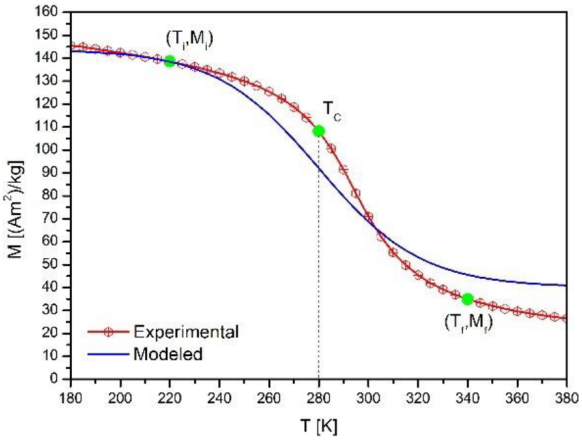

Fig. 1. Experimental and modeled temperature dependence of magnetization evaluated for the $LaFe_{11.0}Co_{0.8}Si_{1.2}$ alloy (under the change in magnetic field ~ 5 T).

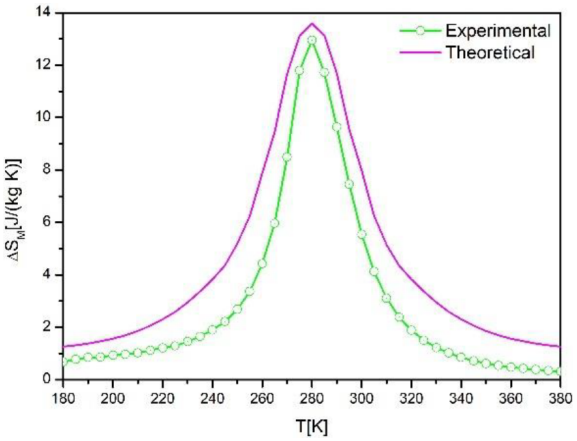

Fig. 2. Experimental and theoretically predicted magnetic entropy change for the $LaFe_{11.0}Co_{0.8}Si_{1.2}$ alloy.

Taking into account potential practical application, the *RCP* parameter is extremely important. In order to determine this parameter, it is required to calculate the full width at half maximum (FWHM) of magnetic entropy change according to the formula

$$\delta T_{\mathrm{FWHM}} = \frac{2}{A}\cosh^{-1}\left(\sqrt{\frac{2A\,(M_i-M_f)}{A\,(M_i-M_f)+2B}}\right). \tag{10}$$

An estimation of *RCP* is possible using relations (2), (9), and (10) in the following form

$$RCP = \left(M_i-M_f-2\frac{B}{A}\right) H_{\max} \times \cosh^{-1}\left(\sqrt{\frac{2A\,(M_i-M_f)}{A\,(M_i-M_f)+2B}}\right). \tag{11}$$

From the above equations, it was possible to reveal magnetocaloric properties, such as magnetic entropy change and relative cooling power, which are collected in Table I.

It is clearly seen in Fig. 1 that the modeled curve corresponds well with experimental dependence. The temperature dependence of magnetic entropy change revealed from experimental data and calculated using the phenomenological model is depicted in Fig. 2. Significantly higher values delivered by theoretical modeling are clearly visible. The differences are especially noticeable for the RCP ($\sim 70\%$) and full width at half maximum ($\sim 60\%$ higher).

The phenomenological model proposed by Hamad [15] delivers a simple way to predict magnetocaloric properties. Calculated values are reliable, reasonable, and comparable with experimental data.

4. Conclusions

The magnetocaloric properties of the $LaFe_{11.0}Co_{0.8}Si_{1.2}$ alloy were studied experimentally and using the phenomenological model. MCE was predicted indirectly by a calculation of magnetic entropy change based on magnetic isotherms. Prepared alloy manifests good properties and is an appropriate candidate for an active element in a magnetic refrigerator. Application of the phenomenological model to predict magnetization, magnetic entropy change, and relative cooling power delivered reliable and reasonable values of these parameters. Calculated values correspond well with experimental studies.

Acknowledgments

The Author would like to thank Professor Jan Świerczek, Head of the Department of Physics, Częstochowa University of Technology, for financial support.

References

[1] A.M. Tishin, Y.I. Spichkin, *The magnetocaloric effect and its applications*, CRC Press, New York, 2003.

[2] V.K. Pecharsky, K.A. Gschneidner Jr., *J. Magn. Magn. Mater.* **200**, 44 (1999).

[3] A. Diaz-Garcia, J.Y. Law, P. Gębara, V. Franco, *JOM*, **72**, 2845 (2020).

[4] V.K. Pecharsky, K.A. Gschneidner Jr., *Phys. Rev. Lett.* **78**, 4494 (1997).

[5] A. Fujita, Y. Akamatsu, K. Fukamichi, *J. Appl. Phys.* **85**, 4756 (1999).

[6] X.B. Liu, D.H. Ryan, Z. Altounian, *J. Magn. Magn. Mater.* **270**, 305 (2004).

[7] P. Gębara, J. Marcin, I. Skorvanek, *J. Electron. Mater.* **46**, 6518 (2017).

[8] P. Gębara, J. Kovac, *Mater. Des.* **129**, 111 (2017).

[9] P. Gębara, J. Kovac, *J. Magn. Magn. Mater.* **454**, 298 (2018).

[10] A. Yan, K.H. Muller, O. Gutfleisch, *J. Alloys Compd.* **450**, 18 (2008).

[11] P. Gębara, P. Pawlik, *J. Magn. Magn. Mater.* **442**, 145 (2017).

[12] P. Gębara, P. Pawlik, M. Hasiak, *J. Magn. Magn. Mater.* **422**, 61 (2017).

[13] P. Gębara, J. Marcin, *Acta Phys. Pol. A* **133,** 648 (2018).

[14] P. Gębara, M. Cesnek, J. Bednarcik, *Curr. Appl. Phys.* **19**, 188 (2019).

[15] M.A. Hamad, *Phase Transitions* **85**, 106 (2012).

[16] K.A. Gschneidner Jr., V.K. Pecharsky, *Annu. Rev. Mater. Sci.* **30**, 387 (2000).

Proceedings of "Applications of Physics in Mechanical and Material Engineering" (APMME 2023)

Influence of Arrangement for Elements of Bed to Flow and Heat Transfer

E. Szymanek[a,*] and P. Szymanek

Czestochowa University of Technology, 42-201 Czestochowa, Poland

Doi: 10.12693/APhysPolA.144.363 *e-mail: ewa.szymanek@pcz.pl

The article presents numerical simulations of the flow and heat transfer for beds with an ordered and shifted arrangement of elements. The numerical model applied is based on the unsteady equation of heat conduction (3D) and the Navier–Stokes equations. A high-order compact method in combination with the weighted essentially non-oscillatory scheme and predictor–corrector method is applied for the spatio-temporal discretisation. The flows of air and heat in the bed are modelled using the immersed boundary technique, which allows the use of Cartesian meshes for objects with very complex geometric shapes. The influence of the shift of elements in the bed on the temperature and velocity field was analysed. For two of the selected beds, the influence of arrangements of elements on the flow and heat exchange was analysed, which can lead, for example, to an improvement in the heating properties and to eliminating defects in the construction of reactor fillings.

topics: computational fluid dynamics (CFD) modelling, granular material, heat transfer

1. Introduction

Analysing the distribution of granulates in the beds, it can be concluded that numerical simulations of the flow in granular layers are carried out for configurations with both deterministic and random arrangements of elements. An example can be work [1], where pressure drops in a fixed bed of spheres in different arrangements are examined. In [2], the authors analysed the flow in a catalytic reactor with different types of arrangement of granular elements. In this case, a thorough understanding of flow dynamics is important, especially regarding the voids between bed elements. The aim of this work is to analyse heat flows through packed beds of granular materials using advanced numerical simulations and investigate to what extent changed arrangement elements can influence flow. The applied numerical model provides the temperature distributions and their variability over time inside the solid objects and around them. It is based on the unsteady equation of heat conduction (3D) and the Navier–Stokes equations for modelling the fluid flow between the layers made of solid objects. Complex structures of the beds are modelled using the immersed boundary technique (IB). The results of the analyses show that the structure of the layer and the size of the elements have a decisive influence on the flow parameters (pressure drop, mixing intensity, velocity). An innovative computational algorithm was used, which combined the IB method with a computational algorithm dedicated to the analysis of flows with a low Mach number. The use of the IB method allowed for simulations to be performed on Cartesian grids, which eliminated the need to generate computational grids adjusted to solid surfaces.

2. Mathematical model

Variable density, variable temperature, and low Mach number flows are described by the continuity equation, the Navier–Stokes equations, and the energy equation defined as

$$\partial_t \rho + \nabla \cdot (\rho \boldsymbol{u}) = 0, \tag{1}$$

$$\rho\Big(\partial_t \boldsymbol{u} + (\boldsymbol{u} \cdot \nabla)\, \boldsymbol{u}\Big) + \nabla p = \nabla \tau + f^{\mathrm{IB}}, \tag{2}$$

$$\rho C_p\Big(\partial_t T + (\boldsymbol{u} \cdot \nabla)\, T\Big) = \nabla \cdot (\kappa \nabla T) + f_T^{\mathrm{IB}}, \tag{3}$$

where ρ stands for the density, T — temperature, p — hydrodynamic pressure, $\boldsymbol{u}$ — velocity vector, C_p — heat capacity, and κ — heat conductivity. The set of three equations is complemented with the equation of state $p_0 = \rho RT$, where p_0 denotes the thermodynamic pressure, and R is the specific gas constant. In open flows with inlet/outlet boundaries, p_0 is constant in space and time [3], and in this work, it is assumed to be 101325 Pa. The molecular viscosity (μ) within the viscous stress tensor τ is computed from the Sutherland law.

2.1. IB-VP source term

The source terms f^{IB} and f_T^{IB} originate from the immersed boundary volume penalization approach (IB-VP). Their role is to penalize a difference between the actual and assumed velocity and temperature of the solid body. They act on a fluid in such a way as if there were solid objects immersed in the flow domain, and they are defined as

$$f^{\mathrm{IB}} = -\frac{\rho}{\eta}\,\Gamma(x)\big(\boldsymbol{u} - \boldsymbol{u}_s\big), \tag{4}$$

$$f_T^{\mathrm{IB}} = -\frac{\rho C_p}{\eta}\,\Gamma(x)\big(T - T_s\big), \tag{5}$$

where $\boldsymbol{u}_s$ and T_s are the velocity and temperature of the solid body, the parameter $\eta \ll 1$ is the so-called penalization parameter with a dimension of time unit, and Γ — the phase indicator defined as

$$\Gamma\,(x) = \begin{cases} 0, & \text{for } x \in \Omega_f, \\ 1, & \text{for } x \in \Omega_s, \end{cases} \tag{6}$$

where Ω_f and Ω_s are the regions of fluid and solid part of the computational domain. For $\Gamma(x) = 1$, discrete forms of (2) and (3) with the time step Δt reduce to $\boldsymbol{u}^* \approx \nabla(t\boldsymbol{u}_s)/(\eta + \Delta t)$ and $T^* \approx \nabla(tT_s)/(\eta + \Delta t^n)$, which for $\eta \ll \Delta t$ leads to $\boldsymbol{u}^* \approx \boldsymbol{u}_s$ and $T^* \approx \nabla(tT_s)$ Thus, the forcing terms enforce the no-slip boundary conditions and set the required temperature of the solid objects. The simplicity of the IB-VP method has, however, direct consequences in lowering solution accuracy. Similarly as in the classical IB method with a stepwise approach (i.e., without the interpolation [4]), the formal order of the IB-VP method is at most equal to one [5].

2.2. Solution algorithm

The solution algorithm for (1)–(3) is formulated in the framework of a projection method for pressure–velocity coupling. The time integration is based on a predictor–corrector approach (Adams–Bashforth/Adams–Moulton), and the spatial discretisation is performed using 6th/5th order compact difference and WENO (weighted essentially non-oscillatory) schemes on half-staggered meshes. The verification of the proposed model can be found, e.g., in work [6]. The validation of the method showed very good agreement of the results with exemplary data.

3. Numerical results and discussion

The main configuration is placed in the computational domain (box $0.05 \times 0.35 \times 0.05$ m^3) and consists of a layer of $10 \times 10 \times 10$ hot spheres with a temperature $T = 400$ K and diameter $D = 0.008$ m (Fig. 1). The spheres are separated by 0.0001 m. At the lower boundary, we assumed a uniform velocity of 0.1959 m/s and a temperature of

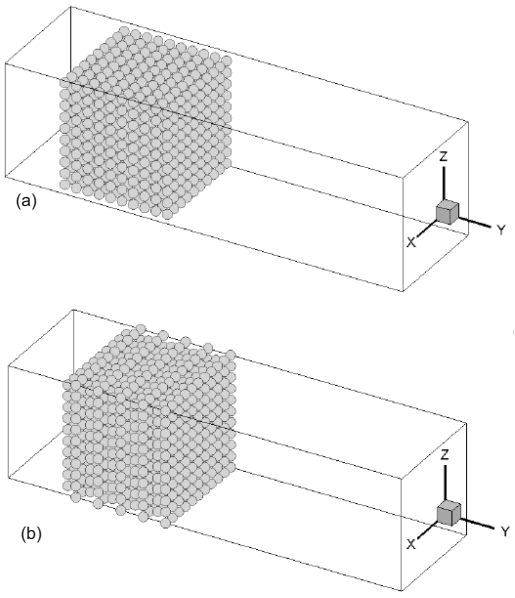

Fig. 1. Computational domain with: ordered bed — Config. 1 (a) and shifted bed — Config. 2 (b).

300 K (Re = UD/ν=100). The computations were performed with the use of a Cartesian mesh consisting of $137 \times 480 \times 137$ nodes.

Additionally, we consider configuration, which differs in distribution of the spheres. In the configuration denoted as Config. 2, there are $N = 10 \times 10 \times 10$ spheres, in which alternate layers are shifted towards the centres of the preceding layer.

Figure 2 shows contour plots showing temperature and velocity distributions in the central plane of the beds. It can be observed that the flow is clearly faster in the intergranular spaces for configuration denoted as Config. 1. Where air hits the spheres, the flow slows down. This creates recirculation zones that lead to more heat transfer. The situation is different in the case of Config. 2 with shifted spheres. In this case, no rapid increase in velocity is observed because there is no empty space for an undisturbed stream between the spheres. It turns out that the accelerating fluid in the intergranular space of one layer is inhibited by the spheres of the next layer. However, as a result, the mixing process is very intense, which favours rapid heat transfer. This can also be seen in Fig. 3, where the distributions of vectors for both configurations are presented. As the fluid gets hotter, its density decreases, and the forced fulfilment of the law of conservation of mass causes its velocity to increase. It can be seen that in the case of shifted layers, the velocity at the ends of the layers is much higher compared to their initial values. Nevertheless, the locally highest velocity values were recorded for the ordered configuration, where the medium could move with little disturbance.

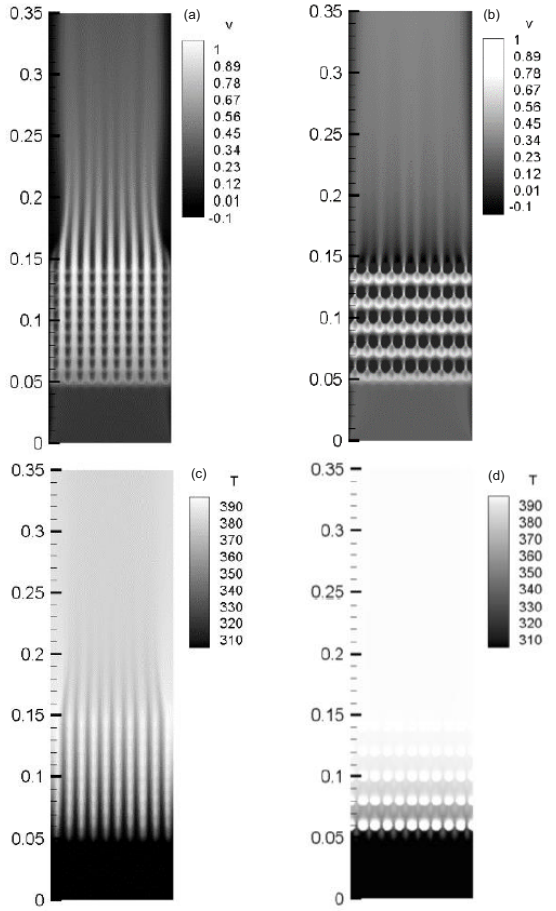

Fig. 2. (a, b) Velocity and (c, d) temperature distribution on the planes from the middle part of the bed: Config. 1 on the left and Config. 2 on the right, along y direction.

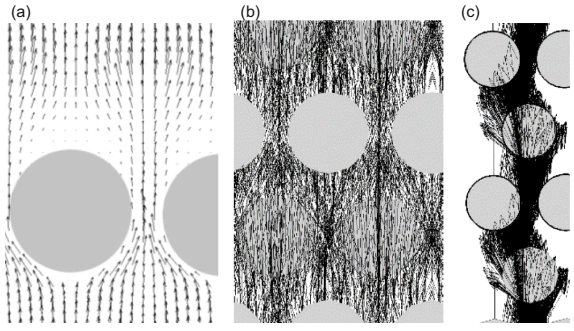

Fig. 3. Vector distribution around ordered (a) and shifted (b, c) bed spheres.

Figure 4 shows the velocity, temperature, pressure and vorticity profiles along the bed height (y direction). The values presented in the graphs have been averaged in the x–z planes and normalized by the input values. In both cases, there is a rapid rise in temperature. However, already in the first part of the bed, differences in temperature values can be seen, which persist until the end of the domain.

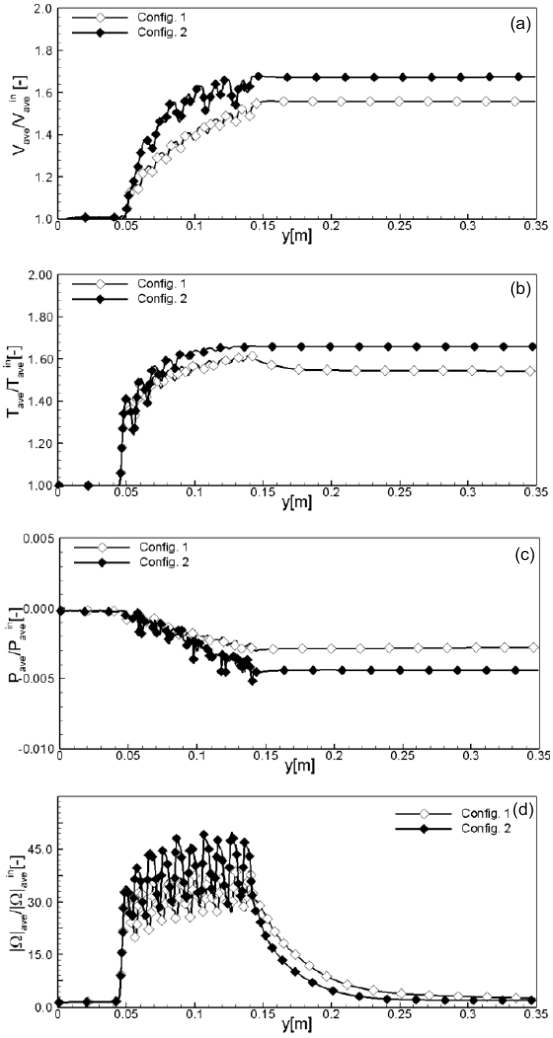

Fig. 4. (a) Spatially averaged velocity, (b) temperature, (c) pressure, and (d) vorticity profiles along the computational domain.

In the initial section of the layers, the fluid heats up with varying intensity, which is manifested by the wavy shape of the profiles. Significant differences can also be observed in the velocity profiles. The vorticity profiles show a very non-uniform flow field. In both cases, the vorticity between the individual layers changes rapidly and reaches significantly higher values in the "shifted" bed (Config. 2). Hence, it can be concluded that higher vorticity values mean areas with increased mixing intensity, and therefore the heat exchange taking place in such configurations is the most effective.

4. Conclusions

The paper presented numerical studies on the heat and flow transfer in the layers of spheres for ordered arrangement and shifted distributions. An

advanced numerical method based on high-order discretisation combined with the immersed boundary (IB) method was applied. The applied model allowed for deep analysis of the flow and temperature distributions between the spheres and above the layers. It was shown that it characterises a very complex structure and that the configuration of the layer significantly affects the effectiveness of the mixing and heat transfer. It was found that even a small interference in the arrangement of the bed elements (shift) can result in an improvement in the heating properties.

References

[1] S. Ahmadi, F. Sefidvash, *Chem. Eng. J.* **2**, 14 (2018).

[2] H.P.A. Calis, J. Nijenhuis, B.C. Paikert, F.M. Dautzenberg, C.M. van den Bleek, *Chem. Eng. Sc. J.* **56**, 1713 (2011).

[3] A. Tyliszczak, E. Szymanek, *Num. Heat Tr. Part. A* **76**, 737 (2019).

[4] E.A. Fadlun, R. Verzicco, P. Orlandi, J. Mohd-Yusof, *J. Comp. Phys.* **161**, 35 (2000).

[5] B. Kadoch, D. Kolomenskiy, P. Angot, K. Schneider, *J. Comp. Phys.* **231**, 4365 (2012).

[6] E. Szymanek, A. Tyliszczak, *Tech. Mech.* **39**, 85 (2019).

Proceedings of "Applications of Physics in Mechanical and Material Engineering" (APMME 2023)

Numerical Modeling of the Influence of Flat Solar Collector Design on Its Thermal Efficiency with the Use of Fractional Calculus

P. Szymanek*

Czestochowa University of Technology, 42-201 Częstochowa, Poland

Doi: 10.12693/APhysPolA.144.367 *e-mail: przemyslaw.szymanek@pcz.pl

The present study is dedicated to the issue of the operation of flat plate solar collectors with different tube cross-sections and different absorbers. Here, the flow of the working medium is analyzed in order to assess the influence of the type of tube cross-section and the type of absorber on the thermal parameters of the installation. Numerical tests were carried out on full-scale simulations with the use of Ansys Fluent software. The analysis showed that the efficiency of the system can be significantly improved by installing an appropriate absorber system. The results also show that changing the thickness and type of material the absorber is made of has a large impact on the efficiency of the collector. In this paper, to describe the phenomenon in question and to verify the obtained data, a mathematical model based on fractional order differential calculus is proposed. After comparing the flow of the working medium through collectors with different tube cross-sections with different types of absorbers, it was shown that the best results were obtained for a collector with a circular cross-section of tubes and an absorber made of copper with a thickness of 0.5 mm.

topics: flat plate solar collector, thermal efficiency, computational fluid dynamics, fractional calculus

1. Introduction

The most popular and most frequently tested and modernized type of solar collectors are flat plate collectors. There are many studies in the literature devoted to investigating the influence of the shape of the pipe on the operation of a flat plate collector. The use of triangular pipes allowed to increase the temperature of the water at the outlet. Authors of [1] compared round and elliptical pipes and found that the round pipe provides the maximum temperature of the water at the outlet with the same heat flux and inlet temperature. Numerical methods based on CFD (computational fluid dynamics) models are used to analyze phenomena occurring in solar collectors. Tests are generally performed using commercial Ansys Fluent software. The paper attempts to verify numerical data with a model based on fractional differential calculus. The growing interest in this method in various fields of engineering and science is mainly due to the possibility of obtaining accurate mathematical models of real objects, with particular emphasis on models with memory properties. Karayer et al. [2] introduced the fractional method for some aspects of quantum mechanics. Jena et al. [3] showed that the damping characteristics when solving the damped beam equation are well defined by the fractional derivative and solved the model of the large membrane vibration equation using Caputo derivatives. This description does not go into structure, but assumes a degree of heterogeneity. Using an ordinary differential equation containing a combination of left-hand and right-hand derivatives of fractional order, we obtain a model without penetration of the structure and without such a number of coefficients. Equations of this type are obtained by modifying the principle of least action and applying the principle of fractional integration by parts. The results obtained on the basis of the proposed model were used to verify the calculations carried out using the Ansys Fluent program. Based on the obtained results, it can be concluded that changes in these parameters significantly affect the thermal efficiency of the systems.

2. Fractional model

2.1. Fractional differential equations

Due to the complex character of the heat and mass flow processes, it becomes necessary for such processes to use the appropriate mathematical models describing the individual processes taking place in the course of the flow working medium. This paper used an ordinary differential equation containing a composition of left- and right-sided fractional order derivatives considered within a limited area [4].

We consider an ordinary fractional differential equation with the composition of left and right Caputo derivatives of order $\alpha \in (0,1)$ in the following form

$$ {}^{C}D^{\alpha}_{a+}\,{}^{C}D^{\alpha}_{b-}T(x) - \lambda T(x) = 0, \qquad x \in [a,b], \tag{1}$$

where the fractional derivatives have following forms [5]

$$ {}^{C}D^{\alpha}_{a+}T(x) = \frac{1}{\Gamma(1-\alpha)} \int_{a}^{x} \mathrm{d}\tau \; \frac{T'(\tau)}{(x-\tau)^{\alpha}}, \tag{2}$$

$$ {}^{C}D^{\alpha}_{b-}T(x) = -\frac{1}{\Gamma(1-\alpha)} \int_{x}^{b} \mathrm{d}\tau \; \frac{T'(\tau)}{(\tau-x)^{\alpha}}. \tag{3}$$

Now, (1) is supplemented by the following boundary conditions $T(a) = Ta, T(b) = Tb$.

2.2. Numerical solution

The form of the analytical solution of the considered equation is complicated and cannot be applied to the model. Therefore, the equation is discretized. We introduce homogenous grid $a = x_0 < x_1 < \ldots < x_i < x_{i+1} < \ldots < x_n = b$, where $x_i = i\Delta x$ and $\Delta x = (b-a)/n$. Then we write (1) with the boundary conditions consistent with [5] in the discrete form

$$\begin{aligned} &T_a = Ta, \qquad\qquad T = Tb, \\ &\sum_{k=i}^{n} \left[v(n-i, n-k) \sum_{j=0}^{k} v(k,j) T_j \right] + \lambda T_i = 0, \end{aligned} \tag{4}$$

for $i = 1, \ldots, n-1$; where T_i is a value of the function T at the node x_i and coefficients v are given by the formula

$$ v(i,j) = \frac{(\Delta x)^{\alpha}}{\Gamma(2-\alpha)} \times \begin{cases} -i^{1-\alpha} + (i-1)^{1-\alpha}, & \text{for } j = 0; \\ (i-j+1)^{1-\alpha} - 2(i-j)^{1-\alpha} + (i-j-1)^{1-\alpha}, & \\ & \text{for } j = 1, \ldots, i-1; \\ 1, & \text{for } j = 1. \end{cases} \tag{5}$$

3. Numerical results and discussion

In addition, it was checked how the proposed calculation method translates into the accuracy of the results obtained for flow problems, taking into account heat transfer. The test case was selected to reflect the flow phenomena occurring in the pipe in the solar collector, i.e., recirculation zones, stagnation points, and interactions between vortices formed around pipe bends. The simplicity of the selected configurations allowed for the preparation of body-fit meshes that were needed for the calculations performed using the Ansys Fluent code. The calculations performed in the Ansys Fluent program were conducted using the second-order discretization method on tetrahedral meshes fitted to the body, accurately reflecting the shapes of the objects. The results obtained from the Ansys Fluent code with the proposed calculation method and the literature numerical results [6] practically overlap (see Fig. 1), which means that their accuracy is very good.

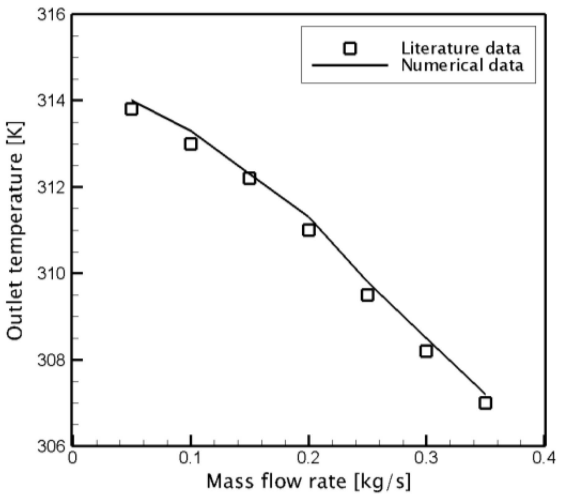

Fig. 1. Comparison of the results obtained using the Ansys Fluent with the literature data [6].

3.1. Influence of tube flattening on the thermal efficiency of collectors

In order to investigate the influence of the tub cross-section shape on heat transfer in flat plate solar collectors, three models with different tube shapes were designed. All configurations were simulated under constant Reynolds number, inlet fluid temperature, and solar radiation.

Figure 2 shows the changes in water temperature along the tube. The collector with a circular cross-section tube had the best performance as it exhibited the lowest velocities, which reduced pressure drop and improved ambient heat transfer to the fluid.

3.2. Comparison of the results of the numerical model and the mathematical model

In this part, a comparison of the proposed model with the results of numerical calculations using the Ansys Fluent program is presented. As shown in Fig. 3, for the circular cross-section of the tube, the results based on the mathematical model differ only slightly from the results of the numerical simulation. We can see that most of the deviations were at a similar level.

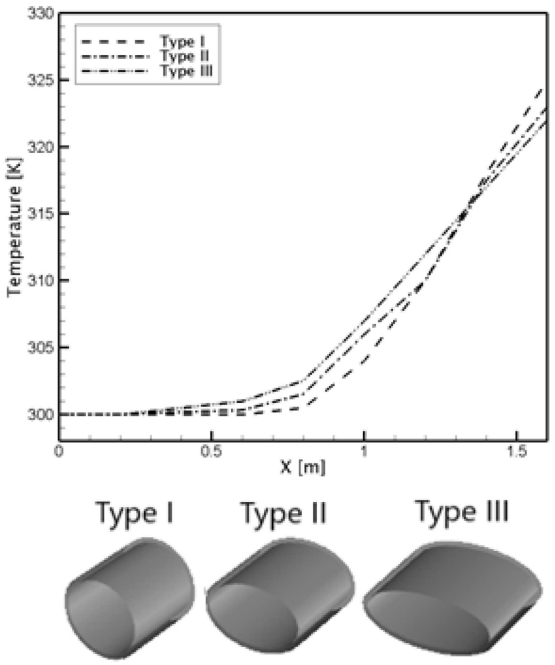

Fig. 2. Temperature profiles in the three tubes under consideration.

Depending on the measuring point, the results are overestimated and underestimated in relation to the numerical data. These fluctuations did not occur regularly, and therefore, their origin could not be identified. Generally, when comparing the numerical data with the results of the fractional model, it can be noticed that the differences are small. The method proposed in the paper allows for the modeling of actual temperature changes inside the collector tube and for the analysis of the temperature distribution inside the tubes.

3.3. Thermal efficiency

The further part of the work focuses on the calculations of the efficiency of collectors with selected pipe cross-sections. The round tube collector (Type I) has proven to be the most efficient collector type. In fact, the efficiency of the collector is reduced by the greater flattening of the cross-section. This is because convective heat transfer is very low for non-circular ducts. The round tube collector is 6.5% and 13% more efficient than Type II and Type III elliptical collectors, respectively. For further research, the collector with the best efficiency (Type I) was selected, and it was

analyzed whether and what impact the thickness of the absorber and the material it is made of have on the thermal efficiency. The efficiency of the collector increases with the thickness of the absorber, e.g., when the thickness is increased from 0.1 to 0.6 mm, the efficiency increases by up to 15%, which results from the greater resistance with a greater thickness of the absorber and, thus, lower

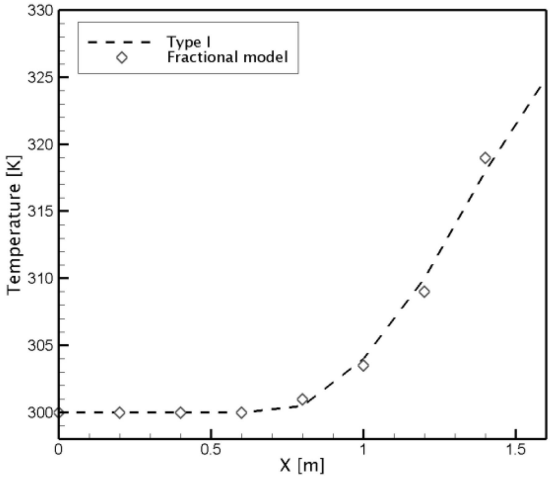

Fig. 3. Comparison of the numerical solution of Ansys Fluent with numerical solution of (1).

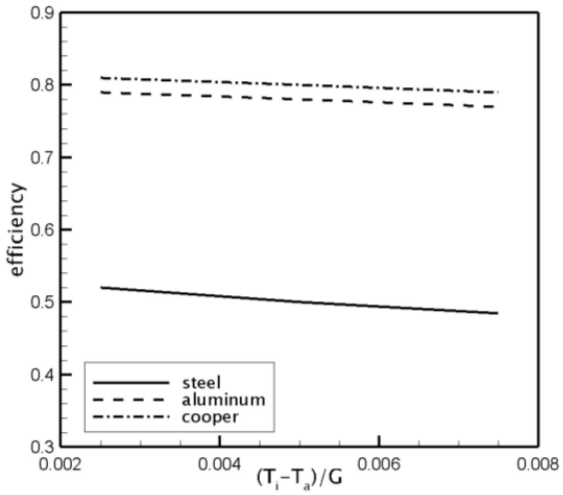

Fig. 4. Collector efficiency of various absorber materials.

heat transfer. One of the most important components of a solar collector is the absorber plate, which absorbs the sun's energy and transfers the heat to the pipes and fluid. Absorber plates made of copper, aluminum, and steel with different thermal properties were compared, and the results are presented in Fig. 4. The efficiency of the copper absorber is 3.4% and 35% higher than that of the aluminum absorber and the steel one, respectively.

4. Conclusions

A three-dimensional numerical simulation was carried out to investigate the efficiency of the flat plate solar collector. Commercial Ansys Fluent software was used to numerically solve the equations of fluid flow and heat transfer. The results showed that the collector with circular ascension tubes is more

efficient than the collectors with the elliptical cross-section of the tubes. It was shown that Type I section collector had the best efficiency, where the fluid reached temperatures higher up to 324.8 K at the exit of the tube and achieved an efficiency of 62%, higher than Type II and Type III, which showed an efficiency of 58 and 55%, respectively. Moreover, the thermal efficiency of the collectors significantly changed with the change of the absorber material (the best efficiency for copper and aluminum). The thickness of the absorber also had a great influence, having a significant effect up to a thickness of 0.6 mm. The obtained results of the temperature distribution for the selected case (Type I) correspond to those estimated by the mathematical model. In the obtained distributions, as compared to (1), the differences in temperature values were consistent with the results estimated with the mathematical model. The use of fractional differential equations as a mathematical description of a complex system has the advantage that it does not require detailed information about the analyzed system. The results presented in the paper show that the proposed model describes the temperature profiles well.

References

[1] V. Shelke, C. Patil, *Int. J. Sci. Eng. Res.* **3**, 118 (2015).

[2] H. Karayer, D. Demirhan, F. Büyükkılıç, *Comun. Theor. Phys.* **66**, 12 (2016).

[3] R.M. Jena, S. Chakraverty, S. Kumar Jena, *J. Appl. Comput. Mech.* **5**, 355 (2019).

[4] E. Szymanek, T. Blaszczyk, M.R. Hall, P. Keikhaei Dehdezi, J.S. Leszczynski, *Granul. Matter* **16**, 687 (2014).

[5] O.P. Agrawal, *J. Math. Anal. Appl.* **272**, 368 (2002).

[6] J.A. Rangababu K.K. Kumar, S.S. Rao, *Proc. Eng.* **127**, 63 (2015).

Proceedings of "Applications of Physics in Mechanical and Material Engineering" (APMME 2023)

Calorimetric Analysis of Grain Modified Mg–Li Alloy

M. Król*

Department of Engineering Materials and Biomaterials, Faculty of Mechanical Engineering, Silesian University of Technology, Konarskiego 18a Str., 44-100 Gliwice, Poland

Doi: 10.12693/APhysPolA.144.371 *e-mail: mariusz.krol@polsl.pl

Nowadays calorimetric analysis is a widely used method to study phase transformations occurring in the liquid or solid state in metals and alloys. Information on enthalpy, kinetics and transition characteristics can be obtained with the appropriate configuration of analytical apparatus and establishment of test procedures. In this work, an analysis of the transitions taking place in the grain-modified dual phase α(Mg) + β(Li) Mg–9Li–1.5Al alloy was carried out on the samples taken from casts. The latent heat of the analysed alloys was captured using the UMSA device. The solidification process has been analysed using cooling curve analysis. The latent heat at a natural cooling rate 0.5°C/s was calculated based on the first derivative of the cooling curve. The released latent heat during crystallisation was estimated by applying the Newtonian technique of baseline. The results confirmed that calorimetric analysis can be successfully applied to study phase transitions in this type of magnesium alloy. The work uses thermal derivative analysis to present the possibility of specifying the latent heat of modified ultralight Mg–Li cast alloys.

topics: latent heat, thermal derivative analysis (TDA), grain modification, Mg–Li alloy

1. Introduction

Thermal analysis (TA) of magnesium alloys is a field of materials science that focuses on studying the thermal behavior and properties of magnesium-based materials. It focuses on the application of various techniques to analyze how magnesium alloys respond to changes in temperature, including their phase transformations, thermal stability, and thermal expansion characteristics. Thermal analysis techniques commonly used for studying magnesium alloys include [1–7]:

- **Differential scanning calorimetry (DSC)** DSC measures the heat flow into or out of a sample as a function of temperature. It can detect phase transitions such as melting, solidification, and precipitation reactions, providing information about the alloy's thermal behavior and energy changes.
- **Thermogravimetric analysis (TGA)** TGA measures the change of sample weight as a function of temperature. It can be used to study processes like oxidation, desorption of gases, and decomposition reactions in magnesium alloys.
- **Differential thermal analysis (DTA)** DTA measures the temperature difference between a sample and a reference material as they are subjected to a controlled temperature program. It can identify phase transitions, crystallization and other thermal events.
- **Thermo-mechanical analysis (TMA)** TMA measures the dimensional changes of a sample as a function of temperature. It provides information about the coefficient of thermal expansion (CTE) and thermal deformation behavior of magnesium alloys.

By examining the derivative of a property, thermal derivative analysis (TDA) provides information about thermal events occurring in a material, such as phase transitions, crystallization, decomposition, and other thermal effects. It can help identify characteristic temperatures associated with these events, including onset temperatures, peak temperatures, and completion temperatures [8–15].

This data is useful for understanding the characteristics and behavior of materials in various fields, including materials science, chemistry, and engineering. TDA is commonly employed in research, quality control and product development processes [16, 17].

These thermal analysis techniques allow researchers to characterize the thermal properties of magnesium alloys, understand their phase transformations, evaluate their thermal stability, and optimize their processing conditions. This information is crucial for designing and engineering magnesium alloys for various applications, including automotive, aerospace and consumer electronics, where thermal performance and reliability are important factors [18, 19].

TABLE I

Chemical composition [wt%] of analysed alloys.

Alloy	Li	Al	Si	B	Ti	Sr
Mg–9Li–1.5Al	8.99	1.72	–	–	–	–
Mg–9Li–1.5Al + 0.2TiB	8.93	2.1	0.031	0.0012	0.0067	–
Mg–9Li–1.5Al + 0.2Sr	8.37	1.83	0.065	–	–	0.026
Mg–9Li–1.5Al + 0.2TiB + 0.2Sr	8.72	1.78	0.051	0.0020	0.011	0.025

2. Research methodology

In the preparation of Mg–Li alloys, the following steps were taken:

1. selecting high-purity magnesium (Mg) and lithium (Li) metals with minimal impurities to ensure the desired alloy properties,
2. melting at 720°C in a furnace capable of withstanding the high temperatures required to melt magnesium,
3. preheating the crucible to minimize oxidation,
4. adding measured quantities of Mg and Li into the crucible and heating up till the metals melt,
5. stirring the molten mixture to ensure proper mixing and homogenization,
6. pouring the molten alloy into suitable molds.

The analysis of the chemical composition of the alloy was performed using ICP-OES Optima 5300 V, made by PerkinElmer. The chemical composition of the analysed composites is presented in Table I.

A test sample had dimensions of 18 mm (diameter) and 20 mm (height). The K-type thermocouple was placed at the center of the sample height and linked to the personal computer with high-speed National Instrument data acquisition system (UMSA) [18–20].

The cooling conditions were kept constant during experiments, i.e., melting temperature 700°C, argon atmosphere, holding time 90 s, cooling rate 0.5°C/s. Every TA trial was repeated three times. To increase the precision of the data without distorting the signal tendency, the achieved cooling curve was smoothed by a Savitzky–Golay digital filter.

The latent heat of crystallization of the alloys was determined from the equation [21–23]

$$Q = m\, c_p \int_{t_N}^{t_{sol}} \mathrm{d}t \left[\frac{\mathrm{d}T}{\mathrm{d}t} - \left(\frac{\mathrm{d}T}{\mathrm{d}t} \right)_c \right]. \tag{1}$$

3. Results

In the presented work, thermal-derivative analysis was applied to register cooling curves and calculate their corresponding first derivatives of the investigated Mg–Li alloys.

TABLE II

Thermal characteristics of the analysed alloys.

Heat capacity	Liquid state		Solid state	
c_{p_l} [J/(g °C)]	1.498		1.248	
Analysed alloy	Mg-9Li-1.5Al	Mg–9Li-1.5Al+0.2 TiB	Mg–9Li–1.5Al+0.2Sr	Mg–9Li–1.5Al+0.2TiB+0.2Sr
Latent heat of sample, Q [J]	860	1082	1477	1247
Latent heat per gram [J/g]	157.5	161	171	159.6

The literature shows that the thermal and thermodynamic data are unavailable for the ultra-light Mg–Li grain modified alloys. Moreover, the presented paper analysed the influence of grain modifiers on the latent heat released during the crystallisation process of the α(Mg) + β(Li) Mg–9Li–1.5Al alloy.

Figure 1 presents the thermal-derivative curves of the grain-modified Mg–9Li–1.5Al alloy with the corresponding crystallisation curves and baselines on which characteristic points can be identified. Those characteristic peaks reflect the observed phase changes corresponding to the transformation of liquid metal during crystallisation.

Peak T_L (see Fig. 1b, c and b) is related to the initial time of the nucleation process and the growth of the α(Mg) + β(Li) phase, which lasts up to temperature T_s, where crystallization of the melt ends and the solid phase volume reaches 100%. Between the liquidus and solidus temperatures, a slightly visible peak T_η can be noted. This event represents the formation of the η phase, which is related to the precipitation of the lithium–aluminium phase (LiAl) [23].

It can be seen that the shape of the cooling curves strongly depends on the grain modifiers used in the investigated magnesium–lithium alloys.

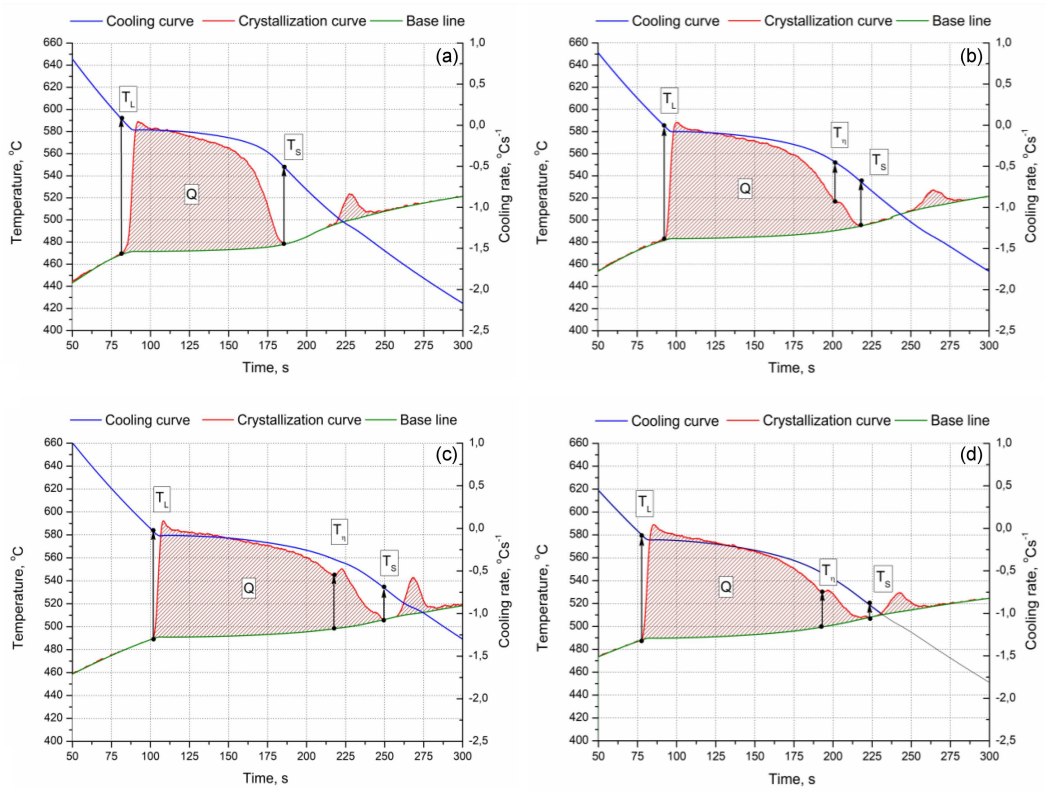

Fig. 1. Thermal analysis of (a) Mg–9Li–1.5Al, (b) Mg–9Li–1.5Al + 0.2TiB, (c) Mg–9Li–1.5Al + 0.2Sr, (d) Mg–9Li–1.5Al + 0.2TiB + 0.2Sr.

The thermal analysis presents that the addition of 0.2 wt% TiB and Sr affects the beginning of the nucleation of $\alpha(\mathrm{Mg}) + \beta(\mathrm{Li})$ from 596 to 579°C and the duration of the crystallisation process from 47 to 59°C of the investigated alloys.

Strontium significantly influences the shape of crystallisation curves. The addition of Sr decreases the nucleation and the solidus temperature from 596 to 587°C and 549 to 536°C, respectively.

The analysis of the obtained results indicates that adding modifiers in the form of TiB or Sr is responsible for the additional exothermic peak T_η generated by the nucleation and crystallization of the intermetallic phase η(LiAl). Nucleation of the intermetallic phase η(LiAl) occurs at 552°C, 559°C, and 546°C for Mg-9Li–1.5Al + 0.2TiB, Mg–9Li–1.5Al + 0.2Sr, and Mg–9Li–1.5Al + 0.2TiB + 0.2Sr alloys, respectively. In the case of nucleation of the η(LiAl) phase, the addition of TiB has the most significant influence.

The calculated latent heat of the investigated grain-modified Mg–9Li–1.5Al alloy has been presented in Table II. The study revealed that the alloy with the addition of Sr has a higher latent heat, and the TiB content has some impact on the amount of released latent heat, but is not as significant as Sr.

The highest latent heat was generated by the alloy Mg–9Li–1.5Al modified with Sr and was equal to 171 J/g. The addition of TiB causes an increase in the total enthalpy to 161 from 157 J/g. The addition of the modifiers TiB and Sr also causes an increase in the total heat of enthalpy to approximately 159 J/g.

The presented results show that the thermal derivative analysis carried out by the UMSA device can be an extremely helpful tool for calculating thermal and thermodynamic data of ultra light Mg–Li grain-modified alloys. Appropriate numerical calculations based on the obtained test results can be successfully used in the application of artificial neural networks to determine individual parameters of the crystallisation process on the course, as well as the proportion of the solid fraction and the volume of the generated latent heat. The results indicate that the use of the UMSA device can decrease the costs of research concerning the crystallisation of metal alloys by eliminating the necessity to use specialised and expensive testing apparatus.

4. Conclusions

The thermal derivative analysis of the grain-modified Mg–9Li–1.5Al alloy with TiB and Sr and the thermal behavior was investigated.

The following conclusions can be drawn:

- TiB and Sr control the solid fraction and temperature of the nucleation of the η(LiAl) phases and the influence the amount of latent heat released.

- Additions of grain modifiers cause changes in the crystallization process, i.e., the beginning of nucleation and the solidus temperatures.
- Application of Sr as a modifier leads to significant increase of the generated latent heat $\approx 10\%$.

References

[1] S. Luo, L. Wang, Y. Cao, *J. Therm. Anal. Calorim.* **148**, 4049 (2023).

[2] J. Li, R. Chen, Y. Ma, W. Ke, *Thermochim. Acta.* **590**, 232 (2014).

[3] M.A. Malik, K. Majchrzak, K.N. Braszczyńska-Malik, *Arch. Foundry Eng.* **12**, 109 (2012).

[4] S. Farahany, H. Ghandvar, *J. Therm. Anal. Calorim.* **148**, 5247 (2023).

[5] Y. Gan, L. Hu, L. Shi, Q. Chen, M. Li, L. Xiang, T. Zhou, *Trans. Nonferrous met. Soc. China* **33**, 1373 (2023).

[6] Z. Zhao, Z. Sun, W. Liang, Y. Wang, L. Bian, *Mat. Sci. Eng. A-Struct.* **702**, 206 (2017).

[7] M.B. Djurdjevic, *Metall. Mater. Eng.* **27**, 457 (2021).

[8] H. Şevik, S.C. Kurnaz, *J. Magn. Alloys* **2**, 214 (2014).

[9] S. Erturk, L. Kumruoglu, A. Ozel, *Acta. Phys. Pol. A* **131**, 370 (2017).

[10] S.M. Liang, R.S. Chen, J.J. Blandin, M. Suery, E.H. Han, *Mater. Sci. Eng.* **480**, 365 (2008).

[11] R. Sudheer, K.N. Prabhu, *Mater. Des.* **95**, 198 (2016).

[12] E.M. da Costa, C.E. da Costa, F.D. Vecchia, C. Rick, M. Scherer, C.A. dos Santos, B.A. Dedavid, *J. Alloys Compd.* **488**, 89 (2009).

[13] B. Jeż, P. Postawa, M. Nabiałek, *Bull. Pol. Acad. Sci. Tech. Sci.* **71**, e144608 (2023).

[14] B. Jeż, M. Nabiałek, *Bull. Pol. Acad. Sci. Tech. Sci.* **71** e144163 (2023).

[15] P. Rezaei-Shahreza, H. Redaei, P. Moosavi, S. Hasani, A. Seifoddini, B. Jeż, M. Nabiałek, *Arch. Metall. Mater.* **67**, 251 (2022).

[16] G. Golański, A. Zieliński, M. Sroka, J. Słania, *Materials* **13**, 1297 (2020).

[17] H. Purzyńska, G. Golański, A. Zieliński, J. Dobrzański, M. Sroka, *Mater. High Temp.* **36**, 296 (2019).

[18] H.M. Ahmed, H.A. M. Ahmed, M. Hefni, E.B. Moustafa, *Metals* **11**, 1825 (2021).

[19] I. Bednarczyk, *Arch. Metall. Mater.* **67**, 1179 (2022).

[20] G. Tian, J. Wang, C. Xue, X. Yang, S. Wang, H. Su, *Calphad* **81**, 102556 (2023).

[21] M. Król, J. Hajnyš, *J. Therm. Anal. Calorim.* **148**, 10505 (2023).

[22] L.A. Dobrzański, B. Tomiczek, M. Pawlyta, M. Król, *Arch. Metall. Mater.* **59**, 335 (2014).

[23] M. Król, *Acta. Phys. Pol. A* **142**, 117 (2022).

Proceedings of "Applications of Physics in Mechanical and Material Engineering" (APMME 2023)

Influence of the Spin Wave Stiffness Parameter in Amorphous Materials on Saturation Magnetisation Value

B. Jeż[a], M. Nabiałek[b], P. Postawa[a], J. Godnro[b], M.M.A.B. Abdullah[c], S. Walters[d], B. Koczurkiewicz[e] and N.I. Muhammad Nadzri[f,g]

[a] *Department of Technology and Automation, Faculty of Mechanical Engineering and Computer Science, Czestochowa University of Technology, al. Armii Krajowej 19c, 42-200 Częstochowa, Poland*
[b] *Department of Physics, Faculty of Production Engineering and Materials Technology, Czestochowa University of Technology, al. Armii Krajowej 19, 42-200 Częstochowa, Poland*
[c] *Center of Excellence Geopolymer & Green Technology (CeGeoGTech), Faculty of Chemical Engineering Technology, Kampus Dragon, Kompleks Pusat Pengajian Jejawi 3, 02600 Arau, Perlis, Malaysia*
[d] *Advanced Engineering Centre, University of Brighton, BN2 4GJ, Brighton, United Kingdom*
[e] *The Institute of Plastic Working and Safety Engineering, Faculty of Production Engineering and Materials Technology, Czestochowa University of Technology, al. Armii Krajowej 19, 42-200 Częstochowa*
[f] *Center of Excellence Geopolymer and Green Technology, Universiti Malaysia Perlis, Taman Muhibbah, 02600 Arau, Perlis, Malaysia*
[g] *Faculty of Chemical Engineering and Technology, Universiti Malaysia Perlis, Taman Muhibbah, 02600 Arau, Perlis, Malaysia*

Doi: 10.12693/APhysPolA.144.375 *e-mail: barlomiej.jez@pcz.pl

Depending on their other constituent elements, Fe-based amorphous materials can exhibit good soft magnetic properties. By determining the directional coefficient b for the relationship of $\mu_0 M(\mu_0 H)^{1/2}$ according to the best linear fit, it is possible to determine the parameter of spin wave stiffness D_{spf}. This parameter, amongst others, is related to the distribution of magnetic atoms around the central atom, which is reflected in the value of saturation magnetisation. This work has examined the structure of specially prepared alloy samples and analysed the influence of the spin wave stiffness parameter on the value of saturation magnetisation. Three alloys with different constitutions, based on the Fe matrix, were analysed.

topics: amorphous alloys, primary magnetisation curve, saturation magnetisation, spin wave stiffness parameter

1. Introduction

Modern electronic and electrical components require increasingly improved materials that meet relevant requirements. A particular example is the magnetic cores used in all smartphones, tablets, computers and many other modern devices. The most suitable magnetic materials for this type of application are materials with soft magnetic properties [1–3], i.e., low remagnetisation losses, high magnetic permeability, and relatively high values of Curie temperature and saturation magnetisation. Limiting the losses per remagnetisation cycle helps to increase the efficiency of electrical devices, concurrently reducing the temperature and noise emission associated with their operation [4, 5].

In amorphous soft magnetic materials, the phenomenon of magnetostriction is significantly reduced, with some alloys containing cobalt reaching magnetostriction values close to zero (near-zero magnetostriction) [6, 7]. This phenomenon is widely known and manifests itself in a change in one or more dimensions of the material with changes in the direction of magnetisation. For decades, work has been carried out to reduce the phenomenon of magnetostriction in materials commercially used in the electrical energy and electronic industries. The Curie temperature is a very important parameter for characterising the operation of soft magnetic materials. This temperature sets a certain limit, determining the point of change of magnetic structure from ferromagnetic to paramagnetic [8]. This means

that above the Curie temperature, ferromagnetic properties are lost. Another important parameter for describing soft magnetic materials is saturation magnetisation; it determines the state of magnetic saturation, i.e., it describes the state at which an increase in the strength of an external magnetic field does not cause any further increase in the magnetisation of the material. In the case of the tested alloys, a state close to the saturation state is achieved in relatively low magnetic fields of about 1 T. Above that value, in strong magnetic fields, the magnetisation process and increase in magnetisation value are no longer associated with the presence of structural defects, and the main factor affecting the changes in magnetisation is that of spin waves. These waves are collectively induced spin systems. Systems of interacting spins are described in Heisenberg's model [9].

Using the relationship of $\mu_0 M(\mu_0 H)^{1/2}$, it is possible to determine the D_{spf} spin wave stiffness parameter associated with parameter b, which is described by the following formula [10]

$$b = 3.54 g\mu_0\mu_{\mathrm{B}} \left(\frac{1}{4\pi D_{spf}}\right)^{3/2} k_{\mathrm{B}} T (g\mu_{\mathrm{B}})^{1/2}, \quad (1)$$

where:

μ_0 — magnetic permeability of a vacuum,
H — magnetic field,
k_{B} — Boltzmann's constant,
μ_{B} — Bohr magneton,
g — gyromagnetic factor,
T — temperature.

This parameter is related to the number of nearest magnetic neighbours. The value of this parameter is directly related to the value of saturation magnetisation.

The aim of this research was to study the structure and to determine the parameter of spin wave stiffness for samples of the bulk amorphous alloy family — $Fe_{65}Nb_5Hf_{5-x}Y_{5+x}B_{20}$ (where $x = 0, 1,$ or 2). The tested samples were soft magnetic ferromagnets in the form of a plate with a thickness of 0.5 mm.

2. Materials and methods

The samples prepared for this research were made in two stages. The first stage consisted of weighing and melting the alloy component elements to obtain crystalline ingots. All the alloy components used at this stage were of high purity: Fe — 99.99 at.%, Nb — 99.99 at.%, Hf — 99.99 at.%, Y — 99.95 at.%, B — 99.9 at.%. The ingredients were melted on a copper water-cooled plate under a protective gas atmosphere. The polycrystalline ingots were remelted four times on each side to improve their homogeneity. Each melt was preceded by the melting of pure titanium, which was used as an absorbent of the remaining oxygen in the chamber. The prepared alloy ingots were divided into smaller pieces, which were used to make rapidly cooled samples. The samples were produced in the form of plates with a thickness of 0.5 mm and an area of 100 mm^2 using an injection-casting method — the liquid alloy was forced, under argon pressure, into a copper water-cooled mould. The structure of the resulting samples was evaluated by means of a Bruker ADVANCE D8 X-ray diffractometer equipped with a cobalt lamp. The samples were tested over the range of 2θ angle from 30 to 100°, with an exposure time per measuring step of 5 s at a resolution of 0.02°. The magnetic properties of the samples were investigated using a Lakeshore 7307 vibrating sample magnetometer. Measurements of the primary magnetisation curves were carried out within the range of magnetic field strength of up to 2 T.

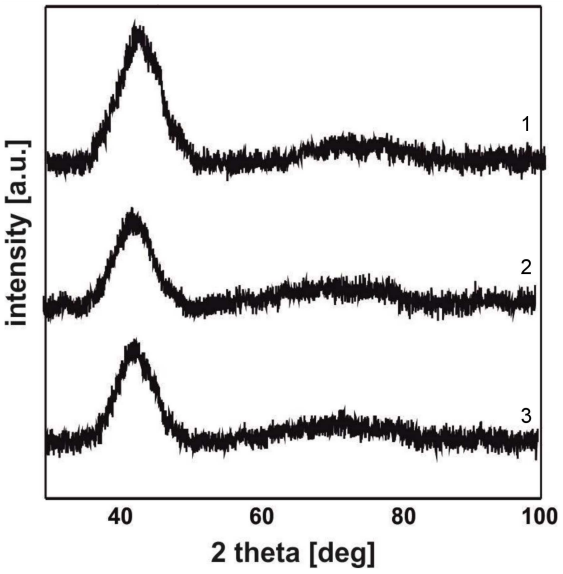

Fig. 1. X-ray diffraction patterns for the plate-form samples of the investigated alloys: $Fe_{65}Nb_5Hf_5Y_5B_{20}$ (curve 1), $Fe_{65}Nb_5Hf_4Y_6B_{20}$ (curve 2), $Fe_{65}Nb_5Hf_3Y_7B_{20}$ (curve 3).

3. Results

Figure 1 shows the X-ray diffraction images measured for the tested alloys.

In the measured diffractograms, wide, fuzzy maxima (amorphous halos) are visible in the range of 40–55° of 2θ angle. These maxima are related to X-rays scattered on atoms randomly distributed in the volume of the alloy.

Figure 2 shows static magnetic hysteresis loops measured for the investigated alloys.

The measured loops for alloys with an yttrium content of 6 at.% and 7 at.% are similar to each other. The curve for $Fe_{65}Nb_5Hf_5Y_5B_{20}$ is characterised by a different trajectory — the alloy

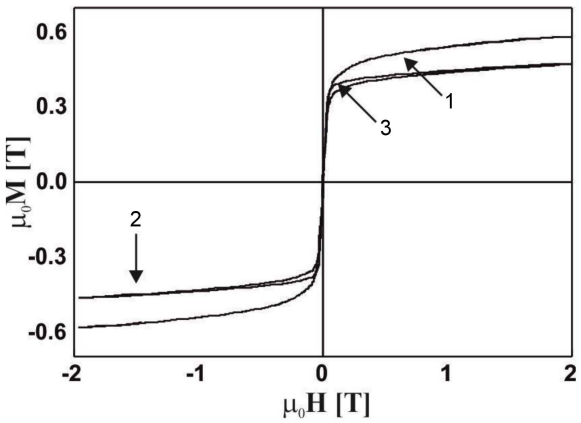

Fig. 2. Static magnetic hysteresis loops for the investigated alloys: $Fe_{65}Nb_5Hf_5Y_5B_{20}$ (curve 1), $Fe_{65}Nb_5Hf_4Y_6B_{20}$ (curve 2), $Fe_{65}Nb_5Hf_3Y_7B_{20}$ (curve 3).

TABLE I

Magnetic properties of the investigated alloys.

Alloy	M_S [T]	H_C [A/m]	$H_{\mathrm{H-P}}$ [T]	D_{spf} [meV nm^2]
$Fe_{65}Nb_5Hf_5Y_5B_{20}$	0.58	189	0.43	27
$Fe_{65}Nb_5Hf_4Y_6B_{20}$	0.47	129	0.31	32
$Fe_{65}Nb_5Hf_3Y_7B_{20}$	0.47	42	0.13	38

reaches a much higher saturation magnetisation value. Figure 3 shows the magnetisation curves as a function of $(\mu_0 H)^{1/2}$.

A linear fit was made to the trajectory of the magnetisation as a function $(\mu_0 H)^{1/2}$. The parameter b and the magnitude of the external magnetic field, at which the magnetisation process of the alloy is associated with the so-called Holstein–Primakoff paraprocess (attenuation of thermally induced spin waves), were determined. Magnetic properties, based on the static magnetic hysteresis loops and magnetisation as a function of $(\mu_0 H)^{1/2}$, are shown in Table I.

Despite minor differences in the chemical composition of the alloys, their magnetic properties differ significantly. The addition of the Y element, at the expense of the Hf element, causes a significant decrease in the value of the coercivity field and the field at which the Holstein–Primakoff paraprocess begins. The alloy sample with 7 at.% of Y element exhibits a much easier magnetisation process. Moreover, it is worth noting that the value of the D_{spf} parameter increases with increasing addition of the Y element. As previously mentioned, this parameter is closely related to the number of nearest magnetic neighbours (Fe atoms) and thus to magnetisation. The increase in the value of the D_{spf} parameter is associated with changing distance between the Fe atoms. Given the simultaneous decrease in the value of saturation magnetisation, it can be concluded that there is a local anti-ferromagnetic order in the tested samples. In some areas of the alloys, the Fe atoms are close enough to each other that they force anti-ferromagnetic spin alignment, which results in a decrease in the value of saturation magnetisation.

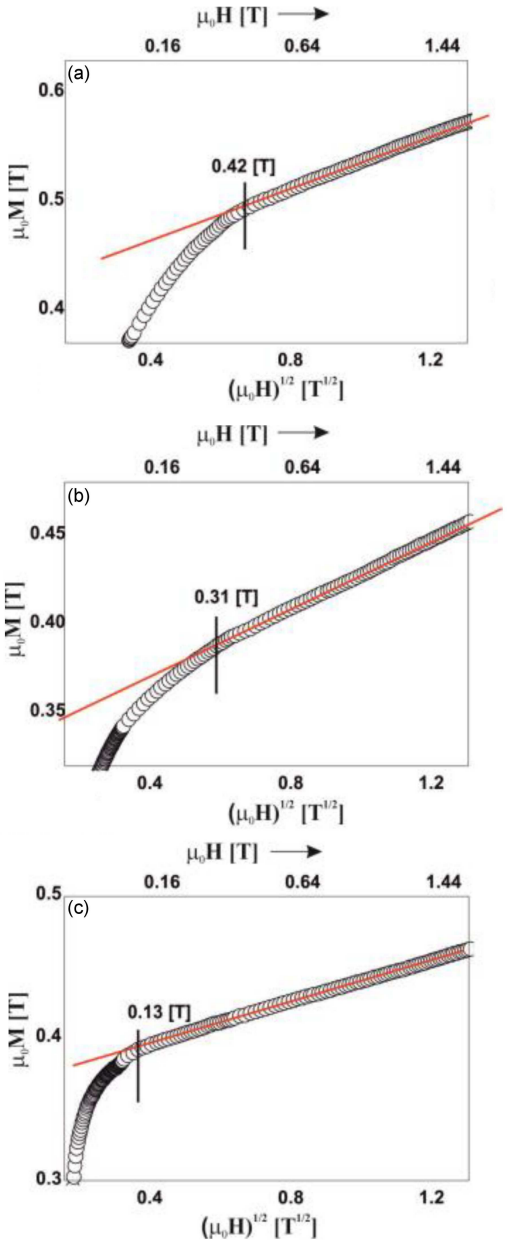

Fig. 3. Magnetisation as a function of $(\mu_0 H)^{1/2}$ for the investigated alloys: (a) $Fe_{65}Nb_5Hf_5Y_5B_{20}$, (b) $Fe_{65}Nb_5Hf_4Y_6B_{20}$, (c) $Fe_{65}Nb_5Hf_3Y_7B_{20}$.

4. Conclusions

This paper presents the results of research into the influence of Y and Hf element content on the structure and properties of bulk rapidly cooled alloys based on the Fe matrix. All the studied alloys

are characterised by an amorphous structure. Studies of the magnetic properties have shown that these alloys exhibit soft magnetic properties. It has been shown that the addition of the Y element at the expense of the Hf element affects the distribution of Fe atoms in the volume of the alloy — the distances between these atoms change. Therefore, there is an increase in the value of the D_{spf} parameter with a simultaneous decrease in the value of saturation magnetisation. This suggests the presence of local anti-ferromagnetic order in the volume of the alloys. Importantly, the existence of this magnetic order has no effect on the drastic increase in the value of the coercive field.

References

[1] X. Li, Z. Shi, T. Zhang, *J. Alloy. Compd.* **784**, 1139 (2019).

[2] F. Wang, A. Inoue, Y. Han, F. Kong, S. Zhu, E. Shalaan, F. Al-Marzouki, A. Obaid, *J. Alloy. Compd.* **711**, 132 (2017).

[3] M.E. McHenry, M.A. Willard, D.E. Laughlin, *Prog. Mater. Sci.* **44**, 291 (1999).

[4] R. Piccin, P. Tiberto, H. Chiriac, M. Baricco, *J. Magn. Magn. Mater.* **320**, 806 (2008).

[5] M. Nabiałek, S. Walters, K. Błoch, K. Jeż, M. Talar, M.A.A. Mohd Salleh, D.S. Che Halin, B. Jez, *Acta Phys. Pol. A* **139**, 503 (2021).

[6] G. Herzer, *Acta Mater.* **61**, 718 (2013).

[7] Y. Wu, T. Bitoh, K. Hono, A. Makino, A. Inoue, *Acta Mater.* **49**, 4069 (2001).

[8] Z. Hou, J. Zhang, S. Xu, C. Wu, J. Zhang, Z. Wang, K. Yang, W. Wang, X. Dua, F. Su, *J. Magn. Magn. Mater.* **324**, 2771 (2012).

[9] J. Coey, *Magnetism and Magnetic Materials*, Cambridge 2009.

[10] T. Holstein, H. Primakoff, *Phys. Rev.* **58**, 1098 (1940).

Proceedings of "Applications of Physics in Mechanical and Material Engineering" (APMME 2023)

Characterization of Doped ZnO Thin Film for Ammonia Gas Sensing Application

S. Johari[a,b,*], F.A. Hasbullah[a], A.S. Rosman[a], M.M. Ramli[a,b], M.F. Ahmad[a,b], N.A. Karim[b], N.H. Osman[c], D. Darminto[d], A.H. Reshak[e,f] and S. Garus[g]

[a] *Faculty of Electronic Engineering and Technology, Universiti Malaysia Perlis (UniMAP), Pauh Putra Campus, 02600 Arau, Perlis, Malaysia*
[b] *Institute of Nano Electronic Engineering, Universiti Malaysia Perlis (UniMAP), 01000, Kangar, Perlis, Malaysia*
[c] *Applied Electromagnetic Laboratory 1, Department of Physics, Faculty of Science, Universiti Putra Malaysia (UPM), 43400 UPM Serdang, Selangor, Malaysia*
[d] *Department of Physics, Faculty of Science and Data Analytics, Institut Teknologi Sepuluh Nopember, Campus ITS Sukolilo, Surabaya 60111, Indonesia*
[e] *Physics Department, College of Science, University of Basrah, Basrah 61004, Iraq*
[f] *Department of Instrumentation and Control Engineering, Faculty of Mechanical Engineering, CTU in Prague, 616607 Prague, Czech Republic*
[g] *Department of Mechanics and Fundamentals of Machinery Design, Faculty of Mechanical Engineering and Computer Science, Częstochowa University of Technology, Dąbrowskiego 73, 42-201 Częstochowa, Poland*

Doi: 10.12693/APhysPolA.144.379 *e-mail: shazlinajohari@unimap.edu.my

This paper reports on the characterization of Sn- and Al-doped zinc oxide thin film for potential ammonia gas detection. The sol–gel method has been used to deposit the dopant onto the glass substrate at an annealing temperature of 500°C for three different doping concentrations, which are 0.5, 1.0, and 1.5 at.%. The method used to produce this thin film is sol–gel, as it is cheap, easy, and can be employed at low temperatures. The studies involve the investigation of the morphological structures and electrical and optical properties of doped ZnO. In terms of structural properties, scanning electron microscope images of Sn- and Al-doped ZnO change as the dopant concentration is increased. The doped thin film response and recovery towards 200 ppm of ammonia were observed and recorded. Both dopants show good gas sensing response. The recorded resistance reading suggests that Al is the superior dopant in gas sensing as it produces a low resistance reading of 230 Ω as opposed to 140 kΩ produced by Sn-doped ZnO thin film.

topics: gas sensor, semiconductor, ammonia, doped ZnO thin films

1. Introduction

Ammonia (NH_3) is a colorless, smelly nitrogen and hydrogen gas found in agriculture, household, and commercial cleaning products [1]. Ammonia is an irritant and corrosive substance. The nose, throat, and respiratory system will be swiftly burnt if exposed to high levels of ammonia in the air. Low amounts of ammonia in the air or solution might cause immediate skin or eye discomfort [2].

Metal oxide semiconducting (MOS) gas sensors are inexpensive and have a high level of vapor detection accuracy. They are good candidates for commercial gas detectors because of their simplicity of manufacture, high ruggedness, and simple interface electronics. Zinc oxide (ZnO) was chosen as one of the favorite metal oxide semiconductor elements because it has a large band gap of 3.37 eV, which allows it to be modified by adding dopants to boost electron mobility and lower the band gap of thin films [3]. ZnO gas sensors typically operate at high temperatures ranging from 300 to 500°C. To address this issue, ZnO gas sensor preparation techniques and doping can assist in lowering operating temperature while also enhancing material stability, sensitivity, and selectivity. The electronic characteristics of ZnO solids may be tweaked using a variety of dopants, most commonly group 13 elements, including aluminum (Al), tin (Sn), gallium (Ga), and indium (In).

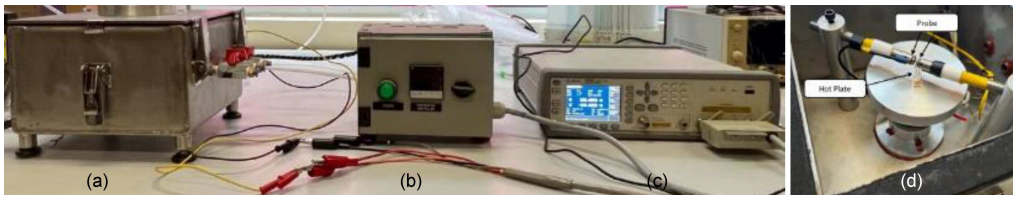

Fig. 1. Ammonia measurement setup with (a) closed chamber, (b) temperature controller, (c) LCR meter, and (d) inside view of closed chamber, where the sensor is placed on the hot plate, and the probe to connect it to LCR meter for resistance recording.

Some of the technologies that have been introduced for ZnO gas sensor preparation include sputtering, thermal evaporation, radio frequency (RF) sputtering using a magnetron, reactive sputtering with a direct current magnetron, co-electrodeposition, the sol–gel technique, and thermal decomposition. The sol–gel process provides the most flexibility in terms of creating vast areas of zinc oxide (ZnO) coating for technological applications [4]. One of the elements that has been doped with ZnO is tin (Sn). Tin is one of the elements that can help improve the structural and electrical characteristics of ZnO. This combination is appropriate for a chemical sensor. Sn has a high heat conductivity, which affects thin film resistance.

Doping ZnO with other elements is one technique to improve gas sensing characteristics. Dopants affect the structure and surface area of thin film crystals based on loading concentration and inherent features like atomic size and charge. Finding the right dopant to dramatically improve ZnO ammonia gas detecting capability is difficult since each dopant has its own set of features, and uniform dispersion of the solution is difficult [5]. The sol–gel method is both cost-effective and simple to use. It is also quite homogeneous and can be worked with at low temperatures. It also ensures a strong bond between the substrate and the topcoat material. Hence, in this paper, the sol–gel method will be used to prepare ZnO solutions doped with two dopants, namely Sn and Al. The effect of dopants on ZnO will be characterized in terms of morphology, and the doped thin film will be exposed to ammonia gas, and its sensing response will be recorded.

2. Materials and method

Doped ZnO solutions were prepared using the sol–gel method following our previous work [6]. The concentrations of both Sn and Al dopants were set to 0.5 at.%, 1.0 at.%, and 1.5 at.%. The resultant solution was stirred at 80°C for 1 h. Then, the solution was aged for 24 h to yield a homogenous solution. Spin coating was used to prepare the ZnO and dopant solution at the rotation speed of 2000 rpm for 60 s. Then, the thin film was soft-baked for 10 min at 150°C. The process of spin coating and soft baking was repeated 6 times. After that, the samples were annealed in a furnace at 500°C for 5 h. A scanning electron microscope (SEM) was used to investigate the morphological structures of the film. The prepared solution was then spin-coated on Au interdigitated electrode at 500 rpm for 40 s. Then, the electrode substrate was soft-baked for 10 min at 150°C to remove any organic residue. The ammonia measurement physical setup is shown in Fig. 1.

The electrode is placed inside the closed test chamber ($25 \times 15 \times 25$ cm^3) on a hotplate. The test chamber is connected to a temperature controller that sets the chamber to a certain temperature so that the device can operate as a gas sensor. The variation in resistance values is recorded using the E4980A Precision LCR Meter.

3. Results and discussion

In SEM images in Fig. 2, it can be observed that there is a significant difference in terms of the structure of the grains between the undoped and doped thin films. This obviously shows the strong dependence of the surface structure on the tin doping concentration [7]. Undoped ZnO appears to be closely packed with non-spherical particles of a hexagonal wurtzite structure and evenly spread on the film surface.

However, Sn-doped ZnO has completely different crystal structures, with their own sizes and shapes of crystals, for dopant concentration changing from 0.5 at.% to 1.5 at.%. It seems that the material is not as tightly spread as in the case of the undoped structure. There is a variant shape that appeared at both 0.5 and 1.0 at.% concentrations. Sn is detected due to its tetragonal-shaped crystal structure, as shown in Fig. 2b–d.

The shape is confirmed to be Sn because Ilican et al. [8] found that Sn has a tetragonal crystalline structure, as shown in Fig. 2. There is also visible white shining in certain parts for undoped ZnO and with 0.5, 1.0, and 1.5 at.% Sn dopant concentration. According to [7], this phenomenon is known as a white cluster, which is caused by electrons assembled at the film surface. Here, instead, it is due to the uneven surface of the ZnO films deposited on the glass substrate. The SEM images of Al-doped ZnO also change as the dopant concentration is increased (see Fig. 2e and f). Al dopant with

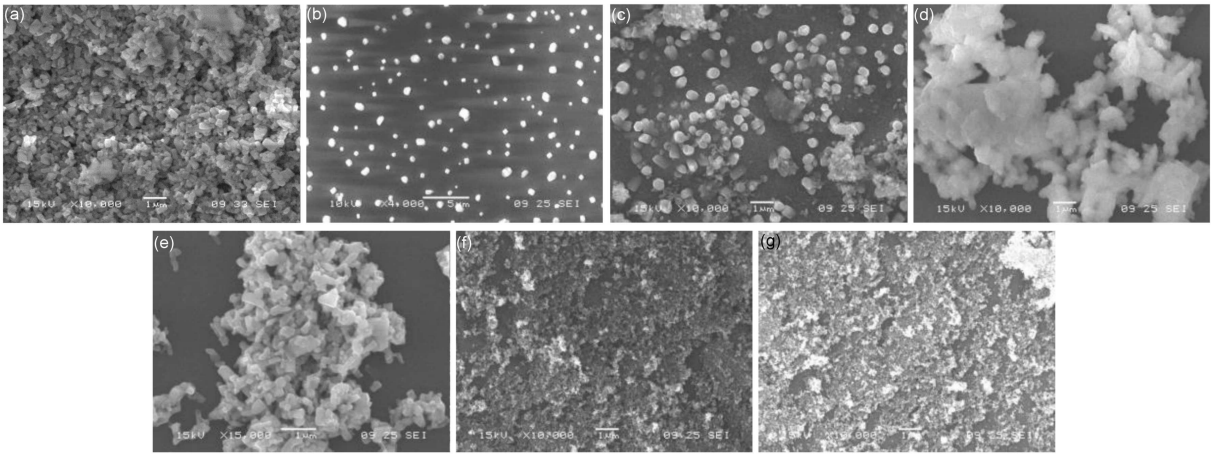

Fig. 2. SEM images of (a) undoped ZnO and ZnO doped with Sn dopant concentration of (b) 0.5 at.%, (c) 1.0 at.%, (d) 1.5 at.%, and Al dopant concentration of (e) 0.5 at.%, (f) 1.0 at.%, (g) 1.5 at.%.

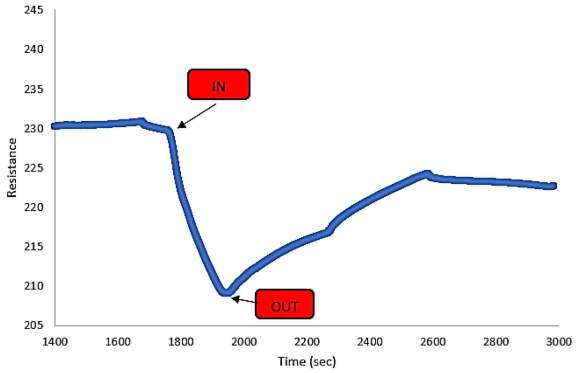

Fig. 3. Response and recovery of Al-doped ZnO at the exposure of 200 ppm ammonia.

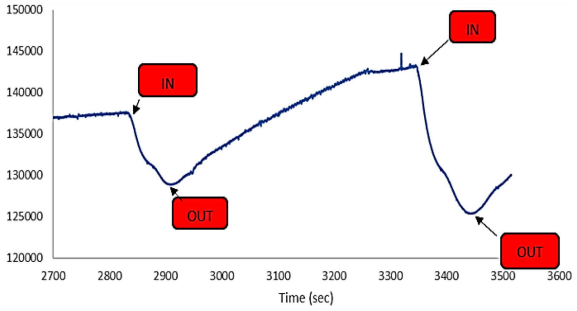

Fig. 4. Response and recovery of Sn-doped ZnO at the exposure of 200 ppm ammonia.

the lowest concentration seems not to be evenly distributed at some areas of the surface. However, it can be observed that the dopants are wrapped around the ZnO particle, as shown in Fig. 2e.

An Agilent LCR meter was used to measure the electrical characteristics of doped ZnO thin films. The DC two-probe method was used to measure the resistivity of the doped ZnO films exposed to ammonia. For initial proof of application, only doped ZnO with 0.5 at.% dopant concentration was used for ammonia gas sensing. For gas sensing applications, there are a few sensing performances that are typically analyzed, such as sensitivity, stability, response time, and recovery time [9]. However, in this work, we only focus on the response and recovery of the sensor as we want to prove the main concept of metal oxide semiconductor gas sensing. The experiment was conducted using both Sn- and Al-doped thin films. Response and recovery time is the time required for a sensor to achieve and return to 90% of the original baseline signal upon injection and removal of targeted gas. Figure 3 shows the ammonia detection response and recovery for Al-doped ZnO at the temperature of 120°C.

Based on the presented figures, it can be seen that the doped thin film reacts to ammonia exposure at a concentration of 200 ppm. Initially, dry air flowed into the chamber for 10 min. This was to ensure that the chamber was not contaminated with outside particles that could affect the ammonia sensing. After that, the flow of dry air was turned off, and ammonia flowed into the chamber for 10 min. For Al-doped ZnO, the resistance dropped from 230 to 210° when ammonia was introduced after 200 s. After 5 min, the ammonia was turned off and we could see that the resistance increased gradually to its original resistance value. This shows that the sensor responds well to the ammonia exposure in the chamber.

For the Sn-doped ZnO (Figure 4), the initial resistance value once ammonia is introduced is recorded at 137 kΩ, and it drops to 127 kΩ after approximately 200 s after ammonia introduction. When the gas was turned off, the resistance value returned to a slightly higher resistance of 142 kΩ, 3.5% higher than the initial resistance value. The gas flow was turned on again after 10 min, and the resistance showed a similar reading pattern as the first gas cycle of gas exposure. This shows that Sn-doped ZnO has good a response towards ammonia gas.

Metal oxide semiconductor gas sensing mechanism depends on the structural response and change in resistance due to the adsorption and desorption of the target gas molecules.

In terms of dopants, the resistance reading suggests that Al is the superior dopant in gas sensing as it produces a low resistance reading of 230 Ω as opposed to 140 kΩ produced by Sn-doped ZnO thin film. This implies that the Al atoms are successfully incorporated in the ZnO lattice as Al dopants provide higher conductivity due to the small ionic radii of Al atoms. ZnO is a metal oxide semiconductor with a wide band gap of 3.37 eV and a large binding energy of 60 meV [10]. This wide band gap has a lot of advantages since it can withstand high temperatures, has mechanical robustness, and is stable [11]. The gas sensing mechanism is based on the chemiresistivity principle, where when atoms or molecules interact with the surface of a metal oxide semiconductor, it affects the conductivity of the sensor. ZnO detects gas through the changes in resistance of the material because resistance changes when exposed to the targeted gas [12]. In general, there are two functions in chemical sensors, i.e., a receptor function and a transducer function. The function of the receptor is to recognize the chemical substance, while the transducer transduces the chemical substance into an output signal. When a metal oxide semiconductor interacts with the target gas, it will act as the donor or acceptor of charge carrier, which is called the receptor function, and then will change the resistivity of the metal oxide semiconductor (transducer function). The value of the resistance depends on the majority carrier in the metal oxide semiconductor and the targeted gas. When Sn and Al dopants are introduced, it will change the surface morphology and grain size of the ZnO thin film. The grain size of doped ZnO reduces as the dopant prevents the crystal structure growth rate. This will improve the sensing performance as a small-sized particle has a high surface area, consequently improving the chemisorbed oxygen ions. The initial results of gas sensing performance reported in this paper suggest good agreement with the previously reported work [13], as similar patterns in gas response and recovery have been obtained.

4. Conclusions

Sn- and Al-doped ZnO thin films were successfully deposited using the sol–gel method for three different concentrations of 0.5, 1.0, and 1.5 at.%. Surface morphology characterization was conducted using SEM. For undoped ZnO, hexagonal wurtzite structures are visible, and dopants have been observed to be wrapped around the ZnO structure. As the dopant concentration increased, the structures became slightly bigger and less smooth. Resistance measurements indicate that Al is a better dopant for gas sensing than Sn because it provides low resistance readings of 230 Ω as opposed to 140 kΩ for ZnO thin films that are doped with Sn.

References

[1] K. Ravichandran, A. Manivasaham, *J. Mater. Sci. Mater. Electron.* **28**, 6335 (2017).

[2] R.S. Ganesh, E. Durgadevi, M. Navaneethan, V.L. Patil, S. Ponnusamy, C. Muthamizhchelvan, S. Kawasaki, P.S. Patil, Y. Hayakawa, *Sens. Actuators A Phys.* **269**, 331 (2018).

[3] P. Nakarungsee, S. Srirattanapibul, C. Issro, I.M. Tang, S. Thongmee, *Sensors Actuators, A Phys.* **314**, 112230 (2020).

[4] K. Ravichandran, A.J. Santhosam, M. Sridharan, *Surf. Interfaces* **18**, 100412 (2020).

[5] K. Radhi Devi, G. Selvan, M. Karunakaran, I.L. Poul Raj, V. Ganesh, S. AlFaify, *Mater. Sci. Semicond. Process.* **119**, 105117 (2020).

[6] S. Ishak, S. Johari, M.M. Ramli, *J. Sol-Gel Sci. Technol.* **95**, 265 (2020).

[7] C.S. Prajapati, A. Kushwaha, P.P. Sahay, *Appl. Phys. A Mater. Sci. Process.* **113**, 651 (2013).

[8] S. Ilican, M. Caglar, Y. Caglar, *Appl. Surf. Sci.* **256(23)**, 7204 (2010).

[9] V.E. Bochenkov, G.B. Sergeev, in: *Metal Oxide Nanostructures and Their Applications*, Eds. A. Umar, Y.-B. Hang, American Scientific Publishers, Valencia (CA) 2010 p. 31.

[10] R. Mohan, K. Krishnamoorthy, S.J. Kim, *Solid State Commun.* **152**, 375 (2012).

[11] S.J. Pearton, F. Ren, *Nanomater. Nanotechnol.* **3**, 1 (2013).

[12] S.R. Morrison, *Sens. Actuators* **12**, 425 (1987).

[13] L.H. Kathwate, G. Umadevi, P.M. Kulal, P. Nagaraju, D.P. Dubal, A.K. Nanjundan, V.D. Mote, *Sens. Actuators A Phys.* **313**, 112193 (2020).

Proceedings of "Applications of Physics in Mechanical and Material Engineering" (APMME 2023)

Changes in the Surroundings of the Central Iron Atom in Amorphous Alloys

P. Pietrusiewicz*

Department of Physics, Faculty of Production Engineering and Materials Technology, Czestochowa University of Technology, al. Armii Krajowej 19, 42-200 Częstochowa, Poland

Doi: 10.12693/APhysPolA.144.383 *e-mail: pawel.pietrusiewicz@pcz.pl

Amorphous alloys are still a challenge for science when it comes to an accurate description of their structure and magnetic properties. There are many techniques for studying the structure, however, the direct observation of the amorphous structure does not bring much to the description of the phenomena occurring in them. In the case of ferromagnetic amorphous alloys, their properties can be studied based on the analysis of transmission Mössbauer spectra and the hyperfine field induction distributions obtained on their basis. The work investigated the influence of changing the surroundings of the central iron atom on the magnetic properties of a soft magnetic amorphous alloy. Samples after solidification and after isothermal annealing at a temperature below the crystallization temperature were tested.

topics: Mössbauer spectroscopy, amorphous materials, soft magnetic materials

1. Introduction

Amorphous iron-based materials are also called metallic glasses (MG). They offer many technical applications and are characterized by very good mechanical and soft magnetic properties. Soft magnetic materials are characterized by a low coercive field of less than 1000 A/m. However, materials with an amorphous structure are characterized by the lack of boundary grains in their structure, unlike materials with a crystalline structure of the same chemical composition. Metallic glasses have been studied for many decades [1–4] in various respects, i.e., magnetic and mechanical properties, structural system, and thermal stability, using various types of measurement methods, including X-ray diffraction (XRD), differential scanning calorimetry (DSC), scanning electron microscopy (SEM), Mössbauer spectrometry, etc. [3–7]. It is also known that the properties of amorphous alloys can be improved by applying appropriate annealing at temperatures below the crystallization temperature. There are many items in the literature regarding the annealing of amorphous materials below the crystallization temperature [8–12]. However, such optimization led to the formation of a nanocrystalline phase, usually α-Fe phase grains embedded in an amorphous matrix.

In the work of T. Naohara [13], it was shown that the optimization process can proceed without the formation of grains of the α-Fe nanocrystalline phase and lead to a reduction of internal stresses in the free volume areas and a change in the immediate surroundings of Fe atoms, which may lead to the stabilization of magnetic properties. Using Mössbauer spectroscopy, changes in the environment of the closest neighbors of Fe atoms can be assessed [14]. Mössbauer spectroscopy is a powerful tool used to study local magnetic properties and chemical and crystallographic disturbances. Based on the analysis of Mössbauer spectra, the influence of changing the surroundings of the central iron atom on the magnetic properties of the soft magnetic amorphous $(Fe_{61}Co_{10}Y_8W_1B_{20})Pt_1$ alloy was investigated. Samples were tested after solidification and after isothermal annealing at a temperature below the crystallization temperature.

2. Experimental procedure

The research material with atomic composition $(Fe_{61}Co_{10}Y_8W_1B_{20})Pt_1$ was melted in an arc furnace in a protective atmosphere of inert gas (Ar). High-purity elements were used to produce the alloys, namely Fe — 99.98%, Co — 99.95%, Y — 99.9%, W — 99.95%, B — 99.5%, and Pt — 99.99%. Amorphous ribbons were produced using the melt-spinning method with a rotational speed of a copper wheel of 35 m/s. The produced ribbons, 5 mm wide and 35 mm thick, were annealed at three temperatures: at 600 K for 1 h, at 700 K for 1 h, and at 800 K for 1 h. After each annealing stage, the ribbon samples were tested using a Mössbauer transmission spectrometer with a ^{57}Co source in an Rh

TABLE I

Results of analysis of Mössbauer spectra, where IS — isomer shift, B_{hf} — hyperfine magnetic field, D_{am} — standard deviation, Q_{UA} — quadrupole splitting, $A23$ — relative line intensity ratio.

	IS [mm/s]	B_{hf} [T]	D_{am} [T]	Q_{UA} [mm/s]	$A23$
As-cast	−0.091(2)	19.685	5.357	−0.0206(8)	2.396(6)
600 K	−0.091(2)	19.646	5.349	−0.0224(1)	2.599(9)
700 K	−0.092(1)	19.669	5.353	−0.021(2)	2.451(6)
800 K	−0.092(6)	20.092	5.417	−0.0207(9)	2.557(6)

matrix with an activity of 100 mCi. The spectrometer speed calibration was performed on α-Fe foil with a purity of 4 N, the hyperfine field of which is $B_{hf} = 33.1$ T at room temperature. Mössbauer spectra were fitted using NORMOS software.

3. Results and discussion

Experimental Mössbauer spectra recorded for samples of the $(Fe_{61}Co_{10}Y_8W_1B_{20})Pt_1$ alloy are shown in Fig. 1. The spectra of each sample were recorded in the same transmission geometry and with similar measurement times. Each of the measured spectra was decomposed into a set of 34 elementary Zeeman sextets and fitted using the least squares method. Each spectral line was expressed using hyperfine parameters such as hyperfine magnetic field (B_{hf}), isomeric shift (IS), and quadrupole splitting (Q_{UA}), and the ratio of the intensities of lines 2 and 5 to lines 3 and 4 of the Mössbauer spectrum was determined. Quadrupole splitting was used for fitting due to the possible noncubic symmetry of atomic configurations around ^{57}Fe [15]. All fitting parameters of the Mössbauer spectra are listed in Table I.

Based on the measured Mössbauer spectra, it can be concluded that the tested materials are ferromagnetics with an amorphous structure. The wide asymmetric lines of the Mössbauer spectra correspond to different surroundings of Fe atoms.

Different environments in the nuclei of ^{57}Fe atoms in the tested samples confirm the bimodal distributions of the magnetic hyperfine fields $P(B)$ shown in Fig. 2 [3, 16]. The distributions for all tested samples, both after solidification and after annealing at temperatures of 600, 700, and 800 K, are similar and consist of two clearly separated peaks: low and high field. It can be seen that the broad peak with the maximum of the average hyperfine field (B_{hf}) for the sample in the after-solidification state and for samples annealed successively at temperatures of 600 and 700 K occurs at a field induction of $\sim$ 21 T, while for the sample annealed at 800 K, it occurs at field induction $\sim$ 22 T.

However, the low-field component described by the first peak in the hyperfine field distributions has the maximum value of the average hyperfine field induction at an induction field between 10–11 T.

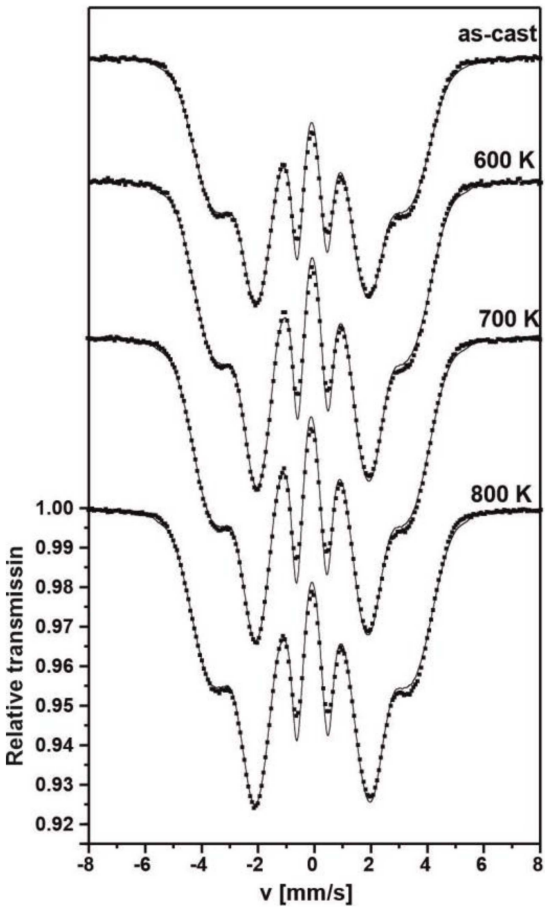

Fig. 1. Transmission Mössbauer spectra for the alloy sample after solidification and after annealing at three temperatures.

In [17], it was postulated that the low-field component corresponds to the presence of Y atoms in near-neighborhood to Fe atoms. This proves that Y in the first coordination zone of Fe, which results in a significant reduction of the hyperfine field [17].

The average hyperfine fields (B_{hf}) remain almost constant for the alloy samples after solidification and annealing at temperatures of 600 and 700 K. This can be related to the stable short-range order in the local surroundings of Fe atoms. Only annealing at a temperature of 800 K resulted in an increase in the average hyperfine field (B_{hf}) to the

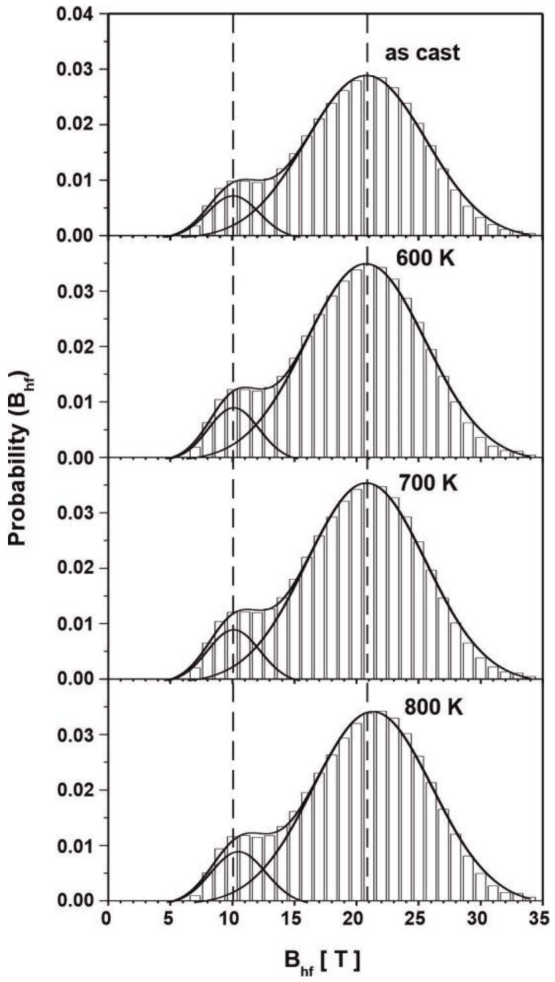

Fig. 2. Distributions of hyperfine fields for samples of the $(Fe_{61}Co_{10}Y_8W_1B_{20})Pt_1$ alloy after solidification and annealing at temperatures of 600, 700, and 800 K.

value of 20.09 T and an increase in the value of decomposition dispersion (D_{am}), which is related to the relaxation of the amorphous phase within the free volumes, which reduces the average distance between Fe–Fe atoms.

The surroundings of ^{57}Fe nuclei in the structure of amorphous materials are also characterized by average values of isomeric shifts (IS). The magnetic anisotropy of these shifts can be characterized by the parameter $A23$, i.e., the ratio of lines 2 and 5 of the split Zeeman sextet to lines 3 and 4. The intensity of these lines in the spectrum is determined by the angle θ between the direction of magnetization of the sample and the radiation γ. In the absence of any stresses in the sample, the magnetic moments can be expected to be aligned along the plane of the tape due to the anisotropy of the shape. In this case, parameter $A23 = 4$. However, if the magnetic structure in the sample is disordered, the intensity parameter $A23 = 2$. By analyzing the $A23$ parameter, the magnetic texture of the tested samples can be assessed [1, 3].

The values of the isomeric shift (IS) and the $A23$ parameter for samples after solidification and annealing at temperatures of 600, 700, and 800 K for 1 h are listed in Table I. It can be seen that annealing did not affect the isomeric shift (IS) value, which may indicate that there are no major deviations in the chemical order of the tested materials. Nevertheless, the value of the $A23$ parameter increased after the first stage of annealing at 600 K for 1 h ($A23 = 2.599$), then decreased slightly after annealing at 700 K ($A23 = 2.451$), and increased again after annealing at 800 K ($A23 = 2.557$). This indicates that the annealing process caused the orientation of the magnetic spins to become orderly towards the plane of the tape.

4. Conclusions

To sum up, it can be said that the tested material is a ferromagnetic with an amorphous structure. Mössbauer spectra and the corresponding hyperfine field distributions $P(B_{hf})$ for samples after solidification and annealing at temperatures of 600, 700, and 800 K for 1 h do not show significant differences. However, the parameters of individual spectra for the sample heated at 800 K for 1 h show a change in parameters, i.e., the average hyperfine field (B_{hf}) and an increase in the dispersion of the distribution (D_{am}), which proves the relaxation of the amorphous phase within the free volumes.

The tested alloy $(Fe_{61}Co_{10}Y_8W_1B_{20})Pt_1$ in the form of a ribbon showed very high thermal stability in a wide temperature range.

References

[1] E. Kuzmann, S. Stichleutner, A. Sápi, L.K. Varga, K. Havancsák, V. Skuratov, Z. Homonnay, A. Vértes, *Hyperfine Interact.* **207**, 73 (2012).

[2] A.K. Bhatnagar, *Hyperfine Interact.* **25**, 637 (1985).

[3] N. Amini, M. Miglierini, J. Dekan, *AIP Conf. Proc.* **1781**, 020020 (2016).

[4] S.L. Panahi, P. Ramasamy, F. Masdeu, M. Stoica, J. Torrens-Serra, P. Bruna, *Metals* **11**, 1293 (2021).

[5] X. Li, K. Zhang, C. Wang, W. Han, G. Wang, *J. Mater. Sci. Technol.* **23**, 253 (2007).

[6] E. Jakubczyk, *Mater. Sci.-Pol.* **24**, 4 (2006).

[7] M.E. McHenry, D.E. Laughlin, in: *Physical Metallurgy*, 5th Ed., Elsevier, 2014 p. 1881.

[8] Y. Yoshizawa, S. Oguma, K. Yamauchi, *J. Appl. Phys. B*, **64** 6044 (1988).

[9] A. Makino, T. Hatani, Y. Naitoh, T. Bitoh, A. Inoue, *IEEE Trans. Magn.* **33**, 3793 (1997).

[10] X. Liang, T. Kulik, J. Ferenc, B. Xu, *J. Magn. Magn. Mater.* **308**, 227 (2007).

[11] J. Zbroszczyk, A. Młyńczyk, J. Olszewski, W. Ciurzyńska, M. Hasiak, R. Kolano, J. Lelątko, *J. Magn. Magn. Mater.* **304**, e727 (2006).

[12] R. Hasegawa, *J. Magn. Magn. Mater.* **304**, 187 (2006).

[13] T. Naohara, *Philos. Mag. Lett.* **78**, 229 (1998).

[14] Nan Zhang, Gang Li, Xin Wang, Tao Liu, Jianliang Xie, *J. Alloy. Compd.* **672**, 176 (2016).

[15] J. Kansy, A. Hanc, J. Rasek, G. Haneczok, L. Pająk, Z. Stokłosa, P. Kwapuliński, *Acta Phys. Pol. A* **119**, 41 (2011).

[16] M. Nabiałek, P. Pietrusiewicz, K. Błoch, *J. Alloy. Compd.* **628**, 424 (2015).

[17] P. Gupta, A. Gupta, A. Shukla, Tapas Ganguli, A.K. Sinha, G. Principi, A. Maddalena, *J. Appl. Phys.* **110** 033537 (2011).

Proceedings of "Applications of Physics in Mechanical and Material Engineering" (APMME 2023)

Study of the Real Structure of Soft Magnetic Amorphous Alloys Using Mössbauer Spectroscopy

B. Jeż[a,*], M. Nabiałek[b], P. Pietrusiewicz[b], M.M. Nabiałek[b], A.V. Sandu[c,d] and T. Stachowiak[a]

[a] *Department of Technology and Automation, Faculty of Mechanical Engineering and Computer Science, Czestochowa University of Technology, al. Armii Krajowej 19c, 42-200 Częstochowa, Poland*
[b] *Department of Physics, Czestochowa University of Technology, al. Armii Krajowej 19, 42-200 Częstochowa, Poland*
[c] *Faculty of Materials Science and Engineering, Gheorghe Asachi Technical University of Iasi, Blvd. D. Mangeron 41, 700050, Iaşi, Romania*
[d] *Romanian Inventors Forum, Str. Sf. P. Movila 3, Iaşi, Romania*

Doi: 10.12693/APhysPolA.144.387 *e-mail: barlomiej.jez@pcz.pl

Studying the real structure of amorphous alloys is not an easy task and requires an appropriate scientific approach. Unlike crystalline materials, for which there is a precise description of the structure based on the structure of the unit cell, in amorphous materials it is not possible to identify it. The amorphous structure is often described as one big defect. Using the technique of Mössbauer spectroscopy, it is possible to study the structure of amorphous alloys and determine the degree of their order. The paper presents the results of Mössbauer tests for amorphous alloys in the state after solidification. The influence of a small change in the chemical composition on the probability of the occurrence of iron surroundings determining specific hyperfine field induction values was determined.

topics: bulk amorphous alloys, Mössbauer spectroscopy, X-ray diffraction (XRD)

1. Introduction

An important parameter indicating the application possibilities of various types of materials is their structure packing density. It is commonly understood as the number of closely packed atoms in a given volume, without distinguishing other relationships between atoms. In the case of ferromagnetic materials exhibiting magnetic properties, especially soft magnetic properties, the distribution of magnetic atoms in the volume of a given material is very important. The improvement in properties is not always related to a larger number of magnetic atoms in a given volume. A parameter that indirectly determines the good magnetic properties of magnetic alloys with soft magnetic properties is the exchange distance of magnetic interactions. This distance determines what distance between magnetic atoms is most favorable to obtain optimal properties described as ferromagnetic and soft magnetic [1, 2]. If this distance is too large, the magnetic interactions between atoms weaken and individual magnetic moments do not interact with each other. If there are too many of these atoms in the analyzed volume, their coupling occurs and the magnetic moments become antiparallel, and we are dealing with an antiferromagnetic interaction. Using Mössbauer transmission spectroscopy, and more precisely, numerical analysis of the obtained measurement results, it is possible to determine the distribution of iron atoms in the alloy volume. The hyperfine field induction distributions show low- and high-field components for amorphous alloys [3]. The change in magnetization was examined in the area where spin waves are thermally damped by the magnetic field and are responsible for its increase. The increase in magnetization in strong magnetic fields when it has almost been reached takes place according to the relationship describing the Holstein–Primakoff paraprocess [4]

$$b\left(\mu_0 H\right)^{1/2}, \tag{1}$$

where the coefficient b is described by the relationship

$$b = 3.54\, g\mu_0\mu_{\mathrm{B}} \left(\frac{1}{4\pi D_{spf}}\right)^{3/2} k_{\mathrm{B}} T \left(g\mu_B\right)^{1/2}, \tag{2}$$

and where:

k_{B} — Boltzmann constant,
μ_{B} — Bohr magneton,
g — gyromagnetic coefficient,
D_{spf} — spin wave stiffness parameter.

In (2), there is a spin wave stiffness parameter (D_{spf}), which is related to the exchange constant (A_{ex}) from the formula

$$A_{ex} = \frac{M_s D_{spf}}{2g\mu_{\mathrm{B}}}. \tag{3}$$

The spin wave stiffness parameter (D_{spf}) can be determined from the equation

$$D_{spf} = \frac{k}{4\pi}\left(\frac{2,612\mu_B\mu_0}{M_0 c_{3/2}}\right)^{3/2}, \tag{4}$$

where:

M_0 — magnetic polarization at 5 K,

$C_{3/2}$ — constant determined by adapting the law of the temperature dependence of magnetization as a function of the magnetic field strength ($\mu_0 H = 1$ T) [5].

Knowing the value of the spin wave stiffness parameter, we can determine the number of neighboring magnetic atoms.

The paper presents the results of tests of the structure and magnetic properties carried out for samples of $Fe_{62}Co_8Y_8Me_2B_{20}$ (Me = Nb or Zr) alloys in the form of ribbons after solidification and with a thickness of 35 μm.

2. Experimental procedure

The test material was prepared from ingredients with a purity of not less than 99.99 at.%. Four- and five-component alloys were made. The alloying base was iron, the content of which exceeded 60% for each alloy. This treatment prevents the loss of boron during remelting. Additionally, the alloys contained Co, Y, and Zr. After weighing 15 grams, the ingredients were pre-melted in an arc furnace. The alloy components were melted on a water-cooled copper plate. This process took place in a protective atmosphere of argon. The initial melting parameters are $\approx$ 250 A. After the first melting of the components, the operating current was increased to 350 A. Each subsequent melting of the ingot was performed after it had been rotated, which allowed for good mixing of the components. This operation was repeated twelve times. The melted alloy components in the form of an ingot were cooled in the furnace for about 15 min. This procedure was aimed at limiting the oxidation of the alloy. After being removed from the working furnace, the cooled ingots were cleaned mechanically and using an ultrasonic cleaner. The cleaned pieces of the alloy were ready to produce test samples in the form of thin ribbons. The ribbons were made using the melt-spinning method. The alloy pieces were placed in a quartz capillary, which was placed in the coil of an induction furnace. The capillary outlet had a diameter of 1 mm. The other side of the capillary was connected to an inert gas source. The copper wheel was accelerated to a linear speed of 30 m/s, and the liquid alloy was sprayed onto it. As a result, ribbons with a thickness of approximately 30–35 μm were produced. The ribbon production process was carried out in a protective atmosphere of argon. The ribbons thus produced were subjected to structure analysis using X-ray diffraction (XRD). An X-ray diffractometer operating in the Bragg–Brentano geometry was used for this purpose. The Bruker X-ray machine model ADVANCE 8 was equipped with an X-ray tube with a copper anode. Samples in the form of ribbons (planar-parallel) after solidification were glued to rotating measuring disks. Scanning of the ribbons using X-rays was carried out in the two theta angle range from 30 to 100°. The density and scanning time were 0.02° and 6 s, respectively. The spin wave stiffness parameter b was calculated based on the relationship from (1). Mössbauer spectra for room temperature were measured on a Polon 2330 spectrometer. The device operated in transmission geometry with constant source acceleration. The spectrometer calibration was performed on α-Fe foil with a thickness of 20 μm. A ^{57}Co Mössbauer source in a rhodium matrix was used for the measurements. The Mössbauer transmission spectra were subjected to numerical analysis using the NORMOS software [6].

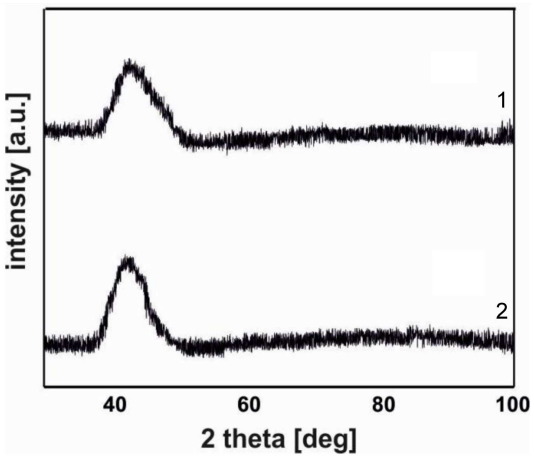

Fig. 1. X-ray diffraction images obtained for samples of the tested $Fe_{62}Co_8Y_8Me_2B_{20}$ in the form of 35 μm thick ribbons: with Zr (curve 1), and with Nb (curve 2).

3. Presentation of results

The X-ray diffractograms measured for the tested alloys are presented in Fig. 1.

The X-ray diffractograms for the tested alloys in the form of a ribbon presented in Fig. 1 are typical for materials with an amorphous structure. We can only distinguish a background of slight intensity. Near the two theta angles corresponding to the component with the highest content in the alloy (iron in our case), a wide diffuse maximum, called an amorphous halo, can be observed. The amorphous

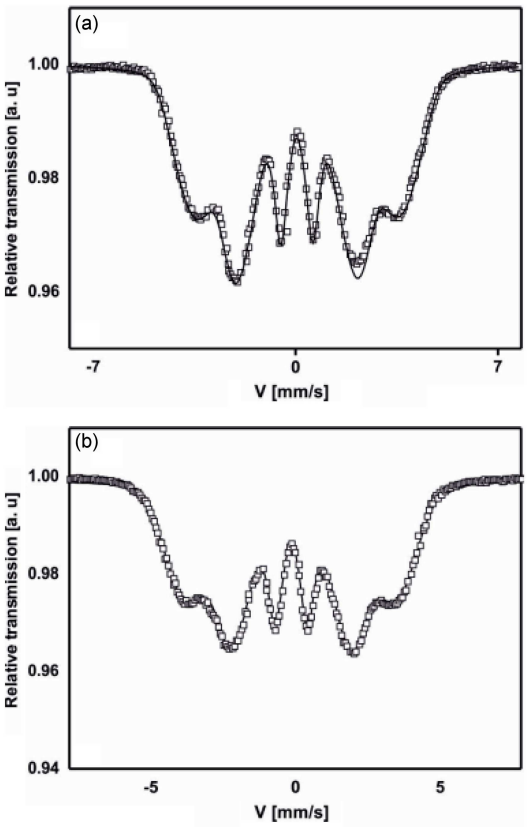

Fig. 2. Mössbauer transmission spectra obtained for the tested $Fe_{62}Co_8Y_8Me_2B_{20}$ in the form of 35 μm thick ribbons: (a) Zr, (b) Nb.

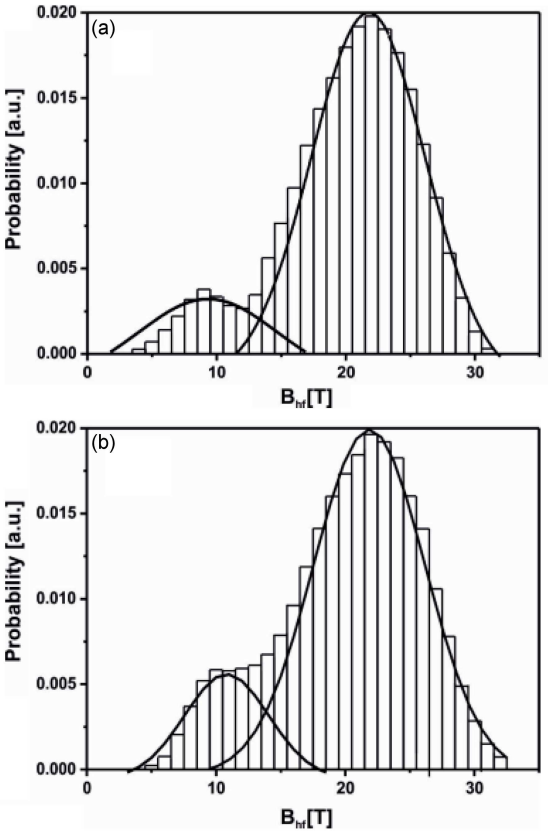

Fig. 3. Distributions of hyperfine field induction obtained based on the analysis of Mössbauer transmission spectra for the tested $Fe_{62}Co_8Y_8Me_2B_{20}$ in the form of 35 μm thick ribbons: (a) Zr, (b) Nb.

nature of the samples was additionally confirmed by tests performed using Mössbauer transmission spectroscopy. Figure 2 shows the Mössbauer transmission spectra obtained for the tested alloy samples.

The Mössbauer transmission spectra presented in Fig. 2 are typical for materials with an amorphous structure. They consist of wide asymmetrical overlapping lines and are asymmetrical. As a result of the numerical analysis of Mössbauer transmission spectra, the distributions of hyperfine field induction on ^{57}Fe nuclei were obtained (Fig. 3).

The distributions of hyperfine field induction on ^{57}Fe nuclei are bimodal. The low- and high-field components present in them indicate a large diversity of the immediate surroundings of iron atoms. This also means that in the volume of the alloy there are areas where the distances between iron atoms are smaller and areas where the distances are larger. The formation of such areas affects the occurrence of topological and chemical disorders in amorphous materials. This can be considered to be the nature of amorphous materials, which distinguishes them from crystalline materials. Figure 4 shows the dependencies $b(\mu_0 H)^{1/2}$ for the tested $Fe_{62}Co_8Y_8Me_2B_{20}$ in the form of 35 μm thick ribbons with Zr (curve 1) and Nb (curve 2).

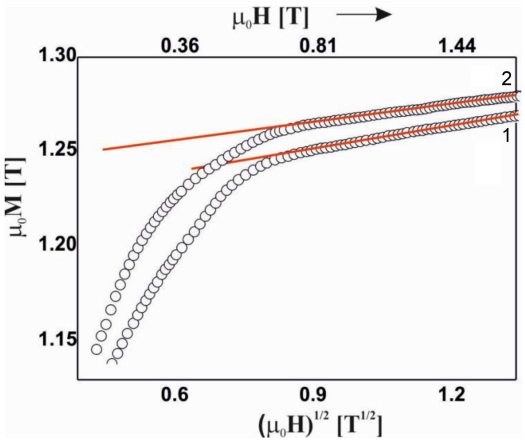

Fig. 4. The relationship $b(\mu_0 H)^{1/2}$ for the tested $Fe_{62}Co_8Y_8Me_2B_{20}$ alloys in the form of 35 μm thick ribbons: Nb (curve 1), Zr (curve 2).

The calculated spin wave stiffness parameter D_{spf} for the sample with the addition of Nb (61.8×10^{-2} meV nm^2) is higher than for the sample with Zr (56.4×10^{-2} meV nm^2). This may mean that in the alloy with the addition of Nb, the distances between magnetic atoms are more favorable for free interaction between magnetic spins.

4. Conclusions

The produced ribbons had an amorphous structure, which was confirmed by tests performed using XRD and Mössbauer spectroscopy. The distributions of hyperfine field induction on ^{57}Fe are bimodal, which is related to the presence of areas with different iron concentrations in the sample volume. In the sample with Nb addition, the average value of the hyperfine field of the low-field component was much higher. The increase in the value of the material parameter D_{spf} is related to the change in the internal parameters of the sample. As a result of a slight change in the composition of the alloy, the distance between the nearest magnetic neighboring atoms changes. The increase in the value of the D_{spf} parameter may be related to the increased number of closest magnetic atoms, which is related to the improvement of the short-range chemical order (SRO).

References

[1] M.-N. Avettand-Fenoel, M. Marinova, R. Taillard, W. Jiang, *J. Alloys Compd.* **854**, 157068 (2021).

[2] B. Jeż, M. Nabiałek, K. Jeż, *Acta Phys. Pol. A* **142**, 14 (2022).

[3] B. Jeż, J. Wysłocki, S. Walters, P. Postawa, M. Nabiałek, *Materials* **13**, 1367 (2020).

[4] T. Holstein, H. Primakoff, *Phys. Rev.* **58**, 1098 (1940).

[5] M. Hirscher, R. Reisser, R. Wurschum, H.E. Schaefer, H. Kronmüller, *J. Magn. Magn. Mater.* **146**, 117 (1995).

[6] R.A. Brand, NORMOS-90, Universität Duisburg, 2002.

Proceedings of "Applications of Physics in Mechanical and Material Engineering" (APMME 2023)

Free Volumes and Their Influence on Disaccomodation of Magnetic Susceptibility

M. Nabiałek*

Department of Physics, Czestochowa University of Technology, Armii Krajowej 19 Av., 42-200 Częstochowa, Poland

Doi: 10.12693/APhysPolA.144.391 *e-mail: marcin.nabialek@pcz.pl

In weak magnetic fields, there are changes in the arrangement of atoms, which are otherwise called magnetic relaxations. The exact phenomenon that will be investigated in this paper concerns the disaccomodation of magnetic susceptibility, which is one of the most frequently observed effects of magnetic lag. During this magnetic delay, there is a reorientation of the axes of pairs of atoms corresponding to two different energy levels. This energy is related to the energies of exchange and spin–orbit coupling. The paper presents the results of magnetic susceptibility disaccomodation and describes its influence on the relaxation time matching spectrum.

topics: bulk amorphous alloy, disaccomodation of magnetic susceptibility

1. Introduction

The phenomenon of magnetic delay, also called magnetic viscosity, in crystalline materials is related to the migration of atoms and defects in the crystal lattice. Based on the equation

$$D_d = \frac{a^2}{36\tau}, \tag{1}$$

where:

τ — relaxation time,

a — lattice constant,

D_d — diffusion coefficient,

the diffusion coefficient can be calculated. As a result of the large dependence between the relaxation time and temperature, the phenomenon of magnetic delay occurs in a narrow temperature range [1, 2]. The result of the narrow temperature range describing the phenomenon of magnetic delay in crystalline alloys is the thermostable nature of this type of material. Changes in magnetic properties in crystalline alloys are abrupt and are related to the presence of well-defined defects in their volume in the form of vacancies or interstitial atoms. It follows that relaxation processes in crystalline materials are the result of providing the system with energy of a specific value in a very narrow temperature range. This energy is called activation energy. However, in amorphous alloys the structure is not well described and is characterized by a metastable state. This means that structural relaxations can occur in amorphous materials even at low temperatures. These relaxations occur in a certain temperature range and are described by the activation energy spectrum [3–5] and not by a discrete value, as in the case of crystalline materials.

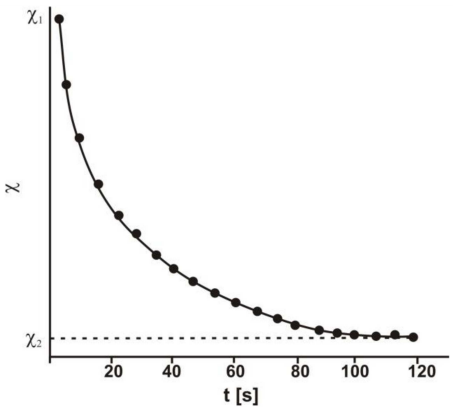

Fig. 1. Magnetic susceptibility disaccomodation curve.

Disaccomodation of magnetic susceptibility involves a decrease in time of the magnetic susceptibility of a sample demagnetized with an alternating current with an amplitude decreasing to zero [6, 7]. The disaccomodation of magnetic susceptibility is calculated according to the equation [7]

$$\Delta\left(\frac{1}{\chi}\right) = \frac{1}{\chi(t_2)} - \frac{1}{\chi(t_1)}, \tag{2}$$

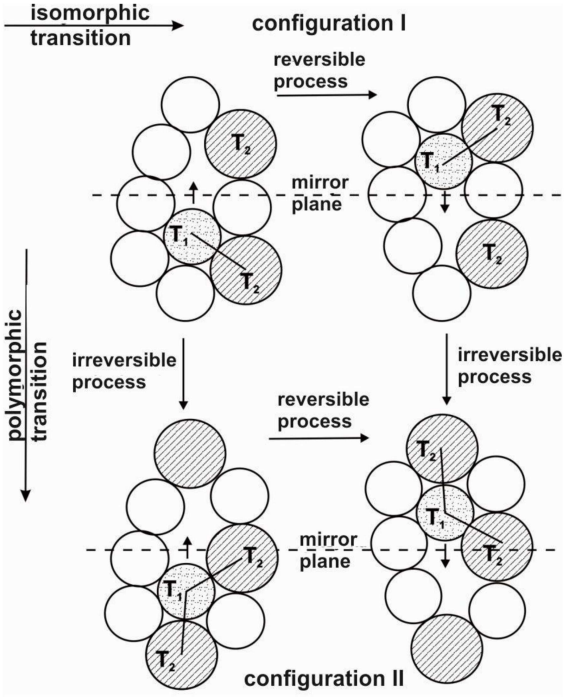

Fig. 2. The hard-sphere model describing two orientations of the axis of atom pairs for two energy levels [8].

where (t_1) and (t_2) are the values of magnetic susceptibility measured during 2 s and 120 s after demagnetizing the sample with an alternating current with amplitude decreasing to zero.

Figure 1 shows the magnetic susceptibility disaccomodation curve. The reduction of susceptibility from the maximum value occurs in the time from the moment of demagnetization to the minimum value for an infinitely long time.

Magnetic relaxation processes in amorphous alloys occur as a result of the reorientation of the axes of atom pairs. It is assumed that in amorphous alloys containing two elements T_1 and T_2, pairs of atoms T_1T_1, T_1T_2, T_2T_2 can be formed. The change in the axis of atom pairs can take two orientations and occurs around free volumes. To change the orientation of the axis of atom pairs, an appropriate amount of energy is needed, called activation energy, most often thermal energy. This phenomenon is well described by the double-well model. As a result of different magnetic interaction energies and different structural configurations between the two orientations of atom pairs, we can determine the splitting energy 2Δ.

This energy is the sum of structural configurations $(2\Delta_s)$ and the energy of magnetic interactions $(2\Delta_m)$ [7], i.e.,

$$2\Delta = 2\Delta_s + 2\Delta_m. \tag{3}$$

For different energy levels, the orientations of the axis of atom pairs can be represented using the hard-sphere model (Fig. 2) [6, 8]. Reversible (isomorphic transition) and irreversible (polymorphic transition) processes occur in amorphous materials. The orientation of the axis of atom pairs is a mirror image in the marked plane. Figure 2 shows the migration of the atom according to the orientation of the arrowhead. The numerical analysis of the magnetic susceptibility disaccomodation curve for the continuous spectrum of relaxation times is presented as [9]

$$\Delta\left(\frac{1}{\chi}\right) = \sum_{i=1}^{l} \int_{-3\beta_{\tau i}}^{+3\beta_{\tau i}} \frac{\mathrm{d}z}{\beta_\tau\sqrt{\pi}} \frac{I_{\mathrm{pi}}T_{pi}}{T} \mathrm{e}^{-(z/\beta_{\tau i})^2} \times \left(\mathrm{e}^{-t_1/\tau_{mi}\exp(z)} - \mathrm{e}^{-t_2/\tau_{mi}\exp(z)}\right), \tag{4}$$

where:

τ_m — average value of the relaxation times τ,

T — temperature, at which the maximum occurs,

I_{pi} — intensity,

β — distribution width

z — intensity of the i-th process at the peak temperature.

This function allows to present the temperature dependence of magnetic susceptibility disaccomodation for several relaxation processes.

The paper will present the results of magnetic susceptibility disaccomodation tests performed for a bulk amorphous alloy $Fe_{63}Co_8Y_8W_1B_{20}$ in the form of a rod with a diameter of 1 mm and a ribbon after solidification.

2. Experimental procedure

Test samples were made of high-purity ingredients: Fe — 99.99 at.%, Co — 99.999 at.%, Y — 99.99 at.%, Nb — 99.9999 at.%, Zr — 99.99 at.%. Boron was introduced in the form of an alloy with the chemical composition of $Fe_{45.6}B_{54.4}$. The first stage of producing test samples was the preparation of a crystalline ingot. Weighed alloy components in 10 g portions were melted in an arc furnace. Smelting took place in an inert gas atmosphere. The ingots were melted three times on each side to mix the alloy components well. The ingots prepared in this way were cleaned mechanically and in an ultrasonic bath. Then they were divided into lighter pieces, which were used in the further process of preparing research material. Prepared portions of the material were placed in a quartz capillary, which was placed between a copper mold and compressed argon. The alloy melted using eddy currents was injected under argon pressure into a copper mold with a hollow core in the form of a rod with a diameter of 1 mm and a length of 20 mm. The structure of the rods was checked using a Bruker X-ray diffractometer, model ADVANCE 8. The sample was scanned in the 2θ angle range from 30 to 100° with a measurement step of 0.02° and a measurement time

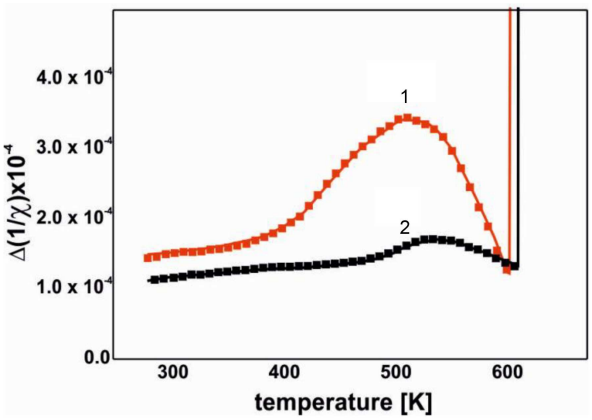

Fig. 3. Isochronous disaccomodation curves of magnetic susceptibility for the $Fe_{63}Co_8Y_8W_1B_{20}$ alloy in the form of: (line 1) ribbons with a thickness of 30 μm, (line 2) rod with a diameter of 1 mm.

of 3 s. The disaccomodation of magnetic susceptibility was measured on an automated system based on the transformer method. The measurement was made from room temperature to the temperature at which the Hopkinson peak was observed. The rods were closed with a yoke made of superpermalloy, which allowed the magnetic flux to flow. Then, 30 turns of the secondary and primary windings were wound on the sample.

3. Results

Figure 3 shows the temperature dependence of the disaccomodation of the initial magnetic susceptibility measured in the temperature range from 300 to 600 K. Disaccomodation is a measure of the temporal stability of magnetic susceptibility, which can be observed in the range of low magnetic fields up to $0.4H_C$, the so-called Rayleigh area.

Magnetic susceptibility disaccomodation measurements carried out for samples of the tested alloy after solidification were performed three times in a given temperature range, which was intended to remove irreversible structural relaxations (polymorphic transitions) occurring during the measurement. These relaxations constitute a more stable energy configuration compared to that corresponding to reversible relaxation processes (isomorphic transitions).

Isochronous magnetic susceptibility disaccomodation curves are clearly dependent on the manufacturing method. Higher magnetic susceptibility disaccomodation rates can be observed for the sample produced at a higher cooling rate during melt-spinning. For the injection method, the magnetic susceptibility disaccomodation curve is much lower.

The isochronous disaccomodation curve of the magnetic susceptibility can be divided into three areas:

1. The area where only temperature-independent relaxation amplitudes are observed,
2. The area where the maximum of disaccomodation occurs, describing precisely the intensity of this phenomenon, where all thermal features of the entire process can be observed,
3. An area where a sharp decrease in the intensity of disaccomodation is observed, occurring just below the Curie temperature. This behavior of disaccomodation is related to the so-called Hopkinson maximum [10], which occurs when there are rapid changes in the constants of the ferromagnetic material near the ferro–paramagnetic phase transition.

The second area is where most point relaxations occur. These relaxations are related to the cooling rate of the alloy and not to its chemical composition itself.

4. Conclusions

The shape of the isochronous disaccomodation curves of magnetic susceptibility is related to the presence of free volumes. A larger amount of free volumes occurs in the sample produced at a higher cooling rate. The structure then suddenly freezes, which results in an increased number of free volumes being created. The extended solidification time favors the free movement of atoms in the sample volume and the creation of configurations with lower internal energy. This state of affairs has a direct impact on the reduction of free volumes, which is clearly shown by the research results presented in this work.

References

[1] E. Kneller, *Ferromagnetismus*, Springer-Verlag, Berlin 1962.

[2] J.W. Moroń, *Postępy Fizyki* **22**, 623 (1971) (in Polish).

[3] P. Allia, F.E. Luborky, R. SatoTurtelli, G.P. Soardo, F. Vinai, *IEEE Trans. Magn.* **17**, 2615 (1981).

[4] B. Jeż, P. Postawa, A. Kalwik, M. Nabiałek, K. Błoch, S. Walters, A.V. Sandu, *Acta Phys. Pol. A* **142**, 157 (2022).

[5] J. Schneider, B. Springmann, K. Zaveta, in: *5th Int. Conf. on Rapid Quenched Metals*, Eds. S. Steeb, H. Warlimont, Elsevier Science Publisher B.V., Amsterdam, 1985 p. 1295.

[6] K. Błoch, M. Nabiałek, B. Jeż, J. Gondro, A.V. Sandu, M.M.A.B. Abdullah, *Acta Phys. Pol. A* **142**, 160 (2022).

[7] M. Bourrous, H. Kronmuller, *Phys. Stat. Sol. (a)* **113**, 169 (1989).

[8] H. Kronmüller, M. Fähnle, *Micromagnetism and the Microstructure of Ferromagnetic Solids*, Cambridge University Press, 2003.

[9] W.H. Ciurzyńska, *Seria: Fizyka nr 2*, Wydawnictwo WIPMiFS, Częstochowa 2002 (in Polish).

[10] J. Olszewski, L.K. Varga, J. Zbroszczyk, W. Ciurzyńska, M. Hasiak, A. Błachowicz, *J. Magn. Magn. Mater.* **215–216**, 416 (2000).

Proceedings of "Applications of Physics in Mechanical and Material Engineering" (APMME 2023)

Effect of Nitrogen Doping on the Electrochemical Properties of Lithium Battery Anode of Activated Carbon

P. Trihutomo[a,*], P. Puspitasari[a] and M. Nabiałek[b]

[a] *Mechanical Engineering and Industrial Department, Universitas Negeri Malang, Jl Semarang 5, Malang, 65114, Indonesia*
[b] *Department of Physics, Faculty of Production Engineering and Materials Technology, Czestochowa University of Technology, al. Armii Krajowej 19, 42-200 Częstochowa, Poland*

Doi: 10.12693/APhysPolA.144.395 *e-mail: prihanto.trihutomo.ft@um.ac.id

This research discusses the effect of using nitrogen-doped activated carbon as an anode material for lithium batteries on the resulting electrochemical properties. The performance of pure activated carbon was compared with that of nitrogen-doped activated carbon with concentrations of 1:3 and 1:5. Activated carbon that has been synthesized into nitrogen-doped activated carbon is tested for its physical properties through Fourier-transform infrared spectroscopy and scanning electron microscopy instruments. The galvanostatic charge–discharge test results showed that each sample had a smaller loss of capacity as the nitrogen doping concentration increased. Pure activated carbon has a specific capacity of 105.549 mAh/g, 1:3 nitrogen-doped activated carbon of 108.214 mAh/g, and 1:5 nitrogen-doped activated carbon of 113.635 mAh/g.

topics: activated carbon, nitrogen doping, anode, lithium battery

1. Introduction

New and renewable natural resources are needed, especially due to increasing global warming and limited fossil resources [1]. One of the most important aspects of utilizing new renewable energy sources is access to energy transmission and storage technology. Currently, the limited development of renewable energy is hindered by storage and transmission technologies due to their environmental impacts [2]. Lithium batteries are one type of excellent energy storage device that can convert chemical energy into electrical energy. However, producing these batteries with high energy density and power density through economical and environmentally friendly processes is still a big challenge.

Current anode materials exhibit high specific capacity, cycle stability, and safety, but their high cost and relatively small current density limit their practical application [3]. Activated carbon, which has a large surface area, high absorption, and minimal charging time, is suitable for application in several materials, including anode materials in batteries. In maximizing the potential of activated carbon in the form of its capacitance properties, nitrogen doping can be utilized to increase the capacity of activated carbon [4].

Doping nitrogen in the carbon structure will result in a reduction of solutes in the battery cell electrolyte. This mechanism makes the electron capture greater, and the battery performance increases [5]. This research discusses the effect of nitrogen doping on the electrochemical properties of lithium battery anodes. Activated carbon was synthesized with the addition of nitrogen doping and then tested for physical properties using scanning electron microscopy (SEM), X-ray diffraction (XRD), and Fourier-transform infrared spectroscopy (FTIR). The synthesized material was fabricated in the form of battery cells and then tested for performance using galvanostatic charge–discharge (GCD).

2. Materials and method

The main materials used include activated carbon, urea ($(NH_2)_2CO$) as a doping source, and KOH as an activator. Other materials include distilled water and HCl acid.

Activated carbon was impregnated in a solution of urea and KOH activator. The mass ratio of activated carbon:KOH:urea is (12 g):(24 g):(36 and 60 g). The solution was homogenized using a magnetic stirrer for 2 h at 750 rpm. The resulting

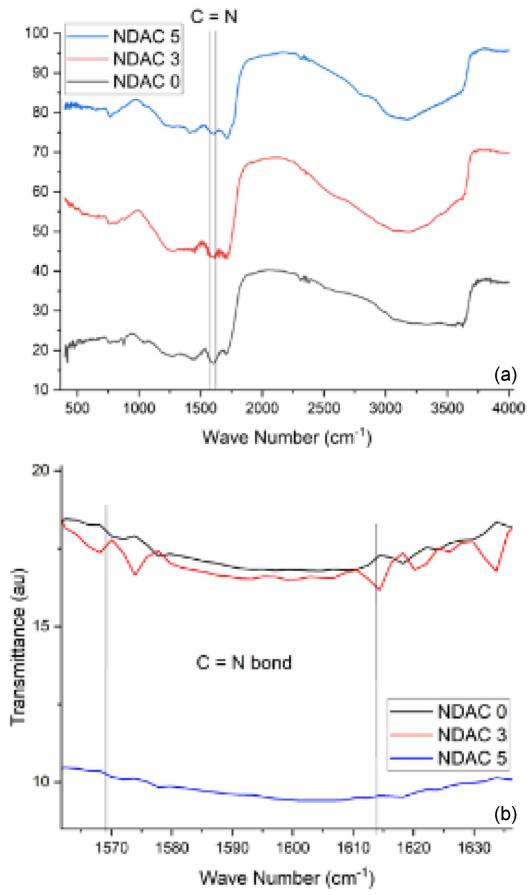

Fig. 1. (a) Result of FTIR functional group (b) C=N bonding functional group.

solution was then sonicated for 30 min. After sonication, the solution was heated in an oven at 200°C for 4 h. The resulting material was crushed for 1 h. The resulting powder was then soaked in an HCl solution for 24 h to neutralize the pH. Then, the solution was filtrated with filter paper and dried in the oven. After that, the resulting material was crushed for 1 h and sieved through a 200 mesh. Each sample was named according to the doping ratio of urea as a nitrogen source (NDAC 3 and NDAC 5), and pure activated carbon was named NDAC 0.

3. Results and discussion

Figure 1 shows the transmittance intensity of the C=N bond at wave numbers from 1565 to 1615 cm^{-1}. The decrease in transmittance absorption value in each sample indicates an increase in C=N absorption intensity as the nitrogen doping concentration increases [6]. This increase causes the breaking of inter-carbon bonds by nitrogen atoms [4]. This nitrogen doping affects the structure of the carbon battery anode, causing the grain size to decrease, the structure to become more crystalline, and the surface area to increase [7].

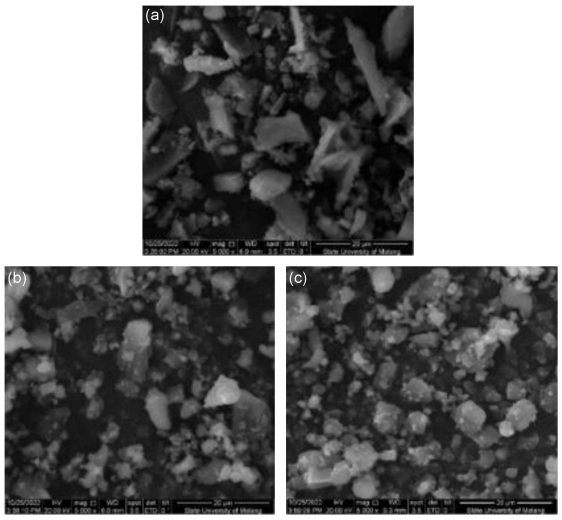

Fig. 2. The morphology of samples (a) NDAC 0,(b) NDAC 3, (c) NDAC 5.

SEM morphology is shown in Fig. 2. The morphology of the pure activated carbon sample (NDAC 0) shows a larger grain size compared to the NDAC 3 and NDAC 5 samples. This morphology is influenced by nitrogen doping and the addition of KOH, which reacts to form CO and CO_2. The smaller grain size results in a higher surface area of the activated carbon. This high surface area improves the absorption of the electrolyte by the anode. This mechanism also increases the good electronic conductivity of the electrode [7].

Figure 3 shows the specific capacity of each sample at 0.2 C of C_{rate}. The specific capacity is influenced by the amount of current that the material can store, voltage, Crate, the number of test cycles, and battery conditions. The amount of voltage is directly proportional to the specific capacity of the battery [8]. The more cycles the battery passes, the smaller the specific capacity produced. This is due to the formation of the solid electrolyte interphase (SEI) layer by lithium ions [9].

Figure 3 shows the slope of the graph that occurs in the range from 3.4 to 4 V, which indicates a change in chemical potential due to changes in the concentration of the electrolyte solution due to the incoming and outgoing currents during the battery charge–discharge process [10]. The addition of nitrogen doping affects the specific capacity, which makes the carbon structure more porous. An optimized porous structure can increase ion/electron transfer faster [11]. Nitrogen doping results in a smaller sample grain size, thanks to which the surface area is high and the capacity is higher [3].

Figure 4 shows that battery capacity tends to decrease as the battery usage cycle increases. This is due to the poor condition of the battery. Figure 4 also shows that nitrogen-doped samples tend to have lower capacity loss compared to pure activated carbon samples. The decrease in battery

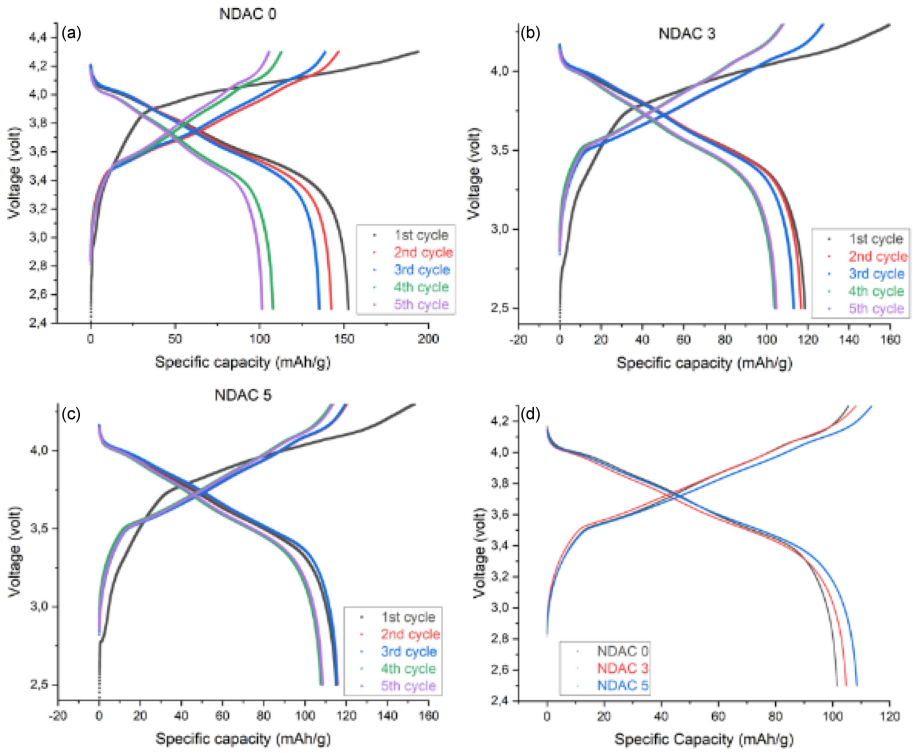

Fig. 3. Graphic of specific capacity of battery anode materials at 5 testing cycles (a) NDAC 0, (b) NDAC 3, (c) NDAC 5, (d) 5th cycle of each sample.

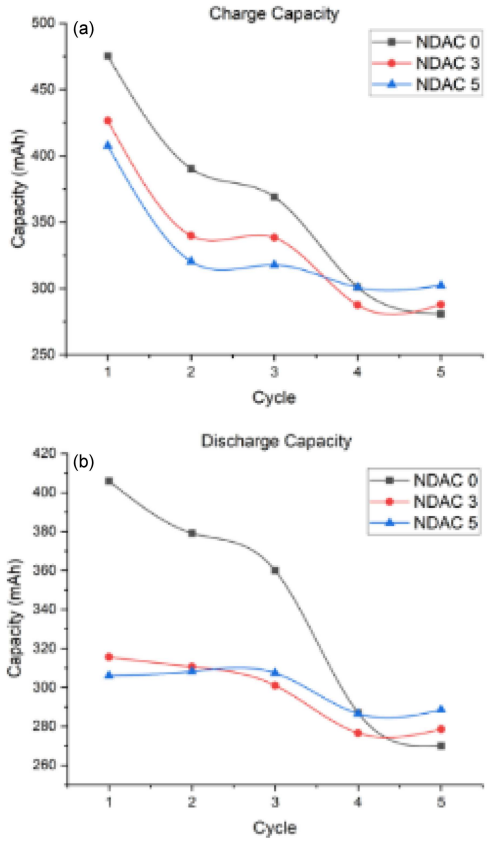

Fig. 4. Response and recovery of Sn-doped ZnO at the exposure of 200 ppm ammonia.

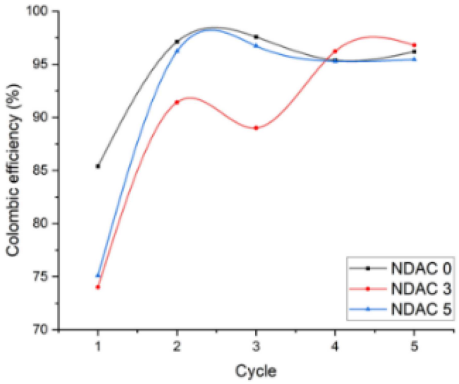

Fig. 5. Coulombic efficiency at 5 cycles for each sample.

capacity is mainly caused by intercalation and deintercalation in the battery, as well as electrolyte decomposition [7]. The addition of nitrogen is proven to break the bonds between carbons, reducing the grain size and increasing the crystallinity, thus making the loss of capacity in the battery smaller [4].

Figure 5 shows that the Coulombic efficiency tends to fluctuate in each sample. The poor Coulombic efficiency in the first cycle is due to the battery being new and the thickening of the SEI film [12]. The Coulombic efficiency of each sample is also affected by the electrical conductivity of the anode due to the addition of nitrogen, which affects the physical properties of the material [13].

4. Conclusions

Nitrogen doping causes an increase in the bonding intensity of carbon atoms and nitrogen atoms. This leads to an increase in the size of the smaller grains. Nitrogen doping also affects the capacity and Coulombic efficiency of the battery.

References

[1] S. Zong, M.Sc. thesis, University of South Africa, 2021.

[2] A.D. Roberts, X. Li, H. Zhang, *Chem. Soc. Rev.* **43**, 4341 (2014).

[3] J. Wang, W. Zhang, J. Li, B. Wang, C. Xu, C. Lai, *J. Mater.* **7**, 1083 (2021).

[4] M. Inagaki, M. Toyoda, Y. Soneda, T. Morishita, *Carbon N.Y.* **132**, 104 (2018).

[5] J. Yan et al., *Adv. Funct. Mater.* **27**, 1 (2017).

[6] B.H. Stuart, *Infrared Spectroscopy: Fundamentals and Applications*, 2005.

[7] J.P. Paraknowitsch, A. Thomas, *Energy Environ. Sci.* **6**, 2839 (2013).

[8] Y. Qian, S. Jiang, Y. Li et al., *Adv. Energy Mater.* **9(34)**, 1 (2019).

[9] C. Wang, S. Mutahir, L. Wang, W. Lei, X. Xia, X. Jiao, Q. Hao, *Appl. Surf. Sci.* **509**, 144882 (2020).

[10] M. Qi, J. Long, Y. Ding, X. Diao, Y. Meng, L. Wang, Z. Pan, J. Liu, *J. Alloys Compd.* **889**, 161733 (2022).

[11] J. Zhan, S. Deng, Y. Zhong, Y. Wang, X. Wang, Y. Yu, X. Xia, J. Tu, *Nano Energy* **44**, 265 (2018).

[12] X. Du, H. Zhao, Z. Zhang, Y. Lu, C. Gao, Z. Li, Y. Teng, L. Zhao, K. Świerczek, *Electrochim. Acta* **225**, 129 (2017).

[13] Y. Xu, F. M. Mulder, *Int. J. Hydrogen Energy* **46**, 19542 (2021).

Proceedings of "Applications of Physics in Mechanical and Material Engineering" (APMME 2023)

Multiscale Analysis of the Mechanical Properties of the Crack Tip Region

S. Zhufeng[a], M.A.A. Mohd Salleh[b,*], B. Jeż[c] and N. Yusoff[a]

[a]*School of Mechanical Engineering, Engineering Campus, Universiti Sains Malaysia, 14300 Nibong Tebal, Penang, Malaysia*
[b]*Faculty of Chemical Engineering and Technology, Universiti Malaysia Perlis, 02600 Arau, Perlis, Malaysia*
[c]*Department of Technology and Automation, Faculty of Mechanical Engineering and Computer Science, Czestochowa University of Technology, al. Armii Krajowej 19c, 42-200 Częstochowa, Poland*

Doi: 10.12693/APhysPolA.144.399 *e-mail: menorwahida@usm.my

This paper attempts to find the possibility of describing the supplementary parameters of the macroscopic crack strength field based on the variation at the microscopic level. The analysis focuses on the development of cracks in the vicinity of the crack tip of a central crack panel made from iron material with a cubic crystal structure under tensile loading. We use the combination of finite element and molecular dynamics simulation methods. Molecular dynamics simulation analysis shows that the motion velocity of molecules near the crack tip region is less than the Rayleigh wave velocity, V_R, which is about 0.22 V_R. The average velocity is smaller in other directions that are not parallel to the crack. The velocity of the molecular near the crack tip indicates the ductile phenomenon of the crack tip region because it comes from the potential energy, which means that on the crack extension line, the kinetic energy of the molecular motion is greater than that in the other directions but is close to that in the 45° direction. It shows that the crack expansion direction is still mainly along the crack extension line under the load.

topics: multiscale analysis, molecular dynamics simulation, finite element modeling, lattice constant

1. Introduction

Due to the singularity of the crack tip, the definite condition of stress fields at the crack tip and the crack tip extension are difficult to characterize through finite element methods (FEM). Researchers have tried to find the intrinsic reason for the dynamic extension of the crack tip by using multiscale modeling, which is an alternative approach to studying local physical phenomena in a large structure with microstructural features. Many multiscale analyses of the crack tip region from orders of centimeters to orders of nanometers have been conducted [1–5], focusing on explaining the change in crack extension from the microscopic level.

Recently, finite element and molecular dynamics techniques have been introduced in this aspect to model the material nonlinearity of the crack tip region. However, the common difficulty in creating such cross-scale models is determining how to properly handle the transition relationship between the lattice model and the continuum solid model. The cause of this problem arises from the essence of the internal force at different scales.

Because of the difficulty of accurately describing the crack tip stress field with the parameter J-integral, the present study proposes a combination of finite element and molecular dynamics simulation of the extension of the crack tip region, aiming to find a fittable parameter associated with the microscopic crack extension, along with the macroscopic parameter to describe the crack tip stress field. The analysis framework relies on the common nodes of the FEM area and the molecular dynamics (MD) zone, in combination with the stress field of the MD region obtained through finite elements. Through this, the applied load is transmitted to the MD area for relaxation, so that the internal atoms are fully relaxed and the movement of the atoms in the MD area at the crack tip can be observed at each time step.

2. Materials and method

2.1. Finite element modeling and analysis

To explore the development of the crack under load, the MD simulation of the crack tip region of the central crack panel under tension was conducted using open-source software, XMD. The central crack panel (CCP) specimen with $a/W = 0.5$, $W = H = 20$ mm, which is subjected to a uniform tensile load, is shown in Fig. 1a. Considering the

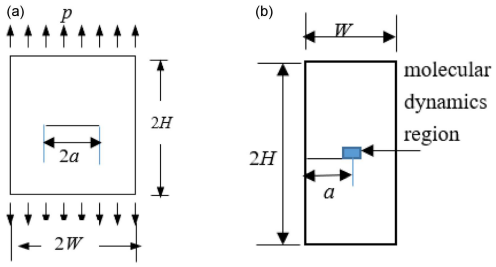

Fig. 1. (a) Central crack panel model. (b) The molecular dynamics region of central crack panel model.

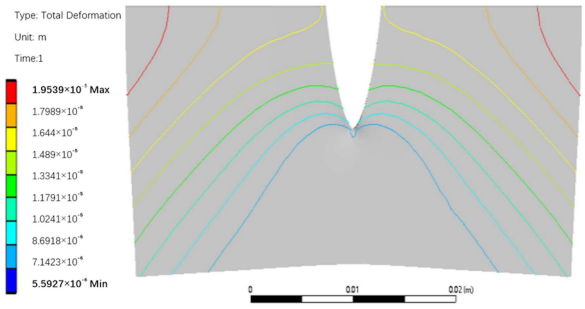

Fig. 2. The total deformation under tensile load of 100 MPa.

symmetry of the geometry and the load, only half of the specimen is taken for finite element modeling. The material is assumed to be 304 stainless steel with a yield stress, σ_0, of 205 MPa. For molecular dynamics simulations, the MD region of the central crack panel model is shown in Fig. 1b, which is the lattice constant of the material.

For a body-centered cubic (BCC) lattice ferrite material, its lattice size is about 10^{-7} mm, so it needs the tension load to make the MD region easily reachable in a yield state. It is necessary to make the yield crack region big enough for the MD calculation. The displacement for the MD calculation is the average displacement field of the grid nodes in the MD region, which is obtained through finite element calculations. For this purpose, a uniform tensile load $p = 100$ MPa was applied to generate a ductile state at the crack tip, with a maximum equivalent von Mises stress being 871.29 MPa, which is higher than the yield stress of the material. The generated total deformation is 0.0056 mm, as shown in Fig. 2, which is fit for the MD simulation.

2.2. Kinetic analysis of the cross-scale crack tip zone

Figure 3a shows the crack tip of the molecular dynamics region obtained through the finite element calculations, which is 44 lattices up, 22 latices left, and 23 latices right from the lattice node of the displacement field. Considering the difference between

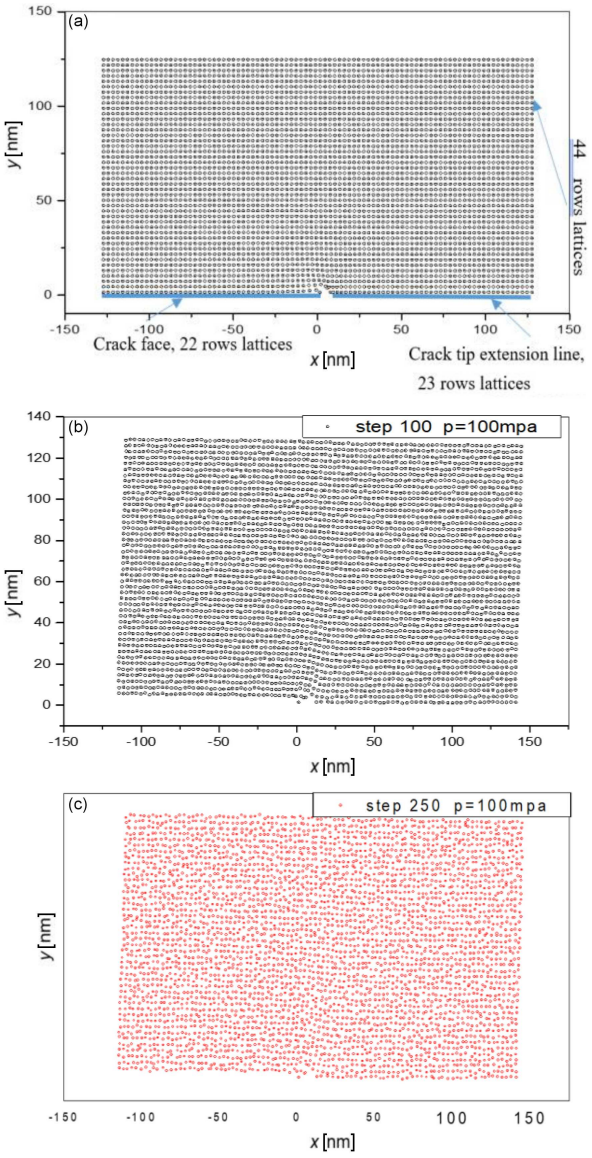

Fig. 3. (a) Molecular dynamics zone at (b) 100th step, and (c) 250th step.

the continuum and the discretized models, the displacement field obtained by the finite elements is appropriately modified by the means of multiplication of the flexibility coefficient as an applied displacement field for the molecular dynamic simulation. The empirical many-body embedded atom method (EAM) potential function is used to relax the molecules and obtain the motion velocity and kinetic energy of the atoms under the applied displacement field and the potential function.

In this study, the tracking analysis of the atomic motion in front of the crack tip under external loading was conducted. The mechanism of the crack expansion was configured by increasing the external load, repeating one or two steps until the crack begins to expand, and then observing the movement of the atoms in the MD area. The initial position of the atoms in the MD region is shown in Fig. 3a.

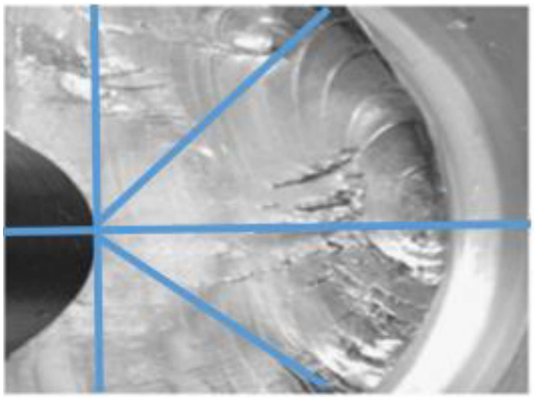

Fig. 4. The three characteristic lines clearly appearing in a part-through surface crack profile [6].

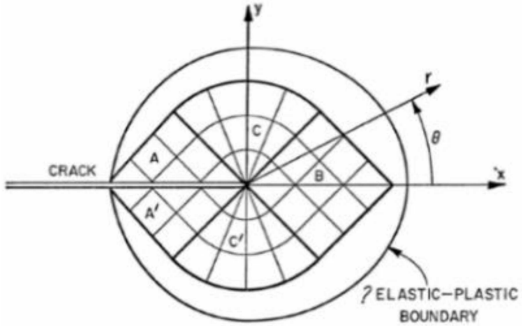

Fig. 5. Prandtl slip line field.

TABLE I

Atomic motion and kinetic energy in different directions in the crack tip region.

	Angle [°]		
	0	45	90
Average speed [nm/s]	300.88	266.8	257.3
Kinetic energy ($\times 10^{-9}$) [J]	1.413	1.172	1.095

The crack tip region was analyzed with MD software, and the positions of the atomic relaxation at the 100th and 250th steps are shown in Fig. 3b and Fig. 3c, respectively.

3. Results and discussion

The molecular dynamics simulation shows that there are nanoscale slip lines at the crack tip, which are also seen in a part-through surface crack profile shown in Fig. 4 [6]. The simulated average velocity and kinetic energy of the atoms at the crack development line at angles 0°, 45°, and 90° under loadings are summarized in Table I.

The data show that the kinetic energy of the lattice is lowest in the direction perpendicular to the crack line, and as compared to this direction, the kinetic energy of the lattice at the 45° line is about 7% higher and about 29% higher in the crack extension line. This kinetic energy variation indicates that the residual strength of the crack tip is different in different regions. The three characteristic lines suggest that the material is no longer isotropic in the crack tip region, which explains why the passivation of the crack tip region strengthens the extension of the crack and affects the extension direction of the crack in the microstructure perspective.

The MD simulation results also agree well with the Prandtl slip line field (Fig. 5), which assumes plasticity surrounds the crack tip completely. The consistency of these findings ensures that joining the characteristic-line-related parameter and the J-integral parameter to describe the crack strength field is feasible.

4. Conclusions

The molecule along the crack path ahead of the crack tip is shown to have higher energy than the other directions. It is the energy aggregation band under the external load, which is in a relatively unstable state and is the most likely direction for the crack to grow.

Due to the stress concentration at the crack tip, the plastic yield zone will appear in the crack tip zone in response to the external load. By then, the material in this zone is anisotropic, and the deformation in this area is no longer elastic. Therefore, the characterization of the stress intensity factor becomes difficult.

As molecular kinetic energy changes with line angles related to the direction of the crack extension, a fittable parameter related to the changes of characteristic lines can be considered as an alternative parameter describing the microstructural changes. Therefore, together with the macro stress field, the crack tip stress fields can be described more accurately.

References

[1] E.B. Tadmor, R.E. Miller, *Modell. Simul. Mater. Sci. Eng.* **25**, 071001 (2017).

[2] S. Kohlhoff, P. Gumbsch, H. Fischmeister, *Philos. Mag. A* **64**, 851 (1991).

[3] S. Erkoc, *Phys. Rep.* **278**, 79 (1997).

[4] H. Rafii-Tabar, L. Hua, M. Cross, *J. Phys. Condens. Matter* **10**, 2375 (1998).

[5] J. Chen, X. Wang, H. Wang, J.D. Lee, *Eng. Fract. Mech.* **77**, 736 (2010).

[6] R.J. Shipley, W.T. Becker, 2002. *ASM Handbook*, 2002, p. 11.

Proceedings of "Applications of Physics in Mechanical and Material Engineering" (APMME 2023)

Comparing C_3N and C_3B Anode Materials with Graphene Using DFT Calculations

G.T. Kasprzak*

Institute of Physics, Czestochowa University of Technology, Armii Krajowej Ave. 19, 42-200 Częstochowa, Poland

Doi: 10.12693/APhysPolA.144.402 *e-mail: grzegorz.kasprzak@pcz.pl

The growing demand for lithium, which is essential for the production of batteries, has led to a significant rise in the price of lithium. The quest for novel materials that could enhance battery performance has thus become a key challenge for scientists. In this regard, the author conducted a comparative analysis of materials based on graphene, using density functional theory and *ab initio* molecular dynamics methods. The materials considered for comparison include graphene, C_3B, and C_3N. For the calculations, two-layer systems of pristine graphene and graphene modified by substituting carbon atoms with boron and nitrogen were constructed. The stability of these systems was examined using the Quantum Espresso and CP2K software at 0 K and 300 K, respectively. In the search for an alternative to lithium, systems incorporating sodium and lithium intercalated between graphene layers were also included in the comparison.

topics: C_3N, C_3B and graphene, electronic properties, electrode materials, density functional theory (DFT) calculations

1. Introduction

The use of density functional theory (DFT) calculations has increasingly demonstrated its efficacy across various scientific domains, encompassing the modeling of biological systems and the exploration of novel superconductors [1, 2], and the identification of anode materials [3, 4]. In the pursuit of discovering new materials, two-dimensional materials have garnered significant attention. Notably, graphene [5], phosphorene [6–8], borophene [9], silicene [10], among others, have emerged as the most prominent examples. Employing atomic-scale modeling facilitates the exceptional opportunity to investigate and assess the stability of materials. In this study, a comparative analysis was conducted on pristine graphene and C_3N and C_3B — two graphene-like structures. The examination of the C_3N bilayer serves as a continuation of previous research on the C_3N monolayer, employing first-principles DFT calculations [11]. Notably, the study reveals the preference of Li and Na atoms to occupy the hollow sites. Within this article, comparative investigation of graphene-based materials will be presented. *Ab initio* molecular dynamics (AIMD) calculations were applied to single- and double-layer C_3B, graphene, and C_3N systems. The exploration of graphene materials is undertaken within the context of their potential as electrode materials in batteries. Hence, a comparison of these materials' properties, specifically with regard to the incorporation of lithium and sodium ions, is indispensable. The Quantum Espresso (QE) program was utilized to calculate the geometric aspects of the structures, while the CP2K program assessed their stability at a temperature of 300 K.

2. Computational methods

To study the electronic properties of the investigated material, first-principles calculations are performed within the framework of density-functional theory (DFT) [12] as implemented in the Quantum Espresso package [13]. The generalized gradient approximation of Perdew–Burke–Ernzerhof (GGA-PBE) is used for the exchange-correlation functional together with the projector-augmented wave (PAW) method. A vacuum of 20 Å was applied along the z-axis to prevent interlayer interactions from the periodic images. Van der Waals forces were taken into account in the simulation. Values of ecutrho = 50, ecutwfc = 500 and k-points = $(18, 18, 1)$ in the QE calculations were taken. Figure 1 shows the visualization of the investigated bilayer structures.

3. Results and discussion

The crystal structure of the C_3B, graphene, and C_3N monolayer has $P6/mmm$ symmetry with a hexagonal lattice. As with graphene, C_3B and C_3N

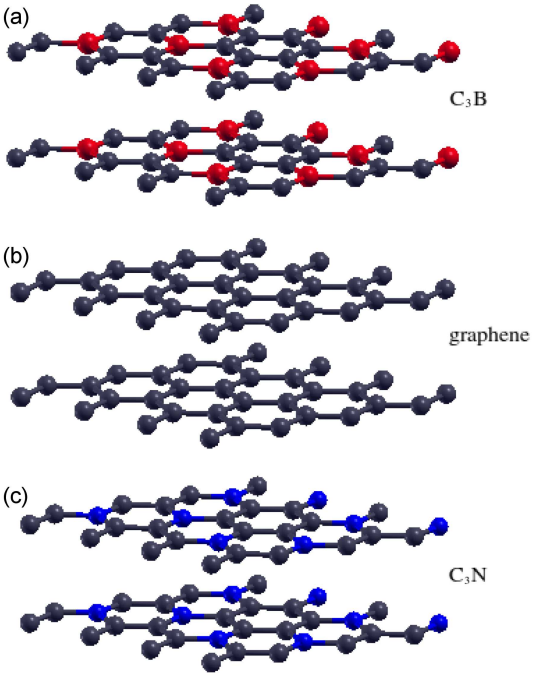

Fig. 1. Visualization of investigated bilayer materials: (a) C_3B, (b) graphene, and (c) C_3N.

have a flat structure because all B, C, and N atoms are sp^2 hybridized. In order to determine the geometry of the systems, basic cells containing a single layer of the tested materials were relaxed. In the next step, a two-layer system was created for each of the tested materials. The relaxation results of two layers with 8 atoms in the layer, and a total of 16 atoms in the cell, gave us distances between layers equal 3.6382 Å, 3.5185 Å, and 3.3661 Å for C_3B, graphene, and C_3N, respectively. Once the final coordinates of the pristine bilayer were found, the systems were intercalated with four Li/Na atoms per cell put in the hole sites. The most important parameter describing materials is binding energy. To determine the stability of the tested pristine bilayers, the binding energy value was calculated according to the following formula

$$E_{\text{b.bilayer}} = E_{\text{bilayer}} - 2E_{\text{monolayer}}. \tag{1}$$

The binding energy of Li and Na atoms between the layers was calculated as follows

$$E_{\text{b.Li/Na}} = E_{\text{bilayer.Li/Na}} - E_{\text{bilayer}} - 4E_{\text{Li/Na}}. \tag{2}$$

According to the definitions of binding energies, the negative value of binding energy suggests that the presented bilayer systems are energetically more favorable and stable at temperature 0 K. Table I contains all relevant calculations from the point of view of stability and degeneracy. After Li intercalation, the distance decreases slightly for C_3B and increases slightly for graphene. Na intercalation causes a significant increase in the distance between the layers for both C_3B (19.27%) and graphene (37.68%).

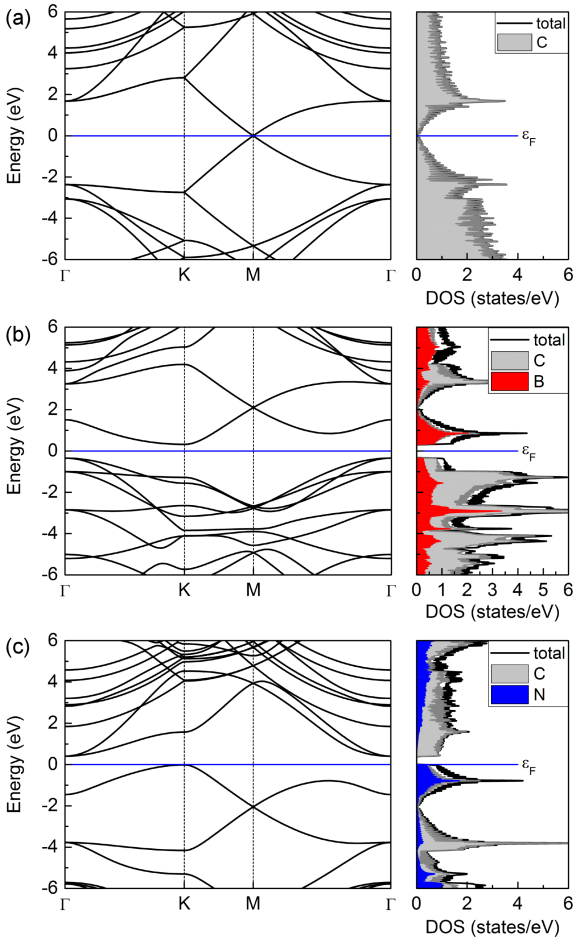

Fig. 2. Electronic band structure with partial density of states (DOS) along the Γ–K–M–Γ high-symmetry line for monolayers: (a) graphene, (b) C_3B, (c) C_3N.

TABLE I

The calculated binding energies ($E_{\text{b.bilayer}}$, $E_{\text{b.Li}}$, and $E_{\text{b.Na}}$) and interlayer distance (d) for pristine bilayer systems and for systems after intercalation by Li/Na atoms.

	C_3B	graphene	C_3N
$E_{\text{b.bilayer}}$ [Ry]	−0.0929	−0.0864	−0.0745
$E_{\text{b.Li}}$ [Ry]	−0.7792	−0.2324	no data avail.
$E_{\text{b.Na}}$ [Ry]	−0.2133	0.3149	no data avail.
d_{pristine} [Å]	3.6382	3.5185	3.3661
$d_{\text{int.Li}}$ [Å]	3.6062	3.5991	no final coord.
$d_{\text{int.Na}}$ [Å]	4.3393	4.8443	no final coord.

Nitrided graphene C_3N can be excluded as a potential anode material because, after Li/Na intercalation, final coordinates were not found.

Calculations of the density of electronic states and the energy gap were made in order to answer the question of whether the investigated structures belong to insulators, semiconductors, semimetals or conductors. That is shown in Fig. 2 and Fig. 3

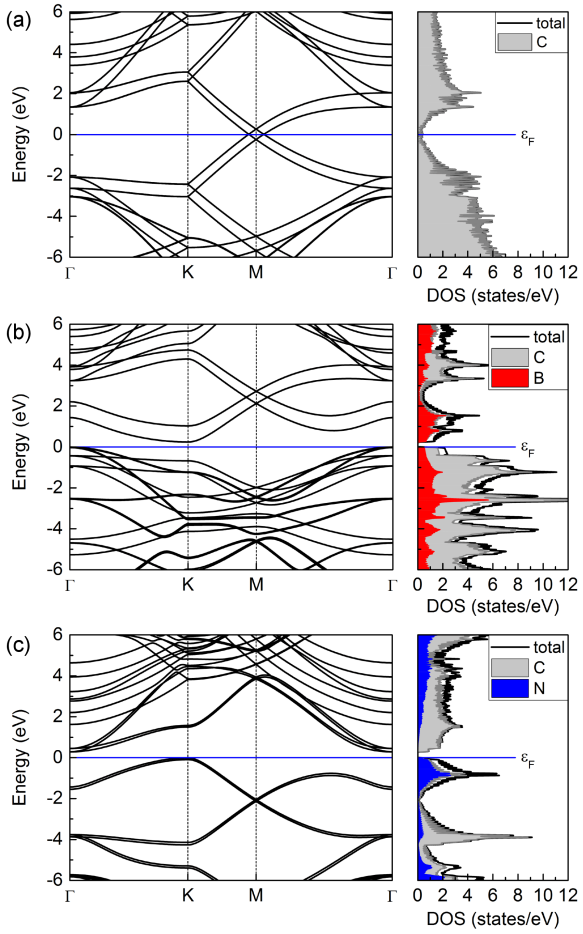

Fig. 3. Electronic band structure with partial density of states (DOS) along the Γ–K–M–Γ high-symmetry line for bilayers: (a) graphene, (b) C_3B, (c) C_3N.

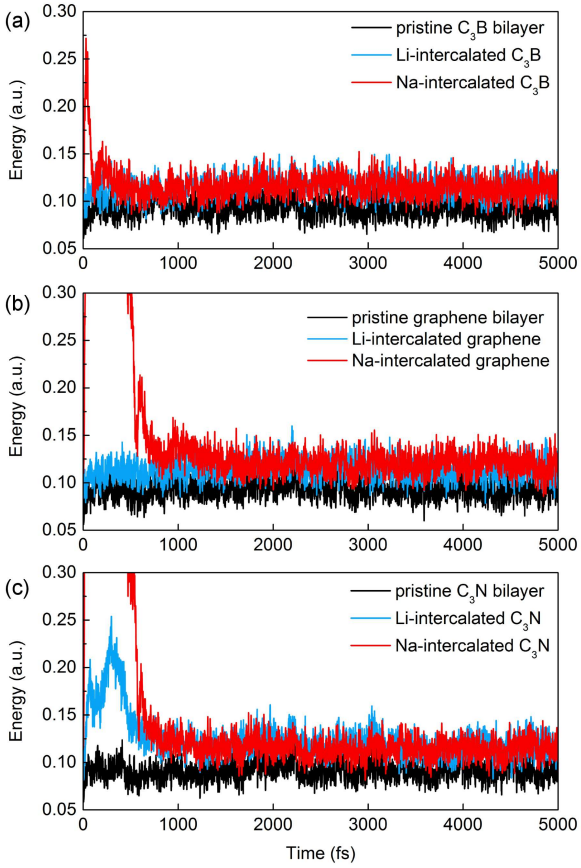

Fig. 4. Kinetic energy of (a) pristine and intercalated C_3B bilayer, (b) pristine and intercalated graphene bilayer, and (c) pristine and intercalated C_3N bilayer as a function of time.

for monolayer and bilayer pristine systems, respectively. As we see, monolayer graphene is semimetal with a Dirac cone at the Fermi level, while bilayer graphene presents a metal character. When it comes to systems with boron or nitrogen, we are dealing with semiconductors with a small band gap.

To explain dynamic stability at room temperature, all materials were investigated with CP2K. Calculations were made for pristine bilayer systems and after Li/Na intercalation. The kinetic energies as a function of time are presented in Fig. 4. All pristine materials show structural stability at room temperature. After intercalation, the C_3B material shows the greatest stability for both lithium and sodium.

4. Conclusions

First-principles calculations based on density functional theory have been carried out to investigate the potential of anode material of two C_3B layers, graphene, and a C_3N system with intercalation of Li and Na atoms. As Quantum Espresso calculations show, all bilayer pristine systems are stable at 0 K. AIMD calculations confirm the stability of pristine at room temperature. In addition, AIMD calculations showed an interesting fact of layer shifting in the case of graphene and C_3B, while C_3N shows a strong attraction between the layers. The distance between the layers is the greatest for the system with boron and the smallest for the one with nitrogen. After Li/Na intercalation, nitrogen systems do not return final coordinates, so the lowest energy ground state cannot be found. In the case of the C_3B system, after lithium intercalation, the distance between the layers slightly decreases by 0.88%, while after intercalation with sodium it significantly increases by 19%. For graphene after lithium intercalation, the increase in the distance between the layers is insignificant by 2.3%, sodium intercalation causes a significant increase in the distance between graphene layers by 37.7%. In the case of the C_3N material, it can be excluded as a potential material in the context of anode construction. In turn, replacing one in four carbon atoms with boron can improve the physical properties of the anode for both lithium and sodium electrolytes.

Acknowledgments

This research was supported in part by PLGrid Infrastructure.

References

[1] A.P. Durajski, R. Szczęśniak, Y. Li, C. Wang, J.-H. Cho, *Phys. Rev. B* **101**, 214501 (2020).

[2] A.P. Durajski, R. Szczesniak, *Phys. Chem. Chem. Phys.* **23**, 25070 (2021).

[3] G.T. Kasprzak, R. Szczesniak, A.P. Durajski, *Comput. Mater. Sci.* **225**, 112194 (2023).

[4] A.P. Durajski, G.T. Kasprzak, *Physica B* **660**, 414902 (2023).

[5] K.S. Novoselov, A.K. Geim, S.V. Morozov, D. Jiang, Y. Zhang, S.V. Dubonos, I.V. Grigorieva, A.A. Firsov, *Science* **306**, 666 (2004).

[6] A.P. Durajski, K.M. Gruszka, P. Niegodajew, *Appl. Surf. Sci.* **532**, 147377 (2020).

[7] A. Khandelwal, K. Mani, M.H. Karigerasi, I. Lahiri, *Mater. Sci. Eng. B* **221**, 17 (2017).

[8] M. Alidoust, M. Willatzen, A.-P. Jauho, *Phys. Rev. B* **99**, 125417 (2019).

[9] A.J. Mannix, X.-F. Zhou, B. Kiraly et al., *Science* **350**, 1513 (2015).

[10] H. Oughaddou, H. Enriquez, M.R. Tchalala, H. Yildirim, A.J. Mayne, A. Bendounan, G. Dujardin, M. Ait Ali, A. Kara, *Prog. Surf. Sci.* **90**, 46 (2015).

[11] G.T. Kasprzak, K.M. Gruszka, A.P. Durajski, *Acta Phys. Pol. A* **139**, 621 (2021).

[12] R. Parr, W. Yang, *Density-Functional Theory of Atoms and Molecules*, Oxford University Press, Oxford 1989.

[13] P. Giannozzi, O. Andreussi, T. Brumme et al., *J. Phys. Condens. Matter* **29**, 465901 (2017).

Proceedings of "Applications of Physics in Mechanical and Material Engineering" (APMME 2023)

Study of Airfoil Flow Control with Microcylinders Using Optical Method

R. Gnatowska[a,*], K. Gajewska[a] and T. Blejchař[b]

[a] *Czestochowa University of Technology, Dąbrowskiego 69, 42-201 Czestochowa, Poland*
[b] *VŠB-Technical University of Ostrava, 17. listopadu 15/2172, 708 00 Ostrava-Poruba, Czech Republic*

Doi: 10.12693/APhysPolA.144.406 *e-mail: renata.gnatowska@pcz.pl

This study aims to evaluate the effect of circular-shaped microcylinders on the flow field around an airfoil, using time-resolved particle image velocimetry. The results show that microcylinders can significantly modify the flow pattern around the NACA 0012 airfoil. The optimal configuration of microcylinder-airfoil depends on the angle of attack and the position of the microcylinder. The obtained results have practical implications for the development of more efficient and sustainable aircraft designs and wind turbine blades. The paper presents a physical analysis of flow fields using streamlines and vorticity structures to illustrate mechanisms of flow control for improving the aerodynamic properties of the airfoil. Overall, this work provides new insights into the fundamental physics of flow control using microcylinders, including general physics and optics, with potential application in various contexts, such as aerodynamics, flow control, airfoil design, optical diagnostics, and particle image velocimetry techniques.

topics: velocity measurements, optical method, experiments, time-resolved particle image velocimetry (TR-PIV)

1. Introduction

Airfoils are objects commonly studied by scientists due to their wide range of applications in aviation and wind turbine technologies [1]. The main focus of scientists is to improve the aerodynamic properties of airfoils in order to enhance their efficiency and performance. One of the parameters that intensively affect the airfoil performance is flow separation at high angles of attack (AOA) on the suction surface and the wake region behind it. Increased angles of attack lead to a sudden expansion of the wake region, causing stall occurrence, resulting in a notable increase in drag coefficient and decrease in lift coefficient. Reducing skin friction drag is also crucial for enhancing aerodynamic performance. Therefore, it is crucial to understand the physics of the flow as it governs the emerging interactions within modern engineering structures [2]. Various methods, both passive and active, have been proposed to enhance aerodynamic performance. These methods include the application of a sinusoidal surface [3], the use of air jets [4], the vortex generators [5], the implementation of split blades [6], and the combination of airfoils with vortex generators [7] on their surface and microcylinders [8].

Among the limited research conducted, the circular microcylinder stands out as the most commonly studied shape for supplementary objects. It was shown that the size, angle of attack, as well as the position of the microcylinder and the Reynolds number have an impact on the improvement of aerodynamic parameters. Existing studies in the literature have indicated that the optimal diameter of the cylinder should be $d/c = 0.01$, as microcylinders with smaller diameters do not significantly affect the flow [9]. The impact of microcylinders is most often tested at large rake angles of 16–23°, as these angles generate boundary layers that are influenced by strong pressure gradients [9]. The addition of microcylinders delays flow detachment [8]. An important factor influencing the effectiveness of microcylinder additions is their location relative to the airfoil. Placing the microcylinder too close to the leading edge of the airfoil blocks the flow and negatively affects the lift of the airfoil. As the gap increases, flow blockage decreases, resulting in increased lift. However, this also reduces the influence of the microcylinder on the airfoil flow. Hence, the gap cannot be excessively large [9]. This suggests that the effectiveness of the microcylinder in modifying the flow characteristics is dependent on the diameter of microcylinder and its

location, emphasizing the importance of considering these parameters when studying aerodynamic interactions between microcylinders and airfoils.

A numerical study conducted by Mostafa et al. [10] revealed that the impact of adding a microcylinder in front of an airfoil is more pronounced at higher Reynolds numbers (5×10^5, 7.5×10^5, 1×10^6) compared to a lower Reynolds number (3.5×10^5), where the effect of the microcylinder addition was relatively smaller.

The main objective of the conducted optical studies is to gain insight into the aerodynamic behavior of the NACA 0012 airfoil and to explore the potential applications of flow control to improve its performance at high angles of attack and low Reynolds number. In the further part of the work, the effect on the flow characteristics around the NACA 0012 airfoil after adding a circular microcylinder at high angles of attack was checked.

2. Methodology

The experiment was carried out in a wind tunnel with a square cross-section of 0.3×0.3 m^2 and a length of 2 m. The object of the research, the NACA 0012 airfoil-microcylinder configurations, was located in the centre of the measurement section of the wind tunnel. The NACA 0012 airfoil had a chord dimension of $c = 0.2$ m and a span of 0.26 m. The circular-shaped microcylinder with dimension $d/c = 0.015$ was added to the airfoil and the distance s between the microcylinder and the surfaces of the airfoil was $s = 0.025c$, see Fig. 1. The inlet velocity was $U_\infty = 5$ m/s, and the Reynolds number equaled 66400.

The research utilized the particle image velocimetry (PIV) method with hardware and software provided by Dantec Dynamics. The flow images were recorded using the SpeedSense VEO340 CCD camera. For illumination, a two-pulse laser emitting two pulses with a power of 25 mJ and a wavelength of 527 nm, with a repetition frequency of up to 20 kHz, was employed to illuminate DEHS oil particles with an approximate size of 1 μm.

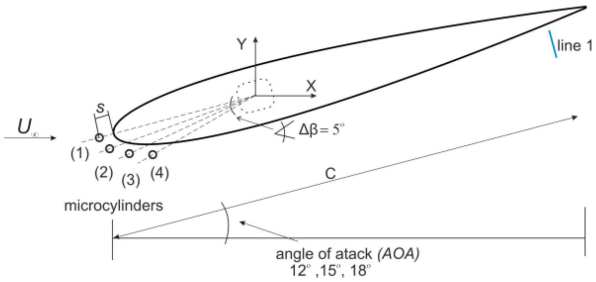

Fig. 1. Scheme of measuring the profile of a NACA 0012 airfoil with added microcylinders.

3. Results

The PIV measurements were conducted at high angles of attack (AoAs) ranging from 12 to 18° on both the controlled and uncontrolled airfoil. The velocity field attended as the observable parameter, allowing for qualitative and quantitative comparisons through the PIV tests. The normalized streamwise velocity U/U_∞ (a) and turbulent kinetic energy $TKE/(U_\infty)^2$ (b) are shown in Fig. 2.

After analyzing the results, the qualitative change in the airflow around the airfoil at different angles were observed. As the angle of attack (AoA) increases from 15 to 18° compared to the 12° angle, we observe earlier detachment of the boundary layer at the lower edge of the airfoil. In addition, under the separation point, there is an area of velocity acceleration for all angles. In terms of normalized turbulent kinetic energy, an intensified turbulence field appears at the lower edge of the airfoil for angles 15° and 18°, which is not observed at the 12°

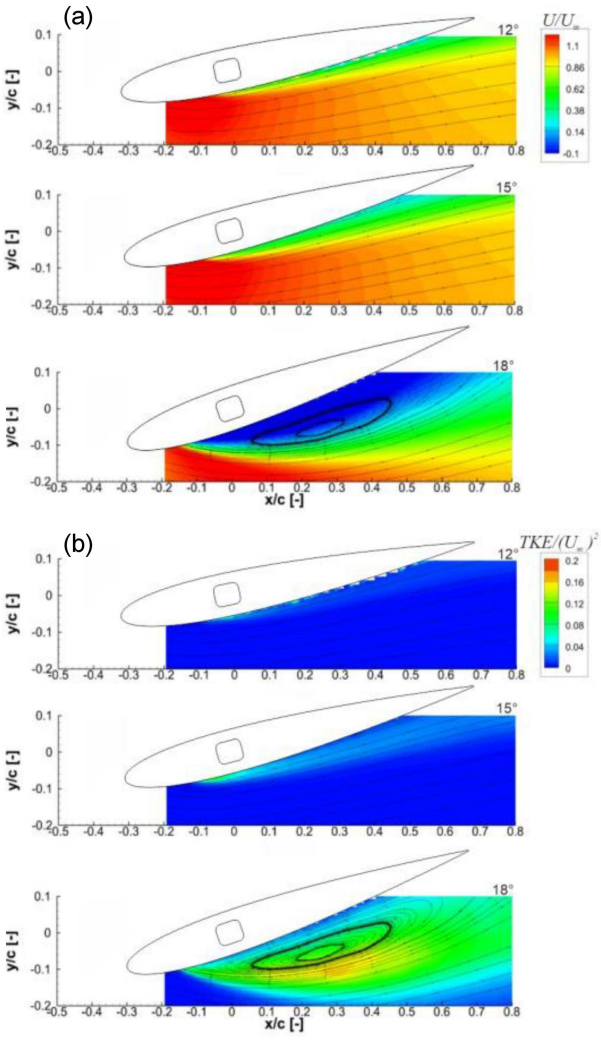

Fig. 2. The streamwise velocity U/U_∞ and the turbulent kinetic energy $TKE/(U_\infty)^2$ for different angle of attack (AoA).

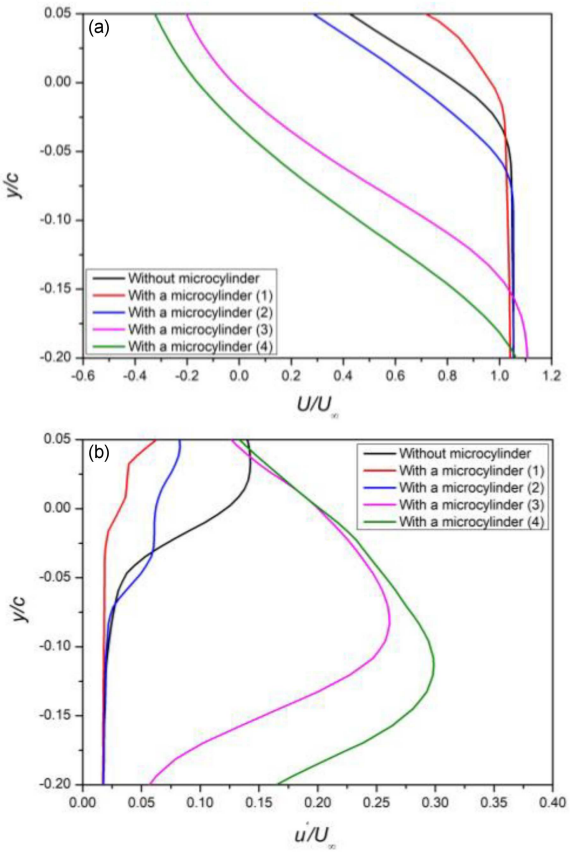

Fig. 3. The streamwise velocity component (a) and the fluctuation velocity component (b) along line 1 at AoA = 15°, both without and with microcylinder added at positions 1–4.

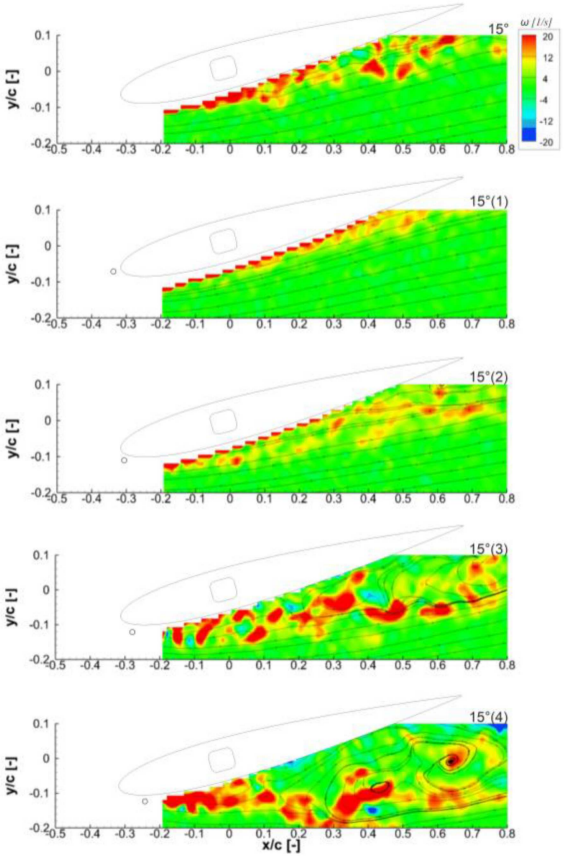

Fig. 4. The instantaneous vorticity (ω [1/s]) at AoA = 15°, both without microcylinder and with microcylinder added at positions 1–4.

angle. The streamlines have been added to highlight flow variations in both the normalized streamwise velocity U/U_∞ fields and the normalized turbulent kinetic energy $TKE/(U_\infty)^2$ near the lower edge of the airfoil.

In the second part of the experiment, microcylinders were introduced at four specific positions in relation to the airfoil: two positions in front of the leading edge (position 1 and 2), and at two positions below the lower edge of the airfoil (position 3 and 4). These additions were implemented at the selected angle of 15°, which was chosen for further investigation due to its significant quantitative differences compared to the 12° angle. Furthermore, at the 15° angle, an increase in the turbulence field along the suction surfaces of the airfoil was observed, which is considered a undesirable phenomenon.

Figure 3a illustrates the normalized streamwise velocity profiles for an angle of 15°, for both situations, without microcylinders and with microcylinders at four distinct positions. The location from which the profiles were downloaded is marked on the diagram in Fig. 1. Upon analyzing the graph (Fig. 3a), it is evident that the normalized velocity profile without added microcylinders exhibits an enlarged region with lower velocity values near the lower edge, especially from $y/c = 0.025$ to 0.05. Conversely, the introduction of microcylinders at position 1 results in an increase in velocity (U/U_∞) in this region to approximately 0.5, concurrently reducing the area of this velocity from y/c = 0 to 0.05. This is the most favorable outcome because it minimizes the drop in inlet velocity near the lower edge of the airfoil. For position 2, a slight decrease in velocity is observed in comparison to the configuration without the microcylinder. However, positions 3 and 4, as depicted in Fig 3a, exhibit a significant reduction of velocity, indicating an earlier detachment of the boundary layer compared to the case without the microcylinder.

In the same cases, the distribution of fluctuations u'/U_∞ is depicted in the graph in Fig. 3b. It is worth noting that a slight increase in fluctuations is observed in the region from $y/c = -0.05$ to 0.05 for cases with microcylinders 1 and 2, compared to the case without microcylinders. For cases 3 and 4, the fluctuations are substantially larger in the range $y/c = -0.2$ to -0.05.

Figure 4 shows the instantaneous vorticity at AoA = 15°, both without microcylinders and with the inclusion of microcylinders at four different positions. Analyzing the presented results, it is evident

that an intensified vortex field forms beneath the lower edge of the airfoil. Following the addition of circular-shaped microcylinders, the most significant reduction is observed for position 1. However, for positions 2–4, the reduction is smaller in comparison to the case without microcylinders, but still greater than that observed for position 1. For positions 2, 3, and 4, there is no reduction compared to the case without microcylinders, and the results have even deteriorated. An intensified vortex field is observed under the lower edge of the airfoil.

4. Conclusions

Summarizing the presented results, a significant qualitative changes are observed when comparing angles 12° and 15°. At angle of 15°, there is an increase in negative velocity fields and a larger region of higher turbulence along the on the suction surface of the airfoil. The introduction of the microcylinder had a positive effect at positions forward the leading edge of the airfoil. Particularly, the placement of a microcylinder at position 1 yielded the most substantial improvements, as indicated by the graphs and the observed instantaneous vortex fields.

Acknowledgments

This work has been supported by the statutory funds BS/PB-1-100-3016/2023/P and the Polish National Agency of Academic Exchange under Grant PPI/APM/2019/1/00062.

References

[1] S. Yarusevych, P. Sullivan, J.G. Kallava, *J. Fluid Mech.* **632**, (2009).

[2] M. Awasthia, D.J. Moreaua, C.J. Doolana, *Exp. Thermal Fluid Sci.* **99**, 94 (2018).

[3] J.C.S. Lai, M.F. Platzer, *AIAA J.* **37**, 1529 (1999).

[4] S.A. Prince, V. Khodagolian, C. Singh, T. Kokkalis, *AIAA J.* **47**, 2232 (2009).

[5] M. Manolesos, S.G. Voutsinas, *J. Wind Eng. Ind. Aerodyn.* **142**, 130 (2015).

[6] M. Moshfeghi, S. Shams, N.Hur, *J. Wind Eng. Ind. Aerodyn.* **167**, 148 (2017).

[7] R. Gnatowska, K. Gajewska, R. Kańtoch, *Acta Phys. Pol. A* **139**, 586 (2021).

[8] J.S. Wang, J. Wu, J.J. Wang, *Exp. Fluids* **64**, 4 (2023).

[9] D. Luo, D. Huang, X. Sun, *J. Wind Eng. Ind. Aerodyn.* **170**, **256** (2017).

[10] W. Mostafa, A. Abdelsamie, M. Mohamed, D. Thévenin, *IOP Conf. Ser. Mater. Sci. Eng.* **973**, 012040 (2020).

Proceedings of "Applications of Physics in Mechanical and Material Engineering" (APMME 2023)

The Phenomenon of Magnetic Anisotropy in Amorphous Materials Produced Using the Injection-Casting Method

M. Nabiałek[a], J.J. Wysłocki[a], T. Jaruga[b], K. Błoch[a], A.V. Sandu[c,d], V.V. Savinkin[e], M.A.A. Mohd Salleh[f,g] and B. Jeż[b,*]

[a]*Department of Physics, Faculty of Production Engineering and Materials Technology, Czestochowa University of Technology, al. Armii Krajowej 19, 42-200 Częstochowa, Poland*
[b]*Department of Technology and Automation, Faculty of Mechanical Engineering and Computer Science, Czestochowa University of Technology, Al. Armii Krajowej 19c, 42-200 Częstochowa, Poland*
[c]*Faculty of Material Science and Engineering, Gheorghe Asachi Technical University, 64 Dumitru Mangeron Blvd, 700050 Iaşi, Romania*
[d]*Academy of Romanian Scientists, 54 Splaiul Independentei St., Sect. 5, 050094 Bucharest, Romania*
[e]*Department "Transport and Mechanical Engineering", Faculty of Transport and Mechanical Engineering, M. Kozybayev North Kazakhstan University, 86 Pushkin str., 150000, Kazakhstan, Petropavlovsk*
[f]*Center of Excellence Geopolymer and Green Technology, Universiti Malaysia Perlis, Taman Muhibbah, 02600 Arau, Perlis, Malaysia*
[g]*Faculty of Chemical Engineering and Technology, Universiti Malaysia Perlis, Taman Muhibbah, 02600 Arau, Perlis, Malaysia*

Doi: 10.12693/APhysPolA.144.410 *e-mail: barlomiej.jez@pcz.pl

The magnetisation process of magnetic materials is extremely important due to the potential applications of these materials. During the magnetisation process, a delay in the increase in magnetisation is observed when the magnetic field strength increases. This behaviour may be explained by the magnetic anisotropy of the studied material. The paper presents the results of research on primary magnetisation curves for magnetic alloys that exhibit soft-magnetic properties. The tested alloys are the so-called amorphous materials in which determining the preferred direction of magnetisation is difficult due to their structure. However, as our research indicates, it is in fact possible to distinguish directions of relatively easy and difficult magnetisation in amorphous materials, which implies that the phenomenon of magnetic anisotropy occurs in them.

topics: magnetic anisotropy, primary magnetisation curve, saturation magnetisation, injection casting method

1. Introduction

Amorphous alloys are an interesting field of study. Due to their disordered structure, their properties differ from their crystalline counterparts with the same chemical composition [1]. Amorphous alloys are characterised by excellent mechanical properties (Ti, Zr, Fe alloys [2–4]) and/or corrosion resistance [5, 6]. Alloys with a sufficiently high proportion of ferromagnetic elements possess very good soft magnetic properties, i.e., low coercivity field value, low re-magnetisation losses and high saturation magnetisation value [7–10].

Due to the lack of an ordered structure, the domain walls can rotate quite freely, which facilitates the process of magnetisation in these materials. In crystalline materials, the magnetic structure is associated with the orientation of the crystals [11, 12]. In the case of amorphous alloys, despite the absence of an ordered structure, the easy direction of magnetisation can be determined; this is associated with the production process of these alloys [13]. So far, this phenomenon has not been fully explained, including the effect of individual alloy components on the change in anisotropy values.

The aim of this study is to investigate the effect of Cu addition on the effective anisotropy found in soft magnetic amorphous alloys based on Fe matrix.

2. Experimental procedure

The base alloy for the production of the rapidly-cooled samples was produced in an arc furnace. The ingots, each weighing 10 g, were melted and formed from high-purity ingredients: Fe, Co, Y, Cu — 99.99%, B — 99.9%. The elements were weighed with an accuracy of 0.0001 g. The mixture of elements was placed in a recess on a water-cooled copper plate. The re-melting process was carried out under a protective atmosphere of argon using a tungsten electrode. The ingots were re-melted six times physically inverting them each time in order to mix the ingredients.

Bulk, rapidly-cooled samples were produced using an injection method. The process was carried out under a protective atmosphere of argon, after having previously obtained a high vacuum in the working chamber. The base alloy was placed in a quartz crucible (with an opening of 1 mm diameter) and melted using eddy currents. The liquid alloy was forced under argon pressure into a copper mould. The samples were obtained in the form of rods, each with a length of 20 mm and a diameter of 0.5 mm.

The structure of the alloys was studied using a Bruker D8 Advance X-ray diffractometer. The diffractometer is equipped with a Cu K_α lamp. Measurements were carried out within the 2θ angle range of 30–100° on samples subjected to low-energy pulverisation.

Primary magnetisation curves and static magnetic hysteresis loops were measured using a Lake Shore 7307 vibrating sample magnetometer within the range of external magnetic field strength of up to 2 T.

3. Results

Figure 1 shows X-ray diffraction images for the investigated alloy samples. In the diffractograms, single wide maxima are visible, indicating the disordered structure of each alloy. There are no narrow peaks of significant intensity that would be associated with the presence of crystalline phases.

Figure 2 shows the static magnetic hysteresis loops measured in three directions, i.e., parallel to the casting direction, perpendicular to the casting direction, and perpendicular to the sample surface. The loops measured for the $Fe_{35}Co_{35}Y_{10}B_{20}$ alloy in the direction parallel to the casting direction and perpendicular to the casting direction are identical.

The curve measured perpendicular to the surface of the alloy (green colour) is characterised by a different shape — the alloy achieves a higher

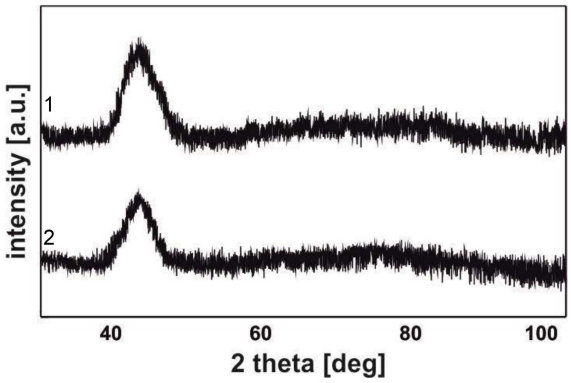

Fig. 1. X-ray diffraction patterns for the rod-form samples of the investigated alloys: curve 1 — $Fe_{35}Co_{35}Y_{10}B_{20}$, curve 2 — $(Fe_{35}Co_{35}Y_{10}B_{20})_{99}Cu_1$.

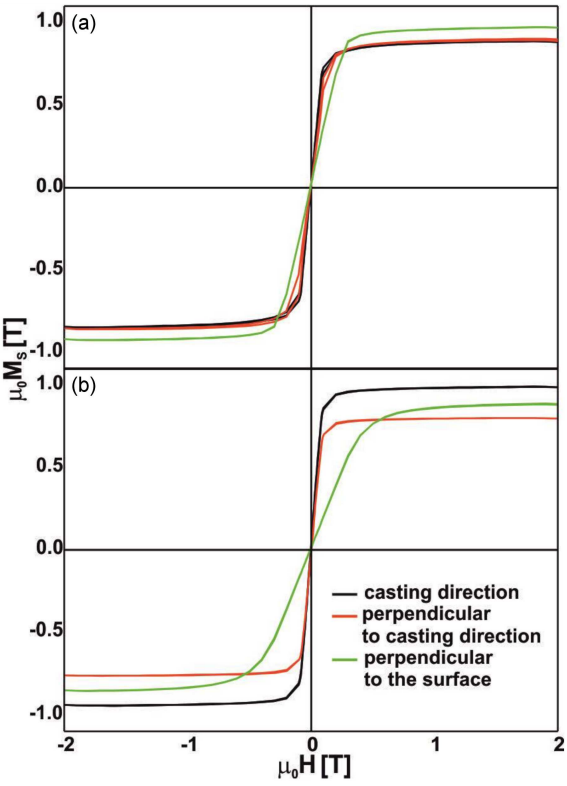

Fig. 2. Static magnetic hysteresis loops for tested amorphous alloys: (a) $Fe_{35}Co_{35}Y_{10}B_{20}$, (b) $(Fe_{35}Co_{35}Y_{10}B_{20})_{99}Cu_1$.

TABLE I

Calculated parameters: $\mu_0 M_S$ — saturation magnetisation [T], H_C — coercivity field [A/m], P_1 — anisotropy field in the first direction [kJ/m^3], P_2 — anisotropy in the second direction [kJ/m^3], P_3 — anisotropy in the third direction [kJ/m^3].

	$\mu_0 M_S$	H_C	P_1	P_2	P_3
$Fe_{35}Co_{35}Y_{10}B_{20}$	0.96	230	83	105	127
$(Fe_{35}Co_{35}Y_{10}B_{20})_{99}Cu_1$	0.95	135	55	35	207

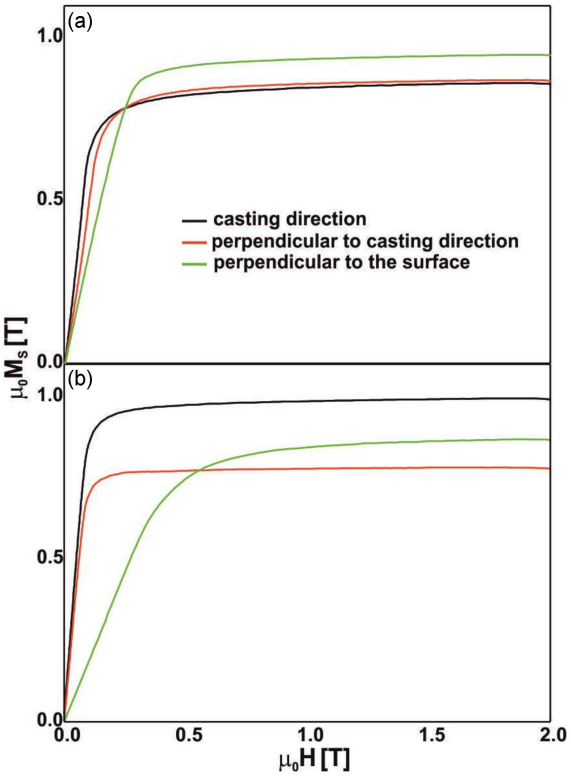

Fig. 3. Initial magnetisation curves, measured in three directions 1, 2, 3, for the tested alloys: (a) $Fe_{35}Co_{35}Y_{10}B_{20}$, (b) $(Fe_{35}Co_{35}Y_{10}B_{20})_{99}Cu_1$.

saturation of magnetisation value (M_S), but at lower values of magnetic field strength it attains a lower magnetisation value. For the alloy with the addition of Cu, similar relationships were observed, except that the curve for the perpendicular direction differs to a greater extent from the other two. The other curves (black and red) have a very similar course; however, where the sample was measured parallel to the casting direction, a much higher M_S value was achieved. The coercivity field values, measured for all three directions, reached similar values (shown in Table I).

Figure 3 shows the initial magnetisation curves, measured using the same system as the static magnetic hysteresis loops. Based on the shapes of the curves, the effective anisotropy was calculated. The results are given in Table I.

The addition of Cu causes a significant change in the shape of the primary magnetisation curves, and thus in the value of effective anisotropy. For the two easy magnetisation directions (perpendicular and parallel to the casting direction), a significant decrease in the values of P_1 and P_2 and an increase in the P_3 value were observed. In addition, the value of the coercivity field for the alloy with the addition of Cu is almost halved. Therefore, it should be assumed that the addition of Cu affects the formation of a certain short-range order in the alloy volume, and therefore the directivity in certain areas of the alloy (it is possible that, in the volume of the alloy, there are areas similar in atomic configuration to crystalline phases). This arrangement affects the course of magnetisation, promoting it in some directions and hindering in other directions.

4. Conclusions

This paper presents the results of research on the influence of Cu on the value of effective anisotropy occurring in bulk Fe-based amorphous alloys. Based on vibrating sample magnetometer measurements, made in three different directions, it was found that easy and difficult directions of magnetisation occur in the tested alloys. In addition, a 1% addition of Cu was found to influence the degree of this effect. The alloy $(Fe_{35}Co_{35}Y_{10}B_{20})_{99}Cu_1$ is characterised by a much lower value of coercivity field and — for the easy direction of magnetisation — a much lower value of effective anisotropy.

Acknowledgments

Publication supported by IRN AP14869177 project "Development and implementation of a new high-performance mobile railway complex with resource-saving technology for laser restoration of railway wheel sets".

References

[1] M.E. McHenry, M.A. Willard, D.E. Laughlin, *Prog. Mater. Sci.* **44**, 291 (1999).

[2] S. Hasani, P. Rezaei-Shahreza, A. Seifoddini, *Metall. Materi. Trans. A* **50**, 63 (2019).

[3] Y.J. Yang, B.Y. Cheng, J.W. Lv, B. Li, M.Z. Ma, X.Y. Zhang, G. Li, R.P. Liu, *Mater. Sci. Eng. A* **746**, 229 (2019).

[4] K. Lee, S.E. Kang, *Arch. Metall. Mater.* **65**, 1357 (2020).

[5] S. Wang, Y. Li, X. Wang, S. Yamaura, W. Zhang, *J. Non-Cryst. Solids* **476**, 75 (2017).

[6] D.D. Liang, X.S. Wei, T.C. Ma, B. Chen, H.R. Jiang, Y. Dong, J. Shen, *J. Non-Cryst. Solids* **510**, 62 (2019).

[7] M. Nabiałek, B. Jeż, K. Błoch, J. Gondro, K. Jeż, A.V. Sandu, P. Pietrusiewicz, *J. Alloys Compd.* **820**, 153420 (2020).

[8] B. Jeż, J. Wysłocki, S. Walters, P. Postawa, M. Nabiałek, *Materials* **13**, 1367 (2020).

[9] Y. Han, J. Ding, F.L. Kong, A. Inoue, S.L. Zhu, Z. Wang, E. Shalaan, F. Al-Marzouki, *J. Alloy Compd.* **691**, 364 (2017).

[10] T. Suetsuna, H. Kinouchi, N. Sanada, *J. Magn. Magn. Mater.* **519**, 167475 (2021).

[11] L. Zhu, S.S. Jiang, Z.Z. Yang, G.B. Han, S.S. Yan, Y.G. Wang, *J. Magn. Magn. Mater.* **519**, 167513 (2021).

[12] S. Walters, M.M.A.B. Abdullah, A.V. Sandu, S. Garus, M.A.A. Mohd Saleh, D.S. CheHalin, F.F. Zainal, *Acta Phys. Pol. A* **139**, 568 (2021).

ACTA PHYSICA POLONICA A
Volume 144 — Number 5

Proceedings of "Applications of Physics in Mechanical and Material Engineering" (APMME 2023), Częstochowa, Poland, June 29, 2023